PRESSURE STIMULATED VOLTAGE DETECTION IN MANMADE AND GEOLOGICAL MATERIALS

James William Archer

BEng (First Class Hons.)

Sensor Technology Research Centre

Department of Engineering and Design

University of Sussex

This dissertation is submitted for the degree of Doctor of Philosophy

January 2017

This thesis is dedicated to my parents for all their love and support and putting me through the best education possible. I appreciate their sacrifices and wouldn't have been able to get to this stage without them.

DECLARATION

This dissertation is the result of my own work and includes nothing, which is the outcome of work done in collaboration except where specifically indicated in the text. It has not been previously submitted, in part or whole, to any university or institution for any degree, diploma, or other qualification.

Signed: _____

Date: *26/01/2017*

James William Archer BEng

University of Sussex

ABSTRACT

This thesis investigates pressure stimulated voltages (PSVs) in manmade and geological materials using a field capable and commercially viable electric potential sensor (EPS) technology. Sensing technologies are of great importance for the structural health monitoring (SHM) of manmade and geological structures and are critical for improving the health and safety of humans and infrastructure. A wide variety of sensing technologies are needed to assess damage over structures. Work by others involves measuring pressure stimulated electrical emissions (PSEs) (i.e. the study of pressure stimulated voltage, electric field and current) that are related to acoustic emissions (AEs) in rock and cement mortar, and also mechanical properties. Although these studies yield promising results, the measurement tools (laboratory electrometers and electromagnetic emissions (EME) antennas) are not suitable for field use. This is predominantly because of the need of Faraday shielding to reduce noise, plus the impracticalities and high costs associated with using laboratory instruments for SHM. However, the EPS developed at the University of Sussex is capable of measuring PSVs in rocks and is field capable.

In this thesis, PSVs in rocks and man-made materials were measured using two EPS variants. An existing capacitively coupled sensor was used to measure high frequency (25.5 mHz to 750 kHz) transient PSVs associated with cracking. In addition, a novel directly coupled smart EPS was developed for monitoring low frequency (DC to 250 Hz) PSVs associated with applied stress. A signal conditioning and data reduction procedure was developed for PSV emissions analogous to methods used for AE. A new robust method for measuring PSV was established in which cylindrical material specimens were instrumented with strain gauges, piezo transducers and EPSs to measure strain, AE and PSV respectively and a force transducer was used to measure the applied load.

The results showed that PSVs were detected in a wide range of piezo and non-piezo rocks and for the first time in concrete, in the range of millivolts (0.32 mV – 1180 mV). Faraday shielding the experiments was not necessary as with other PSE monitoring technologies.

For oven dried materials there was some degree of correlation between PSV high frequency transient signals and AE (i.e. cracking). Rocks had cross-correlation coefficients ranging from 0.13 to 0.86, and the cross-correlation coefficient for concrete (0.24) was lower than most rock lithologies. Environmental conditions and the stage of uniaxial deformation of materials influence PSV-AE cross-correlations. Water or saline saturation of materials generally reduced the PSV-AE cross correlation coefficients. During the cyclic loading of various rock lithology, a work hardening effect was observed in the PSV emissions analogous to the well-known Kaiser and Felicity effect of AE. A likely reason for the PSV-AE correlations is that PSVs are generated by the movement and separation of fresh charged fracture surfaces. EPS could be a cost effective and more advanced technology for detecting cracking in structures and in combination with piezo transducers, could be used to identify material deformation stages.

There was a linear relationship between applied stress and DC/low frequency PSV in piezo rocks ($r^2 = 0.84$) but not non-piezo rocks ($r^2 = 0.0063$). The piezoelectric effect of quartz is the most likely generation mechanism behind the PSV-stress relationship. The novel, directly coupled, smart EPS is a successful design as it has the necessary high input impedance and low noise characteristics for measuring PSVs noninvasively at low frequencies. EPS could be the first non-invasive technology for in-situ stress measurement in quartz bearing rocks; current methods involve disturbing the rock mass and are expensive to implement.

In conclusion, the results show that the EPS-PSV measurement technique is viable for the SHM of rocks and concrete. Although, factors such as material composition, environmental condition and type of material deformation influence PSV characteristics and would need to be accounted for in real world applications.

Future directions for the research would involve the development of a “real time” PSV event detection system for long term monitoring of structures for SHM applications. Additionally, large scale testing of different material samples in different environmental conditions and the testing of larger structures using arrays of EPS would be necessary before commercialisation.

Future commercialisation could result in a restively coupled broadband monolithic semiconductor EPS being developed for SHM to monitor PSVs associated with applied stress and cracking events simultaneously. This would produce a more cost effective and advanced tool than existing technologies, such as piezo transducers for monitoring AE and in-situ stress monitoring techniques.

ACKNOWLEDGEMENTS

Undertaking a PhD has been a rewarding and life changing experience for me and would not have been possible without the guidance and support of many people.

First of all, I would like to thank my supervisor Prof. Robert Prance for his support and encouragement throughout the duration of the PhD. His academic and technical knowledge was invaluable and this thesis would not have been possible without his guidance and feedback. I would also like to thank Dr Ahmet Aydin for convincing me to embark on a PhD, introducing me to project partners at the British Geological Survey and teaching me the principles of material testing.

This project would not have been possible without the in-kind use of the British Geological Survey's Rock Mechanics and Physics Laboratory and guidance and expertise from their staff. The laboratory manager Marcus Dobbs contributed a huge amount to the project including sourcing of rocks, material testing and co-authoring journal papers and conference proceedings. His knowledge of material testing and rock mechanics is second to none. I would also like to thank Dr Helen Reeves for supervising the project at BGS and also Mathew Kirkham, Dr David Gunn and Dr Audrey Ougier-Simonin for assisting in the project.

Everyone at the University of Sussex Sensor Technology Research Centre was incredibly encouraging and enthusiastic over the years and helped me develop my ideas and myself as an academic. Martin Nock's (aka uncle Martin) is an incredibly helpful and skilled research technician and helped me to debug my electronic designs, advised me about technical aspects of the project and even fixed my bike. Working in the lab was made more enjoyable with constant banter and our Iranian colleagues teaching us "useful" phrases in Farsi.

Last but not least, I would like to thank my friends and family for putting up with me over the course of my PhD and for all of the good times and pleasant memories we shared. Without their encouragement, I would not have got this far.

CONTENTS

LIST OF TABLES

LIST OF FIGURES

List of Abbreviations and Acronyms

ADC	–	analogue to digital converter
AE	–	acoustic emission
ASR	–	anelastic strain recovery
BGS	–	British Geological Survey
CAM	–	computer aided manufacturing
CT	–	computed tomography
DAC	–	digital to analogue converter
DAQ	–	data acquisition
DSCA	–	differential strain curve analysis
EDL	–	electrical double layer
EME	–	electromagnetic emission
EMR	–	electromagnetic radiation
EPIC	–	electric potential integrated circuit
EPS	–	electric potential sensor
FBG	–	fibre Bragg grating
FR	–	Felicity ratio
FRF	–	frequency response function
GF	–	gauge factor
GHM	–	global health monitoring
GUI	–	graphical user interface
HDT	–	hit definition time
HLT	–	hit lockout time
HPC	–	high performance cluster
HPF	–	high pass filter
HYTPF	–	hydraulic test in pre-existing fracture
IC	–	integrated circuit
IO	–	input output
ISRM	–	International Sociality of Rock Mechanics
LCD	–	liquid crystal display

LHM	–	local health monitoring
LPF	–	low pass filter
MARSE	–	measured area of the rectified signal envelope
NDT	–	non-destructive testing
OFS	–	optical fibre sensors
PC	–	personal computer
PCB	–	printed circuit board
PDT	–	peak definition time
PEPS	–	persistence electric potential signals
P-holes	–	positive holes
PML	–	previous maximum load
PSC	–	pressure stimulated current
PSE	–	pressure stimulated electrical emission
PSV	–	pressure stimulated voltage
PZT	–	lead zirconate titanate
RAM	–	random access memory
RO	–	reverse osmosis
RTD	–	ramp to destruction
RTI	–	referred to input
SHM	–	structural health monitoring
SLS	–	step like stress
SMD	–	surface mount device
SRS	–	seismic radio wave signals
STRC	–	Sensor Technology Research Centre
SVOW	–	surface vibration optical wave
TEPS	–	transient electric potential signals
VLF	–	very low frequency

1 INTRODUCTION

The aim of this chapter is to provide background information to the thesis (section 1.1); an overview of the research objectives, originality and significance (section 1.2); to highlight the research outcomes (section 1.3). This chapter concludes with an outline of the following chapters (section 1.4).

1.1 Background

Structural health monitoring (SHM) is of great importance for the safety of people and infrastructure. Frequently the assessment of civil and geological structures is carried out by engineers trained in visual inspection. This sometimes proves to be an inaccurate method for damage detection, especially if defects are internal to the structure [1]. There is a need for the development of SHM technologies in order to improve accuracy, cost effectiveness and reduce labour intensity for damage detection of civil and geological structures.

In the US the Federal Highway Agency has a mandate to evaluate the condition of over 500,000 highway bridges every two years [2]. Currently traditional evaluation methods are used involving visual inspection and tap tests; these methods typically are only useful for identifying damage on the surface of the structure. Although the US Federal spending for structurally obsolete bridges is ~$8 billion per year [3], bridges are unnecessarily retrofitted, replaced or even worse damage goes undetected. This is because of the large number of bridges and limited number of staff combined with flaws in the traditional evaluation methods.

In the UK, there are many offshore structures, such as wind turbines in the North Sea now reaching or having exceeded their original design life. A wide range of sensing technologies and techniques have been evaluated for SHM by the British Health and Safety Executive [4] to address this problem. These SHM technologies can demonstrate continued safe operation of the structure even after its original design lifetime has been exceeded, thus helping with maintenance and upkeep of the structures.

The monitoring of geological structures is also important; landslides resulting from rock slope factures are major hazards and have killed more than 50,000 people on a global basis in the 20th century [5]. The monitoring of rockslide movement provides critical information for short-term and long term predictions and for risk management [5]. Often it is too financially expensive to stabilise a rock slide, however SHM technologies can be used to set up early warning systems, giving time for people to evacuate the area.

Over the past two decades there has been great interest in innovation of SHM sensing technologies as well as development of large scale SHM systems in engineering and academia [6-9]. Despite the great potential of SHM technologies they have not been employed on a large scale [1], mainly because there are a lack of reliable and affordable generic monitoring systems [10].

1.2 Research objectives and significance

This thesis investigates pressure stimulate voltages (PSVs) in manmade and geological materials using a cost effective and commercially viable electric potential sensor technology (EPS).

The most significant aspect of the research presented in thesis is that the EPS technology used, could be the first viable sensing technology for the field monitoring of pressure stimulated electrical emissions (PSEs) in structures outside of the laboratory setting. Laboratory studies by others have used benchtop electrometers and electromagnetic emissions (EMEs) antennas for monitoring PSEs in various materials. The measurement methods used are not likely suitable for field use outside of the laboratory setting, as described in section 3.3.

The PSV-EPS method is unique in that the monitoring of crackling events and in-situ stress could be achieved simultaneously. The implications of using EPSs for PSV detection could be a new non-invasive and more cost-effective method for crack detection and in-situ stress determination in insulating materials such as rocks and concrete; that could either replace or complement existing technologies.

There have not been any studies by others investigating PSEs in wide variety of different rock lithology. This thesis aims to addresses this problem; eight different rock lithology including rocks with little to no piezoelectric minerals and rocks high in piezoelectric minerals were tested in chapters 6, 8 and 9 to investigate the effects of rock lithology on PSV during uniaxial loading. The resulting outcomes contribute to the scientific communities understanding of PSE generation mechanisms and a PSE based SHM technique for geological structures was developed.

Concrete is one of the most widely used materials in civil structures; an objective of this thesis was to develop a method and detect PSVs in this material. Experiments were carried out to investigate PSVs in concrete specimens during uniaxial loading in chapter 7, PSVs were detected and a hypothesis dawn about their generation mechanisms. In fact, this thesis is there first study investigating PSVs in concrete.

Most laboratory studies by others investigating PSE, used dry materials. This is an unrealistic approach; for real world SHM problems the materials are likely to have varying degrees of water or saline saturation from the surrounding environment. Although, there have been laboratory studies by others investigating the electrokinetic effect of water movement [11, 12] and transmission of PSEs in wet rocks [13]. This thesis is the first study investigating the effect of environmental conditions on PSE behaviour. This was achieved by assessing how varying degrees of water and saline saturation effect PSV emissions in a wide range of rock lithology and concrete.

Two different variants of EPS were used to measure PSVs in manmade and geological materials. An existing capacitively coupled EPS was used to measure high frequency (25.5 mHz to 750 kHz) transient PSVs, that appear to correlated with acoustic cracking events. In addition, a novel directly coupled smart EPS was developed for motoring low frequency (DC to 250 Hz) PSVs that appear to be related to applied stress within the material.

To accurately characterise PSVs a measurement method for their detection in rock and manmade materials was developed. Several capacitive coupling methods were refined, to be effective in different environmental conditions (oven dried, air dried, water saturated and saline saturated) that might occur in SHM applications outside of the laboratory setting. Additionally, a directly coupled flexible electrode structure was developed for robust connections between the directly coupled smart EPSs and material specimens.

A material testing method was refined using piezo transducers, EPS, strain gauges and force transducers to measure AE, PSV, strain and force respectively; and a servo controlled load frame was used to apply load. All testing was carried out in accordance with the International Society of Rock Mechanics (ISRM) [14] testing standards.

1.2.1 Development of new SHM method for crack detection by the non-invasive measurement of PSVs using an existing capacitively coupled EPS

Damage in structures is related to crack development and propagation, which is currently monitored using costly acoustic emissions (AEs) systems. The monitoring of PSVs using EPSs could be used as a more cost effective alternative or complimentary technology.

The relationship between cracking and PSVs are not fully understood, however research in this area is of great importance for developing new SHM tools. Currently there is only one published article [15] investigating statistical correlations between AEs (i.e. cracking) and PSEs and this was only conducted for cement mortar specimens.

An objective of this thesis was to investigate statistical relationships between PSV and cracking events in a wide range of materials and in different environmental conditions. Experiments were conducted and statistical correlations between PSVs and AEs in eight different rock lithology and concrete specimens were observed. There was some degree of correlation in all materials, the cross-correlations coefficients between PSE and AE emissions varied from 0.13 to 0.86 in oven dried rocks the coefficient (0.24) for oven dried concrete was less than most rock lithologies.

PSV-AE correlations were also tested in different environmental conditions to help produce a more robust SHM technique for applications outside of the controlled laboratory environment. In general, it appears that water and saline saturation decreases the cross-correlation coefficients between PSV and AE events. The results indicate that the PSV emissions are partly generated by the movement and separation of fresh charged fracture surfaces. Therefore, the EPS-PSV method could be a viable SHM tool for monitoring cracking, and for advancing the scientific communities knowledge of PSE generation mechanisms.

A PSV event detection method was developed to reduce data size analogous to the widely implemented AE event detection methods. The objective of this procedure was to prove the principle for PSV event detection. This procedure reduces data size and thus allows the possibility of long term monitoring of

structures, without sacrificing the high sampling rates needed for crack detection. The results of material testing in chapters 6 and 7 showed that the PSV event detection method is successful.

1.2.2 Development of new SHM method for stress monitoring by the non-invasive measurement of PSVs using a novel directly coupled smart EPS.

Currently there is not a method for monitoring in-situ stress non-invasively, however this would be of great importance for underground excavation and design for civil, mining, nuclear waste storage and petroleum engineering. However, the monitoring of PSEs could provide a means of non-invasive in-situ stress determination.

Work by others [16-18] has involved measuring pressure stimulated current (PSC) using laboratory electrometers; this is an electrically invasive method, that discharges the material specimens in the process of the measurement. Thus, the research has been limited to investigating the relationship between dynamic stress and PSC due to the limitations of the measurement method.

However, PSV measurement using EPSs is electrically non-invasive due to the ultra-high input impedance nature of EPSs. Previous EPS research [19, 20] for monitoring PSVs in rocks, utilised capacitively coupled sensors and thus low frequency signals could not be measured. The development of a directly coupled EPS for monitoring low frequency PSVs (DC to 250 Hz) allowed for the measurement of PSV signals associated with static in-situ stress. In this thesis a directly coupled smart EPS was designed and its specifications are documented in thesis section 4.6.

Material testing experiments in chapter 9 were carried out using the novel directly coupled smart EPS, to investigate relationships between low frequency PSV with applied stress in quartz rich and quartz poor rock lithologies during uniaxial loading. The results show a strong linear relationship between applied stress and PSV in sandstone (r^2 = 0.84) but not in calcite (r^2 = 0.063), likely due to the piezoelectric effect of quartz. This is significant because the results show PSVs are associated with applied stress and the EPS-PSV technique could be the first non-invasive method for in-situ stress determination.

1.3 Research outcomes

1.3.1 Journal publications

J. W. Archer, M. R. Dobbs, H. J. Reeves, R. J. Prance; Measurement and correlation of acoustic emissions and pressure stimulated voltages in rock using an electric potential sensor; International Journal of Rock Mechanics and Mining Sciences; August 2016.

1.3.2 Conference talks

M.R. Dobbs, **J. W. Archer**, H.J. Reeves, R.J. Prance; Physical and mechanical factors affecting stress induced electric potential field in rock; 10th Euroconference on Rock Physics and Rock Mechanics; May 2014.

J. W. Archer, M.R. Dobbs, H.J. Reeves, R.J. Prance; Measuring pressure stimulated electric potential in dielectric materials; Institute of Physics - Early Career Researcher Colloquium; September 2015.

J. W. Archer, M.R. Dobbs, H.J. Reeves, R.J. Prance; Measuring stress in rock using the electric potential sensor; Institute of Physics - Sensors & their Applications XVIII 2016; September 2016.

1.3.3 Conference posters

J. W. Archer, M.R. Dobbs, H.J. Reeves, R.J. Prance; Measuring Stress in Rock using Electric Potential Sensor Technology; 11th EURO-conference on Rock Physics and Geomechanics; September 2015.

1.4 Thesis outline

Chapter 1 – Introduction. The aim of this chapter is to provide background information to the thesis (section 1.1); an overview of the research objectives, originality and significance (section 1.2); to highlight the research outcomes (section 1.3). This chapter concludes with an outline of the following chapters (section 1.4).

Chapter 2 – Background. This chapter provides a background to structural health monitoring (SHM) including a definition of SHM (section 2.1); key components of the SHM process (section 2.2); and an introduction to the concepts of local and global health monitoring (section 2.3). In addition, a background to commercial SHM sensors and monitoring techniques are outlined with detailed descriptions of strain gauge technologies (section 2.4.1); acoustic emissions (AEs) instrumentation (section 2.4.2); and in-situ stress measurement methods (section 2.4.3).

Chapter 3 – Literature Review: Pressure Stimulated Electrical Emissions. This chapter introduces pressure stimulated electrical emissions (PSEs), i.e. the study of pressure stimulated voltage, electric field and current. PSE research motivation and its relationship with earthquakes is discussed in section 3.1. Followed by a literature review of the PSE generation mechanisms (section 3.2). To conclude an overview of the PSE measurement technologies is described in section 3.3.

Chapter 4 – The Electric Potential Sensor System. This chapter provides an introduction to the electric potential sensor (EPS) (section 4.1); followed by, an overview of electrometer and EPS circuit design principles (section 4.2 and 4.3) and methods of EPS characterisation in terms of input impedance, frequency response and noise (section 4.4). In addition, the detailed circuit designs for the capacitively coupled EPS (section 4.5) and information about previous research using the capacitively coupled sensor for PSV measurement (Section 4.5.4) are presented. Detailed circuit designs for the novel directly coupled smart EPSs (section 4.6), as well as EPS signal processing methods (section 4.7) can also be found in this chapter. Future directions for EPS design and commercialisation are discussed at the end of the chapter in section 4.8.

Chapter 5 - Materials and Methods. The aim of this chapter is to provide an overview of the material properties and preparation of materials for uniaxial testing experiments (section 5.1), presented in chapters 6, 7, 8 and 9. The preceding sections describe methods of coupling the electric potential sensors

(EPSs) to material specimens (section 5.2); material testing equipment details (section 5.3); uniaxial loading profiles applied during material testing experiments (section 5.4); and a definition of the stages of loading for brittle materials (section 5.5). In addition, information about sensor data acquisition (section 5.6), statistical methods (section 5.7) and control testing (section 5.8) are discussed.

Chapter 6 - Uniaxial Compressive Stress Testing of Rocks in Different Environmental Conditions using Capacitively Coupled EPSs. This chapter begins by stating the motivations behind the experiments carried out in this results chapter (section 6.1). A selection of results pages containing detailed observations of pressure stimulated voltage (PSV), acoustic emissions (AEs), stress and strain and statistical relationships between each measurement quantity, are provided in section 6.2. The results are then compared and discussed in the last part of the chapter (section 6.3).

Chapter 7 – Uniaxial Compressive Stress Testing of Manmade Materials in Different Environmental Conditions using Capacitively Coupled EPSs. This chapter describes the motivations behind the experiments carried out and presented in this results chapter in section 7.1. Followed by a section of results pages containing detailed observations of pressure stimulated voltage (PSV), acoustic emissions (AE), stress and strain for each material specimen tested and statistical relationships between each measurement quantity (section 7.2). Finally, all of the experimental results for each material specimen are compared and discussed in section 7.3.

Chapter 8 – Uniaxial Compressive Cyclic Stress Testing of Materials in Different Environmental Conditions Using Capacitively Coupled EPSs. In this chapter an introduction to the Kaiser and Felicity effect of acoustic emissions (AE) and the motivations behind the experiments carried out and presented in this chapter are presented in section 8.1. Followed by a selection of results pages (section 8.2) showing observations of pressure stimulated voltages (PSV), acoustic emission (AE) and stress for each material specimen tested. Each of the results pages presented shows a truth table indicating the presence of various effects observed in the PSV and AE activity. The results of each material specimen tested are compared and discussed in section 8.3 at the end of the chapter.

Chapter 9 – Uniaxial Compressive Step Like Stress Testing of Rocks Using Directly Coupled Smart EPSs. This chapter provides an introduction and motivations behind the experiments carried out and presented in this chapter in section 9.1. Followed by a selection of results showing detailed observations of PSV and applied stress for each material specimen tested (section 9.2) In addition the results pages give details of statistical relationships between pressure stimulated voltage (PSV) and applied stress for each material specimen. The last part of the chapter compares the results of all of the materials tested and discusses the outcomes (section 9.3).

Chapter 10 - Conclusions and Future Directions. The aim of this chapter is to conclude the findings of experiments presented in all results chapters 6, 7, 8 and 9 and explain future research objectives. Section 10.1 provides an overview and conclusions drawn from the ramp to destruction testing of manmade and geological material experiments, presented in chapters 6 and 7. The chapter continues in

section 10.2, by presenting an overview and conclusions drawn from the cyclic loading of manmade and geological material experiments, presented in chapter 8. For the step like stress experiments presented in chapter 9, the overview and conclusions are detailed in section 10.3. Future directions for pressure stimulated voltage (PSV) research using electric potential sensor (EPS) technology are outlined in section 10.4; followed by comments on the viability of a PSV-EPS based structural health monitoring (SHM) tool, in section 10.5.

Appendices. This chapter contains fully annotated software code used for key elements of work presented in this thesis as well as descriptions of the code structure. Code for the following devices and procedures are presented: EPS control interface device, automatic bootstrap calibration procedure and PSV event detection in Appendix. A, Appendix. B and Appendix. C respectively.

2 BACKGROUND

This chapter provides a background to structural health monitoring (SHM) including a definition of SHM (section 2.1); key components of the SHM process (section 2.2); and an introduction to the concepts of local and global health monitoring (section 2.3). In addition, a background to commercial SHM sensors and monitoring techniques are outlined with detailed descriptions of strain gauge technologies (section 2.4.1); acoustic emissions (AEs) instrumentation (section 2.4.2); and in-situ stress measurement methods (section 2.4.3).

2.1 Structural health monitoring (SHM)

SHM has been utilized since the early 19th century; an example of this is wheel tapping. In the age of steam locomotives, the job of the wheeltapper was to hit each individual train wheel with a special hammer and listen to the ringing sound it made thus evaluating the structural integrity of the wheel. If the wheel was cracked it would make a different sound to an intact wheel, like how a cracked drum symbol or bell would sound different to their intact counterparts.

2.1.1 Modern definition of SHM since 2004

In order to understand this definition properly we must first define the damage state of a structure. It can be defined as part of a five step process as described in [21]. The damage state can be evaluated by answering the following questions:

1) Is there damage in the system (existence)?
2) Where is the damage in the system (location)?
3) What kind of damage is present (type)?
4) How severe is the damage (extent)?
5) How much useful life remains (prognosis)?

"Structural Health Monitoring (SHM) is the process of implementing a damage detection strategy for engineering infrastructure" [21].

This thesis is focused on damage detection in materials and thus the definition of damage will be limited to changes in geometrical properties and connectivity. An example of damage could be the formation of cracks in a material altering the geometry and connectivity between fracture surfaces or changes in geometry due to strain in the material. In terms of damage time scales, damage first occurs at the material level (e.g. concrete), progresses to the component level (e.g. a bridge beam) and then to system level damage (e.g. failure of the bridge itself) [7].

Damage can accumulate over long time scales in a system as a result of fatigue or corrosion, for instance passing traffic over a bridge and weather corrosion. Discrete events such as earthquakes can also damage a system on a shorter time scale [7]. The fundamental idea behind detecting damage is that damage will change the stiffness, energy dissipation or mass of the system and thus the system frequency response

will be altered. The input to the system could be the load of a train passing over a bridge or a controlled vibration and the response of the system (the bridge) are measured using sensors before damage occurs so that the onset of damage/deterioration can be logged. Using statistical and structural modelling a prognosis estimating the condition and useful life of the structure can be produced.

This thesis focuses on damage detection on a material level using established (strain gauges and piezo transducers) and novel sensing technologies (the electric potential sensor (EPS)) to detect changes in strain, cracking events and electrical properties respectively in response to uniaxial loading.

2.2 Components of a SHM

The SHM process shown is Figure 2-1 involves measuring the system response over a length of time using an array of sensor technologies. The extraction of damage features from the sensor measurements and statistical analysis of these features determines the structural health of the system [7]. Although there have been significant advancements in sensor technologies to detect damage in structures the fundamental principles remain the same as the age old wheeltapper.

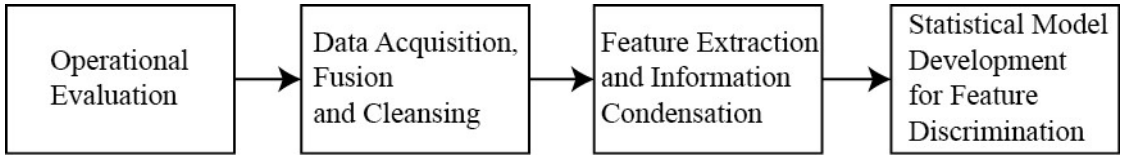

Figure 2-1 The SHM problem, a four part process [7].

2.2.1 Operational and Environmental Evaluation

2.2.1.1 Operation constraints

Operational constraints occur when the structure being monitored is in use, for example it may not be viable to close off a major bridge for the sole purpose of SHM thus the structure's frequency response will be measured from the excitation of moving traffic crossing the bridge. This can obscure damage detection results due to a lack of instrumentation (sensors can only be placed in an area where the bridge is not being used by traffic). The excitation from the traffic is also unregulated, vehicles may travel at different speeds and apply different loads to the structure.

2.2.1.2 Environmental constraints

Environmental constraints such as changes in mass, temperature and material expansion and contraction can have a large effect on the measured frequency response function (FRF) of a structure.

One publication [22] discuses a model of a canter lever beam and how its FRF is effected by crack formation and changing the length of the beam. It was observed that a crack 2 % of the beam's length effected the FRF by a factor of 40 times less than the effect of increasing the beam length by 2 %. Another publication [23] investigating environmental effects on piezoelectric sensors shows that temperature and ambient vibrations have a negative effect on the sensor's performance, causing identification of impacts to be difficult to discern.

It is evident that environmental effects can cause more significant changes in the structure's FRF than structural damage. However, a statistical test for evaluating uncertainty in FRF was developed in 1997 to help eliminate this problem [24].

2.2.2 Data Acquisition, fusion and cleansing

2.2.2.1 Data acquisition

For each SHM process this is application specific, however the following technical variables need to be considered:

- **What are the quantities to be measured?**
  For instance, if fracture rate was of interest, considerations must be made about the frequency of the acoustic events up to the fracture occurrence and the degree of sensitivity needed to measure it.
- **Types of sensor needed?**
  Sensors have different optimal applications, the correct sensor selection is very important and often multiple sensor types are used in SHM. For example, one could measure the rate of acoustic events with piezo transducers whilst determining the axial strain using strain gauges.
- **Sensor sensitivity**
  Sensor resolution and bandwidth limitations need to be evaluated. If the resolution is too high there may be problems with ambient noise, to low and the useful information could be undetected. The measurement bandwidth of the sensor needs to be wide enough to detect the frequency of events being measured in accordance with the Nyquist maximum frequency [25] to avoid aliasing.
- **Sensor topography**
  The number of sensors needed and their positioning on the structure are vital for accurate measurements and will be dependent on the physical quantities being measured and the type of structure.
- **Acquisition hardware**
  Suitable hardware needs to be chosen to record the sensor signals at the desired sampling rate and resolution. Suitable data storage needs to be implemented and if wireless sensor arrays are needed, a wireless communication network must be set up.

Economic constraints may affect the technical hardware choices listed above. For instance, fitting an array of vibrating wire strain gauges may be more expensive financially than typical foil strain gauges; there is trade-off between measurement accuracy and sensor cost. Sampling the sensor outputs at a lower rate may lead to a more cost effective analogue to digital converter (ADC) and data storage system. An economical factor to consider is the frequency of data collection. Continuous data acquisition could be memory intensive and thus expensive, however event driven acquisition is a more memory efficient approach but runs the risk of missing key events if the event threshold is not set correctly.

A compromise must be made between economic limitations and hardware performance in most SHM applications.

2.2.2.2 Fusion

This is a process by which data from different sensor sources across the structure are combined in such a manner that a more robust and confident decision can be made about the FRF changes. Usually this is achieved in an unsophisticated manner, however in recent years complex algorithms have been developed to fuse data using artificial neural networks [26]; this is more suitable for large sensor arrays.

2.2.2.3 Cleansing

This is the process of choosing data to accept for monitoring the structure which is usually implemented by a professional with technical experience. Signal processing techniques such as decimation, down sampling and filtering would also be considered as cleansing.

2.2.3 Feature Extraction and Information Condensation

2.2.3.1 Feature extraction

This is the process in which sensor data from the vibration response of a structure is analysed and damage sensitive properties in the response are identified. This provides a way to distinguish between a damaged and undamaged structure, methods for achieving this are application specific. One highly cited paper on this topic uses fuzzy pattern recognition to identify damage to a pre-stressed bridge without prior knowledge of the damage [27].

There are different methods for identifying damage features in a vibration response:

- Comparing features from past damage or similar structure
- Numerical simulation of the damaged structure compared to the actual structure
- Fuzzy logic pattern recognition [27]

2.2.3.2 Information condensation

This is needed in most cases because implementation of a feature extraction algorithm for damage detection is usually very data intensive and thus a large amount of data needs to be stored. Most feature extraction algorithms utilize some form of compression; this is especially useful for comparing data sets for the entire lifespan of a structure or if the structure is to be monitored for long periods of time; less storage space will be needed and therefore the data storage method will be more cost effective.

2.2.4 Statistical model development for feature discrimination

Statistical models are developed to work on the extracted feature data to determine the level of damage within a reasonable confidence interval. The statistical algorithms can be defined into two distinct categories:

- Supervised learning (pattern recognition) – data is available from the damaged and undamaged structure.

- Unsupervised learning – applied to data with no examples of the damaged structure.

Statistical analysis is used to answer the five damage questions as defined in the previous section of this report (section 2.1.1) in a quantifiable manor. The questions are answered in order; the more questions the statistical model can quantify, the more is known about the damage state of the structure. Statistical models can make mistakes; a false positive damage report will not affect a structure but will decrease the statistical confidence. However, a false negative could lead to catastrophic failure of a structure. Therefore, it is important that statistical models are tested before implementation.

2.3 Global and local health monitoring

Most global health monitoring (GHM) techniques [2] involve measuring shifts in resonant frequencies or changes in structural mode shapes; these techniques are limited to identifying if there is damage in the structure but not where the damage is located. If damage is detected, further examination of the structure using local health monitoring (LHM) techniques [28] can be used to find the location of the damage.

GHM techniques are often employed as they are inexpensive and quick to install due to the small number of sensors used; only 30 years ago 1 to 3 accelerometers were attached to structures [2]. The major problems with GHM is that only substantial damage to the structure can be detected; often environmental factors such as temperature changes, moisture and wind swamp out changes in frequency response due to more minor damage.

In more recent years the cost of sensors (specifically accelerometers) has decreased massively making it possible to place hundreds of sensors over a structure; as many as 600 sensors have been used on long span bridges [2]. This is sufficient to make the GHM approach a form of LHM on a large scale, thus eliminating most of the problems associated with GHM.

This thesis focuses on the development of a new sensing technology (EPS) for SHM. Due to its low cost semiconductor nature of this device, it lends itself to array formats and thus wide scale LHM.

2.4 Commercial SHM techniques

Sensing technologies are of great importance for modern SHM to compliment the traditional techniques such as tapping or visual inspections. Sensing technologies and SHM techniques are used to improve damage detection sensitivity, reduce labour intensity, and costs compared to traditional methods. Choosing an appropriate sensing technology for the specific SHM application is vital. Commonly used non-destructive testing (NDT) technologies include strain sensors, accelerometers, inclinometers, and AEs [1]. An overview of a wide range of the SHM technologies is explained in literature [4] and an overview of the technologies is shown in Table 2-1.

SHM Method	Operating principle	Measurement quantity	Advantages	Disadvantages
Strain gauges	Changes in strain of a structure results in a change in the gauge properties e.g. resistance (bonded resistance and semiconductor gauges) or reverberation frequency (vibrating wire gauges).	Strain (mm/mm)	Wide variety of gauges for different SHM applications. Bonded resistance gauges are inexpensive and simple to use. Vibrating wire gauges are robust for long term monitoring.	Bonded resistance gauges are vulnerable to temperature, corrosion and electromagnetic interference and have poor fatigue life for long term SHM. Vibrating wire gauges are costly. Difficult to manage arrays of gauges.
Optical fibre sensors	Change in strain of the structure deforms the optical fibre resulting in a changed in reflected light wavelength within fibre corresponding to mechanical strain and or temperature effects.	Strain (mm/mm) Temperature (°K)	High density GHM capabilities. Resistant to electromagnetic interference and corrosion. Suitable for a wide range of civil structures both in embedded and exterior mounted configurations.	Costly. Newer technology and thus trained professionals needed for installation.
Acoustic emissions	AE events are detected by piezo electric traducers converting the mechanical AE stress wave in the structure into an electrical signal than can be analysed using commercial AE processing packages.	Elastic stress waves caused by rapid release stress within the material e.g. cracking.	Passive measurement. Highly sensitive to minor damage events (i.e. micro-cracking) and damage is detected as it occurs. Location of AE events using LHM arrays.	High sampling rate needed produces large volumes of data. AE signal processing and data reduction (event detection) packages are costly. Background noise effects measurement in large structures.
In-situ stress	Involves disturbing the rock mass and subsequently measuring the response in the form of displacement, strain or hydraulic pressure after which the in-situ stress can be estimated.	In-situ stress field magnitude and direction. (Pa)	Range of different in-situ stress measurement methods available for different applications and borehole depths.	Rock mass is damaged in the process, not suitable for monitoring civil structures. Expensive to implement and requires skilled personnel. In-situ stress measurement methods are generally inaccurate.

Tap Tests	Taping areas of a structure with a specialised hammer and listening to the audible response, a change in audible pitch can indicate areas of damage.	Internal and surface defects.	Simple to implement. Specialised hammers have been developed with built in electronic sound analyser to help aid in damage detection.	Labour intensive and time consuming for large structures. Damage may go undetected due to the basic nature of the method.
Visual inspection	Trained personnel inspect civil and geological structures for signs of damage to assess maintenance needs.	Visual defects at the surface	Simple to implement. Penetrating dies can aid in damage detection on the surface of the structure.	Internal damage goes undetected. Damage can go undetected due to human error. Labour intensive.
Vibration based methods	Monitoring the FRF of a structure which is dependent on its mass, stiffness and damping properties that can be altered by the onset and progression of damage.	Internal and surface defects.	Can be applied to many types of structure. Excitation from normal loading e.g. cars passing over a bridge can be used as excitation. Provides global information about the damage state of an entire structure.	Less significant areas of damage may not have a noticeable effect on the FRF and not be detected. FRF is often more sensitive to environmental effects such as temperature rather than damage. Structure may have to be taken out of use to carry out vibration response testing.
Magnetic particle inspection	Structure is magnetised, the magnetic flux of an undamaged structure will be predominantly internal, however a damaged structure will have flux leakage due to cracks/flaws in the surface. Fine iron filings are used to detect surface flux leakages visually.	Surface defects.	Cracks/surface defects can be identified even if they are not visible to the human eye directly. Inexpensive to implement.	Only applicable to metal structures that can be strongly magnetised (i.e. ferric metals). Labour intensive. Requires skilled personal for visual inspection. Human error in visual detection of damage.
Eddy currents	Inducing eddy currents in a structure. Structural damage will affect the measured amplitude and phase of the eddy currents.	Internal and surface defects.	Cracks/defects can be detected below the surface and under paint. Suitable for detecting cracks in welded joints.	Limited Eddy current penetration depth. Structure being monitored has to be electrically conductive. Costly.

				Sensor coil placement/mounting can be difficult.
Radio-graphic	The structure is placed between a radiation source and detector. The greater the structures density and thickness (effected by damage) the greater the radiation is attenuated. Commonly referred to as Computed Tomography (CT) scanning.	Internal and surface defects and their dimensions.	Can detect internal flaws in complex structures. Detects surface and subsurface defects. Measures dimensions and angles of damage inside structures (e.g. cracks).	Radiation health hazard. Large size of test equipment. Costly.

Table 2-1 Overview of different SHM testing methods, adapted from [29].

In this section, NDT technologies including strain gauges, piezo electric transducers to monitor strain and AE events such as cracking respectively are discussed. In addition, destructive SHM techniques (in-situ stress measurement methods) are also discussed as these technologies are directly related to experiments and results presented in this thesis.

2.4.1 Strain gauges

Strain gauges are very commonly used in civil engineering for monitoring the propagation of cracks and deformation of structures. For most SHM processes normal strain is the physical quantity of interest, it can be expressed as the ratio of deformation to the initial displacement as shown in Equation 2-1.

$$S = \frac{\Delta x}{x}$$

Equation 2-1 Normal strain equation [30]: *S = normal strain and x = displacement.*

Sheer strain is slightly different to normal strain; this is quantified as the ratio of the change in angle or shape of the structure to the original angle or shape. Simple mechanical strain gauges are often used; the gauge is rigidly fixed over a crack of interest on the structure, the horizontal and vertical movement of the structure can then be monitored and thus the strain vector can be calculated.

2.4.1.1 Bonded electrical resistance strain gauges

Since 1940, the bonded electrical resistance strain gauge has been the most powerful tool in the field of stress and strain analysis; it is low cost and one of the most accurate, sensitive, versatile and easy to use sensors available [30].

The operating principle of this type of gauge is that the conductive material poses strain sensitivity defined as the ratio of electrical resistance change in the conductor to the change in the conductor's length. The conductor is typically a very fine metallic foil arranged into a grid pattern. The grid is bonded onto on to a thin backing called the carrier which can be attached directly onto a structure using a

bonding agent such as epoxy resin. Thus, the strain experienced by the structure is directly transferred to the strain gauge which corresponds to a linear change in gauge resistance.

The electrical resistance of a conductor is defined by Equation 2-2.

$$R = \frac{\rho l}{A}$$

Equation 2-2 Electrical resistance of a conductor [31]: *R= resistance, l = length, ρ = resistivity and A = cross-sectional area.*

The sensitivity of the gauge can be expressed by as the gauge factor (GF); gauge factor is the ratio of change in electric resistance to fractional change in length (strain).

$$\boldsymbol{k = \frac{\Delta R/R}{\Delta l/l} = \frac{\Delta R/R}{\varepsilon}}$$

Equation 2-3 Gauge factor (strain sensitivity) [31]: *k = gauge factor, R = initial resistance, ΔR = change in resistance, l = initial length and Δl = change in length and ε = strain.*

From Equation 2-2 and Equation 2-3 it is possible to determine the sensitivity of a strain gauge; if the conductor is subjected to elastic deformation for a given change in length (Δl) there will be a reduction in cross sectional area due to the Poisson effect [31]. The two effects are additive at increasing the gauge resistance, assuming the resistivity the conductor is constant and a Poisson's ratio of 0.3 (typical for most resistance materials) the gauge factor will be:

$$k = 1 + 2v = 1.6$$

Equation 2-4 Gauge factor (strain sensitivity) considering Poisson's ratio [31]: *v = Poisson's ratio = 0.3 and k = gauge factor.*

In fact, when testing different strain gauge conductor materials, they have wildly different measured strain sensitives (k). This is because ρ changes with the internal stress in the material, thus the sensitivity is a combination of geometric changes and resistivity change due to internal stresses.

Beyond the elastic limit of the conductive material the change in internal stress →0 and Poisson's ratio →0.5. In this plastic range the resistance change in the conductive material is primarily due to dimensional changes and the sensitivity (GF) is ~ 2.

$$k = 1 + 2v = 2$$

Equation 2-5 Gauge factor (strain sensitivity) considering Poisson's ratio [31]: *v = Poisson's ratio = 0.5 and k = gauge factor.*

This means that conductive materials with a GF appreciatively different from 2, will have a gauge factor of ~2 in the plastic deformation range of the conductor material. Thus conductive alloys with attractively high GF values are nonlinear, making them undesirable for use in strain gauges. Most gauges have a gage factor of ~2 for this reason and are linear over a wide strain range, a coper-nickel alloy is usually used [32].

The most common bonded electrical resistive strain gauge is the foil type; it is basically a small flexible printed circuit board (PCB). The PCB consists of a grid patterned conductive alloy that is a very precise

thickness (3 – 5 µm), sandwiched between a carrier material (usually polyimide) on the base and a laminate film covering the top. Polyimide is often used as carrier because it is extremely tough and durable, can be use over a wide temperature range -195 °C to 175 °C and elongates up to 20 %, making it well suited for strain measurements.

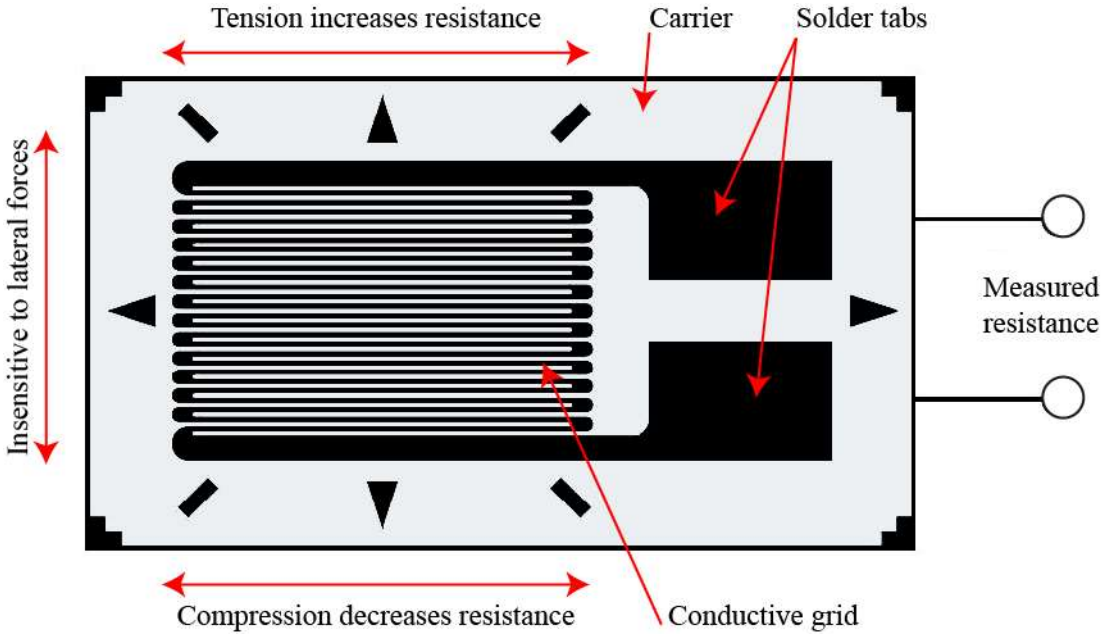

Figure 2-2 Resistive strain gauge diagram (foil type gauge), adapted from [34].

The conductive grid sensing area is formed of a conductive strip in a zig-zag pattern of parallel lines such that strain experienced in parallel to the lines has a multiplier effect on the effective length of the conductor and thus change in gauge resistance [32]. The structure of the conductive grid ensures the gauge is most sensitive in the parallel directions and insensitive in the perpendicular directions. The markings outside of the conductor area are to help align the gauge during installation.

In practice, a structure will only be subjected to small changes in strain (millistrain) and thus very small changes in electrical resistance need to be measured. For example, if a structure undergoes a change in strain of 1 millistrain the change in electrical resistance will be 0.2 % if the gauge has a gauge factor of 2 (typically gauges have a resistance of 120 Ω) in accordance with Equation 2-3 .

$$\Delta R = 120\Omega \times 2 \times 1 \times 10^{-3} = 0.24\Omega$$

$$\frac{\Delta R}{R} = \frac{0.24}{120} = 0.2\ \%$$

The Wheatstone bridge circuit is most commonly used to convert the very small changes in gauge resistance to an amplifiable voltage signal suitable for processing. A circuit diagram of the bridge circuit in shown in Figure 2-3. A stable DC voltage is applied to the input of the bridge circuit, if all four resistor values in the bridge are equal the output of the bridge is zero; this is known as a balanced bridge. If the bridge loses balance the output voltage corresponds to the resistance change [33].

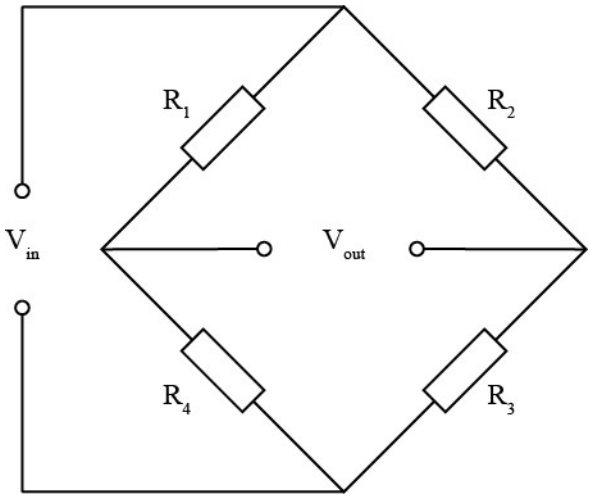

Figure 2-3 Wheatstone bridge circuit.

The most common input configuration is the quarter bridge as shown in Figure 2-4 where one strain gauge is used in one arm of the Wheatstone bridge.

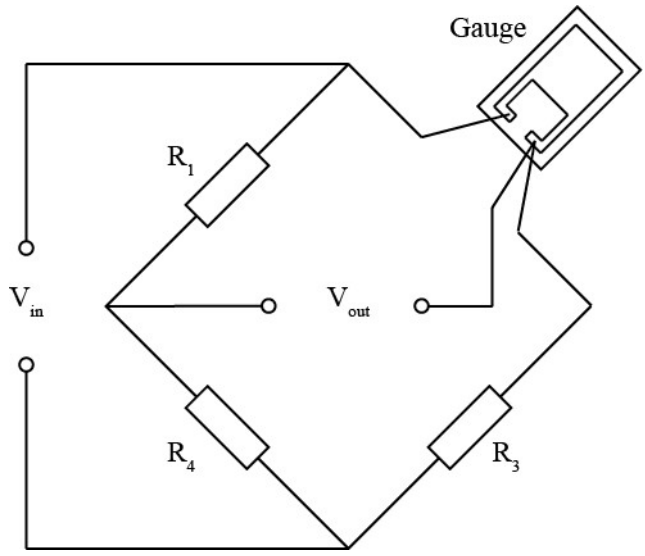

Figure 2-4 Quarter bridge with 3 wire strain gauge connection

Strain experience in the material being measured is transferred to the gauge and thus the resistance of the gauge changes causing an imbalance in the bridge and an output voltage is proportional to the strain as shown in Equation 2-6.

$$V_{out} = \frac{k\varepsilon N V_{in}}{4}$$

Equation 2-6 Strain gauge bridge output [33]: *k = gauge factor, ε = strain, N = number of measurement strain gauges, V_{in} = input voltage and V_{out} = output voltage.*

The quarter bridge setup relies on self-temperature compensating (STC) gauges which reduce the effects of gauge resistance changes due to thermal expansion of the specimen. Strain gauge manufactures often provide a temperature correction curve for specific specimen materials (e.g. steel) so temperature effects may be removed from strain data.

The lead wires connecting the strain gauge to the bridge are also effected by temperature, but this can be compensated for as well. Three lead wires connecting the gauge to the bridge has the following advantages over a two wire setup. 1) the resistance of the lead wires, regardless of their length, does not imbalance the bridge and 2) resistance changes in the lead wires due to temperature fluctuations are cancelled out in the bridge. Although the resistance of lead wires will be small compared to the strain gauge, the temperature coefficient of the copper wires is typically two orders of magnitude higher than the temperature coefficient of the of the gauges, thus the three wire connection is advisable especially if the lead wires are long.

The simplest way to correct for temperature drift is by using a half bridge configuration where two gauges are used in adjacent arms of the Wheatstone bridge as shown in Figure 2-5. The dummy gauge is attached to the same type of material and experiences the same temperature effects as the active gauge but does not experience any mechanical strain. This configuration ensures temperature changes do not unbalance the bridge, however both gauges must have well matched temperature/resistance characteristics.

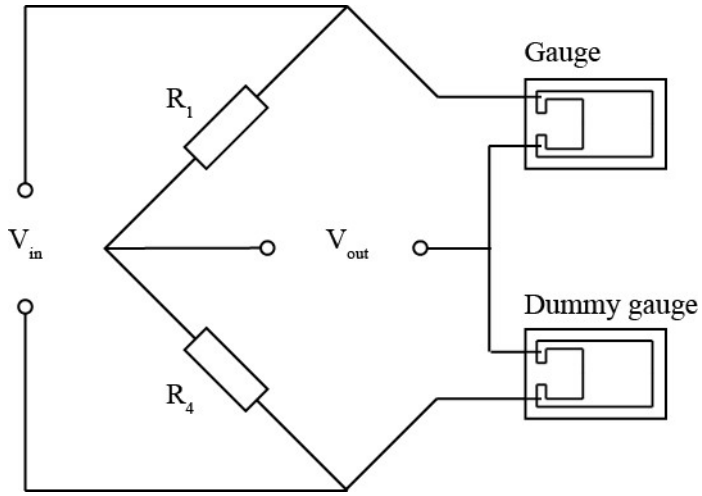

Figure 2-5 Half bridge configuration

The logical extension of the half bridge is the full bridge configuration, where four gauges are used, one in each arm of the bridge. This configuration has improved temperature compensation but its main advantage is that all lead wires including plugs and connectors are identical for each arm of the bridge and thus contribute minimal errors to the system. This configuration is ideal for SHM applications where the lead wires need to be long and where temperature fluctuations are prominent.

2.4.1.2 Semiconductor strain gauges

Can be used in much the same way as bonded resistance gauges. Semiconductor gauges exhibit a change in resistance in response to strain and Wheatstone bridge circuits are used to process the measurements. Semiconductor gauges rely on the piezo resistive effect which is much higher in semiconductor materials compared to their conductive counterparts. Thus, semiconductor gauges are much more sensitive (GF =

50 to 200) compared bonded resistive gauges (GF = ~2). Other advantages include a wide choice of gauge factors and resistance values; compact size; and high fatigue life. Semiconductor gauges however are more expensive, sensitive to temperature changes and more fragile compared to bonded electrical resistance gauges.

2.4.1.3 Mechanical strain gauges

These types of gauge are sometimes referred to as extensometers and measure displacement of buildings, foundations and other structures. The strain gauge is placed parallel to the surface over the point of interest such as an existing crack or area of deformation. The most basic gauges consist of a millimetre grid pattern with an overlaying crosshair, the position of the crosshair relative to the grid determines the direction and amount of movement and thus strain on the surface. However, there are more complex mechanical strain gauges that can measure micro strains. This type of gauge consists of a ridged frame with two contact pointers. One pointer is rigidly fixed to the frame and the other is fixed to another point on the frame via a pivoting lever arm. Any movement on the surface of the structure is amplified by the lever effect and is displayed on a mechanical or digital dial indicator.

2.4.1.4 Vibrating wire

When a wire is under tension between two clamps the natural frequency of the wire will change due to the amount of tension applied. A gauge containing a wire is placed over an area of interest on a structure and the frequency variation of the wire can be measured to determine surface strain of the structure.

2.4.1.5 Optical fibre strain gauges

Unlike fibre optic cables designed for the telecoms industry, for high speed and reliable data transfer, optical fibre sensors (OFSs) are optimised to be sensitive to external perturbations such as strain, which results in changes in the fibres geometrical and optical properties. There are many different types and subtypes of OFSs [34]. One popular technology is fibre Bragg grating (FBG) which utilises a series of gratings inside a glass fibre. As the OFS expands and contracts so does the gap between the gratings and thus there are changes the reflected light wavelength for each grating when the OFS is connected to a light source. The reflected light is measured and the strain can then be calculated from the shifts in wavelength.

OFSs are one of the fastest growing and promising research areas for SHM due to their durability, small size, stability, corrosion resistance and insensitivity to external electromagnetic disturbances [1]. The advantage of OFSs include quasi-distributed or truly distributed measurements along extensive lengths on or inside a structure [35], temperature can also be monitored simultaneously to strain [36]. Standard monitoring practice is based on a relatively small number of discrete strain gauges that are supposed to be illustrative of the global structural behaviour. Quasi distributed OFSs such as FBGs on the other hand can provide mapping of strain distributions over thousands of sensing points; thus global

behaviour of the structure can be evaluated [1]. There have been several influential papers of OFSs [37-39] and also publications demonstrating the applications of these sensors for civil SHM [40-42].

2.4.1.6 Applications

The strain of both ductile (materials that stretch and bend) and brittle materials (materials that crack) can be monitored using the correct choice of strain gauge technology.

Strain gauge technology	Electrical noise immunity	Measurement speed	Sensor configuration	Mounting type
Bonded resistance (foil)	Low	Up to ~100 kHz	Discrete: 1 sensor/channel	Surface-mount
Vibrating wire	Moderate	~1 kHz	Discrete: 1 sensor/channel	Surface-mount and Embeddable
Optical fibre sensors	Complete	A few Hz to hundreds of kHz	Distributed: multiple sensors/channel	Surface-mount and Embeddable

Table 2-2 Strain sensing considerations, adapted from [43]

In controlled environments resistance gauges are a suitable technology as they are cost effective and the technology is well established resulting in a wide range of sensor types, signal conditioning and data acquisition systems being available. Disadvantages of this technology include vulnerability to environmental factors (temperature, corrosion, electromagnetic interference); relatively short life span; and difficulty installing arrays of gauges for global monitoring due to maintenance and management of lead wires. Typically, these sensors are used for dynamic strain applications such as impact testing and semiconductor gauges are more suited for precision engineering applications.

Vibrating wire strain gauges provide reliable and long term strain monitoring and are often embedded into civil structures. However, data acquisition is slow and using arrays of sensor requires multiplexing the sensor signals to reduce the number of wires which inadvertently reduces the sampling rate; thus, high density global monitoring is impractical. Currently vibrating wire gauges are most commonly used for SHM due to their robust nature.

For applications where strain measurement is needed over large geographical areas (global monitoring) or where long term monitoring is needed, OFSs are ideal. OFSs can also be used in environments with high electromagnetic noise, such as near high voltage equipment, whereas vibrating wire and bonded resistance gauges cannot.

2.4.2 Instrumentation for Acoustic emissions monitoring

The definition of AEs defined by [44] is “The class of phenomena whereby transient elastic waves are generated by the rapid release of energy from a localized source or sources within a material, or the transient wave(s) so generated” such as cracking. AEs are a well-established technology and is widely used in SHM applications such as for monitoring fracture behaviour and fatigue detection; detecting faults and leaks in vessels and tanks; and monitoring the progression of corrosion.

2.4.2.1 Piezo transducers

The principle of piezo transducers (often referred to as AE sensors) is to detect transient elastic stress waves and convert them to electrical signals, that can be processed to analyse the fracture and fatigue behaviour of materials. Piezo transducers are usually based on a piezoelectric ceramic element [45]. Piezo electricity is the phenomenon where electric polarization is produced in the material due to the application of stress; or the development of induced strain in the material directly proportional to an applied external electric field. The latter phenomenon is primarily used for precise and compact actuator applications and the former is used for sensing dynamic stress changes (AEs), acceleration from shock or vibration and changes in force [46].

Most piezo transducer ceramic element formulations are based on lead zirconate titanate (registered trademark: PZT). PZT is almost always used for sensing applications because of its high sensitivity, although in high temperature environments, other materials such as lead niobate and lithium niobate are used [46]. Although PZT elements are sensitive, only a relatively small amount of charge is generated from AEs. Thus, charge amplifiers are used to convert the charge to a useable voltage directly proportional to the AEs.

A diagram of a piezo transducer for SHM is shown in Figure 2-6. The transducers PZT element is mounted in a shielded casing to protect against ambient electric fields and the output signal of the sensor is routed through a connector.

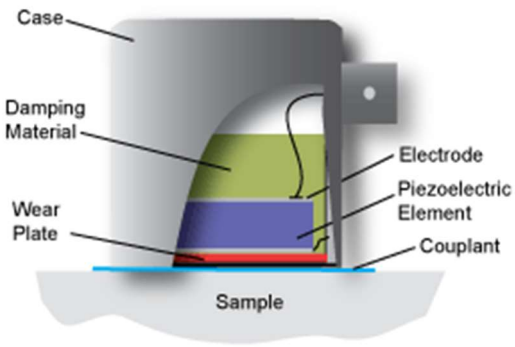

Figure 2-6 Diagram of a piezo transducer (AE sensor), original source [47].

An external preamplifier is usually connected to the sensor via short cables to amplify the signal before frequency filtering and analogue to digital conversion takes place. An integrated piezo transducer has a similar internal structure. However, a preamplifier is built into the sensor housing. A wear plate is usually connected to the sensing surface of the piezo transducer to protect the PTZ element as it is brittle and easily damaged.

There are many different types of piezo transducer each have tailored frequency responses for different SHM applications and they can be divided into two groups wide-band and resonant [29].

Wideband piezo transducers respond uniformly to a wide band of acoustic frequencies. These types of sensor are usually used for research or feasibility studies where the frequency of the AEs are not yet known and thus a flat frequency response is desirable. The experiments presented in results chapters 6,7 and 8 of this thesis used wideband piezo transducers as the frequency of AE events was not yet known.

Resonant piezo transducers are preferred when the frequency content of AE events is not of interest and features such as event amplitude and arrival time are. AEs measured using resonant piezo transducers can only be compared to measurements by other piezo transducer of the same resonant frequency. This is because the measured AE features are affected by the resonant frequency of the piezo transducer. Prior knowledge about the AE frequency range being measured must be considered when choosing a resonant piezo transducer as different applications have different frequency regimes.

2.4.2.2 AE measurement chain

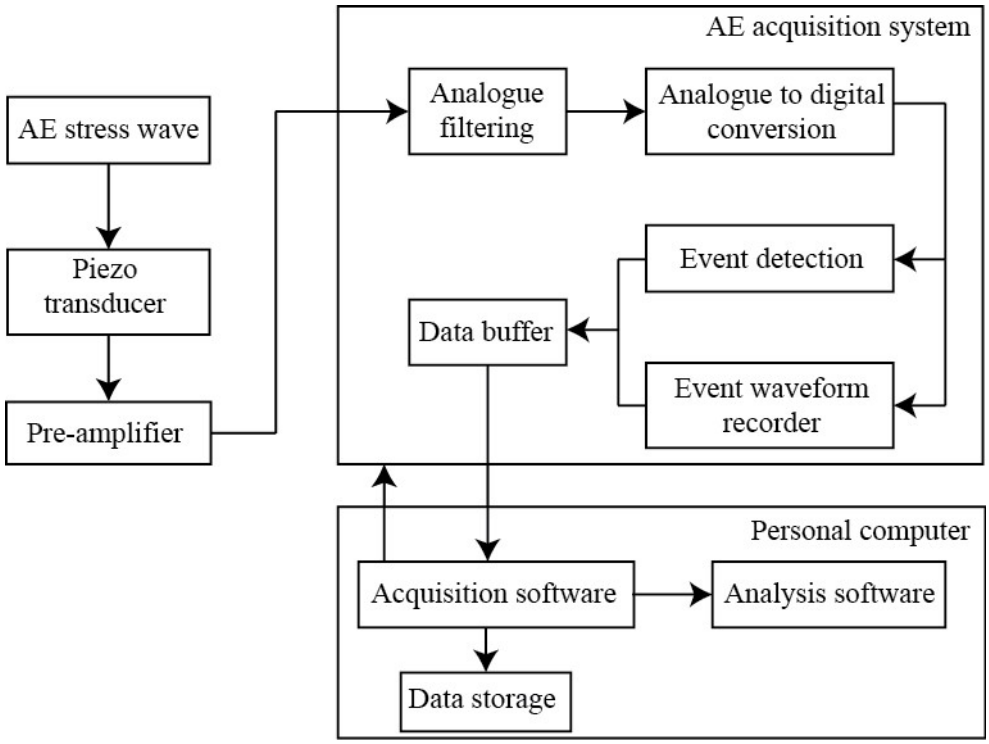

Figure 2-7 AE measurement chain, adapted from [29].

Piezo transducers detect the AEs from the material being monitored. The number of transducers used depends of the application (e.g. global monitoring, local monitoring, fracture location). Arrays of transducers are needed for a determining the location AE sources (e.g. cracking). The transducers are mounted on the structure or material being monitored using adhesives such as epoxy and hot melt glue or by holders with a coupling agent such as vacuum grease between the transducer and material [45].

Pre-amplifiers are needed to accurately measure the voltage produced by the piezo transducers [46]. The pre-amplifiers are usually connected to the sensors via short cables so that the relatively small electrical signals are not greatly attenuated during transmission or sometimes the preamplifier is built into the

sensor housing. AE preamplifiers usually have a gain of 40 dB to 60 dB and can transmit AE signals via cables up to 200 m in length.

The AE acquisition circuitry is usually very complex and high cost. Most acquisition systems use digitally controllable analogue filters to limit the bandwidth of the AE voltages. Different SHM applications monitor AEs over different frequency ranges and filtering can attenuate unwanted noise. The analogue filtering cut off frequencies can be determined through the data acquisition software on a personal computer (PC). High resolution ADCs are used to digitalize the analogue sensor signals, a common and widely used AE system digitalizes at an 18-bit resolution at up to 40 MSs^{-1} [48]. Because of the high resolution and sampling rate needed to monitor AE activity, a form of data reduction is needed. AE acquisition systems detect acoustic events in real time such as high frequency transients associated with cracking and store macro data about the event such as maximum amplitude, energy and the event waveform. Any unwanted data such as periods of inactivity are deleted.

The AE acquisition system communicates with a PC which can be used to setup sampling rates, analogue filter settings and AE event amplitude thresholds. Usually the AE hit data can be displayed and graphed in real time whilst the data is transferred from a memory buffer to hard drive storage on the PCs.

2.4.2.3 AE event data processing

Commercial AE acquisition systems provide customised software for detecting and interpreting AE event data for qualitative real time assessment of AE activity [45].

Event driven data is used to dramatically reduce the AE data size, and is universally used in the SHM community. First an AE amplitude threshold is set above the ambient noise level, data is only recorded when AE activity exceeds this threshold thus the ambient noise is rejected and during periods of inactivity data is not unnecessarily recorded. The recoded transducer signals are known as hits and represent acoustic events.

Most AE systems can also record AE waveforms continuously without converting it to hit data. This is usually only achievable for short periods of time because the resolution and sampling rates needed for AE acquisition are very high and thus lots of data storage capacity is needed. Figure 2-8 illustrates how AE hit data is compiled from the unprocessed AE waveforms.

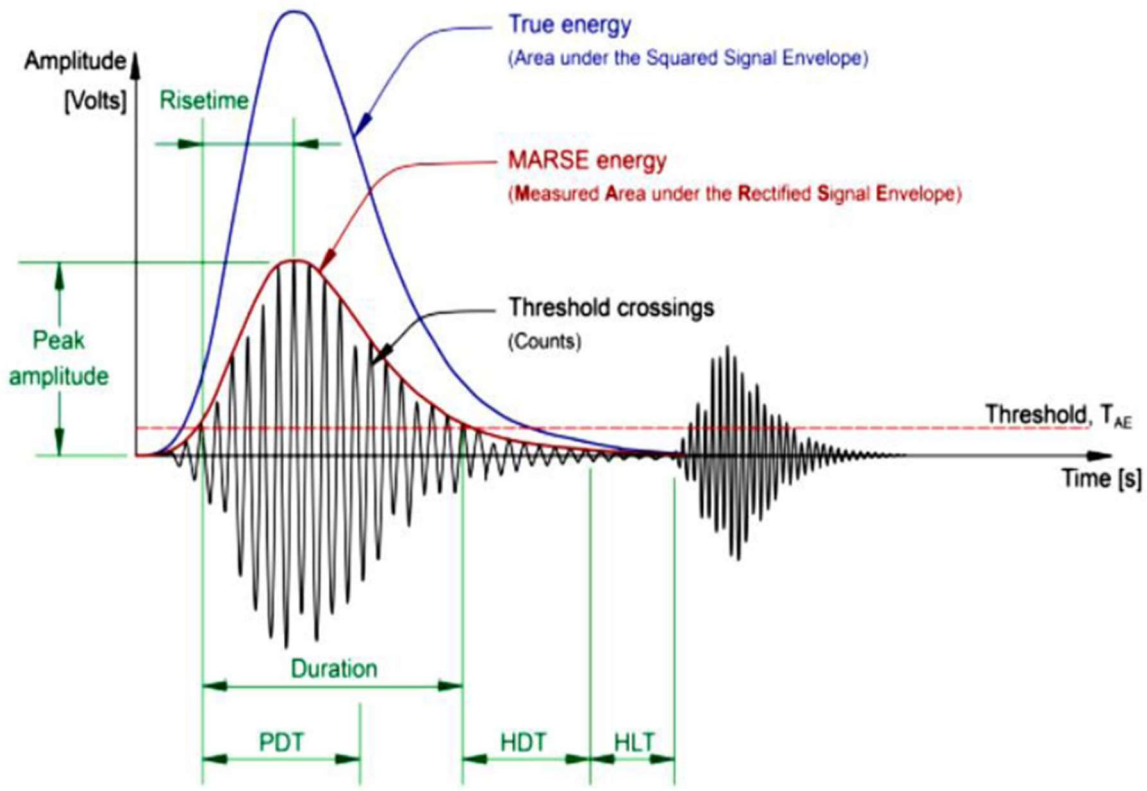

Figure 2-8 AE event detection, original source [49]

Event duration is the time taken from the initial threshold crossing to the last threshold crossing.

Event rate which is a useful parameter for AE analysis and is defined at the number of AE events per unit of time.

Peak amplitude is the highest amplitude during the hit duration and is directly related to the magnitude of the AE source. This amplitude varies from the range of microvolts to volts [49]. The amplitude is usually represented on decibel scale where 1 µV corresponds to 0 dB, 10 µV corresponds to 20 dB and 100 µv corresponds to 40 dB.

Rise time is the time taken from the initial threshold crossing to until the peak amplitude is reached, this parameter is often used by monitoring vibrations and dynamic loading.

Counts are the number of threshold crossing over the duration of the AE events. The number of counts is related to the reverberation frequency of the material being monitored and the resonant frequency of the piezo transducer used.

MARSE energy is the measured area of rectified signal envelope, this is the area below the envelope of the rectified signal measured from the piezo transducer. Energy has become the most widely used measure of AE activity surpassing counts because it is function of the event amplitude and duration [50].

$$S = \sum_{FTC}^{LTC} |V_i| . \Delta t$$

Equation 2-7 Definition of MARSE energy [50]: *S = energy, V_i= successive voltage reading of the piezo transducer signal, ΔT = time interval between V_i readings, FTC = first threshold crossing and LTC = last threshold crossing.*

This energy value is scaled to be broadly similar to the reported counts numbers as this is the feature it replaced, the scaling is also subject to the energy reference gain usually set to 23 dB [50].

Absolute (true) energy is a properly formed energy quantity in accordance with conventional scientific practice. The equation is similar to Equation 2-7 however squared voltage readings are used rather than rectified, the squared voltage readings are summed and divided by a token resistance equal to the input impedance of the pre-amplifier.

$$U = \frac{1}{R} \sum_{FTC}^{LTC} V_i^2 . \Delta t$$

Equation 2-8 Definition of absolute energy [50]: *U = absolute energy, V_i= successive voltage reading of the piezo transducer signal voltage, ΔT = time interval between them between V_i readings, FTC = first threshold crossing, LTC = last threshold crossing, R = input impedance of the preamplifier used.*

Absolute energy is usually quoted in units of attojoules, this quantity has very good resolution and is ideal for monitoring small changes in continuous single levels [51].

AE event detection parameters are set in the AE acquisition software; parameter values to suit different types of materials are commonly listed in the manufactures data sheet. The parameters can also be determined by experimentation. This process involves analysing the AE event waveforms and intelligently setting the AE event detection parameters using knowledge of the parameter definitions described below:

Peak definition time (PDT) is a time window after the first threshold crossing in which the AE event's peak amplitude must occur. The correct setting of this parameter ensures accurate calculation of the peak amplitude and rise time of AE events/hits [48].

Hit definition time (HTD) defines the end of an AE event after the last threshold crossing. If the HDT is set correctly it ensures that each AE event in the AE waveform structure is reported as one event [48]. If the HDT is set too long multiple AE events can be incorrectly classified as a single event.

Hit lockout time (HLT) this is a period of time after the end of an AE event (defined by HLT) in which the system does not respond to threshold crossings. This parameter ensures inaccurate measurements during signal decay are avoided such as reflections and late arriving signals and allows for faster data acquisition [48].

2.4.2.4 Kaiser effect and Felicity effect

The Kaiser and Felicity effect of AEs in rocks [52, 53] and concrete [54] is a well understood phenomenon.

The Kaiser effect is the absence of AEs at loads not exceeding the previous maximum load (PML) level during cyclic loading [52]. The Felicity effect reduces the Kaiser effect, causing AE events to occur before the PML [52] usually at higher levels of stress. Figure 2-9 is a loading diagram representing the Kaiser and Felicity effect and how they are related.

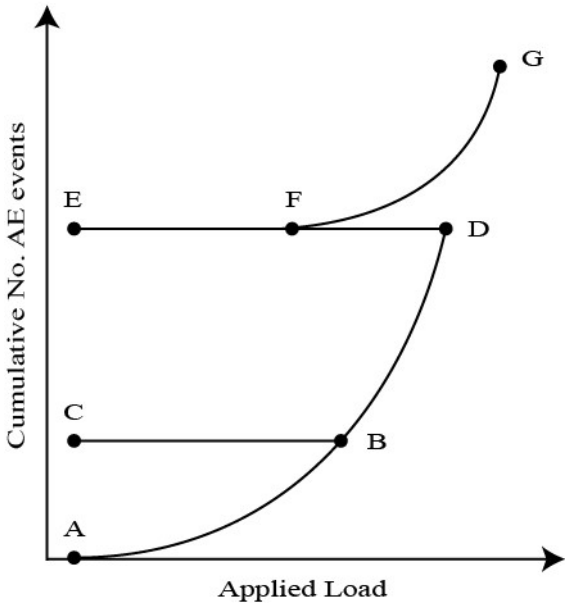

Figure 2-9 Diagram showing Kaiser and Felicity effect, adapted from [52]*. The theoretical AE events resulting from the loading of a brittle material i.e. rock or concrete.*

Initially there is an increase in the number of AE events as the load is applied (A-B); the load is then removed (B-C); and when the load is reapplied but does not exceed the PML (C-B) there are no new AE events; this is the Kaiser effect.

Once the PML is exceeded (B-D) there is an increase in the number of AE events; the load is then removed (D-E); when the load is reapplied there are no new AE events (E-F); this is the Kaiser effect. However, AE events begin to occur prematurely at point F even though the PML at point D has not been reached, this is the Felicity effect reducing Kaiser effect.

Kaiser effect is a measure of damage for materials subjected to load [53] in addition the Felicity ratio can be used to monitor the progression of damage in materials [45]. Felicity ratio (FR) is defined as is the ratio of the load at the onset of an increase in AE activity (x) and the previous maximum load (y) in accordance with Equation 2-9.

$$FR = \frac{x}{y}$$

Equation 2-9 Felicity ratio [55]

If FR = 1 the structure is not significantly damaged (e.g. at point B in Figure 2-9), if FR < 1 permanent damage has occurred and (e.g. at point F in Figure 2-9) and if FR = 0 the structure has reached it ultimate load (failure point) [55].

Kaiser and Felicity effect are useful parameters to monitor for the loading of rocks and concrete because failure is due to the growth and coalescence of cracks in brittle materials [53].

2.4.2.5 Applications

AEs are a very versatile technology as it can use used to monitor a wide range of materials and can be used in many different SHM applications. There are many types of piezo transducer with bandwidths tailored for wide range of materials in including metals, ceramics, polymers, composites, wood, concrete and geological materials [56].

There are many possible sources of AEs including pore collapse; micro-cracking; macro-cracking; slip and dislocation movement; phase transformation; fracture of inclusion particles; fractures of reinforcement particles and fibres; de-bonding of inclusions and reinforcements; realignment of magnetic domains; delamination in layered media; and rock bursts and fault slip [56]. These wide range of sources makes AEs applicable to many applications including monitoring of manufacturing processes, SHM of civil structures, SHM of geological structures (e.g. rocks) and aerospace engineering [49].

In this thesis, the monitoring of pore closure; development of microcracking and macro-cracking; coalescence; and slip and dissociation movement in geological materials (rocks), concrete and ceramic (Macor ®) during uniaxial loading is of interest.

2.4.3 In-situ stress measurement

Rock at depth is subjected to weight from the overlaying material in the vertical direction (vertical stress) and tectonic stress in the horizontal directions (horizontal stress) [57]. The normal and shear forces at a point in the rock are represented by 3 principle ($\sigma_{xx,}$ $\sigma_{yy,}$ σ_{zz}) and 6 shear forces ($\sigma_{xy,}$ $\sigma_{xz,}$ σ_{yx} $\sigma_{yz,}$ $\sigma_{zx,}$ σ_{zy}) respectively as shown in Figure 2-10 [57]. The in-situ stress state is conventionally defined by three principle components: the vertical stress (σ_{zz}) and the horizontal stresses σ_{xx} and σ_{yy} as shown in Figure 2-10. Knowledge of the magnitude and direction of these stresses is essential for underground excavation and design for civil, mining, nuclear waste storage and petroleum engineering.

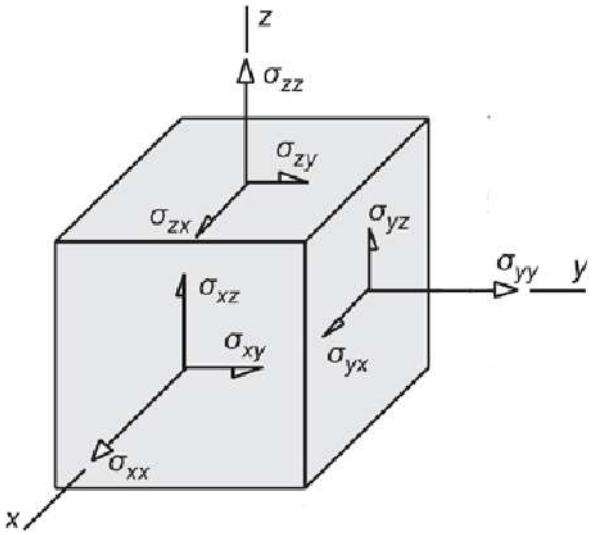

Figure 2-10 In-situ stress components adapted from [58]

It is impossible to measure the in-situ stress state without disturbing the rock mass [59]. Measuring techniques involve disturbing the rock mass and subsequently measuring the response in the form of displacement, strain or hydraulic pressure after which the in-situ stress can be calculated by making assumptions about the rock properties.

2.4.3.1 Hydraulic methods

A borehole is drilled into the rock at areas of interest and fluid is injected into the borehole inside a sealed packet, the fluid pressure is then increased until existing fractures open or new fractures occur [60]. The fluid pressure needed to open, generate, propagate, sustain and reopen fractures is related to the in-situ stress field, the direction of the stress field can be determined by observing the orientation of the fractures [59]. In general, this technique determines the principles stresses on a plain perpendicular to the drilled borehole [60], the most widely used hydraulic methods include hydraulic fracturing [61], sleeve fracturing [62] and hydraulic test in pre-existing fracture (*HTPF)* [61].

2.4.3.2 Relief methods

The general principle of the technique is to isolate a rock sample from the surrounding rock mass and measure its response to being relieved from the in-situ stress field. This technique involves either over or under-coring a borehole, cutting slots or under-excavation. The strains and displacements are then measured in response to the relief in stress in the rock samples, boreholes or surrounding rock mass depending on the technique used [59]. The in-situ stress can then be determined by obtaining rock mass properties from the extracted samples and equations derived from the theory of linear elasticity. Widely used relief methods include borehole relief [63], relief of large rock volumes [59] and surface relief [59].

2.4.3.3 Jacking methods

This method involves cutting slots into the rock mass in order to disturb the equilibrium of the in-situ stress field this results in the formation of deformation/cracks in the vicinity of the slots. The deformations/cracks are then monitored using reference pins or strain gauges then jacks are inserted into the slots. The jacks pressurise the slots until the stress field equilibrium is restored; this occurs when the deformations/cracks disappear/close [59]. When using the flat jack method [64] the equilibrium pressure is a direct estimate of the stress normal to the jack, thus a total of 6 tests need to be carried out to estimate the complete in-situ stress field.

2.4.3.4 Strain recovery methods

The fundamental idea behind this method is extracting core samples from a borehole in the rock mass of interest and monitoring the deformation of the core as it recovers from the in-situ stress field of the rock [59]. There are two commonly used techniques the anelastic strain recovery (ASR) method [65] and the differential strain curve analysis (DSCA) method [66]. The ASR method involves measuring the strain response of the core after being removed from the borehole, the direction of measure strain is assumed to be the same as the in-situ stress field component of the rock mass. In addition, knowledge of the rock's unloading properties are necessary for estimation of in-situ stress [59]. The DSCA method involves cutting a cubic specimen from the core sample and subsequently hydraulically pressurising the cube, until micro-cracks that formed due to the relaxation from the in-situ stress field, close. Six strain gauges are used on the cube to measure the response to hydraulic pressure and thus infer the in-situ stress field [59].

2.4.3.5 Borehole breakout method

The surrounding rock around a borehole may not be able to waistband the surrounding compressive stress as a result of the drilling of the hole itself. For instance, in vertical boreholes zones of enlargement occur diametrically opposite each other and these zones are in the same direction as the minimum horizontal stress [59] thus direction of the horizontal stress field can be determined by visual inspection.

2.4.3.6 Applications

The advantage of hydraulic methods is that the process is relatively simple to implement under the water table and it does not require detailed knowledge about the rock properties.

Relief methods rely on the following: an established stress strain relationship for the rock sample and thus the ability to carry out rock mass property testing on samples and to have instruments sensitive enough to detect the small changes in strain/displacement. The technique was developed for hard rocks and thus success rates for the measurement of soft rocks varies.

The main advantage of jacking over relief methods is that it does not require knowledge of the elastic constants of the rock order to determine the in-situ stress. The equipment used for jacking is rugged and reliable and stresses can be determined over large areas.

An advantage of the strain recovery method, is that the technique is suitable for very deep unground boreholes, where other techniques would not work, as only small core samples are available at that depth.

The bore breakout method can be utilised in deep boreholes up to ~11.6 Km and is useful for stress estimations at great depth, where direct measurements are not possible. Generally, this method can only determine the direction of the in-situ stress field and not its magnitude, however several attempts have been proposed by analysing the breakout geometry.

3 LITERATURE REVIEW: PRESSURE STIMULATED ELECTRICAL EMISSIONS

This chapter introduces pressure stimulated electrical emissions (PSEs), i.e. the study of pressure stimulated voltage, electric field and current. PSE research motivation and its relationship with earthquakes is discussed in section 3.1. Followed by a literature review of the PSE generation mechanisms (section 3.2). To conclude an overview of the PSE measurement technologies is described in section 3.3.

3.1 Introduction

Although the prediction of earthquakes has been researched and studied for over 100 years there has been no obvious success. Many claims of breakthroughs have not been able to withstand scrutiny from the scientific community. Theoretical work suggests that earthquakes are a non-liner process that can be influenced by unmeasurably fine details in the earth, over large volumes and not just in the vicinity of the earthquake centre. Any small earthquake thus has the potential to escalate into a major earthquake and thus the predicting of major earthquakes appears to be almost impossible [67]. Although precursor observations of earthquakes will always be incomplete, as technology advances a more complete data set can be established and thus the possibility of prediction. One promising precursory signal of earthquakes is that of PSEs, which is the primary focus of the work presented in this thesis.

It has been well documented that PSEs are present before and during major earthquakes, since the 1970s, there have been numerous studies in this area of research [67-71].

In Asia unusual animal behaviour has been observed before earthquakes and has long been studied; however, until recently western geophysicists have not believed this phenomenon exists. In December 2000 Japanese researchers documented that when electromagnetic pulses are emitted from granite and basalt samples under uniaxial compression, unusual animal behaviour can be observed in rats, mice, eels and silk worms during compression of the rocks [12]. The visual observation of unusual animal behaviour was observed via video recordings and confirmed in the rats by monitoring the levels of noradrenaline and adrenaline before and after rock compression.

Another study [72] used specially designed monopole antennas (100 – 800 m long) that penetrate the earth to monitor seismic radio wave signals (SRS); the depth of the antennas shielded them from cultural electromagnetic noise. The antennas were placed tens of kilometres away from each other, at areas of interest around Tokyo Japan. Observational frequency bands were chosen: 0.7 Hz (~DC), 0.01-0.7 Hz (ultra-low frequency) and 1-9 kHz (very low frequency). Therefore, the lengths (hundreds of meters) of the monopole antennas (10 cm diameter) had to be optimized for the desired SRS wavelength measurement.

Measurements during earthquakes revealed pulse like, very low frequency (VLF) seismic radio wave signals evolved in accordance with the occurrence of several earthquakes. The SRS were detected over long distances (~500 Km), which indicates a waveguide propagation mode between the ionosphere and the ground was present. The researchers concluded that the VLF band may contain signals that can be used to predict earthquakes for several hours/days before they occur. In addition, there appears to be two sources of VLF signals; one in the ionosphere and the other near the epicentre of the earthquake [72].

The unpredictability of earthquakes and possibility of PSEs being a precursor to earthquakes has motivated many laboratory experiments investigating the characteristics and generation mechanism/s in rocks and manmade materials. Laboratory based studies investigating PSEs have also proven not only to be useful for earthquake prediction but also as a new SHM tool, for the detection of damage in civil and geological structures.

An inherent problem with this research area is that many different generation mechanisms have been proposed and each mechanism appears to be dependent on rock lithology/material type and water saturation. There is not a unified explanation of the generation mechanism/s, however the most commonly proposed mechanisms include the electrokinetic effect of water movement; piezo electric effect; micro-cracking/fracture and movement of fresh charged fracture surfaces; and emissions of charged particles.

3.2 Generation mechanisms

3.2.1 Electrokinetic effect of water movement

This effect involves the coupling of a fluid and solid to produce a solid-liquid charge interface known, as an electrical double layer (EDL) [11]. For instance, a water saturated rock would have water in the rocks pores, which forms an EDL with the rocks internal surfaces. There are a number of accepted models for this phenomena [73-75]; the main electrokinetic effects include streaming potentials, electrophoresis, sedimentation potential and electro-osmosis.

The solid liquid interface has been described as a solid surface having an excess charge of one polarity (e.g. negative ions) compensating for oppositely charged ions (e.g. positive ions) in the nearby fluid this; results in the electric potential [11]. The structure of the solid liquid interaction is shown in Figure 3-1.

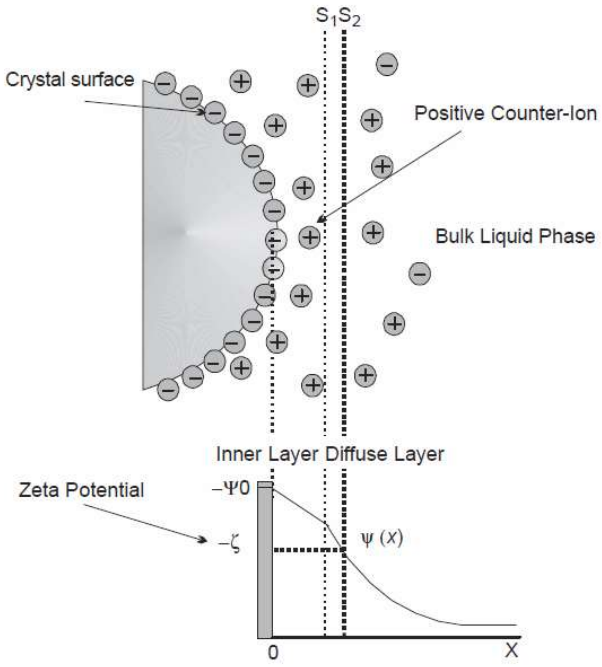

Figure 3-1 Electrokinetic effect - solid-liquid interface, original source [11].

The solid inner layer is formed from positive ions in the fluid being in contact with negative ions in the solid (e.g. rock crystals) due to electrostatic attraction. The outer layer, known as the diffused layer, contains a distribution of ions and is the source of the positively charged counterions. The boundary of these two layers is known as the zeta potential.

For experiments represented in results chapters 6 and 7 of this thesis the liquid is either reverse osmosis (RO) purified water or saline solution. When rock or concrete specimens are saturated with either of these fluids, there will be differences in the distribution of ions in the liquid and thus they will have different zeta potentials. The effect of different ion distributions (i.e. water or saline) is represented by S_1 and S_2 in Figure 3-1. As the zeta potential is a function of distance from the electrical double layer the electric potential generated at the surface during uniaxial compression of rocks saturated with saline or water would be significantly different. The value of the zeta potential is critical for each type of electrokinetic phenomena [76].

When a pressure gradient is created, fluid will flow in the pores of the rock, causing the diffused layer of the fluid to move. The movement of the diffused layer generates an electric current and associated electric field that produces a second equal and opposite current. This results in an electric potential across opposite ends of the rock sample, as represented in the figure, assuming a steady state system [11].

3.2.2 Piezo electric effect

Rocks and manmade materials can contain quartz crystals that are piezoelectric in nature. Piezo materials are defined as becoming electrically charged upon deformation or becoming deformed due to the influence of an external electric field [77]. The polarisation of a quartz crystal largely depends on

the deformation process (weather that be compression, tension or shearing forces) acting on the crystal. Piezo electricity in rock can be determined by the following equations [11].

$$D = d\sigma + \varepsilon_p^{\sigma} E$$

Equation 3-1 Piezo electricity in rock, electric polarisation [11]*: D = electric polarization current, d = matrix of polarisation constants, σ = applied stress, ε_p =permittivity and E = electric field.*

$$\varepsilon = \frac{1}{C^E}\sigma + dE$$

Equation 3-2 Piezo electricity in rock: strain [11]. *Where ε = strain, C = the elastic constant, d = matrix of polarisation constants, σ = applied stress and E = electric field.*

The initial polarisation of a typical quartz crystal is neutralised by the surrounding free moving charges in the rock thus there is no measurable electric potential on the rock surface as shown in part (a) of the Figure 3-2 [11]. A rapid change of stress of a quartz crystal polarized in the same direction as the applied stress would reduce the polarisation equation too.

$$P_i = c_{ijk}(\sigma_{jk}^0 - \Delta\sigma_{kj})$$

Equation 3-3 Piezoelectric polarisation: in response to rapid stress change [11]*: P_i = the i^{th} component of the polarization vector, c_{ijk} = piezoelectric modulus of the third-order tensor of the material and $\Delta\sigma_{kj}$ is the sudden change in stress.*

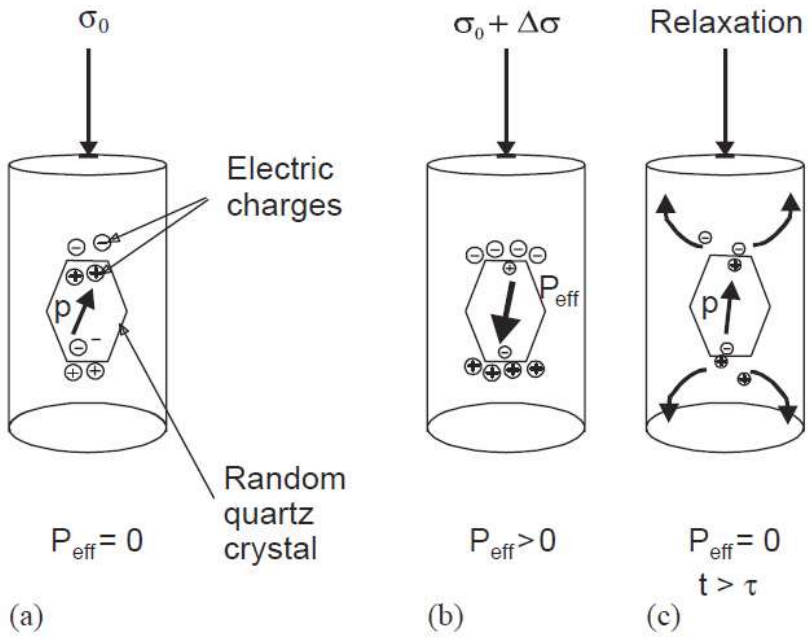

Figure 3-2 Piezo electric phenomenon in quartz bearing rock, original source [11].

A rapid change in stress induces the effective polarization of the quartz crystals inside the rock and thus an electric potential can be measured on the surface of the rock as shown in part (b) of figure. The electric potential then decays through a relaxation process as shown in part (c) of the figure [11].

The piezoelectric law of coal or rock deformation was studied [78] and the results show that as the crack interface barrier (e.g. crack surfaces) increases, so does the measured electric potential, before sample fracture. Sliding friction between crack interfaces causes the largest electric potential amplitudes to be

produced. In addition, there is a major change in the electric potential signal before failure of a coal sample which may be a useful precursor signal warning of imminent failure in coal structures. The coal samples were subjected to compressive loading profiles and a charge amplifier was used to convert the very weak charge, generated at the coal surface to a measurable voltage signal (range of mV), using a single ended (ground referenced setup). However, in order to achieve accurate noise free measurements, the coal sample (50x50x100 mm) had to be shielded from electrical noise sources, using a Faraday cage.

Another study [17] investigated piezo stimulated currents in marble samples (98 % calcite; 0.2 % quartz; and other minerals including muscovite, sericite and chlorite) under uniaxial compression, with samples subjected to variable and constant stress rates. Weak currents were detected during compression in the range of Pico amps, measured using a Keithley [79] electrometer and pair of electrodes. Due to the low signal to noise ratio the current measurement had to be carried out in a Faraday cage shielded environment. The results showed that spikes in current amplitude are present during positive and negative stress steps, where all stress steps lay within the linear elastic limit of the marble (little to no cracking events). In addition, there was a polarity reversal in the current, in response to positive or negative stress steps, as shown in Figure 3-3.

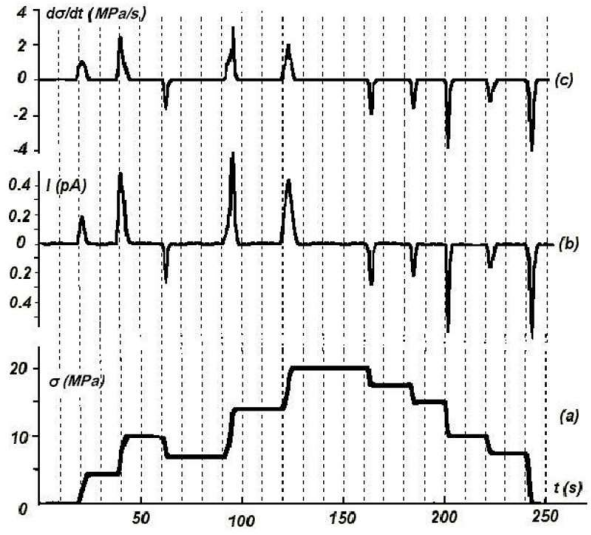

Figure 3-3 Correlation of stress steps and piezo stimulated currents, original source [17]. *a) applied stress, b) piezo stimulated current and c) stress rate.*

In a second set of experiments in the same study, a constant stress rate was applied until material failure occurred. The current reached a peak in amplitude after the linear elastic region (macro-cracking) and polarity reversals were observed before fracture. In this study the generated currents are referred to as piezo stimulated current even though the quartz content of the rock is very low and the current amplitude appears to be directly related to stress rate.

In a separate study [13], the piezoelectric effect was confirmed as a generation mechanism for stress induced polarisation currents, during the uniaxial compression granite samples. The laboratory experiments used a single ended electrometer (ground referenced), with an electrode positioned away

from the surface by 0.5 mm (capacitively coupled), to measure the polarisation currents. In order to improve the signal to noise ratio, the experiments had to be carried out in a Faraday cage. Stress induced polarisation currents were observed before fracture of the granite specimens. It was also possible for the polarisation currents to be transmitted through an unstressed limestone rod; the waveform remained relatively unchanged apart from a drop in amplitude. Propagation through the limestone was attributed to the relative humidity of surrounding air however, as dry limestone did not have conducting properties.

3.2.3 Micro-cracking and charged fracture surfaces

The uniaxial compression of non-piezo Lithium fluoride (LiF) crystals was carried out in the same experimental study [13] as described in the previous section (3.2.2). The results showed that AE and polarization currents were present during loading and that spikes in AEs and current correlated with each other in both the LiF crystal as well as the granite samples. However, when observing the individual micro-cracking events it is apparent that the generation mechanisms of electrical emissions in the LiF and granite are different. As mentioned previously the generation mechanism for the granite is most likely attributed to the piezoelectric effect of quartz. However, a different mechanism is responsible for the LiF crystal as it contains no piezo electric minerals. The loading of the LiF crystal results in the piling of charge dislocations and the hardening of micro-cracks (which have freshly charged fracture surfaces). When micro-cracks open, there is an abrupt acceleration of the charge dipole moment, due to the movement of the micro-crack's charged fracture surfaces and thus electromagnetic emissions occur.

In one study, a theoretical model of micro-crack friction slip is established [66] and supports the generation theory of the aforementioned study of LiF crystals [74]. The results demonstrated that micro-cracks expand during the external loading of rock and that coal and charge break through is caused by slip dislocations and inhomogeneous deformation of crack interfaces.

An experimental study [80] shows the electromagnetic radiation (EMR), emitted from fracturing rock samples (carbonate and igneous), during triaxial loading behaves like a surface vibration optical wave (SVOW) model. EMR was measured using a magnetic one loop antenna (3 cm in diameter) and a micro signal amplifier; the experiment was carried out within a Faraday shield. The proposed generation mechanism of EMR is the breaking of bonds during fracture, atoms on both sides of severed bonds move to un-equilibrium states relative to the surrounding steady state atoms and oscillate around them. Lines of oscillating atoms then move together; larger cracks produce a larger number of oscillating atoms and thus a larger EMR amplitude. The experimental observations of EMR behave like a SVOW model, where positive charges move together in a diametrically opposite phase to the negative ones and decay exponentially into the material like Rayleigh waves. The resulting oscillating electric dipole is the source of EMR.

The Kaiser effect has been investigated [81] with simultaneous measurements of electromagnetic emissions (EMEs) and AEs, during uniaxial cyclic loading of Indiana and Aji granite. The EME measurement relies on pairs of electrodes; the electric potential between the electrodes is amplified,

using a 40 dB AE preamp and the amplified signal is fed into an AE acquisition system when EME events are calculated. The experiment was carried out in an electromagnetic shielded chamber, to improve signal to noise ratio of the EME recording. The results of the cyclic loading of the Inada granite are shown in Figure 3-6.

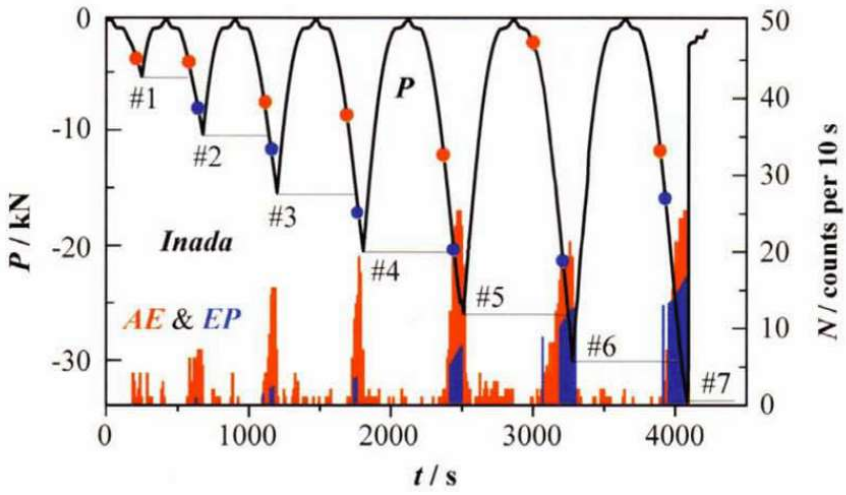

Figure 3-4 Cyclic loading of Inada granite, original source [81]. *where p = applied load.*

The Felicity effect was observed in the AEs, effectively eliminating the Kaiser effect. However, the EME events only appear after the previous maximum load (PML) threshold is reached and exceeded; this demonstrates that the Kaiser effect is present. These observations indicate that EMEs are only released once micro-cracking/fracture begins (i.e. after the PML threshold has been exceeded); thus, EMEs are related to cracking and could be used to assess fatigue/damage in rock.

Another study [82] confirms a memory effect, synonymous to the Kaiser effect of AEs is present in pressure stimulated currents (PSCs) generated in Marble samples (98 % calcite; 0.2 % quartz; and other minerals including muscovite, sericite and chlorite), during uniaxial compression. The experiment was carried out inside a Faraday cage to eliminate external noise sources and the PSC (in the range of Pico amps) was measured using a laboratory electrometer.

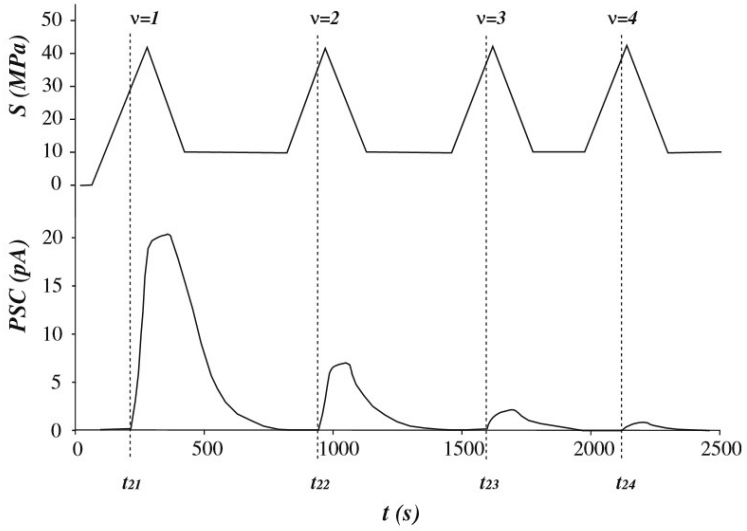

Figure 3-5 The relationship between PSC and uniaxial compression during cyclic loading, original source [82].

The rock sample was subjected to cyclic repetitive loading to the same stress level each time and the resulting weak electric currents reduced in amplitude, with each successive loading cycle showing that PSC in marble has a memory effect. The PSC spikes reduce in amplitude from cycle to cycle, in an exponential like manner. This phenomenon could be useful for detecting fatigue in rocks; the mechanism behind this is that fewer micro cracks are formed with each successive loading cycle and thus PSC is likely to be associated with cracking.

One of the only studies [15] statistically correlating AE and electrical emissions investigates the uniaxial compression of a cement mortar beam (1-part cement: 3-parts sand: 0.5-parts water), using a 3-point bending technique. PSC measurement was carried out using a laboratory electrometer and AE was recorded using a single piezo transducer and Physical Acoustics Cooperation PSCI-2 AE acquisition system [48]. The loading rate of the specimen remained constant up until fracture of the specimen occurred; AEs and PSC (in the range of Pico amps) were detected throughout loading.

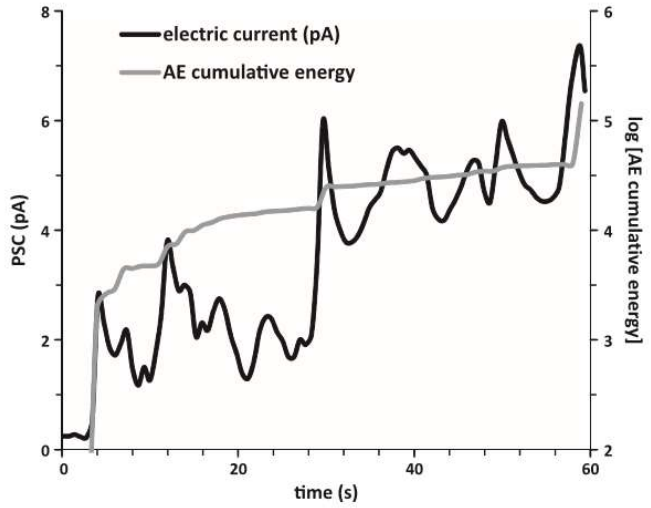

Figure 3-6 Cumulative AE energy and corresponding PSC variation, original source [15].

The results shown in Figure 3-6 show a good correlation between AE events and PSC variations, where PSC variations coexist with high amplitude or high AE event rate, this indicates that peaks in PSC energy correspond with AE cumulative energy fluctuations. When approaching fracture, the PSC amplitude is maintained at high values thus providing some indication of imminent failure of the material. PSC peaks were detected approximately 1 second before corresponding high energy AE events and not simultaneously.

EMEs were shown to be associated with micro-cracking in a separate study [83]; EMEs and AEs were recorded simultaneously from granite specimens (quartz 52.5 %; plagioclase 11 %; alkali feldspar 25.7 %; Biotite 3.4 %; others 7.4 %) during uniaxial compression loading. The rock specimens were instrumented with five acoustic transducers, to detect AE events and five coil antennas, for detection of EMEs. The EME coils had 20 - 40 turns and each antenna had a different resonate frequency, ranging from 80 kHz to 1.2 MHz. The experiment was conducted in an almost completely electrically shielded environment.

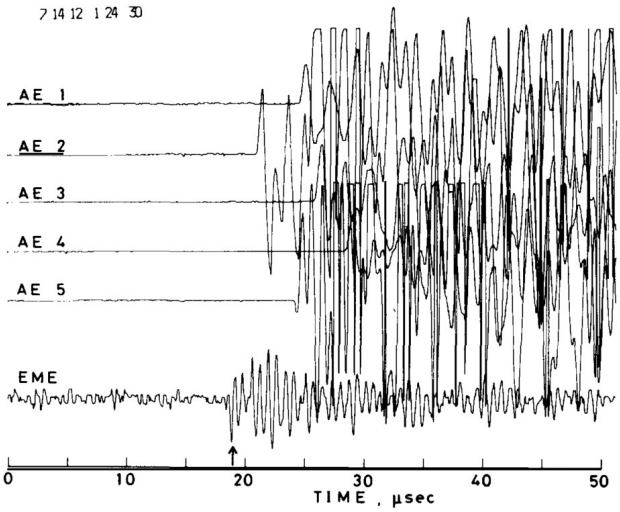

Figure 3-7 Typical example of AE waveforms and EME waveforms during dilating fracture, original source [83].

Approximately 20 % of the AE was associated with EME activity. However, the onset on EMEs coincides with onset of AEs thus EME activity must be directly related to micro-cracking in the sample. Tensile cracks were more efficient at generating EMEs than shear cracks and large and high frequency AE events were more efficient at creating EMEs. The authors suggest that EMEs generation mechanisms are not likely to be associated with the piezo electric effect but instead the contact and separation of fresh charged fracture surfaces.

PSE during dilating fracture has not been studied extensively, however one study [84] investigates this aspect. Cuboid specimens of granodiorite and limestone were instrumented, with twenty EME arenas arranged in close proximity to the rock, with resonant frequencies ranging from 2.5 kHz to 540 kHz inside a magnetic field free space. Holes were drilled into the rock specimen and filled with a non-explosive cracking agent that exerts a swelling force on the rock and produces dilating fracturing.

EMEs were detected in both granodiorite and limestone with peak amplitudes of 80 mV and 40.5 mV respectively and the main spectral components of EMEs reside in two bands of several kHz to 60 kHz and several kHz to 280 kHz. The authors propose the EME generation mechanism could be due to the opening of cracks and the associated stress drop during dilating fracture.

3.2.4 Mechanical loading

During the uniaxial loading of marble samples [16] (98 % calcite; 0.2 % quartz; and other minerals including muscovite, sericite and chlorite) PSC was measured using a laboratory electrometer and the measurements were undertaken inside a Faraday cage, to eliminate ambient electrical noise.

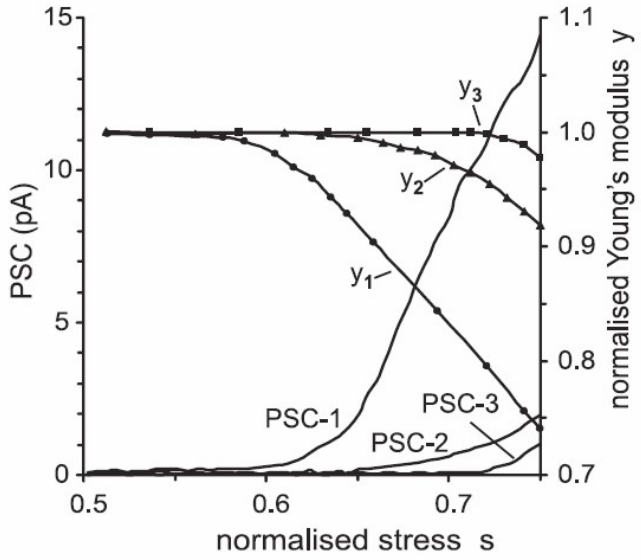

Figure 3-8 PSC variation and corresponding Young's modulus with respect to uniaxial stress, original source [18].

The results show a linear relationship between PSC and stress rate in the linear elastic region of the stress strain curve. This relationship deviates from linearity after the linear elastic region has been exceeded. At this point the relationship between PSC and stress rate is dependent on a scaling factor that is related to the change in Young's modulus of the material. Where the scaling factor is defined as 1/Young's modulus. The maximum amplitude of PSC was detected after the linear elastic region of the marble and variations in PSC amplitude were detected during failure and are thought to be associated with facture.

3.2.5 Emission of charged particles

Impact experiments [85] were carried out on gabbro (no quartz) and diorite (quartz bearing), where the rock samples were impacted by aluminium sphere projectiles inside a vacuum chamber that also acted as a Faraday cage.

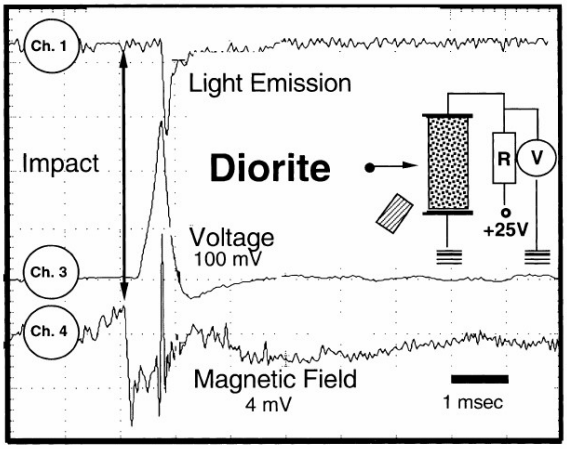

Figure 3-9 Low velocity impact of diorite rock sample, original source [85]. *Showing resulting magnetic field, electric potential and light emissions.*

Three magnetic pickup coils were used to record emissions from the resulting impact plasma plume. Three capacitively coupled electrodes were used and two electrodes were placed directly on the rocks. In addition, photodiodes to measure light emissions were used in the low velocity excipients and two Tektronix digital oscilloscopes were used to record the resulting signals from all sensors simultaneously.

During low velocity testing (~100 ms^{-1}) highly mobile charge carriers were generated in the small volume near the impact point. They spread through the rocks, causing electric potentials in the range of millivolts and light emissions; as the charge cloud spreads through the rock it becomes temporarily conductive. Although the surface potentials are in the order of millivolts, since the charge layer built from within the rock volume is very thin, the associated electric fields will be very high. At rims and edges of the rock the electric field will be even higher, enough to cause dielectric breakdown of the surrounding air, resulting in light emissions and burst of EME [85].

For the medium velocity experiments (~1.5 Kms^{-1}) of granite rock samples, acoustic P and S waves were observed using piezo transducers. After the AE waves had passed, the surface of the granite became positively charged, suggesting the same charge carriers are present, as observed in the low velocity experiments.

The observations of electric potential on the surface of the rock are consistent with the generation theory of positive holes (p-holes), which are the result of defect electrons moving from the oxygen sub-lattice of the rocks. The low impact tests show that p-holes can be generated by low energy mechanisms, such as micro-cracking.

Another experimental study [86] also supports the theory of defect electrons. Electric potential and current were measured in granite (piezo) and anorthosite (non-piezo) rock tiles, using a laboratory electrometer, during uniaxial compression. The results showed an increase in conductivity of the rocks as well as self-generating current when rocks are under stress, especially in the anorthosite (surface potential of 550 mV). The researchers propose that the electrical charges in the rock are the result of stress-activated peroxy links yielding mobile defect electrons (this was deduced by observations of

current and positive potential). The experiments show that charge carriers can spread out of their source volumes to the surrounding unstressed rocks. The defect electrons are likely associated with the oxygen anion sub-lattice of the materials and hence the production of P-holes occurs. The researchers propose that satellites could be used to monitor the P-holes from space and thus show areas of stress build up prior to earthquakes.

3.3 PSE measurement technologies

Almost all of the PSE laboratory studies discussed previously (section 3.2), mention using shielding from electromagnetic noise in order to improve the signal to noise ratio and acquire accurate measurement of PSEs from the material samples [11-13, 15-17, 80-86]. While this approach may be appropriate for laboratory studies it would not be practical to shield large structures for the sole purpose of SHM in the geological or civil field. This downfall is an inherent property of the measurement technologies used. In addition, each of the measurement technologies, including electrometers, AE pre-amps (charge amplifiers) and EME antennas, have their own limitations.

Benchtop electrometers and picoammeters, required for monitoring the weak PSC (Pico amps) from rocks and concrete, are expensive. In almost all cases Keithley Instruments Inc [79] electrometers were used [15-17, 82]. For example, a Keithley Instruments Inc [79] electrometer will cost in the range of ~£2000 to ~£6000. These devices are also bulky and thus not practical for mounting on structures for SHM. All of these factors do not make these devices suitable for field use outside of the laboratory setting, for array setups or for long term monitoring of structures. In addition, there are fundamental problems with the nature of PSC measurement. Firstly, PSCs have only been recorded in the range of Pico amps; thus there are problems with noise. Any cable movement between electrodes and electrometers will generate current and often swamp out the measurement signal; furthermore, shielding from ambient electric fields is necessary [13, 15-17, 82]. Secondly, the measurement relies on pairs of electrodes, which will be some arbitrary distance apart in the geological/civil field and the measurement is electrically invasive.

EME antennas have different inherent problems; the majority of antennas used in PSE studies [12, 72, 80, 81, 83-85] have been loop antennas. They are designed to operate at different frequencies typically ranging from 10 kHz to 228 MHz in the PSE laboratory studies discussed previously 3.2. Although the EME antennas are inexpensive there are some draw backs to the technology. Firstly, electromagnetic shielding is required in order to obtain accurate measurements, as shown in laboratory studies [12, 80, 83-85]. Additionally, monopole pipe antennas have to be installed deep underground (100-800 m, depending on the antenna lengths), in vertical bore holes to attenuate the effect of electromagnetic noise, from populated areas; as shown in a field study [72] that monitored PSE associated with earthquakes. Secondly, a number of the laboratory studies and the field study mention the use of multiple EME

antennas, tuned to different frequencies, in order to monitor a wider frequency range of PSEs. This is a disadvantage compared to a broadband PSE sensing technology.

A small number of PSE laboratory studies [11, 78, 81, 85] used AE preamplifiers and acquisition systems for measuring the charge on the surface of materials. Although AE preamplifiers are robust, compact and are widely used for the field monitoring of AEs, the pre-amps and associated AE acquisition systems are expensive. For example, a 8 channel system from a leading manufacture, Physical Acoustics Cooperation [87] would cost in the range of £14,000 due to the cost of AE pre-amps, they are not viable for PSE electrode array formats for monitoring large structures. In addition, cable movement between the electrode and the preamplifier can introduce noise.

4 THE ELECTRIC POTENTIAL SENSOR SYSTEM

This chapter provides an introduction to the electric potential sensor (EPS) (section 4.1); followed by, an overview of electrometer and EPS circuit design principles (section 4.2 and 4.3) and methods of EPS characterisation in terms of input impedance, frequency response and noise (section 4.4). In addition, the detailed circuit designs for the capacitively coupled EPS (section 4.5) and information about previous research using the capacitively coupled sensor for PSV measurement (Section 4.5.4) are presented. Detailed circuit designs for the novel directly coupled smart EPSs (section 4.6), as well as EPS signal processing methods (section 4.7) can also be found in this chapter. Future directions for EPS design and commercialisation are discussed at the end of the chapter in section 4.8.

4.1 Introduction

The electric potential sensor (EPS), invented at the University of Sussex is an ultra-high input impedance electrometer and integrated electrode structure, capable of measuring electric potential and electric field to a high degree of accuracy. EPSs are made from low cost, readily available semiconductor components that can be fabricated onto small printed circuits boards (PCBs), to form compact, portable and cost effective sensors. The specification of EPSs such as input impedance, electrode structure, signal gain and frequency response can be tailored to almost any application. EPSs have already been successfully applied to a diverse range of research projects, including monitoring electrophysiological signals [88-90], imaging electrostatic fingerprints [91], imaging of materials and active electric circuits [92-94], nuclear magnetic resonance signal acquisition [95] and structural health motioning [19, 20]. In addition, a version of the EPS has been successfully commercialised onto a monolithic semiconductor chip (EPIC), by Plessey Semiconductors for monitoring human electrophysiological signals [96].

4.2 Benchtop electrometers and EPS

This thesis focuses on using EPS technology, for monitoring the pressure stimulated voltages (PSVs), associated with the pressure stimulated currents (PSCs), observed in studies by others [15-17, 82]. PSVs could also be monitored using commercial benchtop electrometers. This section describes the fundamental operating principles of electrometers and how this relates to EPS technology.

The ideal pressure stimulated electrical emission (PSE) monitoring technology, would measure PSV as it has the following advantages:

- PSV has been shown to be in the range of millivolts [11, 19, 20, 97] and have a better signal to noise ratio than the associated PSC (in the range of Pico amps) [13, 15-17, 82, 86]. Almost all PSC studies have mentioned electrically shielding entire experiments, which is an unpractical approach outside of the laboratory; this may not be necessary with the associated PSV measurements.

- PSV could be measured using a single ended (ground referred) electrode; a clear advantage over the PSC measurement method which requires electrode pairs.
- Due to the nature of PSC measurement, current will flow through the ammeter and thus disturb the electrical charge on the surface of the material. Whereas, PSV measurement using an ultra-high input impedance electrometer/EPS, is electrically non-invasive.
- EME antennas rely on electromagnetic shielding from the surrounding environment, in order to detect PSE, this is not a viable approach for field use. PSV detection does not have this issue, because the signal to noise ratio is higher and analogue notch filters can be used to attenuate ambient electric fields.

4.2.1 Electrometer voltmeter circuit design

The fundamental principles of voltage measurement by electrometers, can be understood as operational amplifier circuits.

4.2.1.1 Basic circuit configuration

The circuit configuration shown in Figure 4-1 is that of an opamp voltage amplifier, the voltage gain is determined by the ratio of non-inverting (+) and inverting (-) input voltage, set by the ratio of resistors R_A and R_B.

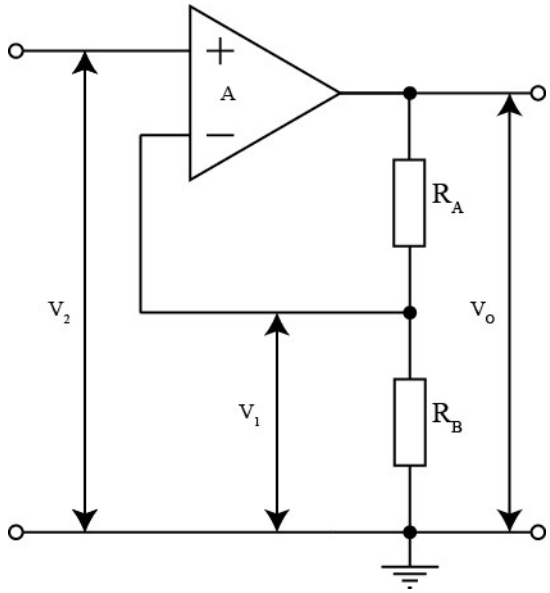

Figure 4-1 Non inverting voltage amplifier, adapted from [98].

The voltage gain can be described by the equation:

$$V_o = V_2\left(1 + \frac{R_A}{R_B}\right)$$

Equation 4-1 Non-inverting amplifier output voltage: *V_o = output voltage; V_2 = input voltage; and R_A and R_B = gain control resistors.*

Voltage measurement from sources with high input resistance (e.g. insulting materials such as rocks and concrete), are subjected to a number of measurement errors, including loading errors due to input resistance bias current, and external shunt resistance and capacitance.

4.2.1.2 Input resistance loading

The input resistance of the electrometer will be in parallel with the source resistance and cause loading errors during voltage measurement; in accordance with voltage divider Equation 4-2.

$$V_M = V_S\left(\frac{R_{in}}{R_S + R_{in}}\right)$$

Equation 4-2 Input resistance loading [98]: *R_{in} = input resistance of electrometer, R_S = source resistance, V_M = measured voltage and V_S = source voltage.*

The electrometer input resistance should be much higher than the source resistance. For instance, if the desired measurement accuracy was ±1 %, then the electrometer input resistance should be x100 larger than the source resistance. Both commercial electrometers, such as the Keithley 6517b [79] (200 TΩ) and the EPS (>10^{13} Ω), have high input resistances in order to obtain high accuracy voltage measurements.

4.2.1.3 Input bias current loading

Due to the nature of the internal instrument circuitry, an internal bias current flows, this develops an error voltage across the source resistance and thus the measured voltage will differ from the source voltage; in accordance with Equation 4-3.

$$V_M = V_S \pm I_{bias}R_S$$

Equation 4-3 Bias current loading [98]: *V_M = measured voltage, V_S = source voltage, I_{bias} = internal bias current and R_S = source resistance.*

Electrometers typically have input bias currents in the range of femtoamps, thus producing a much more accurate measurement compare to digital multi-meters (1pA to 1nA) [98]. EPS bias current compensation methods are discussed in section 4.3.4.

4.2.1.4 Shunt resistance and capacitance guarding

External shunt resistance can be the result of current leakage in cables between electrode and electrometer and can be caused by dirty insulators, in the vicinity of the high impedance input of the electrometer. As the shunt resistance is in parallel with the source resistance, a voltage divider is formed, in accordance with voltage divider Equation 4-4 .

$$V_M = V_S\left(\frac{R_{Shunt}}{R_S + R_{shunt}}\right)$$

Equation 4-4 Shunt resistance loading [98]. *V_M = bias voltage, V_s source voltage, R_s = source resistance and R_{shunt} = shunt resistance.*

This introduces an error in the measured voltage, compared to the actual voltage at the source. A method commonly used to greatly reduce the effects of leakage current in lead wires, is a guard configuration as shown in Figure 4-2.

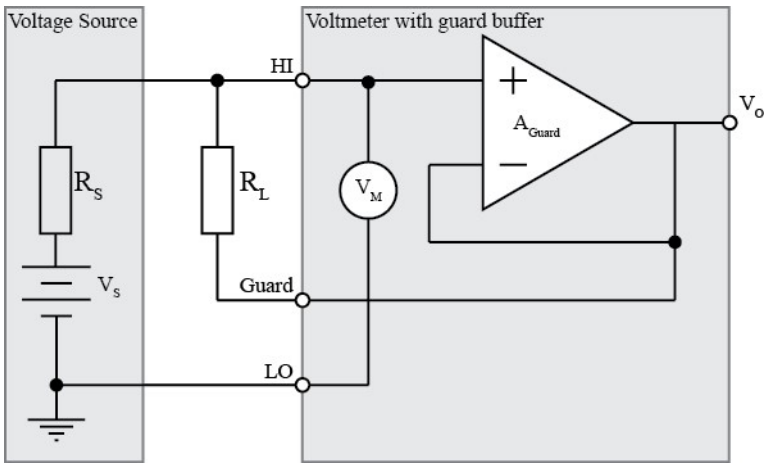

Figure 4-2 Leakage resistance guarding, adapted from [98]. *A_{Guard} = unity gain buffer amplifier, R_L = leakage resistance of the lead, R_S = source resistance, V_M = voltmeter and V_S = source voltage.*

A unity gain buffer amplifier stage is used to drive the guard positioned around the lead wire, to the same potential as the measurement electrode/lead wire, thus greatly reducing the leakage current through the cable leakage resistance. As a result, the measured voltage is much closer to the actual source voltage.

The effective input capacitance of the electrometer, is formed by the leakage capacitance (shunt capacitance) of the lead wire in parallel with the input capacitance of the electrometer itself. This forms a R-C time constant with the source resistance and the effective input capacitance, which reduces the settling time of electrometer, in accordance with the equation:

$$V_M = V_S\left(1 - e^{\left(\frac{-t}{R_S C_{shunt}}\right)}\right)$$

Equation 4-5 shunt capacitance effect on measured voltage, [98]: *V_M = measured voltage, V_S = source voltage, R_S = source resistance and S_{hunt} = shunt capacitance.*

When the source voltage is applied, the measured voltage does not change instantly, instead the voltage rises exponentially. However, due to implementing a driven guard to reduce effects of shunt resistance, this also reduces the effects of leakage capacitance and thus the settling time of the electrometer is reduced.

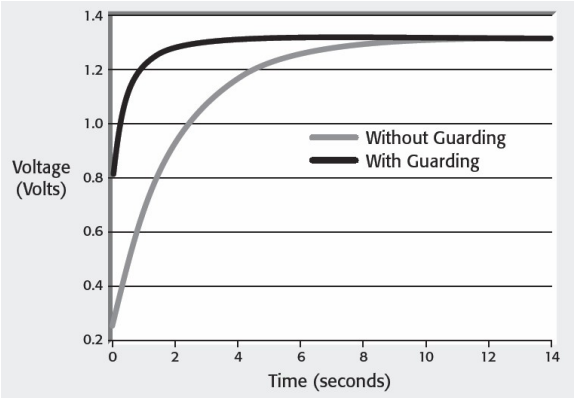

Figure 4-3 Effect of guarding on electrometer settling time, original source [98]. *Voltage source of 1.3 volts through a 2-meter-long triax cable (C_{shunt}) with an internal cable resistance of 100 GΩ.*

EPS technology also implements guarding to improve the effects of leakage resistance and leakage capacitance and is discussed in more detail in the section 4.3.3 of this thesis. The fundamental difference between EPS and electrometers is that EPS is essentially an active electrode structure. Because EPS is a compact device rather than benchtop instrument it can be connected directly to an electrode negating the used of lead wires and their associated shunt resistance and capacitance problems.

4.2.1.5 Electrode lead wires and connections

Selecting an appropriate cable between electrode and electrometer is important; the lead wire insulation resistance must be several orders of magnitude higher than the source resistance [98]. Otherwise, the shunting effects of the insulation will reduce the measured voltage, compared to the source voltage, as discussed previously.

If the insulation resistance of the cables or connectors is compromised, all voltage measurements will be subjected to shunting effects; as this is a consistent error it often will go undetected [98]. Therefore, it is common practice to regularly monitor insulation resistance, with an electrometer ohmmeter to assess the integrity of the cables and associated connectors and replaced or clean them if any irregularities are detected [98].

Furthermore, insulting properties of the cables and associated connectors, with regards to charging and environmental effects need to be considered:

- Volume resistivity and surface resistivity: leakage of current through the insulting material and on the surface of the material respectively.
- Water absorption: the resistivity of insulting material will be reduced due to water absorption.
- Cable movement: due to the piezoelectric effect as a result of mechanical stress or triboelectric effect from as the result of friction between materials, charge unbalances will be created and thus current flow/voltage shift.
- Dielectric absorption: a property of insulators storing and releasing charge over extended periods of time.

Table 4-1 shows the properties of different types of insulator that are commonly used for electrometer front end cables, connectors and fixtures.

The most commonly used material is Teflon; as it has adequate insulation resistance properties, its resistivity is not greatly affected by humidity, it is chemically inert and easily cleaned. Sapphire has the best properties overall, scoring highly in all categories, but this material is relatively expensive and difficult to machine and form.

Material	Volume resistivity (ohm-cm)	Resistance to water absorption	Minimal piezoelectric effects	Minimal triboelectric effects	Minimal dielectric absorption
Teflon® PTFE	$>10^{18}$	+	-	-	+
Sapphire	$>10^{18}$	+	+	0	+
Polyethylene	$>10^{16}$	0	+	0	+
Polystyrene	$>10^{18}$	0	0	-	+
Kel-F®	$>10^{18}$	+	0	-	0
Ceramic	10^{14} - 10^{15}	-	0	+	+
Nylon	10^{13} - 10^{14}	-	0	-	-
Glass epoxy	10^{13}	-	0	-	-
PVC	$5x10^{13}$	+	0	0	-

Table 4-1 Properties of insulating materials, adapted from [98]. *+ = material good in regards to property, - = material poor with regards to property and 0 = material moderately good with regards to property.*

EPSs are active electrodes, thus issues arising from input cables are eliminated or reduced. In the case of the capacitively coupled EPSs and smart EPSs discussed in section 4.3, the electrical paths between electrode and EPS font end are very short (~5 mm and ~20 mm respectively), allowing for very little movement and a reduction in the measurement errors. The commercialised electric potential integrated circuit (EPIC) [96], has the electrode and EPS amplification stages in a single monolithic semiconductor integrated circuit (IC), this essentially eliminates the input cable issues almost completely.

4.2.1.6 Summary

Low level signal measurement instruments, such as Keithley Instruments Inc [79] nanovoltmeters and electrometers, are instruments from the most widely used manufacturer and are capable of PSV measurement. The smallest nanovoltmeter or electrometer in Keithley's low level signal measurement range, is the Keithley 6430 [79], measuring 89 x 213 x 370 mm. The Keithley 6430 is much larger than an EPS device, such as the capacitively coupled EPS (33 x 15 x 10 mm) and directly coupled smart EPS (30 x 50 x 20 mm), discussed sections 4.5 and 4.6 respectively and the commercialised EPIC [96] (10 x 10 x 2 mm). Furthermore, the Keithley 6430 [79] weighs 5.6 Kg, where as an EPS device weights < 200 g.

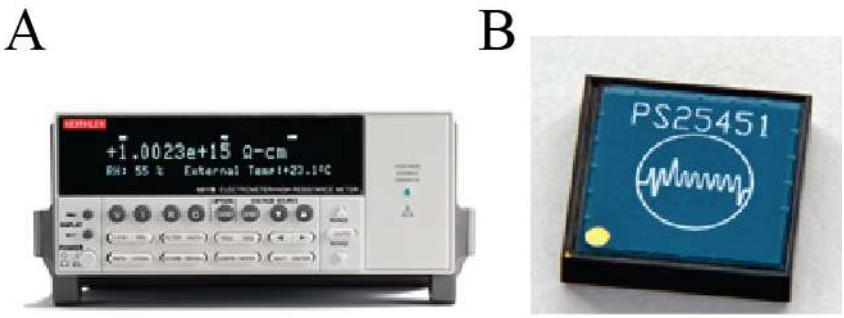

Figure 4-4 Benchtop electrometer and EPS form factor. *A) Keithley Instruments Inc 6430 [79] (89x123x370 mm, 5.6 Kg), B) Plessy Semiconductors EPIC sensor [87] (10x10x2 mm , <100 g).*

Electrometers require cable connections to their measurement electrodes, which in order to reduce measurement error must be fairly short in length <1 m. Therefore, when monitoring PSV on real structures, such as rock faces or bridges, electrometers would have to be mounted onto the structure near to the measurement electrodes, in environmentally controlled enclosures. In addition, the lead wires would have to secured to reduce measurement errors, as a result of cable movement and be thermally insulted to avoid problems with thermoelectric voltages, as a result of temperature gradients. Electrode arrays cannot be connected to a single electrometer and thus a large number of bulky, heavy, expensive electrometers would have to be mounted over a structure; which amongst the other points mentioned makes benchtop electrometers impractical for field use.

In contrast, the relatively compact and light weight EPSs could be mounted onto structures easily, as they are compact (EPIC – 10 x 10x 2 mm) and light weight. As EPSs are application specific devices, they can be tailored to specific situations; e.g. designed to be waterproof/weatherproof for the purposes of SHM. An EPS's amplified output signals and power connections are routed through a single flexible cable; this allows for the EPS's relatively bulky power supply and data acquisition device, to be place in a convenient location away from the measurement electrodes. Movement of the EPS cable would not initiate measurement errors, because the PSV signals are amplified by the EPS and thus have a good signal to noise ratio. The measurement errors caused by cables, including piezoelectric charging, triboelectric charging, dielectric absorption, resistivity changes due to water absorption and thermal electric EMFs are greatly reduced or eliminated, by having an active electrode structure. Arrays of EPSs could be connected to via cables, to a single acquisition device for a more practical approach to SHM.

4.3 EPS design principles

Figure 4-5 shows the fundaments features of an EPS; the sensor is based around a non-inverting amplifier. The EPSs discussed in thesis use non-inverting operational amplifiers (opamps), however the sensors can be made using discrete transistor circuits. The amplifier is non-inverting so the positive feedback pathways are in phase with the input, this is necessary for neutralisation and bootstrapping to be effective at increasing the effective input impedance of the EPS.

The negative feedback loop controls the closed loop gain of the amplifier, where the high impedance input is connected to the low impedance output, thus very little power is drawn from the signal source and loading effects are minimal. The more negative feedback, the lower the gain; if the output were connected directly to the input, a voltage follower circuit would be formed with a gain of 1. Typically, a standard non-inverting opamp circuit is used [99], where a voltage divider controls the feedback and thus gain of the opamp.

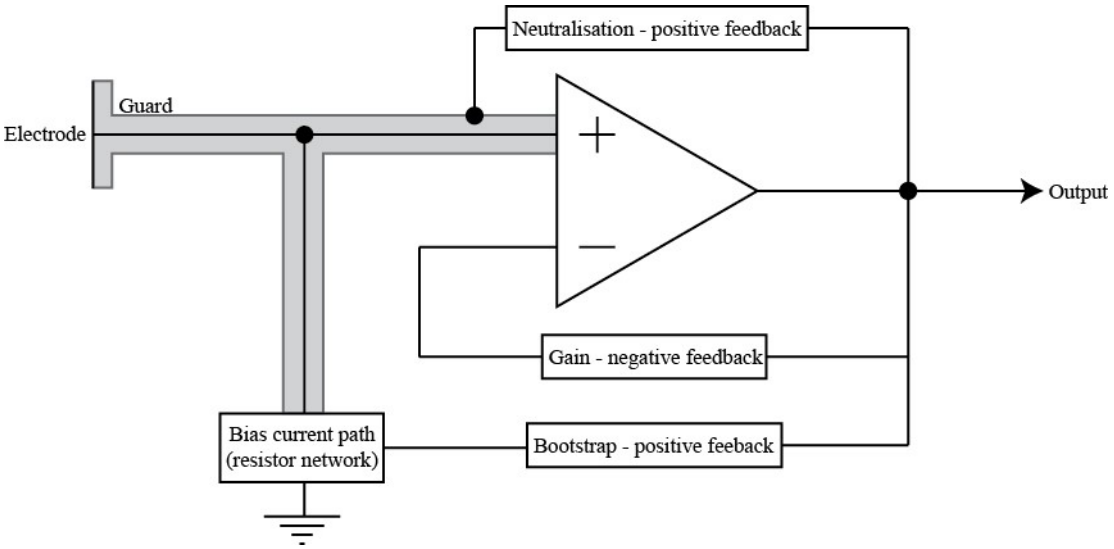

Figure 4-5 Block diagram showing the fundamental EPS components.

4.3.1 Bootstrapping

Bootstrapping is a technique where a percentage of the amplifier output is fed back to the input, to alter the apparent input impedance of the amplifier [100]. The more positive feedback, the greater the apparent input impedance until a point of instability is reached, due to the nature of positive feedback. Without bootstrapping the EPS input resistance is simply the parallel resistance of the large bias current resistor and input resistance of the opamp itself. When applying positive feedback, the apparent input resistance increases by creating a smaller potential difference across the bias resistor.

4.3.2 Leakage current and PCB design considerations

There are many environmental factors that can be a cause disturbance to an EPS design. Dirty PCB tracks can cause leakage at low currents; generally, moisture, oil and even solder flux increase the conductivity of dry dirt and make leakage current problems worse [101]. It is recommended that sub pico-amp circuits such as EPSs be cleaned thoroughly, with deionised water and a solvent based PCB cleaner, to remove any water soluble and oily deposits.

If EPS circuits are exposed to moisture, a galvanic current can be formed between certain combinations of materials, thus affecting measurement accuracy [101]. This is especially important when measuring PSVs from rocks, which contain natural salts and varying degrees of water saturation. Dry air is a good insulator at least at low voltage levels [101], however moisture in the air flowing over conductive elements can produce a small amount of charge and thus effect measurements [101]. To avoid

contamination from moisture and other sources during operation, EPSs must be enclosed from the environment.

Leakage current becomes a major design consideration, when designing sub-picoamp circuits such as EPSs. It might seem logical to use large areas of insulation around low current tracks when designing a PCB; however, this is counter intuitive as it provides a surface to accumulate extra charge. A sensitive part the circuit may pick up this charge and cause issues, with regards to drift or slow settling time of the device. Instead a more sensible approach, is to use large areas of conductive guarding around sensitive areas of the circuit [101], as described in section 4.3.3.

Leakage current performance is largely dominated by the choice of PCB material, if cost is not an issue there are high performance Teflon boards or ceramic hybrids, such as those provided by Rogers Cooperation [102]. These boards have excellent and controlled dielectric properties, but are expensive and toxic. The most common PCB material is FR4, although its dielectric properties are not the most desirable for low current application, it is considerably cheaper and guarding and neutralisation circuit techniques can be used to increase performance.

EPS circuits are also sensitive to ambient electric fields, where the source of the field acts as one plate of a parallel pale capacitor and sensitive nodes of the EPS act as the other plate. These sources of noise can be capacitively coupled to the EPS over fairly large distances (in the range of meters) and may swamp out the desired measurement signal, thus electrical shielding is often necessary.

4.3.3 Neutralisation and guarding

As mentioned previously shielding EPSs is important, the sensor electronics are placed in a grounded metal enclosure and a ground plane is often used across the PCB itself. One downfall of this approach is the shielding creates leakage currents paths and stray capacitances as shown in Figure 4-6.

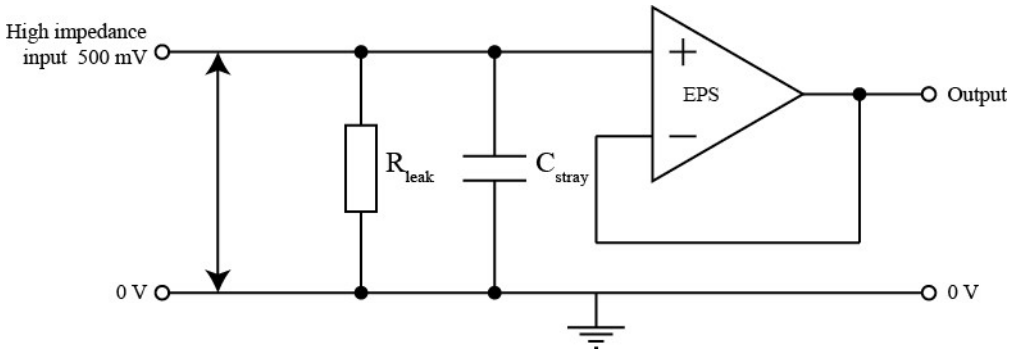

Figure 4-6 EPS leakage current and stray capacitance block diagram.

In the example circuit shown in Figure 4-6, a voltage is induced in the electrode and a potential difference of 500 mV is created between the high impedance input of the EPS and the grounded shielding and/or ground plane on the EPS-PCB. A current will flow through the leakage resistance path and the leakage capacitance will be charged and discharged, this causes problems such as poor settling time and

voltage drift [101]. Adding a guard between the high impedance input and ground shield areas helps to alleviate this problem.

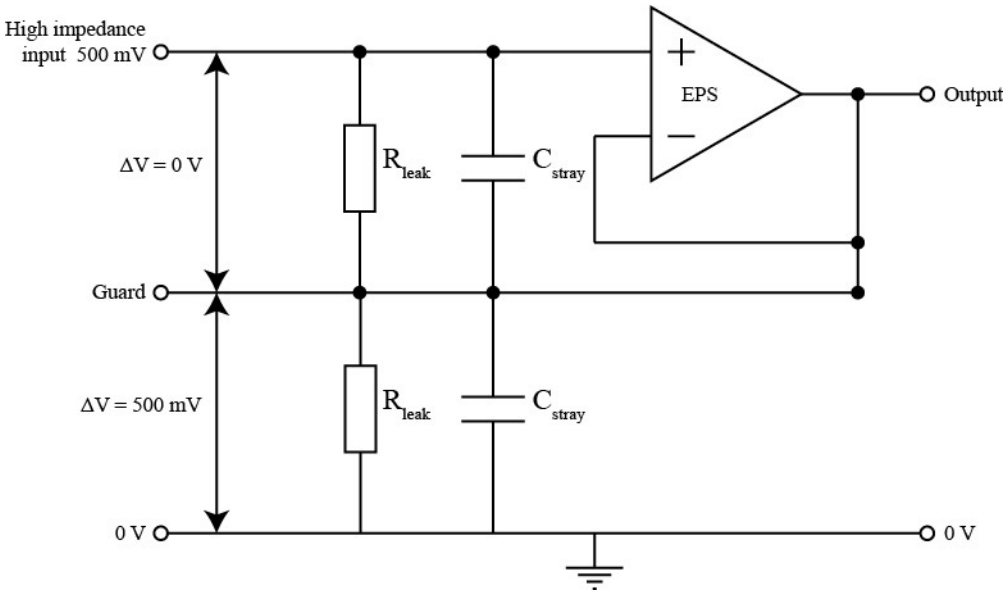

Figure 4-7 EPS neutralisation and guarding principles block diagram.

The guard path is usually positioned around the high input impedance path, between electrode and non-inverting amplifier input and bias current resistor. The guard path can also be placed below the high input impedance tracks on a double-sided PCB. Guarding is useful because it cancels out the input-leakage current and most of the stray capacitance [101]. In the example circuit shown in Figure 4-7, the output of the unity gain amplifier is driving the guard to an equal potential (500 mV) as the input of the EPS. The potential difference between the guard and high impedance EPS input is zero, or in reality a few millivolts, rather than 500 mV as with the unguarded circuit. Thus, a smaller leakage current flows through the leakage resistance path and stray capacitance of the EPS input. External leakages now flow primarily into the guard, rather than the EPS high impedance input.

In addition, the guarding technique reduces the input capacitance of the EPS, as the driving the guard is also a form of bootstrapping [101]. Because the technique uses positive feedback, instability issues can occur if the feedback percentage is too high. Generally, a positive feedback of less than 100 % is used for EPS designs; if the feedback is set too high the output of the EPS will oscillate and no meaningful measurements can be made, until the feedback is reduced causing the sensor to stabilise.

4.3.4 Input bias current errors

A mentioned in the previous section of this chapter, EPSs and electrometers experience bias current loading effects that produce a DC error in the measured voltage of the devices, in accordance with Equation 4-6.

$$V_M = V_S \pm I_{bias} R_b$$

Equation 4-6 Bias current error [98]: *V_M = measured voltage, V_S = source voltage, I_{bias} = internal bias current and R_b = bias resistor.*

EPS technology compensates for this for the error voltage using a capacitively coupled input, this forms first order a high pass filter (HPF), that eliminates the low frequency (DC) voltage error. For instance, if the coupling capacitance was ~ 10 pF and the bias resistor value was 50 GΩ, the HPF cut off frequency would be 0.32 Hz; therefore, any DC voltage errors resulting from bias current loading would be eliminated. However, this is not the case with regards to the directly coupled EPS variants. Sensors with this tomography utilise DC offset circuitry after the first amplification stage, to zero the measured output voltage at the beginning of a measurement.

4.4 EPS characterisation

The EPS performance is determined primarily by its input impedance and noise. Therefore, an accurate method for determining these parameters needs to be undertaken, to fully characterise EPSs.

4.4.1 Characterising EPS input impedance

Figure 4-8 shows an equivalent circuit that is used for calculating input impedance.

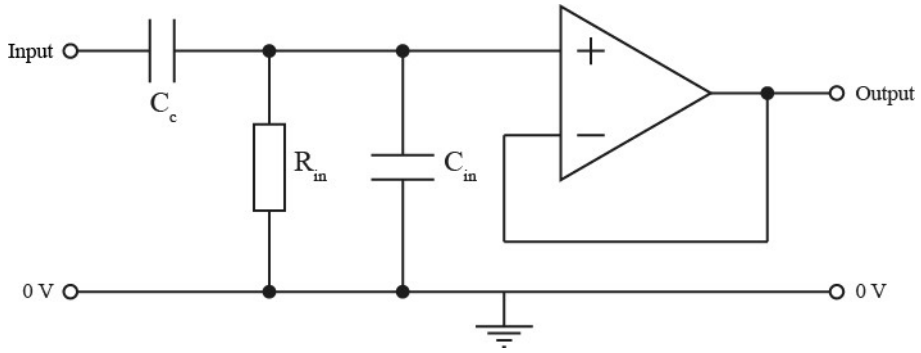

Figure 4-8 Equivalent circuit for calculating EPS input impedance.

If a known coupling capacitance (C_c) is used, then the input impedance Z_{in} (represented by a separate R_{in} and C_{in}) of the sensor can be calculated. In order to calculate the input impedance of an EPS, a known coupling capacitance must be connected to the input of the sensor and then the frequency response of the system (EPS and C_c) must be measured. The frequency response of the system has the same characteristics of a first order high pass filter, as shown by the example system response in Figure 4-9.

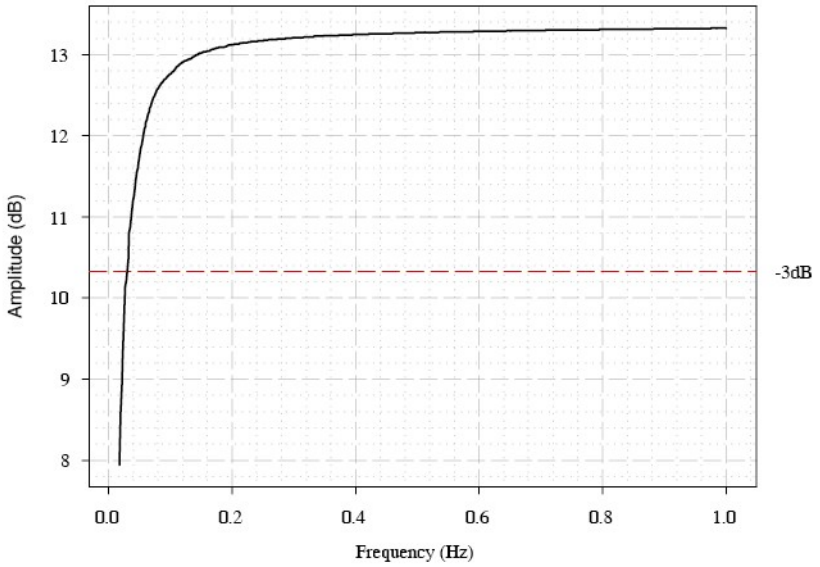

Figure 4-9 Example system response with 154 pF coupling capacitor and EPS with x5 gain.

The response is measured at the output of the amplification stage; therefor, in order to calculate the referred to input (RTI) response before the gain stage of the EPS, one must divide by the DC voltage gain of the opamp circuit. Above the cut-off frequency that is set by R_{in}, the flat region of the response is determined by the capacitive divider formed by C_{in} and C_c, we can therefore calculate the input capacitance of the EPS using the following equation.

$$C_{in} = C_C \left(\frac{A_V}{A_{V,mid}} - 1 \right)$$

Equation 4-7 EPS input capacitance: *A_v = DC calculated voltage gain of the amplifier, $A_{v,\,mid}$ = measured gain of the amplifier and coupling capacitor above the cut-off frequency, Cc = coupling capacitance and C_{in} = input capacitance.*

Once the input capacitance has been calculated, it is then possible calculate the input resistance of the EPS, from the high pass filter corner frequency (-3 dB point) of the system response. The responce is governed by a first order filter equation, with the capacitance term formed by C_c and C_{in}, as shown in Equation 4-8.

$$R_{in} = \frac{1}{2\pi f_c (C_C + C_{in})}$$

Equation 4-8 First order filter EPS input impedance: *f_c = corner frequency (-3 db point), Cc = coupling capacitance, C_{in} = input capacitance and R_{in} = input resistance.*

4.4.2 Characterising EPS input noise

The EPS input noise is comprised of three noise terms, including the resistor thermal noise (e_{th}) and the operational amplifier input current and voltage noise (i_n and e_n). Figure 4-10 shows an equivalent circuit representing the input noise of an EPS.

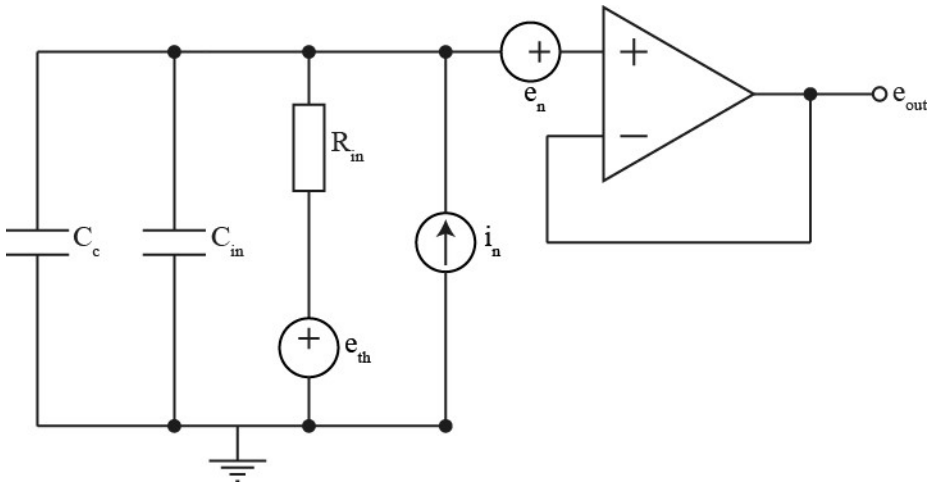

Figure 4-10 Equivalent circuit for EPS voltage noise.

The input capacitance of the EPS has a low pass filter effect on the thermal and current noise terms. The corner frequency of this filter (f_{noise}) is represented by a first order filter equation, where the capacitance term is formed of the input capacitance (C_{in}) and coupling capacitance (C_c) and resistance term is the input resistance of the EPS (R_{in}), as shown in Equation 4-9. At higher frequencies the thermal current noise terms become greatly attenuated and the amplifier voltage noise is dominant.

$$f_{noise} = \frac{1}{2\pi R_{in}(C_{in} + C_c)}$$

Equation 4-9 Thermal and current noise low pass filter effect: *Cc = coupling capacitance, C_{in} = input capacitance and R_{in} = input resistance.*

The resistor thermal voltage (e_{th}) and current (i_{th}) noise terms can be calculated by taking the Norton equivalent of the Nyquist thermal noise relation, as shown in Equation 4-10 and Equation 4-11.

$$e_{th} = \sqrt{4R_{in}K_bTB}$$

Equation 4-10 Input resistor thermal voltage noise: *K_b = Boltzmann's constant, T = absolute temperature, B = bandwidth, R_{in} = input resistance and e_{th} = thermal voltage noise.*

$$i_{th} = \sqrt{\frac{4K_bTB}{R_{in}}}$$

Equation 4-11 Input resistor thermal current noise: *K_b = Boltzmann's constant, T = absolute temperature, B = bandwidth, R_{in} = input resistance and i_{th} = thermal current noise.*

Ideally the amplifier current noise (i_n) should be lower than the thermal input resistor current noise (i_{th}), as the input resistance sets a hard limit on the noise floor of the EPS. The majority of EPS designs utilise a 50 GΩ input resistor, yielding a current noise special density of 0.5 fA/√Hz at 1 kHz. Combining the three noise terms together, gives the output noise of the EPS as shown in Equation 4-12. If i_{th} is larger than i_n, it can be substituted in the equation in place of i_n.

$$e_{out} = \sqrt{e_{th}^2 \frac{1}{1 + (\omega R_{in}(C_c + C_{in}))^2} + i_n^2 \frac{R_{in}^2}{1 + (\omega R_{in}(C_c + C_{in}))^2} + e_n^2}$$

Equation 4-12 Output voltage noise of EPS: *e_n = voltage noise of amplifier, e_{out} = output voltage noise, i_n = amplifier current noise, ω = angular frequency, R_{in} = input resistance, C_{in} = input capacitance and C_c = input capacitance.*

The output voltage noise of an EPS ($\underline{e}_{out}$) can be measured, by using the conventional method of grounding the input of the sensor and measuring the voltage spectral density using a spectrum analyser. The output noise of the EPS is dependent on the coupling capacitance; thus, it is best to measure the noise with the coupling capacitance in place.

4.5 Capacitively coupled EPS for PSV detection

The capacitively coupled EPS sensor was developed at the Sensor Technology Research Centre (STRC), for detecting PSVs expected to be associated with cracking events in geological and manmade materials. Previous work by the STRC shows this sensor is a suitable and robust method for the detection of PSVs, during the uniaxial loading of granite and marble specimens [20]. Experiments in collaboration with the British Geological Survey (BGS), have demonstrated this sensor is capable of PSV detection, in a variety of rock lithologies and concrete [19]. The capacitively coupled EPS was used for all of the capacitively coupled material testing experiments discussed in chapters 6, 7 and 8 of this thesis.

Sensor package

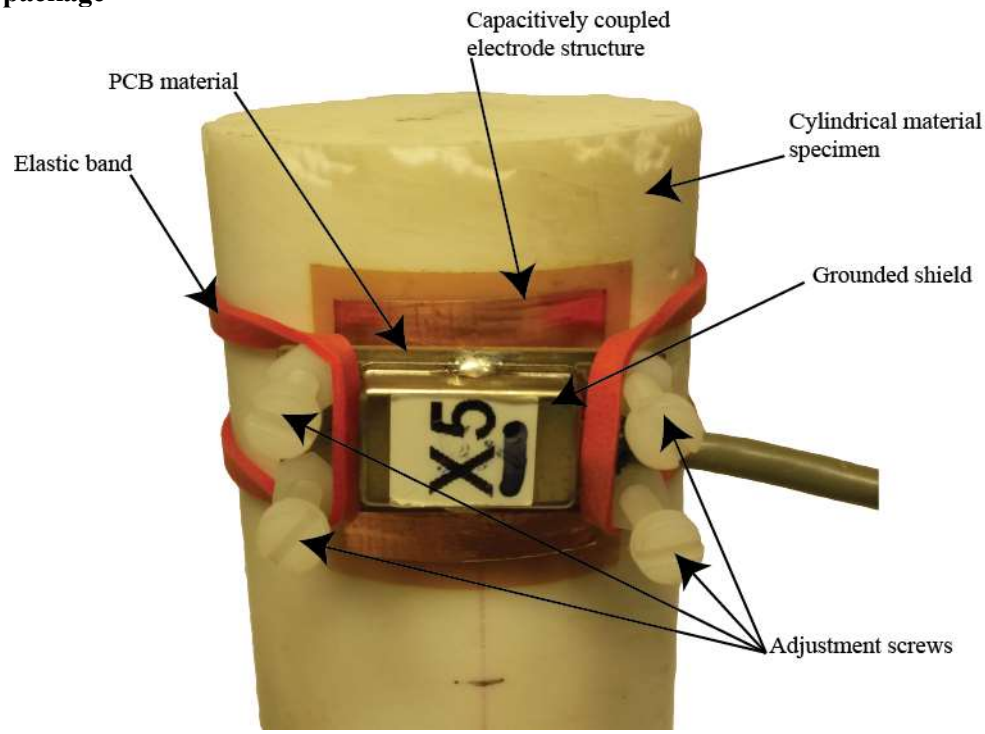

Figure 4-11 Photo of the capacitively coupled EPS attached to a cyclical material specimen.

Specification

Dimensions	X - 33 mm Y - 15 mm Z - 10 mm
Input resistance	39.9 GΩ
Input capacitance	9.12 pF
Gain	x5
Bandwidth	24.5 mHz - 1.3 MHz
Noise (RTI)	25.4 nV√Hz at 1 kHz

Table 4-2 Summary of the capacitively coupled EPS specifications.

Noise characteristics

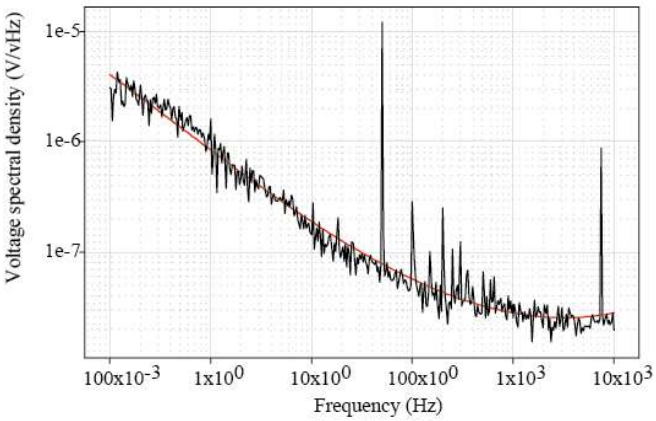

Figure 4-12 Capacitively coupled EPS voltage noise special density plot RTI of the sensor.

The sensor was designed to be compact and mountable onto cylindrical material specimens (~50 mm in diameter). The plastic adjustment screws can be used to ensure the electrode terminal on the back of the EPS. is in contact with the electrode structure that is bonded to the material specimen. The measured input impedance is high (input resistance = 39.9 GΩ, input capacitance 9.12 pF), this ensures the measurement is non-invasive, as no real current is drawn (only displacement current) and the lower cut off frequency is low (25.5 mHz), as demonstrated by Equation 4-8. The Sensor has a wide bandwidth, so correlations between AE and PSV events can be investigated. The bandwidth of the piezo transducers (100 – 1000 kHz) used for all experiment discussed in this thesis, overlaps with the EPS bandwidth (24.5 mHz - 1.3 MHz). In addition, the capacitively coupled EPS has excellent noise performance characteristics (25.4 22 nV√Hz at 1 kHz), the opamp voltage noise (22 nV√Hz at 1 kHz) is the dominant source.

4.5.1 Schematic circuit design

A schematic diagram of EPS circuit in shown in Figure 4-13. The amplifier element of the sensor is a LMC6081 precision CMOS opamp [103], this was selected because it has ultra-low bias current (10 fA), low noise characteristics (22 nV√Hz at 1 kHz), wide gain bandwidth product (1.3 MHz) and high input resistance (< 10 TΩ).

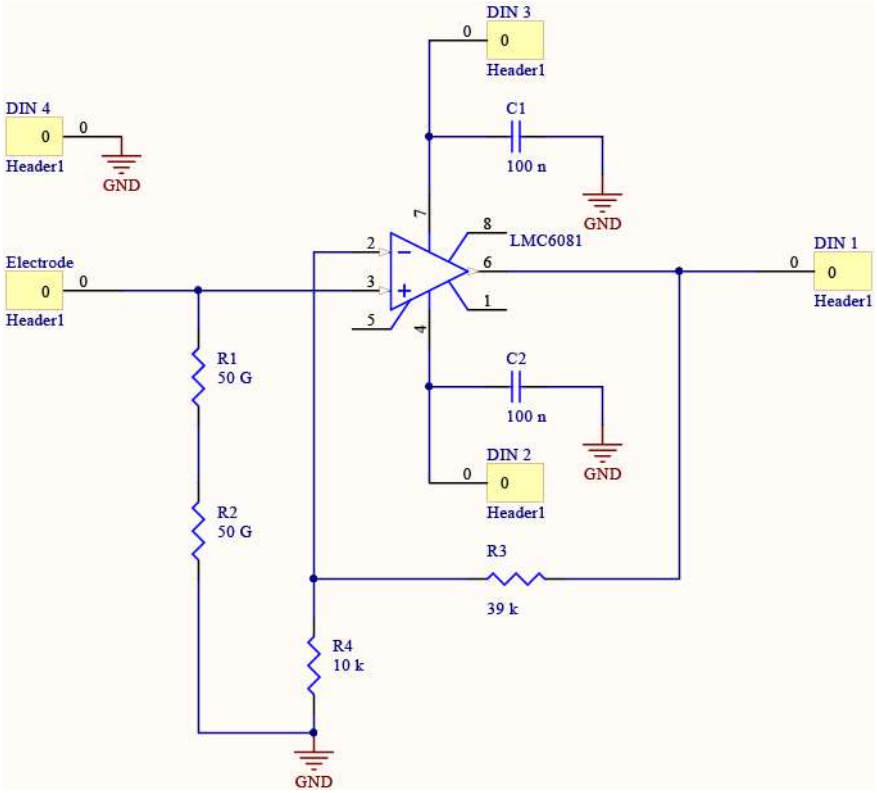

Figure 4-13 Capacitively coupled EPS circuit schematic diagram.

By using this opamp the EPS design achieves the wide bandwidth needed, low noise characteristics and high input impedance. The opamp is configured as a noninverting amplifier [99], with a voltage gain of ~x 5 as shown Equation 4-13.

$$AV = \frac{R_3}{R_4} + 1 = \frac{39\ k\Omega}{10\ k\Omega} + 1 = \ 4.9$$

Equation 4-13 Coactively coupled EPS non-inverting opamp gain.

Capacitors (C_1 and C_2) were used to decouple the opamp from the power supply, noise caused by the power supply is shunted through the 100 nF capacitors. The capacitor values were chosen in accordance with the opamps data sheet [103].

In theory the input resistance of the EPS is formed by the input resistors R_2 and R_1 (100 GΩ) in parallel with the input resistance of the opmap (>10 TΩ), this should equate to a minimum value of:

$$R_{EPS} = \frac{(R_1+R_2)\times R_{opamp}}{(R_1+R_2)+R_{opamp}} = \frac{(50\ G\Omega+50\ G\Omega)\times 10\ T\Omega}{(50\ G\Omega+50\ G\Omega)+10\ T\Omega} = \ 99.01\ \text{G}\Omega$$

Even if the input resistance of the opamp was 100 TΩ, the input resistance of the EPS would still be 99.9 GΩ, thus the input resistors are dominant at setting the input resistance of the EPS. The reason the measured EPS input resistance (39.9 GΩ) is lower, could be because the two input resistors have a tolerance of ±20 %, thus their series value could be as low as 80 GΩ. In addition, the FR4 PCB materials dielectric properties are not optimised for low current designs and thus leakage currents could be responsible for the lower measured input resistance (38 GΩ), compared to the theoretical value (80 GΩ - 100 GΩ).

It was not necessary use any positive feedback bootstrapping or neutralisation techniques to increase the apparent input impedance of the sensor, allowing for the PCB layout to be compact, as shown in Figure 4-14. The PSV signals thought to be associated with cracking events, are relatively large (in the range of millivolts) and can still be detected, even with the attenuating effect of the capacitive divider between the coupling capacitance and input capacitance of the EPS. The PSV signals being measured are also relatively high in frequency and therefore a lower EPS corner frequency (determined by a higher input impedance) is not necessary.

4.5.2 Printed circuit board (PCB) layout

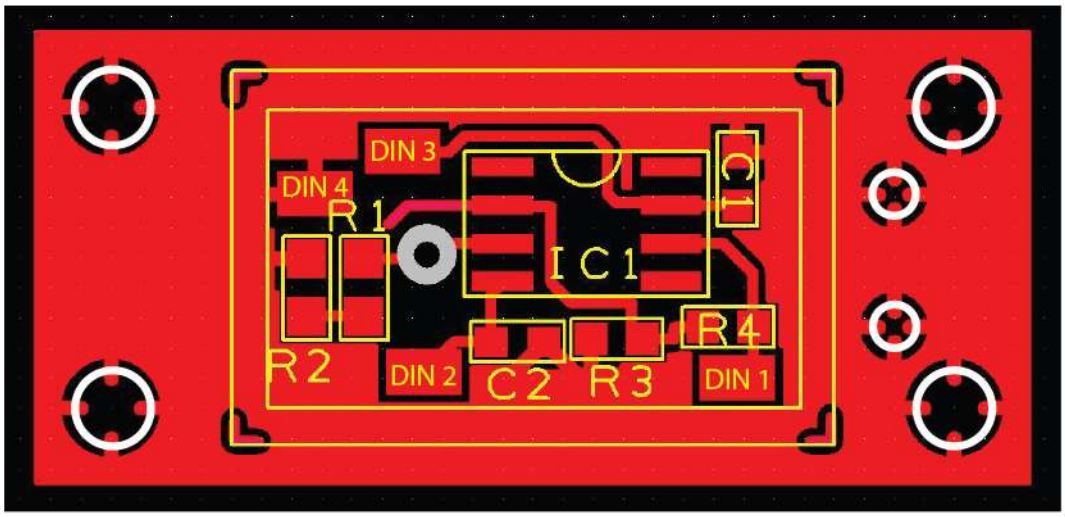

Figure 4-14 Capacitively coupled EPS PCB top layer. *The red areas represent the top copper, the white circles are drilled holes, the grey circles indicate a via connection from the top copper to the bottom copper and the yellow areas represent the component outlines and circuit annotation. Board dimensions: 33 mm by 15 mm.*

The DIN pads on the top PCB layer are soldered to a four-core shielded cable, with a DIN connector on the oppose end of the cable, that can be plugged into an EPS interface. The EPS interface gives the user the option, to apply an analogue 50 Hz notch filter to attenuate ambient electric fields and additional gain can be applied before digitisation. The white circles represent drilled holes in the PCB; the four larger holes at each corner of the PCB are for mounting the plastic adjustment screws and the two smaller holes are used to bind the EPS cable to the PCB, as a form of cable strain relief. Figure 4-15 is a diagram of the bottom layer of the sensor PCB.

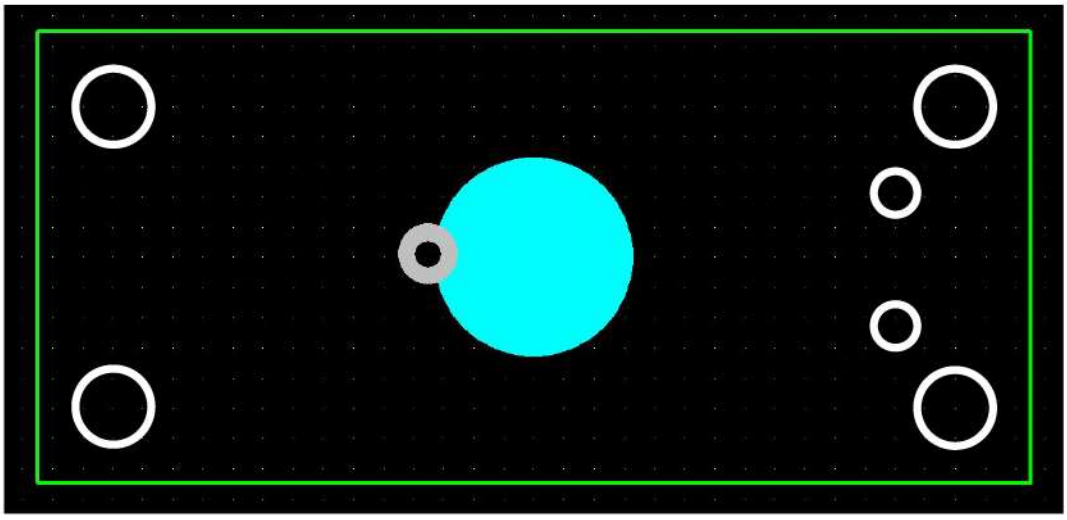

Figure 4-15 Capacatively coupled EPS bottom layer PCB. *The blue area represents the bottom copper, the white circles are drilled holes, the grey circles indicate a via connection from the top copper to the bottom copper and the green lines represent the PCB outline. Board dimensions: 33 mm by 15 mm.*

The blue circle represents the copper electrode terminal that is held in resistive contact with the capacitively coupled electrode structure, bonded to the cylindrical material specimens being tested. The

electrode terminal is connected by a mechanical via connection, to the non-inverting input of the opamp on the top layer of the PCB.

4.5.3 PCB design tools and fabrication

The PCB was designed using Number One Systems Easy-PC software [104], this software package is ideal for designing multilayer PCBs from circuit schematic diagrams. Once the PCB design was finalised, the designed was exported to a Gerber format (.gbr), an industry standard format used to describe PCB images in software.

The double sided PCB was fabricated using LPKF Laser & Electronics computer aided manufacturing (CAM) software (LPKF CircuitPro PM) [105] and PCB fabrication equipment, including a PCB milling machine (LPKF ProtoMat S103) [106] and reflow oven (LPKF ProtoFlow S) [107]. The CAM software generated a tool path for the PCB milling machine from the Gerber files and then the milling machine fabricated the double-sided PCB. The surface mounted devices (SMDs) were placed in their associated positions on top of solder paste, after which the reflow oven melted the paste thus soldering the SMDs in position. Manual hand soldering of the non SMDs such as the shield and cable was necessary.

4.5.4 Pressure stimulated voltage detection using the capacitively coupled EPS

Previous work [19, 20] by Dr Ahmet Aydin has demonstrated that EPS technology is capable of measuring pressure stimulated voltage (PSV) during the uniaxial compression of various rock lithology. Detailed information about EPSs, is presented and discussed in chapter 4 of this thesis.

Dr Aydin's initial research observed PSV emissions during the uniaxial compression of granite and marble cubes (30 x 30 x 30 cm), by a manually operated hydraulic floor press. The Each rock was placed on top of a steel control sample separated by an electrically insulating layer. The rocks-control sample stacks were loaded at a constant stress rate, in small steps, until failure occurred or the load capacity of the press was reached (10 tonnes). Two capacitively coupled EPSs were used to measure differential PSV from opposite sides of the rock cubes perpendicular to the applied load, in the same manor two EPS were used to measure PSV from the control sample and a load cell was used to monitor the load.

The results of loading the granite specimen are shown in Figure 4-16. Cyclic changes in amplitude were observed during stress steps and spikes in PSV amplitude appear to increase as the applied pressure increases up to ~21 MPa, after which the amplitude stabilises. The loading of the granite did not reach material failure due to the limitation of the hydraulic press.

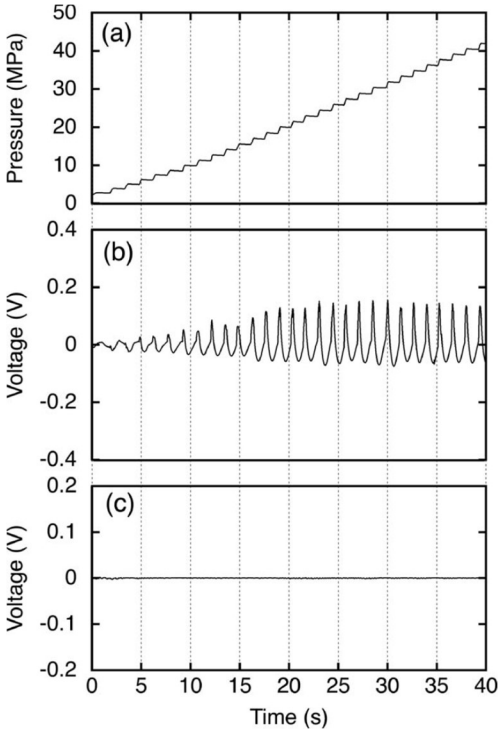

Figure 4-16 Experimental data from a granite sample, original source [20]. *a) applied load, (b) differential PSV referred to the rock surface and (c) PSV referred to the surface of a steel control sample.*

The PSV resulting from the marble sample behaves differently as shown in Figure 4-17. A cyclic response in the PSV is observed, similar to the granite sample (up to ~19 MPa); the PSV amplitude then reduces and then after ~45 MPa the PSV amplitude increases and goes through 6 polarity reversals.

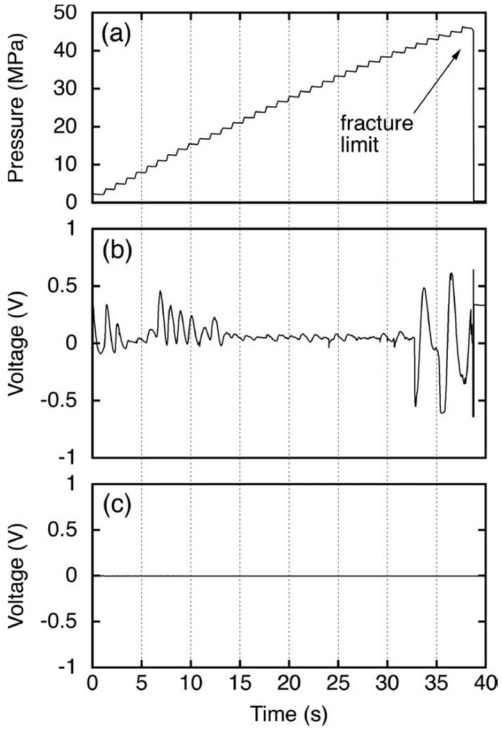

Figure 4-17 Experimental data from a marble sample, original source [20]. *a) applied load, (b) differential PSV referred to the rock surface and (c) PSV referred to the surface of a steel control sample.*

Both experiments presented in this article used a steel control sample (that should not produce any detectable PSV) which was stacked with the rock cube and thus was subjected to the same loading profile. The controls samples were instrumented with capacitively coupled EPSs; they produced no PSV emissions, this demonstrates that PSV in the rocks are not a result of mechanical vibration from the load frame itself. The control tests are shown in part (c) of Figure 4-16 and Figure 4-17.

The article confirms PSV behaves in a similar way to PSC observed in other studies [16, 17]. Monitoring PSV, using inexpensive and field capable EPS technology, is a viable alternative to monitoring PSC, using expensive benchtop electrometers. This study also shows PSV signals are in the order of volts and could yield useable results in field studies. In addition, the cyclic observations of PSV in the marble specimen prior to failure, could be used as a precursory signal for failure prediction.

In another study [19] Dr Aydin, in collaboration with the British Geological Survey (BGS), conducted more advanced experiments using the facilities at BGS's Geotechnical Rock Testing Facility. These studies used uniaxial compressive testing standards set out by the Internal Society for Rock Mechanics (ISRM). Five cylindrical rock specimens (54 mm diameter 108 mm long), including Cordierite-mica Schist, quartzite, gabbro, granite and sandstone, were subjected to either a constant stress rate or axial strain rate until failure occurred. In addition, an aluminium control sample was subjected to a constant stress rate ramp test up to 234 MPa, before being de-loaded, in order to determine if the measured voltages from the rocks were a result of spontaneous potential or an artefact of vibration from the load frame itself.

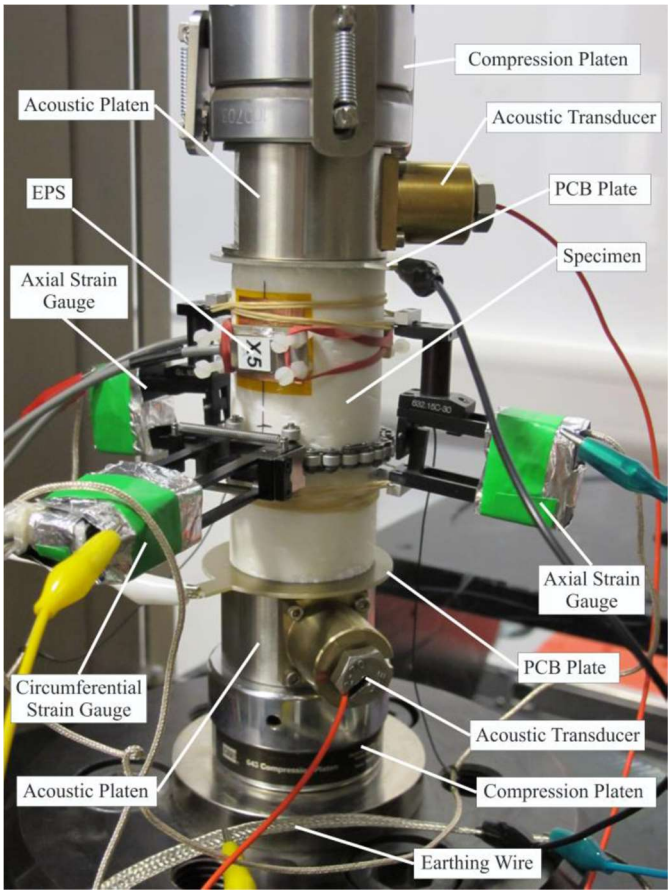

Figure 4-18 Experimental configuration, original source [19].

The experimental configuration is shown in Figure 4-18; cylindrical rock specimens were instrumented with two axial strain gauges, one circumferential strain gauge, two piezo transducers, two capacitively coupled EPS to measure the axial strain, circumferential strain, AEs and PSV respectively; and a load cell was used to monitor the applied load. Single sided printed circuit board (PCB) plates were used to isolate the rock specimens from the load frame. A detailed overview of the experimental setup is described in section 5.3, as the experimental setup is identical to the capacitively coupled oven dried rock experiments discussed in this thesis. However, the results presented in this article [19] did not utilise AE recordings alongside PSV.

The EPS amplified PSV outputs were notch filtered at 50 Hz, to attenuate the effects of ambient electric fields and thus the experiments did not have to be carried out in an enclosed Faraday shield, as with the majority of other PSE studies.

PSV in the lower frequency band, up to 1 kHz, was detected in all rock lithologies regardless of the presence of the piezoelectric mineral quartz. Lithologies that contained little to no quartz (gabbro-0 % and Cordierite-mica Schist 13 %) produce no high frequency (>1 kHz) PSV, apart from transient signals that did not correspond to any features in the stress strain profiles. The presence of these transient signals could be the result of an unknown generation mechanism, Figure 4-19 shows a good example of this phenomenon in the gabbro sample.

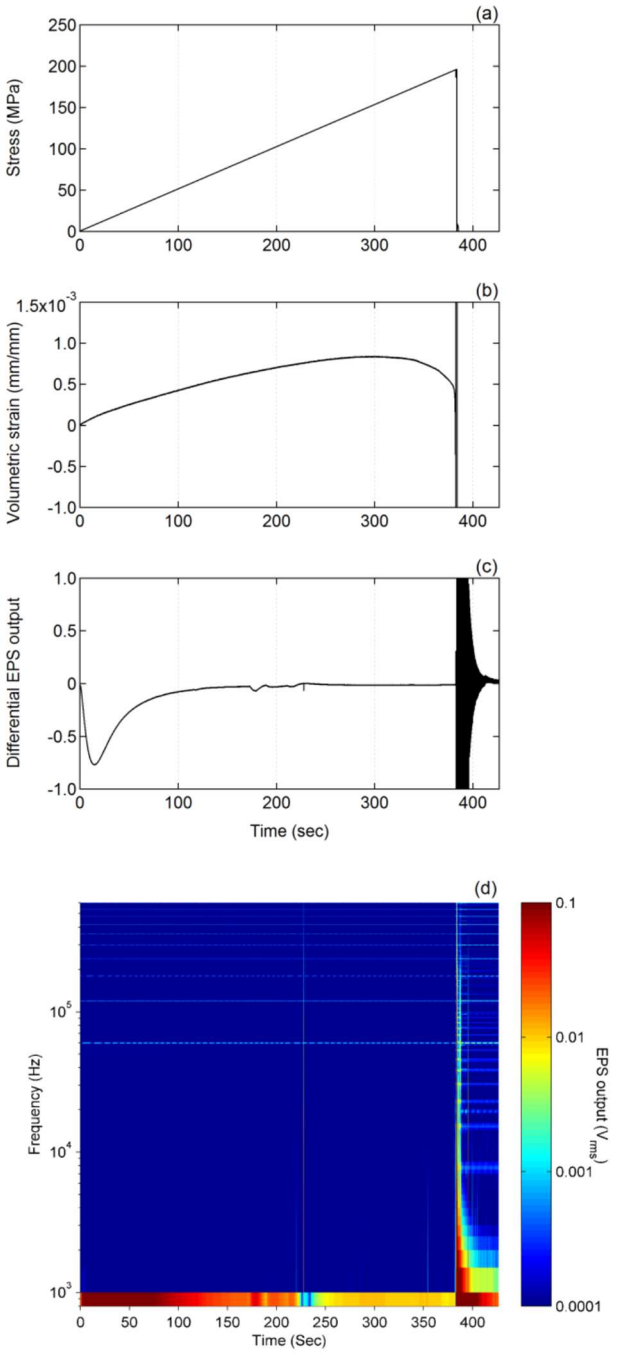

Figure 4-19 Loading data from a gabbro specimen, original source [19]. *(a) applied stress, (b) volumetric strain, (c) resulting differential PSV and (d) differential PSV spectral density.*

In contrast, the lithologies containing high amounts of quartz (sandstone-85 %, granite-35 % and quartzite-91 %) emitted PSV emissions at frequencies of at least 60 kHz and rock lithologies containing greater than 80 % quartz (sandstone and quartzite) emitted wideband PSV. The PSV emissions either increased in frequency and intensity or emitted multiple wide band transient signals prior to failure; this phenomenon could be a promising precursor signal for material failure. A good example of the precursory wideband PSV signals at the lead up to material failure is the sandstone experiment as shown in Figure 4-20.

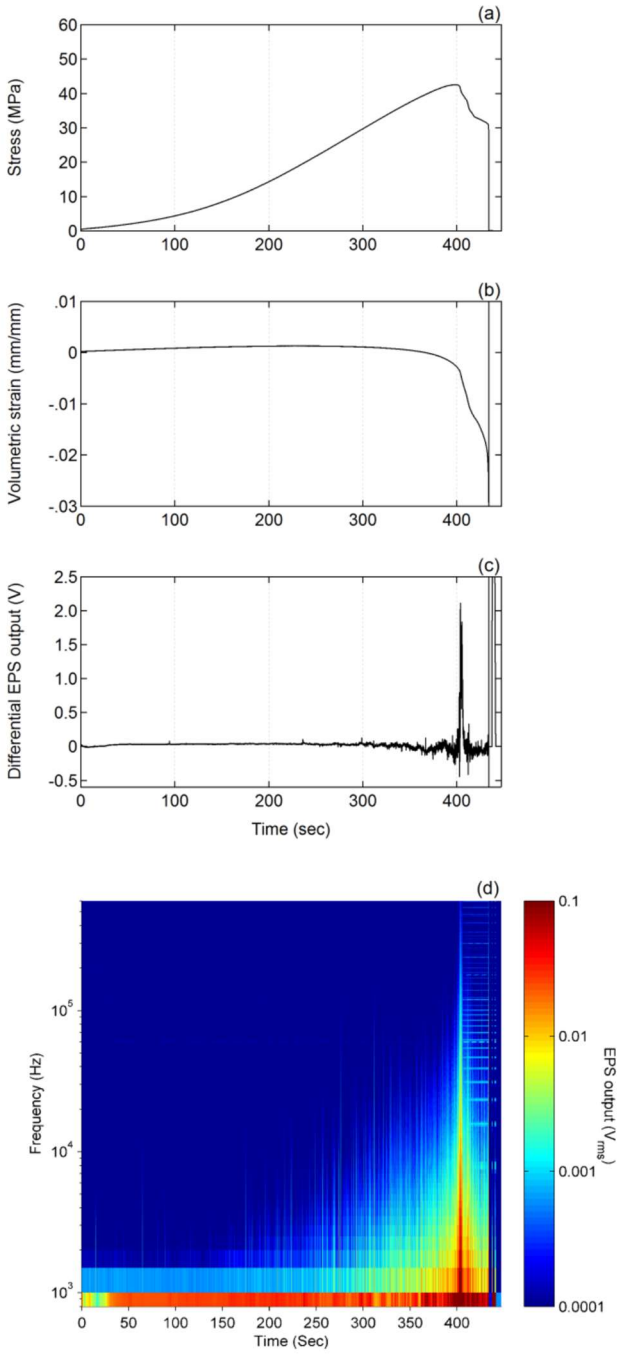

Figure 4-20 Loading data from a sandstone specimen, original source [19]. *(a) applied stress, (b) volumetric strain, (c) resulting differential PSV and (d) differential PSV spectral density.*

The loading of the aluminium control sample confirms that PSV emissions are a result of self-potential within the pressurised rocks and not a result of vibrations from the load frame itself or any other sources such as ambient electric fields.

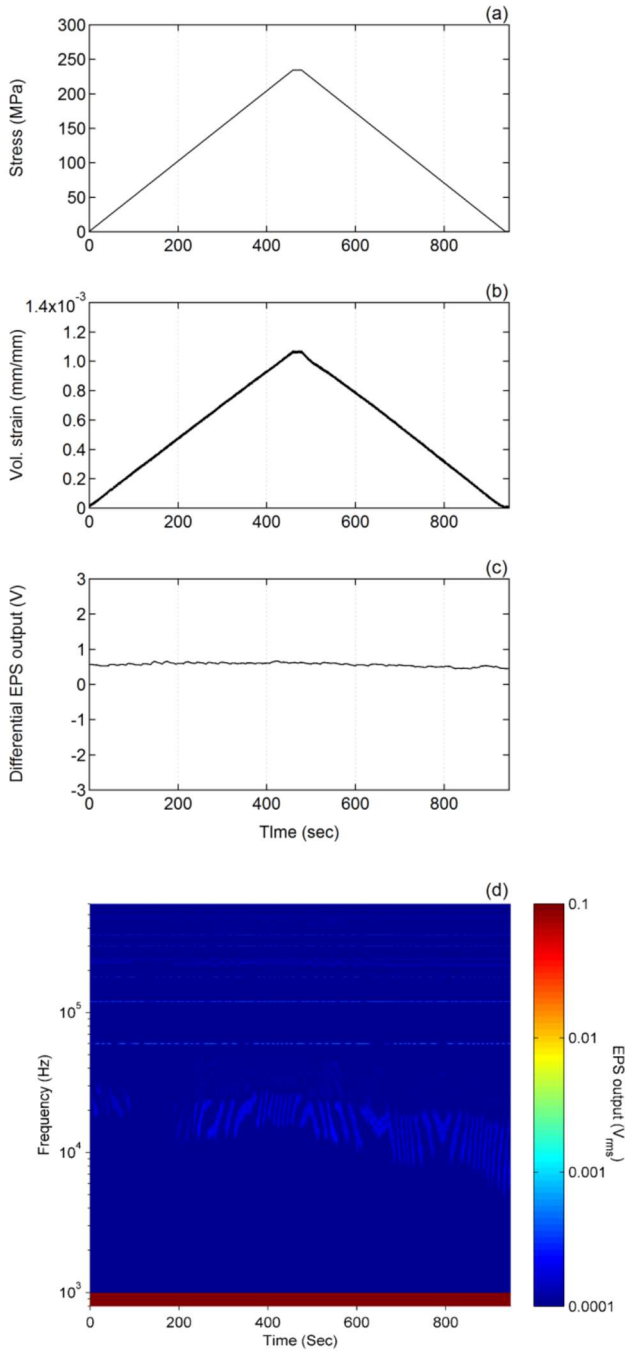

Figure 4-21 Loading data from an aluminium control specimen, original source [19]. *(a) applied stress, (b) volumetric strain, (c) resulting differential PSV and (d) differential PSV spectral density*

Figure 4-21 shows that there is very little PSV activity, in terms of amplitude and frequency in the voltage special density plot and also in the differential PSV time graph during the compression of the aluminium control sample.

4.5.4.1 Conclusions

The research conducted previously by Dr Aydin demonstrates the potential benefit of monitoring PSV using EPS technology for SHM, including:

- PSVs are emitted from various rock lithology in the range of millivolts; PSVs were detected in non-piezo and piezo rock lithologies and PSVs have a better single to noise ratio than the associated PSCs, observed in studies by others [19, 20] .
- The capacitively coupled EPS is a viable alternative to benchtop electrometers and is amenable for field use [19, 20].
- Aluminium control samples were used in both studies [19, 20] demonstrating PSV emitted from the rocks is a result of self-potential of the material and not an artefact resulting from the testing apparatus itself.
- The second study [19] looks at the basic characterisation of the PSV emissions in terms of amplitude and frequency, showing there may be different generation mechanisms involved between high and low quartz and precursory failure signals.
- By collaborating with BGS, an advanced experimental procedure was implemented for sourcing; preparing; characterising rock lithology and mineralogy; and testing rocks in accordance with ISRM standards [19]
- The second study [19] also shows that monitoring PSV using EPS technology does not require the experiment to be contained within a Faraday cage in order to shield from external noise sources thus demonstrating EPS-PSV field capabilities.

Although this research establishes the viability and fundamental measurement techniques for monitoring PSV using EPS technology, PVS's need to be further characterised and the EPS technology developed further in order to create a robust SHM tool:

- Characterising PSV with mechanical loading parameters, such as applied stress and strain and also investigating relationships with AE (cracking), using statistical methods, is necessary rather than performing simple visual observations.
- Investigating the lower frequency range < 1 kHz of PSV signals would be of interest as these were present in all rock samples [19], but attenuated in the measured voltage by the capacitively coupled electrode structure configuration. Therefore, a restively coupled EPS needs to be developed in order to monitor PSV frequencies as low as DC.
- Testing a wide range of rock lithology and manmade materials in different environmental conditions would help characterise PSVs. In addition, statistical relationships between PSV and AE or PSV and stress-strain may help determine generation mechanisms.

This thesis aims to advance the field of PSV-EPS research by addressing all of the aforementioned points with the aim of establishing a new tool for the SHM of geological and manmade structures.

4.6 Directly coupled smart EPS for PSV detection

This sensor is restively coupled and was developed to detect low frequency PSV signals, expected to be associated with applied stress. The results presented in chapter 9 of this thesis demonstrate the sensor is a robust method for measuring low frequency PSV signals. The sensor has a flexible electrode structure for bonding to curved or uneven material surfaces via a conductive epoxy medium; three gain settings; and precisely adjustable input impedance and DC offset. The Input impedance and DC offset adjustments are digitally controllable, by an EPS control interface via the sensors on-board micro USB port. The high input impedance sensor nodes on the PCB are also shielded from ambient electric fields.

Sensor package

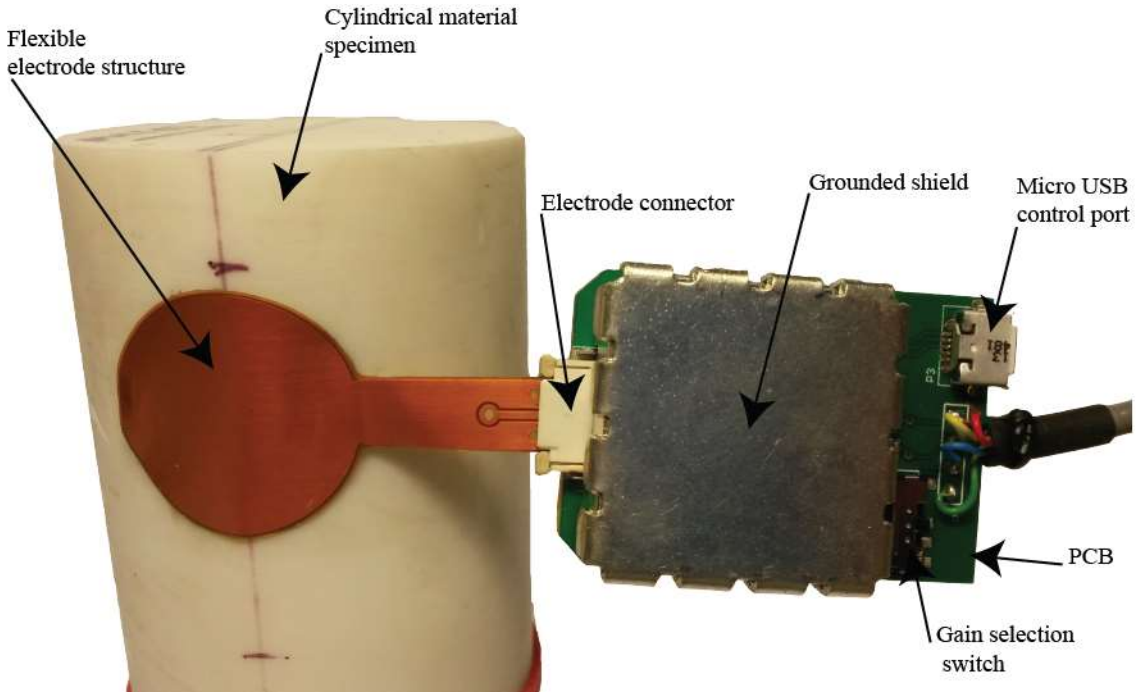

Figure 4-22 Photo of the directly coupled smart EPS attached to a cylindrical material specimen.

Specification

Dimensions	X – 30 mm Y - 50 mm Z – 20 mm
Input resistance	689 GΩ - 3.068 TΩ
Input capacitance	0.67 pF
Gain	x5, x10 and x20
Bandwidth	DC – 500 kHz
Noise (RTI)	31.68 nV√Hz at 1 kHz at 90 % bootstrap

Table 4-3 Summary of the directly coupled smart EPS specifications.

Noise characteristics

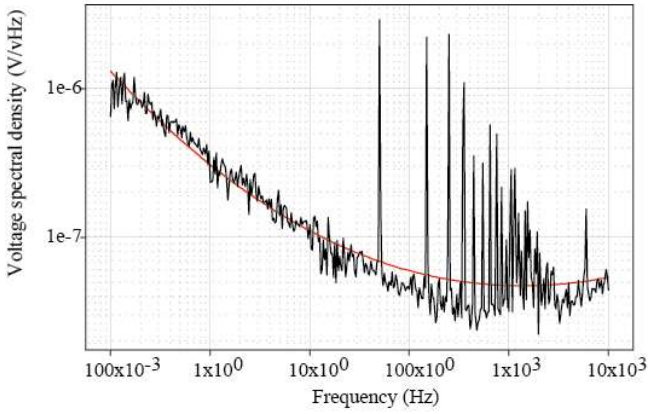

Figure 4-23 Directly coupled smart EPS voltage noise special density plot RTI of the sensor.

Initial prototypes of the sensor revealed that a very high input impedance was needed, in order to detect low frequency PSV signals. This phenomenon occurs because the sensor is restively coupled to insulating materials (i.e. rocks and concrete) and the material acts as coupling capacitor. Therefore, the first order HPF effect determines the lower cut of frequency of the EPS, as shown in Equation 4-8. A design goal of the sensor was to measure PSVs expected to be associated with static stress, thus the input impedance needed to be as high as possible, in order to detect pseudo DC PSV.

During the prototyping stage very large input resistors and also bootstrapping techniques were used to increase the input resistance of the sensor. This was effective at reducing the lower cut off frequency, however there were instability issues. The cause of insatiability was input resistor tolerance; initially standard 1 TΩ resistors were used with a tolerance of (±20 %), the higher resistors values (max = 1.2 TΩ) caused instability and the lower resistor values (min = 800 GΩ) worked effectively. To solve this problem specialised low tolerance (±5 %) 50 GΩ resistors were used, this allowed for consistent stable operation of sensors and allowed for batches of sensors to have similar input resistances.

The prototyping of the sensor also revealed the directly coupled EPS variant is much more sensitive to instability issues from over bootstrapping the sensor, in an attempt to increase input resistance. In addition, the ideal input resistance changes depending on the test material, because the insulting material being tested acts as the coupling capacitance to the sensor. Thus, a method for precisely adjusting the bootstrapping feedback and thus input resistance was developed using digital potentiometers, controlled by a EPS control interface. This method allowed the user to set the input impedance of the sensor to the maximum level before the threshold of instability. The input capacitance was optimised using neutralisation and guarding techniques, the maximum amount of neutralisation positive feedback was ~100 % before instability issues occurred; this fixed value of feedback was applied to the sensors.

An input impedance calibration procedure was developed to calculate the optimal bootstrap feedback percentage, needed for each material; a diagram of the calibration setup is shown in *Figure 4-24*. A copper stimulus electrode (25 mm x 25 mm) was bonded to one side of a cuboid material specimen and the EPS electrode (25 mm diameter) on the opposite face. This forms a parallel plate coupling capacitor, where the dielectric is the material to be tested e.g. marble or sandstone. The step response of the system (material specimen and EPS) is analysed using a script written in the MATLAB® numerical computing environment [108], executed on a computer (NI PXIe1071) [109]. A digital to analogue converter (DAC) and analogue to digital converter (ADC) module (NI PXI-6124) [110], provides the step input signal (0 V – 5 V) and records the step response of the system respectively. The MATLAB® [108] script running on the computer controls the bootstrap feedback percentage and in turn the input resistance of the sensor, via the EPS control interface. This enables the MATLAB® [108] script to find the fastest step response of the EPS at different bootstrap feedback percentages/input resistances. The MATLAB® [108] source code for the bootstrap calibration procedure is detailed in Appendix. B of this thesis.

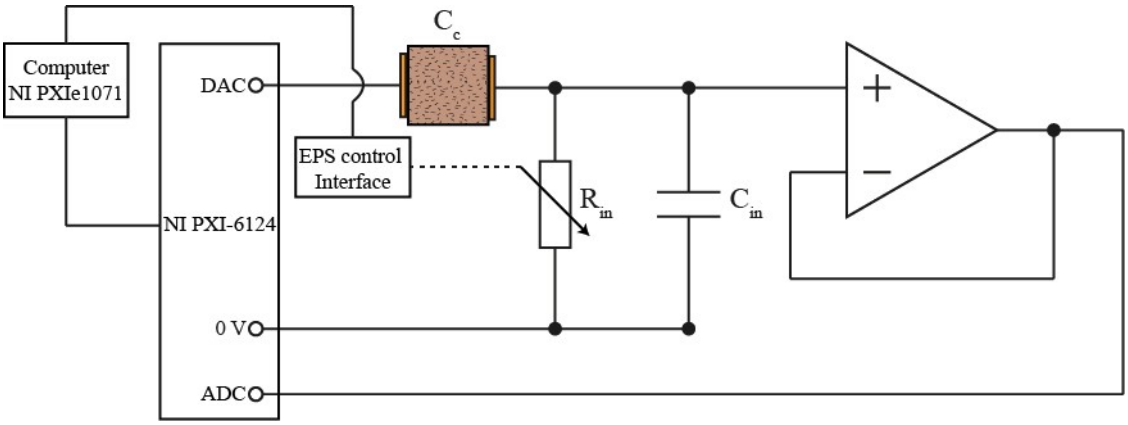

Figure 4-24 Input impedance calibration procedure setup. *The EPS control interface indirectly sets input resistance by altering the bootstrap feedback percentage and the computer monitors the step response of the system (EPS and input capacitance).*

The digital potentiometer controlling the bootstrap feedback percentage has 256 wiper positions, this enables the feedback percentage to be incremented in steps of 0.16 % from ~70 % to ~110 %. However, the sensors generally unstable when exceeding a bootstrap feedback percentage of ~95 %; Figure 4-25 shows the step response of the sensor from ~70 % bootstrap feedback to ~95 % bootstrap feedback and the corresponding minimum and maximum measured EPS input resistances.

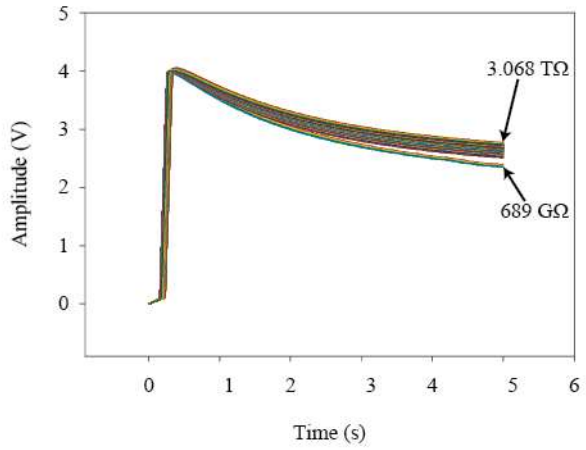

Figure 4-25 Step response of the directly coupled smart EPS and marble specimen.

The optimum bootstrap percentage calculated, is used as a ball park figure for material testing experiments. At the start of each experiment the EPS bootstrap feedback percentage is set to the calculated value, sometimes this causes instability issues. If instability occurs the bootstrap feedback must be reduced until stable operation occurs, then the bootstrap feedback must be increased in small increments using the EPS control interface, to achieve the highest possible input resistance before instability. This process may have to be repeated multiple times until the bootstrap feedback percentage is optimised.

4.6.1 Schematic circuit design

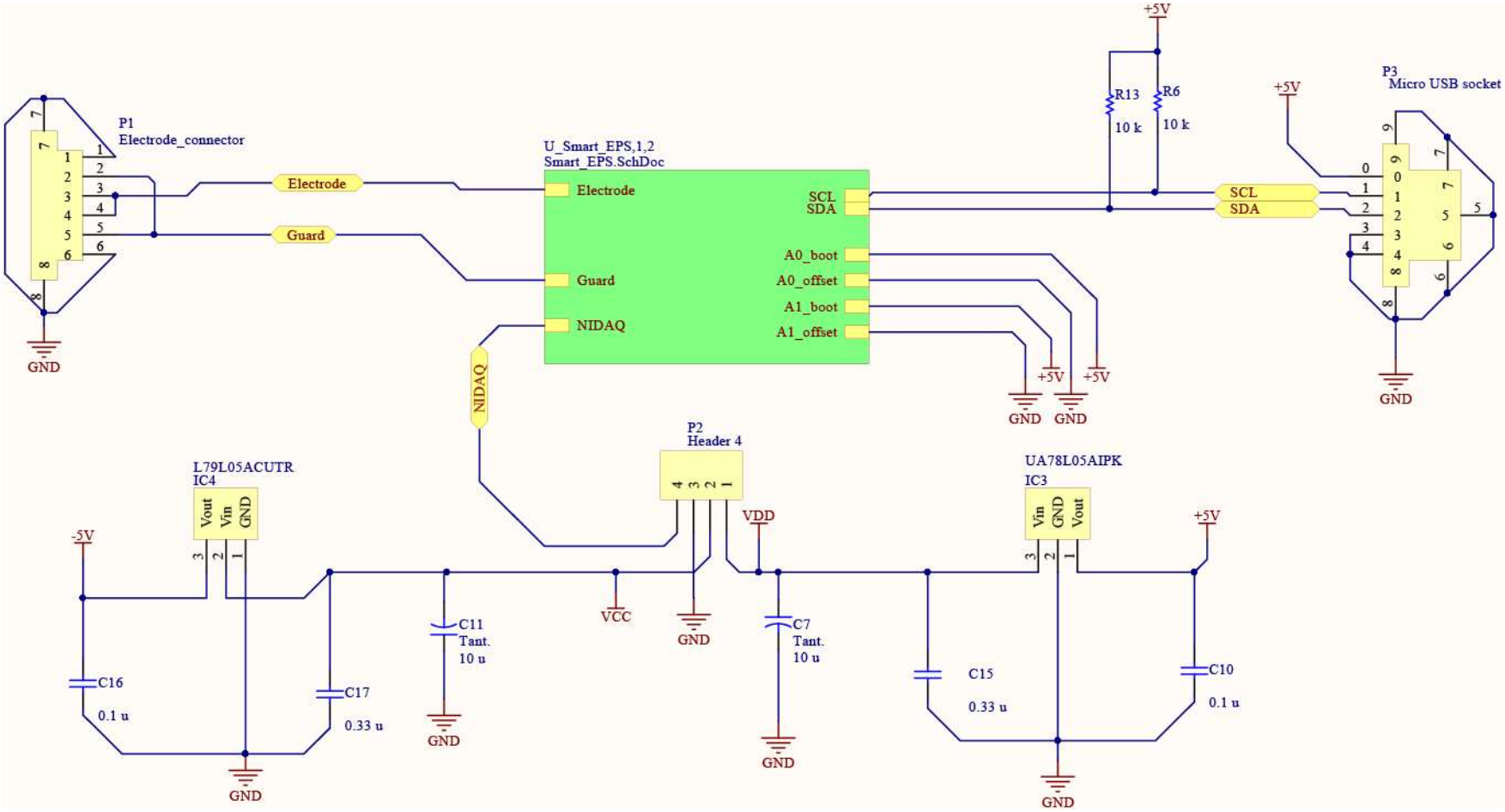

Figure 4-26 Directly coupled smart EPS circuit schematic sheet 1 of 2.

The green box in the schematic sheet 1 as shown in Figure 4-26 represents the circuitry contained in sheet 2 as shown in Figure 4-27; circuit elements are connected between the two sheets via the yellow ports.

Sheet 1 shows the input and output connections to the sensor. The input to the sensor and guard are routed through the electrode connector (P1), where a flexible guarded electrode structure can be connected. The output of the sensor is routed through header 4 (P2), where the DIN sensor cable is attached and signal routed to an ADC.

The A0_boot and A1_boot connection ports are for addressing the digital potentiometer (IC2), that controllers the bootstrap feedback. The A0_offset and A1_offset connection ports, are for setting the address of the digital potentiometer responsible for controlling the DC offset of the device. Both digital potentiometers are connected to the same I^2C data bus that controls the wiper positions, thus a unique address for each potentiometer is needed to control each one separately. I^2C is a serial computer bus typically used to connecting peripherals (e.g. digital potentiometers|) to a micro controller or microprocessor [99]. The I^2C bus (SLA and SDA) is routed to an on board micro USB socket (P3), where it can be connected via a standard micro USB cable to the EPS control interface; pull up resistors (R6 and R13) were used on the bus accordance with the serial protocol.

Power is supplied to the sensor via header 4 (P2), where pin 1 = 7.5 V (VDD), pin 2 = -7.5 V (VCC) and pin 3 is connected to ground; two tantalum capacitors (C7 and C11) were used to decouple the sensor from the power supply. Two voltage regulators UA78L05AIPK (IC3) [111] and L79L05ACUTR (IC4) [112], were used to regulate the supply voltages down to 5 V and -5 V respectively. Each voltage regulator has decoupling capacitors at its input (C15 and C17) and output (C10 and C16) as recommended by the manufactures data sheets for noise reduction. The 5 V and -5 V outputs are used to power the two digital potentiometers.

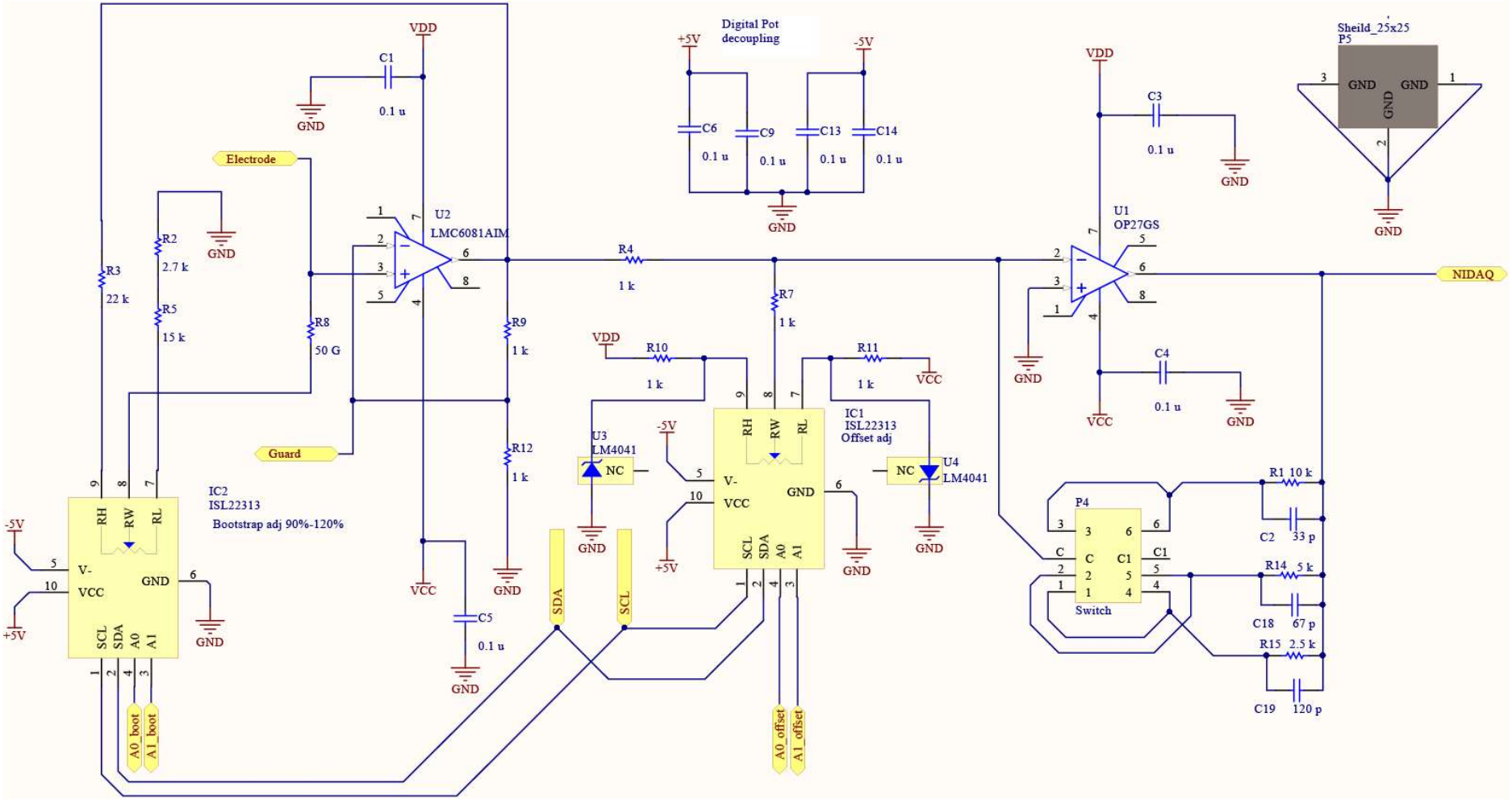

Figure 4-27 Directly coupled smart EPS circuit schematic sheet 2 of 2.

This sensor has two amplification stages, as shown in Figure 4-27. The first amplification stage uses a LMC6081 opamp [103], as with the capacitively coupled EPS in a non-inverting configuration [99]. The gain (x2) is set by resistors R_9 and R_{12}, in accordance with Equation 4-15.

$$AV = \frac{R_9}{R_{12}} + 1 = \frac{1\ k\Omega}{1\ k\Omega} + 1 = \ 2$$

Equation 4-14 Non-inverting opamp gain equation: *AV = voltage gain.*

The second amplification stage uses an OP27GS opamp [113], this opamp was chosen for its low noise characteristics and high speed capabilities (2.8 V/μs slew rate, 8 MHz gain bandwidth). The opamp is in a inverting configuration [99], where the signal gain can be set using a three position switch. Three gain settings are available and set by resistors R_4 and R_1 to give x10 gain; R_4 and R_{14} to give x5 gain; or R_4 and R_{15} to give x2.5 gain, depending of the switch position. The inverting opamp gain is expressed in Equation 4-15.

$$AV = \frac{R_4}{R_{feedback}}$$

Equation 4-15 Inverting opamp gain equation: *AV = voltage gain and $R_{feeback}$ = R1, R14 or R15 (depending on the switch position).*

The feedback capacitors (C_2, $C1_8$ and C_{19}) in parallel with each of the feedback resistors, turns the non-inverting amplifier into an active low pass filter [99], where the filter cut off frequency (f_c) is defined by the following first order filter Equation 4-16. The cut-off frequency was chosen so the sensor is not only capable of measuring pseudo DC signals, expected to be associated with applied stress, but also higher frequency PSV signals up to ~500 kHz expected to correlate with cracking events.

$$f_c = \frac{1}{2\pi R_{feedback} C_{feedback}}$$

Equation 4-16 first order active low pass filter cut off frequency equation: *F_c = LPF cut off frequency, $R_{feeback}$ = R1, R14 or R15 and $C_{feeback}$ = C_2, C_{18} or C_{19} (depending on the switch position).*

As mentioned previously the bootstrap feedback is controlled by the digital potentiometer (IC2), the component (ISL22313) [114] was chosen because of the high wiper position resolution, low noise characteristic and easily implemented I^2C serial control interface. The potentiometer has a resistance of 10 kΩ from pins RH to RL and the wiper position RW, can be set in 256 equal increments between RH and RL. The resistors R_2, R_3 and R_5 and the potentiometer form a voltage divider, limiting the adjustable range of the bootstrap positive feedback, from ~70 % to ~110 %. The voltage divider equation representing the limits of the bootstrap feedback, is show in Equation 4-17 and Equation 4-17.

$$\text{Bootstrap}_{\max} = 200\ \% \times \frac{R_2 + R_5 + 10\ \text{k}\Omega}{R_2 + R_5 + R_3 + 10\ \text{k}\Omega} = 200\ \% \times \frac{2.7\ \text{K}\Omega + 15\ \text{K}\Omega + 10\ \text{k}\Omega}{2.7\ \text{K}\Omega + 15\ \text{K}\Omega + 22\ \text{K}\Omega + 10\ \text{k}\Omega} = 111.47\ \%$$

Equation 4-17 Maximum bootstrap feedback percentage.

$$\text{Bootstrap}_{\text{min}} = 200\ \% \times \frac{R_2+R_5}{R_2+R_5+R_3+1\ \ \text{k}\Omega} = 200\ \% \times \frac{2.7\ \text{k}\Omega+1\ \ \text{k}\Omega}{2.7\ \text{k}\Omega+15\ \text{k}\Omega+22\ \text{k}\Omega+10\ \text{k}\Omega} = 71.23\ \%$$

Equation 4-18 Minimum bootstrap feedback percentage.

Because the opamp (U2) has a gain of x2 the voltage divider calculations for the bootstrap neutralisation feedback must take this into account. Resistors R_9 and R_{12} form a voltage divider providing a fixed neutralisation feedback of 100 % into the guard path, as described by Equation 4-19.

$$\text{Neutralisation} = 200\ \% \times \frac{R_9}{R_9 + R_{12}} = 200\ \% \times \frac{1}{2} = 100\ \%$$

Equation 4-19 Fixed Neutralisation feedback percentage.

Due to the nature of directly coupled EPS measurement, there can be DC offsets at the start of each material testing experiment; due to the material specimen holding charge as a result of residual stress in the material or EPS bias current loading errors. These offsets can be compensated for at the beginning of each experiment, so the full voltage range of the second amplification stage can be utilised. As mentioned previously the DC offset is controlled by a digital potentiometer (IC1), voltage references of 1.2 V and -1.2 V are connected to the RH and RL pins respectively and a voltage divider is formed, where the output is set by the wiper position. A central wiper position injects no DC offset into the input of the second amplification stage and a wiper position at either end injects a DC offset of 1.2 V or -1.2V respectively. A precision shunt voltage reference (LM4041) [115] was chosen because of its low noise characteristics, low output voltage tolerance (± 0.1 %) and compact size. Resistors R_{11} and R_{10} were chosen to provide the required operating current I_Q, ranging from 60 uA to 12 mA needed for the device to operate as shunt regulator.

$$I_Q = \frac{7.5\ V}{1\ K\Omega} = 7.5\ mA$$

Equation 4-20 Shunt regulator operating current: *I_Q = operating current.*

The DC offset is amplified by the same ratio as the signal, as the gain is determined by resistor R_7 and whichever feedback resistor (R_1, R_{14} or R_{15}) is selected by the switch (P4).

Although the sensor uses the same front end, (LMC6081 opamp and 50 GΩ input resistance) the noise floor of the sensor (31.68 nV√Hz at 1 kHz) is higher than the capacitively coupled EPS (22 nV√Hz at 1 kHz). This is because the bootstrapping and neutralisation positive feedback add noise to the circuit. The noise was measured with 90 % bootstrap feedback and with the fixed 100 % neutralisation feedback in operation, as these values were expected to be used during material testing experiments.

Integrated circuits (ICs) were decoupled from the power supply, decoupling capacitors C_1 and C_5 were used for the first stage opamp (U2) and capacitors C_3 and C_4 for the second stage opamp (U1). The two digital potentiometers (IC1 and IC2) were decoupled from the voltage regulated power supplies, each having decoupling capacitors (C_{13} or C_{14}) and (C_6 or C_9) on their -5 V and 5 V supplies respectively.

A PCB mountable shield (P5) is connected to ground to protect the circuit against ambient electric fields.

4.6.2 Printed circuit board (PCB) layout

The PCB was designed to be as compact as possible, this was achieved my choosing compact SMD component packages and routing tracks in an efficient manner. The top and bottom layers of the PCB design are shown in Figure 4-28.

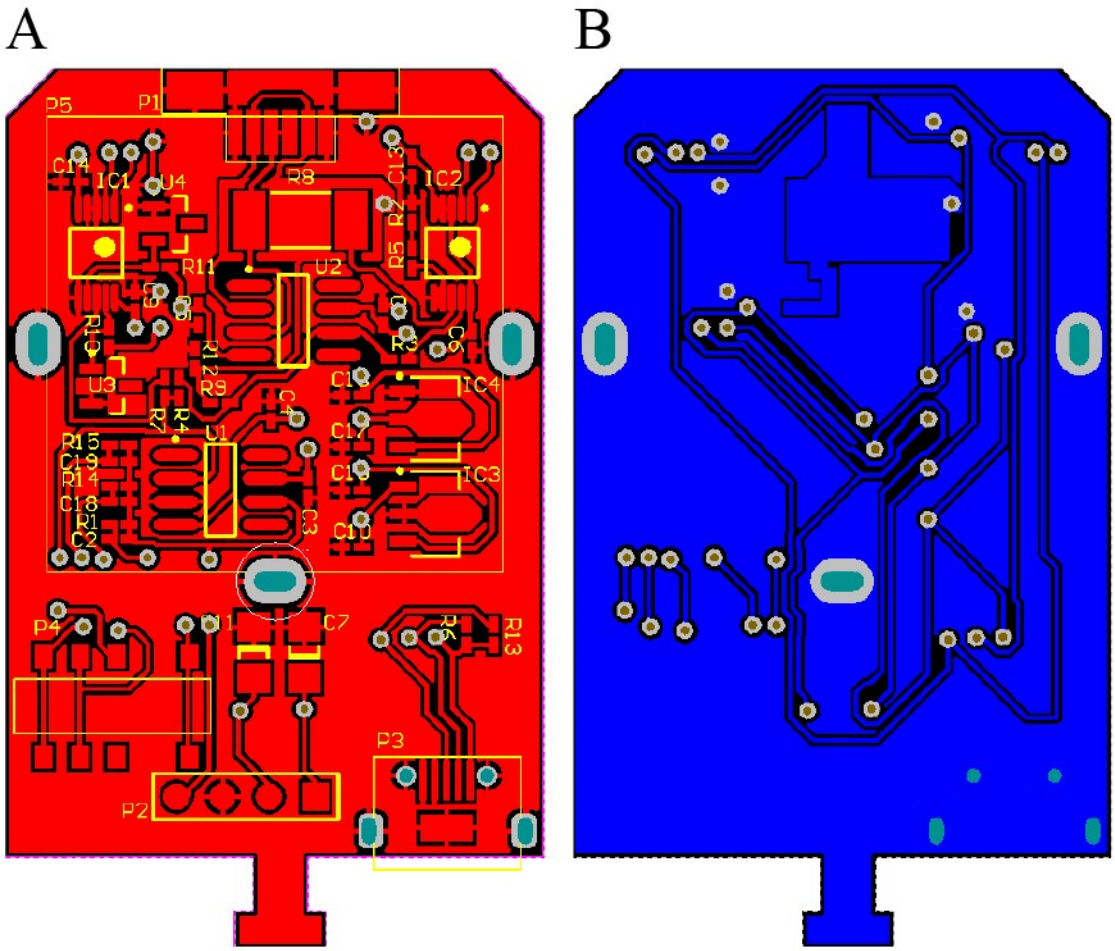

Figure 4-28 Directly coupled smart EPS PCB layout. *A) Top layer and B) bottom layer. The red area represents the top copper, blue area represents the bottom copper, grey areas are via connections joining the top and bottom copper, green areas represent holes in the PCB and the yellow markings represent the silk screen. Dimensions: 30 mm x 50 mm.*

Power connections (5 V, -5 V, 7.5 V and -7.5 V) and the digital potentiometer's I^2C data bus, were routed on the bottom layer of the board and all of the analogue signal paths were routed on the top layer of the board. This measure was implemented to reduce interference from power supply noise and digital signal noise from the sensitive nodes of the EPS.

Decoupling capacitors were placed as close as possible to their associated ICs, as recommended in their data sheets, to decouple the devices from the power supply and shunt noise through the capacitors. At the bottom of the PCB there is a tab where the sensors IO cable is tied to, as a form of strain relief for the solder pads on header (P2).

Both the top and bottom layers of the PCB have a ground plane, this act as a form of shielding. In addition, a 25 mm x 25 mm PCB mountable shield (P5) is connected to the ground plane of the PCB. All of the sensitive nodes of the EPS, are contained within the shield to protect the sensor from ambient electric fields. The digital potentiometer's micro USB connector, associated I^2C bus and pull up resistors; power supply decoupling capacitors C_7 and C_{11}; gain selection switch; and IO connections, are located outside of the shield for ease of access or because shielding is unnecessary for these circuit nodes.

A guard is placed around the input path, from the non-inverting input of the front end opamp (U2), to the electrode connector (P1); the guard also surrounds the input resistor R_8 on the top layer of the board. On the bottom layer of the PCB the guard is placed under the input resistor, non-inverting opamp (U2) pin and input path from the pin to the electrode connector. This layout ensures the guarding and neutralisation feedback is effective at reducing the input capacitance of the sensor and cancelling out the input leakage current and stray capacitances.

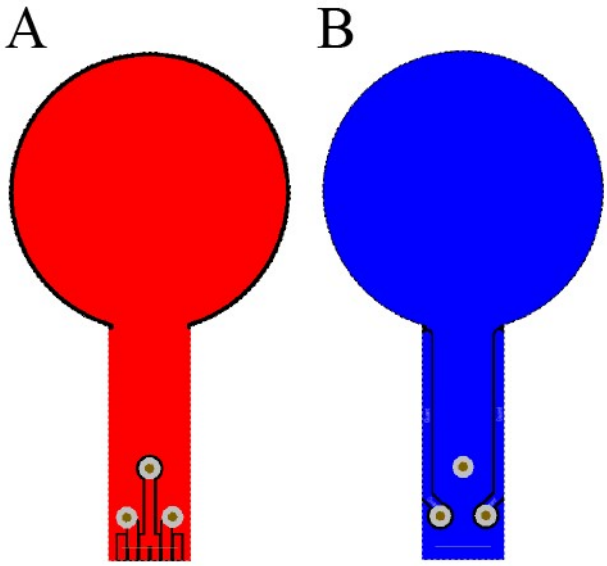

Figure 4-29 Directly coupled smart EPS flexible electrode structure PCB layout. *A) Top layer and B) bottom layer. The red area represents the top copper, blue area represents the bottom copper and the grey areas are via connections joining the top and bottom copper. Dimensions: 25 mm x 45 mm.*

The PCB layout of the flexible electrode structure is shown in Figure 4-29. The bottom layer has an electrode plane over the surface, and on the tab leading up to the round electrode sensing area, a guard is placed on either side. The top layer has a guard plane over the surface and over connection pads to be inserted into the electrode connector on the EPS. The guard plane does not reach the edges of the round electrode sensing area, so as to avoid shorting issues when testing wet materials.

The rendered view of the sensor PCB and flexible electrode structure, is shown in Figure 4-30. On the top side of both PCBs the solder mask covers the entire board, apart from the pads in which components are soldered and the electrode connector pads on the flexible electrode structure. This ensures the electrode guard and sensor circuit elements do not get accidently shorted to neighbouring objects. The

silkscreen layer displays the component identifiers and component outlines, making soldering components to the board easier and more efficient.

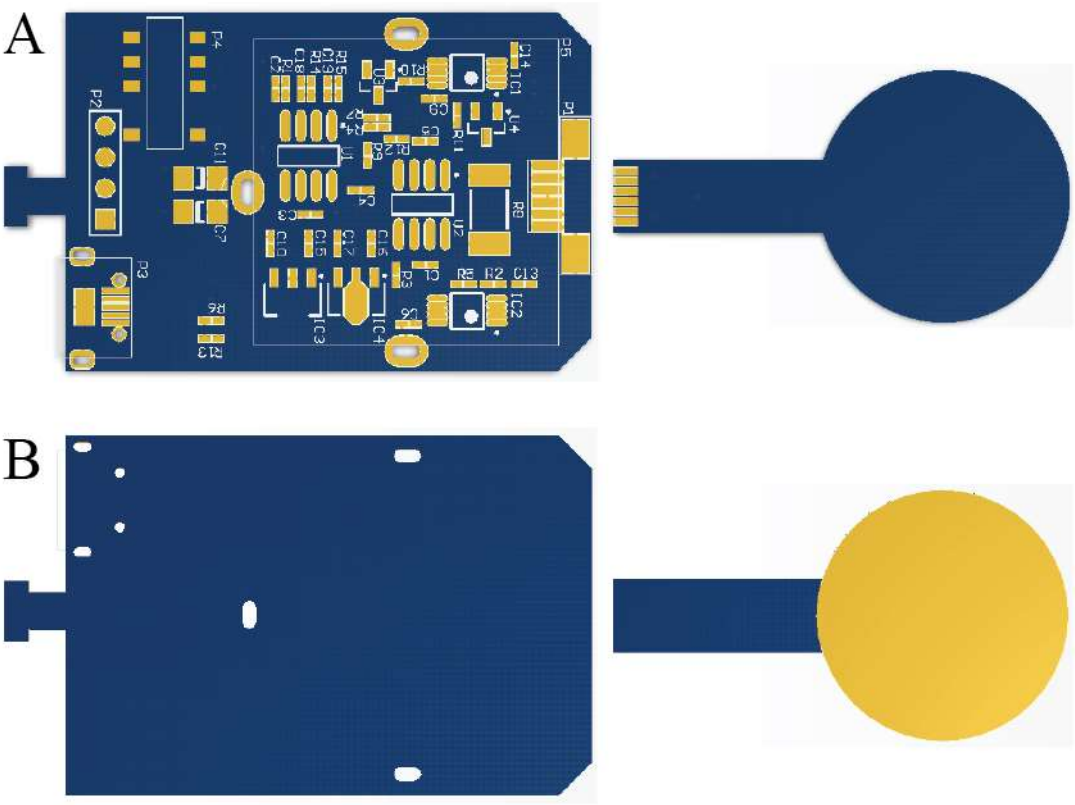

Figure 4-30 Directly coupled smart EPS PCB layout rendered view. *A) top layer sensor and electrode structure and B) bottom layer sensor and electrode structure. The blue area represents the solder mask, white annotations are the silkscreen and yellow areas are exposed component pads and electrode sensing area. EPS PCB dimensions: 30 mm x 50 mm and electrode PCB dimensions: 25 mm x 45 mm.*

The solder mask entirely covers the bottom side of the sensor PCB, including via connections and component through hole connections, thus all components are soldered on the top side. This ensures circuit elements of the sensor, do not accidentally get shorted to the rock surface during testing. The flexible electrode structure PCB has a solder mask over the tab leading up the round electrode sensing area, to project the guard tracks from being accidently shorted to the rock surface.

The PCBs were designed using Altium Designer software [116], this software package is ideal for designing multilayer PCBs from circuit schematic diagrams. This software package was chosen because it has enhanced error checking tools and multiple schematic sheet options, which is ideal for the more complex design of the directly coupled smart EPS. Once the PCB design was finalised, the designed was exported to a Gerber format (.gbr), which is an industry standard format used to describe PCB images in software.

4.6.3 PCB Fabrication

The sensor board Gerber files were sent to a PCB manufacture (PCB Train [117]); ten high quality sensor PCBs were fabricated. The boards are double sided, plated through hole PCBs with a 1.6 mm

FR4 laminate substrate, 1-ounce copper, Au/Ni finish with green solder resist on both sides and white silk green legends. The Au/Ni finish was chosen to protect the exposed component pads from corrosion and thus galvanic current generation, that could occur during device operation from water and natural salts in the test materials.

The components were soldered onto the PCBs using the in house equipment at the STRC, as described previously 4.5.3. The SMDs were placed in their associated positions on top of solder paste, then a reflow oven was used to melt the paste, thus soldering the SMDs in place. Manual hand soldering of the non SMDs, such as the grounded shield and DIN cable was necessary.

The flexible electrode fabrication was outsourced to another PCB manufacture called PW circuits [118]; 50 high quality flexible electrodes were fabricated. The flexible electrodes are double sided; plated through hole PCBs; have a flexible polyimide substrate; have top and bottom copper conductive layers; and have a flexible polyimide solder resist on both sides. In addition, a stiffener was bonded onto the opposite side of the electrode connector pads, this allows the flexible electrode to be inserted into the sensor electrode connector without buckling.

4.6.4 EPS control interface

The user can choose to adjust the EPS bootstrap feedback, DC offset or enter the bootstrap calibration mode using the graphic use interface (GUI) of the EPS control interface. Options are displayed on a 2x16 digit liquid crystal display (LCD) and options can be selected using the push buttons on the controller as shown in Figure 4-31.

The EPS control interface is a standard Arduino Uno microcontroller development board [119], with an LCD shield [120] attached to it. In addition, a simple PCB shield was fabricated for the EPS control interface; this shield connects the sensor to the EPS control interface via USB connection. The shield has a single USB socket and is used to connect the EPS serial bus connection (SCL and SDA) to the Arduino Uno's serial port on pin 0 and pin 1. The EPS control interface is also powered by the EPS it is controlling as the 5 V and GND connections are shared through the USB connection. The Arduino

[119] firmware for the EPS control interface can be found in Appendix. A of this thesis.

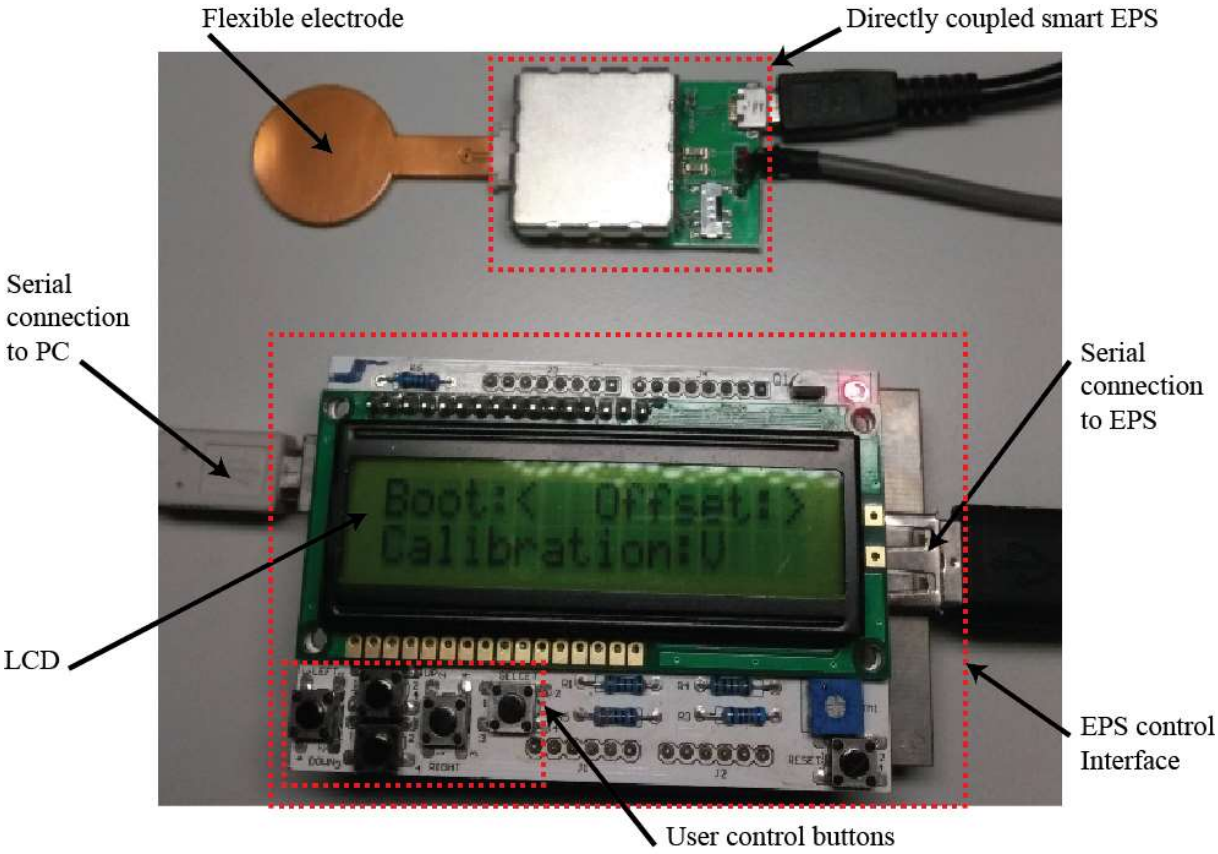

Figure 4-31 Photo of the EPS control interface.

4.7 Signal processing and data analysis

The digital signal processing data analysis was carried out on the University of Sussex high performance cluster computer (HPC), using the MATLAB® numerical computing environment [108]. The HPC is an extremely powerful computing system, comprised of multiple processors linked together to form a single system for heavy computational research, allowing for computing precision beyond the capabilities of a personal desktop computer. This was necessary because of the large quantities of PSV data collected from the capacitively coupled EPS experiments. The directly coupled experiments PSV data was sampled at a much lower rate of 500 Hz, thus a standard desktop computer was used for data processing.

Firstly, the time-based PSV data from the experiments was digitally notch filtered at frequency of 50 Hz to attenuate any ambient electric field effects.

For each experiment, there was a relatively large spike in the PSV amplitude at the instance of applying load to the specimen, caused by EPS movement from the closing of gaps between the material specimen, acoustic platens, PCB insulting platens, and load frame. The spike in amplitude was removed and replaced with null values, as the spike is an artefact resulting from movement. The axial strain and stress values were shifted so the initial values were zero; zeroing at the beginning of experiments is common practice for use with strain gauges.

4.7.1 Capacitively coupled EPS experiments

In order to investigate correlations and relationships between all three data types (PSV, AE and loading data), they were all converted to a uniformly sampled time based format; binning windows of 0.25 s were chosen. The raw loading data (axial strain, and stress) is sampled at uniform intervals of strain or force depending on the load frame control method; the resulting binned data is formed from the average value of axial strain or stress for each 0.25 s interval. The raw AE data is time based event data and thus is not uniformly sampled; the binned data is formed from the average event amplitude for each 0.25 s interval. The binned total number of AE events, is calculated from the raw AE data at the instance of each 0.25 s interval. Because the raw PSV data was already uniformly sampled in time, the binned data was formed by simply averaging in 0.25 s intervals.

PSV event data was calculated from the binned data, because of computational hardware limitations. When attempting to process the raw data sampled at 1.5 MSs^{-1}, even using the HPC the processing time per experiment was ~12 to ~36 hours depending on experiment length, which was not a practical approach. Processing the PSV events using the binned data however, takes a matter of seconds due to the huge difference in data size from (~5 GB ~75 GB) to (~22 kB ~186 KB). The AE events were computed by the PCI-2 hardware and AEwin software [121] in real time, from data sampled at 5 MSs^{-1}. The number of events is thus perceived to be much lower for the PSV compared to AE, this is a computational artefact, because PSV events were defined after binning the data. However, the event rate, i.e. the slope of the cumulative number of events, plotted in chapters 6, 7 and 8 remains accurate.

The PSV event calculation procedure is shown in Appendix. C. Firstly, the binned PSV data (shown in part A) is high pass filtered in order to extract the transient spikes in PSV, that are expected to correlate with the spike like AE events, as shown in the part B of the figure. Then the `peakfinder` MATLAB® function [122] was used to find peaks in the data; this function is designed to quickly find local minima or maxima in data sets, using the alternating nature of derivatives. The `peakfinder` function along with a user defined threshold, is able to correctly identify major peaks in in noisy data. Any local maxima greater than 2 % of the amplitude of surrounding data was classed as a PSV event, as shown in part B of the figure. The PSV event timings were then used to create a vector of cumulative number of events, that can be directly compared to the binned AE cumulative number of events, as shown in part C of the figure.

The MATLAB® [108] script for the PSV event detection is contained within the Appendix. C of this thesis.

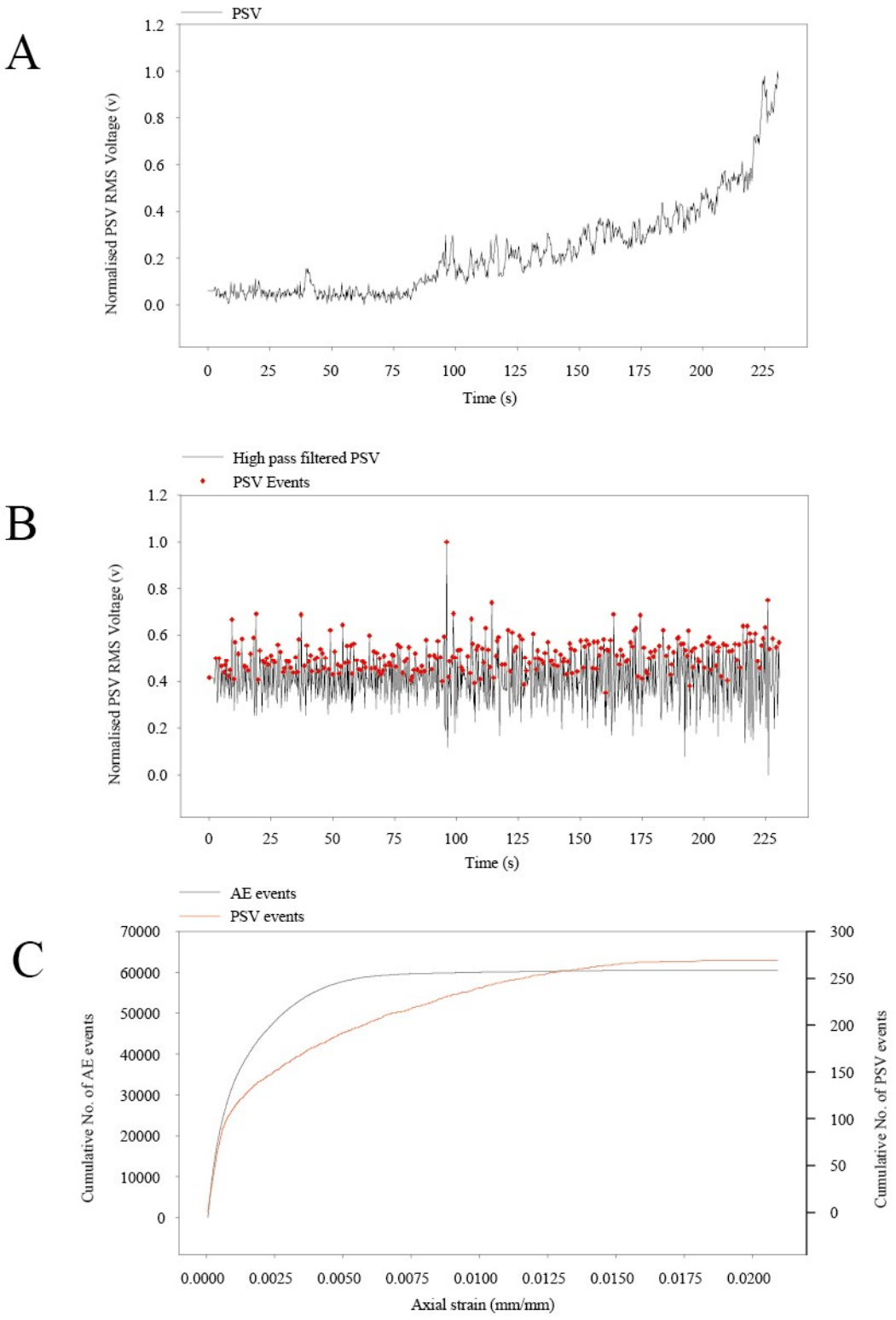

Figure 4-32 PSV event detection. *A) the PSV events are calculated from the binned PSV data; B) the PSV data is high pass filtered to extract transient spikes in PSV associated with AE events, then PSV events are defined as local maxima at least 2 % larger than surrounding data; C) The cumulative number of PSV events are calculated from PSV event timings.*

A future commercialised system for SHM would require the development of a "real time" PSV event detection method, to remove redundant data and enable long-term monitoring of structures, without using excessive amounts of hard drive space. This system would most likely be a field programmable

gate array (FPGA) based technology, as current AE event detection systems [48] utilise FPGAs for digitally controllable filtering and event detection of piezo transducer signals acquired at 5 MSs^{-1}. This system would not need to average out PSV events as with the current PSV event detection method by binning data in 0.25 s time windows. Instead, each PSV event would be individually accounted for, thus allowing for more accurate detection of cracking events in the PSV signals.

4.7.2 Directly coupled smart EPS experiment

The experiments utilized the step like stress (SLS) loading profiles to investigate relationships between applied stress and PSV. Data points were chosen in the PSV at the end of each stress step (where dv/dt → 0) along with corresponding values of applied stress for linear regression analysis. This process did not require the conversion of loading data, to a time-based format as the applied stress was constant for each loading step.

4.7.3 PSV spectrograms

For the capacitively coupled EPS experiments it was useful to study the PSV time-frequency-magnitude spectrograms. There appears to be three main features in the spectrograms, including transient electric potential signals (TEPS), persistent electric potential signals (PEPS) and high frequency noise.

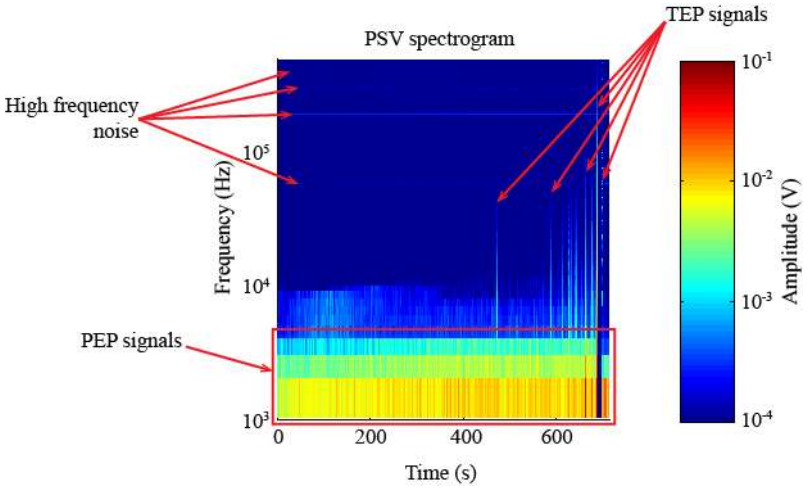

Figure 4-33 PSV spectrogram features. *The persistent electric potential (PEP) signals, some of the transient electric potential (TEP) signals and the high frequency noise bands are highlighted in red in the spectrogram.*

TEPS are defined as a short burst in PSV amplitude and frequency, this feature can be observed in the spectrogram as thin vertical lines with a higher magnitude colour than surrounding data. PEPS are defined as a persistent, low and relatively wide frequency band of PSV actively at a higher magnitude level than the background noise. PEPS are shown in the spectrogram as a horizontal band of a higher magnitude colour compared to the lower magnitude background noise, shown in blue. In some spectrogram there are narrow horizontal bands of relatively high magnitude and frequency PSV actively. The narrow almost constant frequencies of these signals fit the profile of noise generated by surrounding electrical equipment and are not expected to originate from the material specimen.

4.8 Future directions

4.8.1 The design of a directly coupled wideband EPS

An EPS design that could monitor high frequency PSVs associated with cracking like the capacitively coupled EPS as well as low frequency PSV associated with applied stress like the directly coupled smart EPS, would be beneficial to the SHM community. A commercialised EPS modality such as this, would be a more cost effective, advanced and non-invasive alternative to using piezo transducers and in-situ stress monitoring techniques. There is no existing sensor technology that can detect these two physical quantities currently.

Thankfully, the design of such an EPS would not be such a tall order, as the existing directly coupled EPS's frequency response can be easily modified. If the capacitor values for C_2, C_{18} and C_{19} were changed to standard capacitor values of 12 pF, 22 pF and 47 pF respectively the upper frequency response would be close to the capacitively coupled EPS's; in accordance with Equation 4-16 . This new modified sensor would have a frequency response ranging from DC to 1.3 MHz and would therefore be capable of detecting high frequency PSV associated with cracking events and low frequency PSV associated with applied stress.

4.8.2 Monitoring PSV over larger real world structures

The experiments presented in this thesis involve monitoring PSV in relatively small cylindrical test specimens (100 mm – 137 mm in length and ~50 mm diameter). For real world SHM applications the rock or concrete mass will be significantly larger. However, monitoring PSV's on this scale does not require any major changes to the EPS design, as the gain and input impedance are already adjustable to suit different SHM applications.

As discussed in the previous section, directly coupled wideband EPS could be used to monitor PSV's associated with AE and applied stress simultaneously. The EPS electrodes could be bonded onto the structure for long term monitoring using a conductive epoxy medium in the same manner as the test specimens discussed in this thesis, thus ensuring good resistive contact and a DC response from the sensors. However, for larger structures such as concrete beams in buildings or rock faces in mines, one would not simply be able to use a single differential pair of EPS at opposite sides of the structure, as with the test specimens. Instead, an array of EPS would have to be used to monitor AE events and the stress field over a structure to acquire an accurate representation of the structural health.

There are several unknowns about the application of EPS arrays for SHM. For instance, PSV passing through a resistive material (i.e. rocks and concrete) will experience voltage drop over distance, thus the EPS array must be dense enough (possibly in 3-dimentions i.e. embedded EPS may be required) to detect PSV from the source. Data processing techniques would have to be developed for calculating the location of PSV events related to cracking similarly to existing AE location techniques, as well as methods for calculating the stress field over structures. Finally, we know from existing SHM research

that the frequency response function (FRF) of structures commonly use to locate and detect damage, can be more greatly affected by environmental changes such as temperature and humidity than damage itself. Therefore, existing statistical tests for evaluating uncertainty in the FRF would have to adapted for the novel EPS technology. These unknowns could all be evaluated during future EPS-PSV research.

5 MATERIALS AND METHODS

The aim of this chapter is to provide an overview of the material properties and preparation of materials for uniaxial testing experiments (section 5.1), presented in chapters 6, 7, 8 and 9. The preceding sections describe methods of coupling the electric potential sensors (EPSs) to material specimens (section 5.2); material testing equipment details (section 5.3); uniaxial loading profiles applied during material testing experiments (section 5.4); and a definition of the stages of loading for brittle materials (section 5.5). In addition, information about sensor data acquisition (section 5.6), statistical methods (section 5.7) and control testing (section 5.8) are discussed.

5.1 Material properties and preparation

5.1.1 Material preparation

All rock lithologies and concrete specimens were sourced and prepared by the British Geological Survey (BGS). Cylindrical specimens, 100 mm – 137 mm in length and ~50 mm in diameter, were extracted from large block samples (5 – 20 kg), using a water fed diamond core drill-bit. The end of the cylinders were trimmed and ground to ensure they were flat in accordance with International Society for Rock Mechanics (ISRM) 2007 material testing standards [14].

The diameter of the specimens was measured using high accuracy digital callipers, at three points along the length of each cylindrical specimen. The average diameter and applied force measurements were used to calculate the applied stress, during uniaxial loading experiments. The length of each specimen was also measured.

Specimens in this thesis defined as ‘oven dried’ were dried in a fan-assisted oven at 105 °C to 110 °C, until they achieved a constant mass, typically in 24 to 48 hours. The specimens were then placed in a desiccator that contained dry self-indicating silica gel and left to cool down to room temperature before being instrumented and tested.

Specimens defined as ‘air dried’ in this thesis were left to dry naturally indoors at a temperature of 20 °C and in atmospheric humidity, the resulting rocks moisture content was between 0.25% and 0.5 %.

Specimens defined in this thesis as ‘water saturated’, were submerged in water until they reached maximum saturation. The water was purified using reverse osmosis to remove ions, molecules, and larger particles, and the water had a measured electrical conductivity of 474 µS.

In this thesis specimens defined as ‘saline saturated’ were submerged in saline solution, until they reached maximum saturation. The saline solution contained reverse osmosis treated water and dissolved sodium chloride, the electrical conductivity of the saline solution was 56.58 mS (similar to seawater).

5.1.2 Rock lithology

Rock lithology	Rock type	Rock mineralogy
Halite	Sedimentary	Halite – 62 % Anhydrites/clays – 38 %
Quartzite	Metamorphic	Mono quartz – 83 % Poly quartz – 5 % Alkali feldspar – 6 % Plagioclase – 1 % Lithic – 3 % Altered grain – 2 %
Sandstone	Sedimentary	Mono quartz – 66 % Poly quartz -14 % Alkali feldspar – 9 % Lithic – 7 % Altered grain – 4 %
Syenogranite	Igneous	Quartz – 45 % Alkal feldspar – 36 % Plagioclase – 17 % Sericite – 1 % Muscovite - <1 %
Gabbro	Igneous	Plagioclase – 66 % Opaques – 14 % Chlorite – 9 % CPX – 7 % Sericite – 4 % Zircon - <1 %
Granite	Igneous	Quartz – 26 % Alkali feldspar – 27 % Plagioclase – 17 % Muscovite – 12 % Biotite – 6 % Chlorite – 1 % Sericite – 11 % Zircon - <1 %
Marble	Metamorphic	Calcite – 100 %
Schist	Metamorphic	Biotite – 43 % Alkali feldspar – 15 % Sillimanite - 5 % Plagioclase - 4 % Andalusite - 3 % Opaques - 2 %

Table 5-1 Rock lithology and mineralogy summary. *Material properties for all of the rock types tested.*

An expert mineralogist from the BGS determined the lithology type [123-125] and mineral composition by point counting. All of the rock lithologies tested and presented in this thesis are shown in Table 5-1, along with their associated mineral compositions.

5.1.3 Concrete mixture

A single slab of concrete (900 x 500 x 200 mm) was cast at the University of Birmingham, using a normal grade concrete mix as shown in Table 5-2. Cylindrical specimens were extracted from the concrete slab using the techniques described in the previous in section for rocks. A concrete curing time

of at least three months was chosen; concrete usually reaches 99 % of its final strength after 28 days, in accordance with British Standard BS EN 12390-3:2002.

	Cement	Water	Fine Aggregate	Coarse Aggregate
Ratio	1.0	0.5	2.0	2.8

Table 5-2 Concrete mixture ratios.

5.2 EPS Electrode coupling methods

For the capacitively coupled EPS experiments presented in chapters 6, 7 and 8, in which the specimens were air dried or oven dried; 25 x 25 mm adhesive copper electrodes were electrically isolated from the specimen, using a 30 x 30 mm adhesive Kapton® polyimide film, between the specimen and electrode to capacitively couple the sensor. A diagram of the electrode structure is shown in Figure 5-1.

For water and saline saturated experiments presented in chapters 6 and 7, using the capacitively coupled EPSs; the 25 x 25 mm adhesive copper electrodes were electrically isolated from the specimen, by 40 x 40 mm adhesive Kapton® polyimide film, to capacity couple the measurement. In between the Kapton® film and the specimen, a thin layer of Aquagel® a water based lubricating jelly was applied, elastic bands were then used above and below the copper electrode, to hold the electrode structure in contact with the specimen surface. This method was used because the self-adhesive Kapton® film does not bond well to wet surfaces, the Aquagel® is an excellent electrical conductor and the rubber bands ensured good physical and electrical contact with the rock. The larger area Kapton insulator was used to insure any excess Aquagel® did not accidently short the copper electrode directly to the material surface. The lager 40 x 40 mm Aquagel®-Kapton®-copper electrode structure has a capacitance of 187 pF which is not greatly different enough to the smaller 30 x 30 mm Kapton®-copper electrode capacitance of 159 pF to effect the EPS measurement, between wet samples and dry samples. A diagram of the three electrode structures is shown in Figure 5-1.

The flexible Kapton®-copper composite electrode structured used in the directly coupled EPS experiments presented in chapter 9, were bonded to the material surface using CircuitWorks® [126] two-part conductive epoxy medium. Equal amounts of the two-part epoxy medium were thoroughly mixed together on the conductive electrode surface and then pressed firmly to the surface of the material specimen. It was then placed into an oven at 105 °C to 110 °C for 10 minutes; even in the uncured state the epoxy is strong enough to hold the electrodes in place during the curing process. The epoxy mixture and, curing process was carried out in accordance with the manufacture's data sheet [126] to ensure a volume resistivity of < 0.001 Ω-cm.

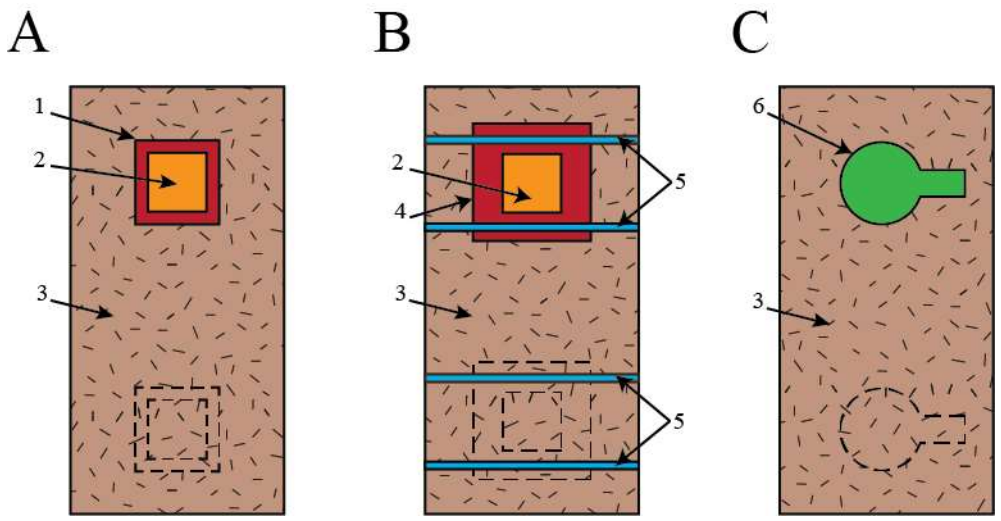

Figure 5-1 EPS electrode structure mounting. *1) Kapton® polyimide film 30 x 30 mm, 2) copper electrode 25 x 25 mm, 3) material specimen, 4) Kapton® polyimide film 40 x 40 mm, 5) elastic band and 6) flexible composite electrode. A) capacitively coupled electrode structure for dry materials, B) capacitively coupled electrode structure for wet materials and C) smart EPS directly coupled composite electrode structure. For each specimen tested two electrodes were place diametrically opposite each other, 10 mm from the top and bottom of the specimen respectively.*

5.3 Material testing apparatus

Each specimen was instrumented with two EPS placed diametrically opposite each other, positioned 10 mm from the bottom and the top of the specimen, respectively. For experiments using the capacitively coupled EPS, the sensor was directly coupled to its electrode structure and held in place with elastic bands around the circumference of the specimen. For experiments using the directly coupled smart EPS, the sensor was connected into its flexible electrode structure via is on board connector terminal; the epoxied electrode structure and sensor connector is strong enough to support the weight of the EPS.

Two wide band (100-1000 kHz) piezoelectric transducers (WSA SN AE18) supplied by Physical Acoustics Corporation [127], were fitted to the side of stainless steel platens by means of brass housings. Adjustment screws were used as well as a thin layer of grease to unsure good acoustic coupling between the piezo transducers and the steel platens.

A direct contact circumferential strain gauge (MTS 632.12-20) [128], was fitted around the centre of the specimen and two direct contact axial strain gauges (MTS 632.11-90) [128], were attached on opposite sides of the specimen. The strain gauges utilize Wheatstone bridge [129] circuits and are able to measure strain accurate to ± 0.0001 mm/mm. Two single sided printed circuit board (PCB) plates (FR4) were positioned between the specimen and each acoustic emission (AE) platen, to earth the platens and load frame and to electrically isolate the specimen. Load was measured using a 1 MN capacity force transducer (MTS 661.98) [130] accurate to ± 0.34 % of the load. A detailed view of the apparatus and sensor positions are shown in Figure 5-2.

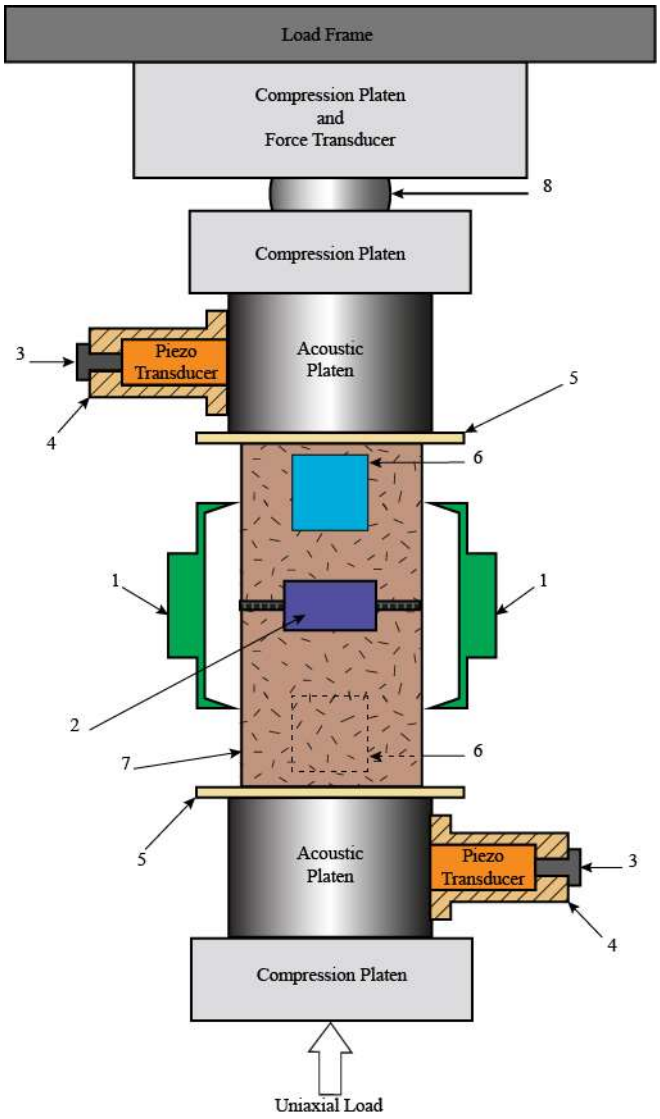

Figure 5-2 Material testing apparatus. *Block diagram of the uniaxial loading apparatus and sensor placement. 1) direct contact axial strain gauge, 2) direct contact circumferential strain gauge, 3) piezo transducer adjustment screw, 4) brass housing for piezo transducer, 5) electrically isolating FR4 plate, 6) EPS and associated electrode structure, 7) material specimen, 8) radial loading bearing.*

A 4.6 MN capacity servo-controlled hydraulic load frame (MTS 815) [131] was used to apply load. Prior to commencing the experiments, a fixed AE threshold was individually determined for each specimen. The AE threshold was determined as the minimum dB threshold at which no hits were detected when a 1 kN load was applied and held on the specimen over a duration of approximately 10 minutes. The difference in threshold levels is a reflection of the seismic attenuation within the samples, which is greater in some material types than others. The ambient acoustic noise from the load frame and surrounding equipment is fairly constant and thus fixed AE thresholds were used rather than floating.

During the 1 kN holding load for experiments utilising the directly coupled smart EPS, the input impedance of the sensor was set. The smart EPS controller was plugged into the EPS via the micro USB port, then the user sets the EPS bootstrap feedback percentage and thus the input resistance of the sensor,

via the controller's graphical user interface (GUI) controller. If the sensor becomes unstable using the recommended bootstrap percentage value from the calibration procedure, the feedback must be reduced slightly until stable EPS operation occurs. The EPS input impedance calibration procedure is used to find a ballpark bootstrap feedback percentage for the material type, where the input impedance is highest without before instability issues occur. Details of the calibration procedure are described in section 4.6.

The Testing apparatus was contained in a temperature controlled room for the duration of all material testing experiments, to eliminate any temperature effects.

5.4 Uniaxial Loading profiles

The uniaxial loading profiles used for the experiments presented in thesis are shown in Figure 5-3, where loading data from marble specimens are used as an example.

For the ramp to destruction (RTD) loading profile shown in part A) of the figure, the load is applied at a constant strain rate or force rate until material failure occurs (in the example a constant strain rate was used). The loading rate was chosen for each specimen based on the theoretical strength of the material, with the aim of inducing material failure in ~5 minutes for the majority of RTD experiments. This test was designed to investigate the correlation between AE and PSV emissions during different stages of rock deformation.

The step like stress (SLS) test shown in part B) applies load in a step like manor using a constant force loading rate until material failure is induced in ~10 loading steps. A constant loading rate was chosen for the (SLS) experiments as a compromise between experiment duration and PSV settling time. This loading profile was designed to investigate relationships between static in-situ stress and PSV amplitude.

The cyclic RTD loading profile shown in part C) of the figure was implemented to investigate correlations between the Kaiser effect and Felicity effect of AE (effects associated with cyclic loading) with PSV activity. Refer to section 2.4.2.4 for a detailed overview of Kaiser and Felicity effect of AE. For each loading cycle the loading is increased at a constant strain rate and for each successive cycle the maximum load is increased. For experiments presented in this thesis, the materials failed within 4 to 6 loading cycles.

The cyclic SLS loading profile was designed to test any relationship between applied static stress and PSV amplitude and if the relationship is affected by Kaiser effect/work hardening, due to repeated loading of the material. The stress is increased and decreased at a constant force rate in uniform steps, for each loading cycle the maximum load is increased one step higher than the previous cycle. The material specimens were subjected to 5 loading cycles, for the duration of the loading cycles the maximum loading was within the linear elastic region of the materials.

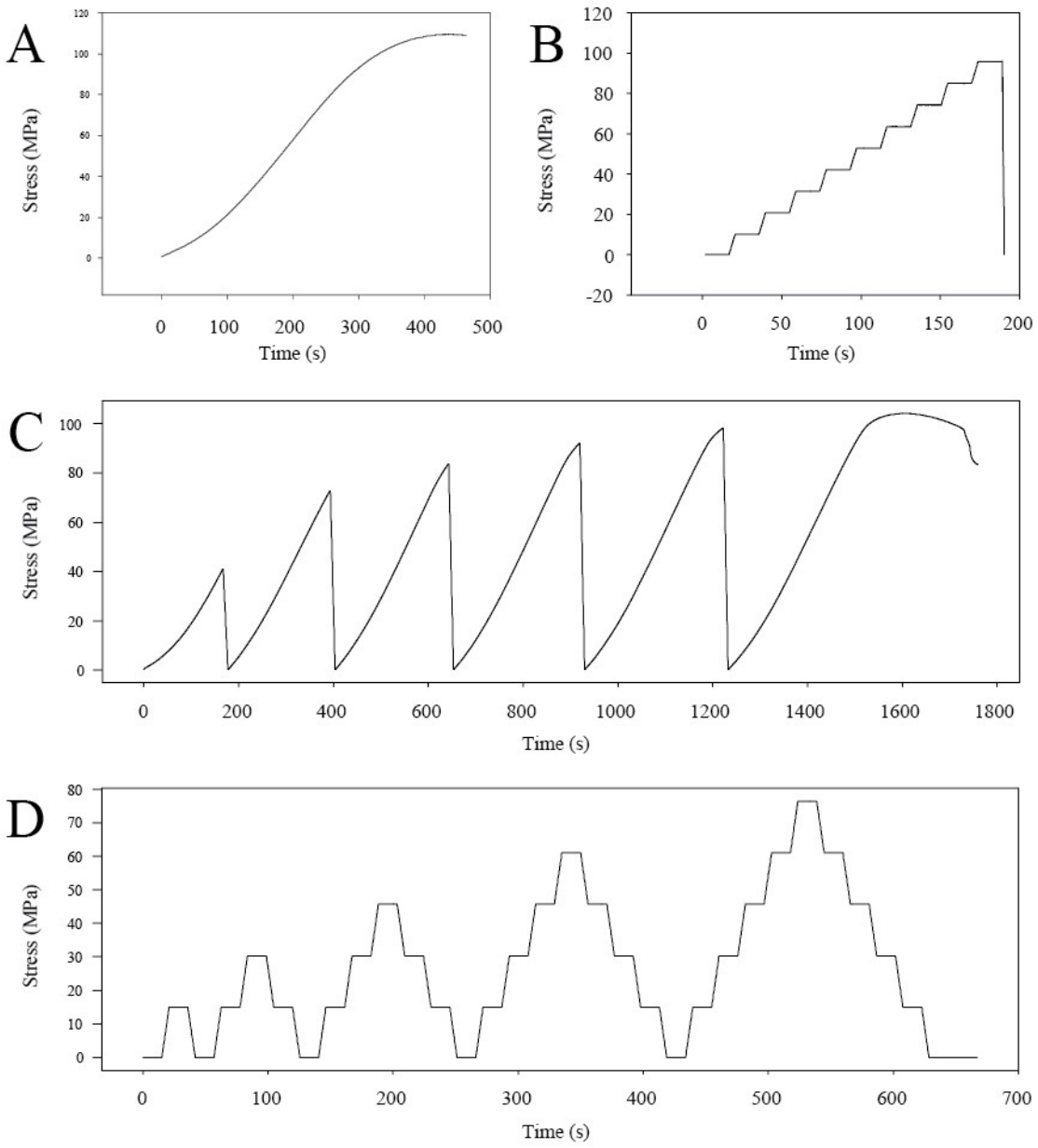

Figure 5-3 Types of loading profile. *Example uniaxial stress profiles used for the experiments presented in this thesis. The stress profiles are for oven dried marble specimens. A) Ramp to destruction (RTD), B) Step like stress (SLS) test, C) cyclic RTD and D) cyclic SLS test.*

Table 5-3 shows a summary of the loading information for all of the RTD experiments for both rock and manmade materials presented in chapters 6 and 7 of this thesis.

Material	Environmental condition	Loading rate	Failure occurrence (s)
Quartzite	Oven dried	$2.5x10^{-6}$ mm/mm/s^{-1}	673.01
Halite	Oven dried	0.18 kNs^{-1}	235.53
Macor ®	Oven dried	2.25 kNs^{-1}	601.99
Syenogranite	Oven dried	$6.5x10^{-6}$ mm/mms^{-1}	330.37
Syenogranite	Air dried	$6.5x10^{-6}$ mm/mms^{-1}	356.00
Syenogranite	Water saturated	$6.5x10^{-6}$ mm/mms^{-1}	226.97
Sandstone	Oven dried	$8.0x10^{-7}$ mm/mms^{-1}	2660.00
Sandstone	Air dried	0.50 kNs^{-1} $1.56 x10^{-5}$ mm/mms^{-1} (>150s)	827.51
Sandstone	Water saturated	$8x10^{-6}$ mm/mms^{-1}	445.94
Sandstone	Saline saturated	$8x10^{-6}$ mm/mms^{-1}	379.02
Granite	Oven dried	$6.5x10^{-6}$ mm/mms^{-1}	1163.34
Granite	Water saturated	$6.5x10^{-6}$ mm/mms^{-1}	382.78
Granite	Saline saturated	$6.5x10^{-6}$ mm/mms^{-1}	428.97
Marble	Oven dried	$6.5x10^{-6}$ mm/mms^{-1}	569.91
Marble	Air dried	$6.5x10^{-6}$ mm/mms^{-1}	414.49
Marble	Water saturated	$6.5x10^{-6}$ mm/mms^{-1}	494.70
Marble	Saline saturated	$6.5x10^{-6}$ mm/mms^{-1}	595.78
Schist	Oven dried	$3.5x10^{-6}$ mm/mms^{-1}	791.32
Schist	Air dried	$6.5x10^{-6}$ mm/mms^{-1}	439.43
Schist	Water saturated	$6.5x10^{-6}$ mm/mms^{-1}	238.58
Gabbro	Oven dried	$6.5x10^{-6}$ mm/mms^{-1}	438.50
Gabbro	Water saturated	$6.5x10^{-6}$ mm/mms^{-1}	468.61
Concrete	Oven dry	$5x10^{-6}$ mm/mms^{-1}	612.55
Concrete	Air dry	$5x10^{-6}$ mm/mms^{-1}	501.00
Concrete	Water saturated	$5x10^{-6}$ mm/mms^{-1}	670.73
Concrete	Saline saturated	$5x10^{-6}$ mm/mms^{-1}	531.07

Table 5-3 RTD experiment loading information. *Summary of the RTD loading rates and failure occurrences for all experiments presented in chapters 6 and 7. The strain controlled experiments used axial strain control, however after 150 s during the air dried sandstone experiment the control method was switched to circumferential strain.*

The loading information for the cyclic RTD experiments presented in chapter 8 of this thesis are shown in Table 5-4.

Material	Loading rate (mm/mms^{-1})	Failure occurrence (s)
Syenogranite	$6.5x10^{-6}$ mm/mms^{-1}	1573.39
Sandstone	$8x10^{-6}$ mm/mms^{-1}	1505.21
Marble	$6.5x10^{-6}$ mm/mms^{-1}	1759.72
Schist	$6.5x10^{-6}$ mm/mms^{-1}	1902.06
Gabbro	$6.5x10^{-6}$ mm/mms^{-1}	1383.62
Concrete	$5x10^{-6}$ mm/mms^{-1}	1327.47

Table 5-4 Cyclic RTD experiment loading information. *Summary of the cyclic RTD loading rates and failure occurrences for all experiments presented in chapter 8. All experiments used a constant strain loading rate and all material specimens were oven dried.*

The loading information for each of the SLS experiments presented in chapter 9 of this thesis are shown in Table 5-5.

Material	Loading profile	Loading rate (kNs^{-1})	Test duration (s)
Sandstone	SLS	0.167 (step 1) 0.083 (step 2) 0.042 (step 3) 0.021 (step 4) 0.010 (step 5)	72.13
Sandstone	Cyclic SLS	1	862.96
Marble	SLS	1	190.42
Mable	Cyclic SLS	1	815.93

Table 5-5 SLS experiments loading information. *Summary of the SLS and cyclic SLS loading rates and test duration for all experiments presented in chapter 9. All experimenters were loaded with a constant strain rate and the maximum load did not exceed the linear elastic region of the materials tested. All material specimens were oven dried.*

5.5 Defining the stages of material deformation

For the all of the RTD experiments the stress strain curves were divided into five recognized stages of deformation [132-134], to investigate the correlations between PSV and AE during different deformation modes. The stress strain curve and resulting AE activity shown Figure 5-4, is an example of typical rock deformation properties.

Stage 1) pre-existing microcrack and pore closure: characterized by strain-hardening behaviour (concave up) and an increase in AE event rate.

Stage 2) recoverable elastic deformation: characterized by linear axial and volumetric deformation with very little or no AE activity (low event rate).

Stage 3) partially recoverable elastic deformation and stable microcrack propagation: characterized by linear axial deformation, onset of volumetric dilatency and an increase in AE activity in terms of amplitude and event rate.

Stage 4) non-recoverable pre-peak inelastic deformation resulting from unstable microcrack propagation and coalescence: characterized by strain-hardening behaviour (concave down), rapid volumetric dilation and acceleration in AE rate and amplitude.

Stage 5) non-recoverable post-peak inelastic deformation resulting from unstable macrocrack and shear plane development: characterized by strain-softening behaviour (concave down), surge in volumetric dilation and AE activity.

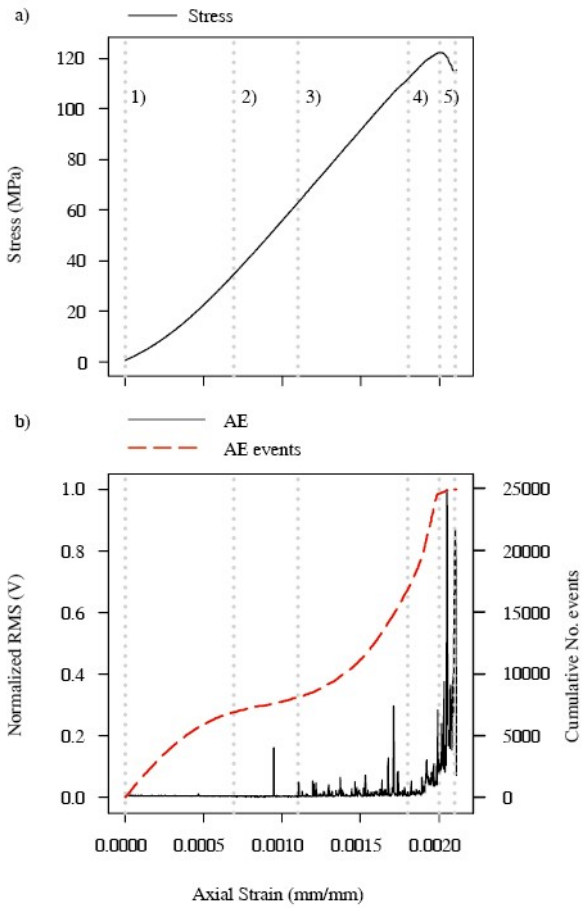

Figure 5-4 Loading stages example. *a) stress strain graph and b) AE event amplitude and cumulative number of events for an oven dried granodiorite specimen subjected to uniaxial loading at a constant strain rate.*

For experiments presented in this thesis, the stages of loading are solely defined by the stress-strain curve characteristics in accordance with the stage definitions described previously in this section. The AE is not always a reliable indicator of deformation stage, as it does not behave in the expected textbook manor as shown in Figure 5-4 for all experiments. However, the stress-strain curve is a reliable indicator; by identifying stages of deformation in the stress-strain curves, one can then observe the effect of deformation stage on PSV-AE correlation.

5.6 Data Acquisition

5.6.1 PSV

Both the directly coupled smart EPS and capacitively coupled EPS were configured with a gain of 5. An analogue notch filter with a frequency of 50 Hz was applied to the output signals from the capacitively coupled sensors, to attenuate the effects of the ambient electric field. The capacitively coupled EPS output signal was digitalized at a sampling frequency of 1.5 MHz and the directly coupled smart EPS output signal at 500 Hz, using a National Instruments [135] analogue to digital converter (NI PXI-6124) [110]. The Nyquist maximum frequency [25] of measured PSV from the capacitively coupled EPS setup is 750 kHz, which is within the expected range of the measured AE, thus allowing for correlations to be investigated between the two. Whereas the Nyquist maximum frequency for the

measured PSV from the directly coupled EPS setup is 250 Hz, ideal for monitoring PSV thought to be associated with static in-situ stress.

The EPS data were acquired using a custom National Instruments (NI) [135] virtual instrument on a computer (NI PXIe1071). The virtual instrument has a GUI, allowing the user to acquire PSV data at a desired sampling frequency and also graphing the data in real time. Because of the high sampling rate of the capacitively coupled EPS setup, the resulting PSV data is large and quickly reaches the capacity of the computers random access memory (RAM). To resolve this problem, the data is saved periodically to the computers high capacity hard drive, once a defined RAM buffer is full. The user can define how many data samples are to be stored in the RAM buffer, using the GUI. The uniformly sampled time based PSV data is saved in binary format (.bin). The data from the capacitively coupled EPS setup is very large in the range from ~5 GB to ~75 GB, depending on experiment duration. However, due to the significantly lower sampling rate of the directly coupled EPS setup, the data is relatively small ranging from ~22 kB to ~186 kB.

5.6.2 AE

Each piezo transducer was connected to a Physical Acoustics Corporation acquisition system (PCI-2) [48] via a 40 dB preamp and the associated AEwin software [121] performed the signal conditioning AE event detection. The PCI-2 system filtered the amplified piezo transducer voltages using a band pass filter between 1 kHz and 1 MHz; this frequency range is typically used for monitoring AE in rocks and concrete [136], thus giving a measurable Nyquist maximum frequency [25] of 500 kHz. In rocks AE frequency components over 500 kHz are not usually significant [137].

The following AE event detection parameters were used in accordance with recommendations from material testing experts at the BGS: peak definition time (PDT) = 200 µs, hit definition time (HDT) = 800 µs, hit lockout time (HLT) = 1000 µs and maximum hit duration = 100 ms. The Physical Acoustics Cooperation PCI-2 AE acquisition system [48] contains a lookup table of AE event detection parameters for different materials, BGS used this as a guide for the setting the AE event detection parameters. The AE event detection parameters were fined tuned by experimentation for optimum event detection in rocks and concrete. This required an understanding the effects of changing each parameter on AE event detection, this is described in more detail in section 2.4.2.3. Correct setting of the PDT parameter ensures accurate calculation of the peak amplitude and rise time of AE events/hits [48]. Setting the HDT parameter correctly ensures each AE event in the AE waveform structure is reported as one event [48]. Correctly setting of the HLT parameter ensures inaccurate measurements during signal decay are avoided and allows for faster data acquisition [48].

Although the PCI-2 AE acquisition system samples the piezo-transducer voltages at a high sampling frequency (5 MSs^{-1}), the “real time” event detection procedure reduces the data size considerably, to the range of ~65 kB to ~200 MB, depending on experiment duration and number of events. The PCI-2

system was connected to the same computer (NI PXIe1071) as the EPS system and both AE and PSV data was acquired and stored simultaneously, to the computer's hard drive during experiments.

5.6.3 Loading data

The strain and loading data were acquired using MTS MultiPurpose TestWare® software [138], on a second PC connected to the force transducer and strain gauges. The strain gauges have built in Wheatstone bridge [129] circuits for temperature compensation and signal conditioning, ensuring accurate strain values are recorded. The software also controlled the load frame and was programmed by an expert at the BGS, to apply the loading profiles to each material specimen tested. The strain and load data are saved in increments of strain or force, depending on whether the material was loaded using a constant strain or force rate respectively; the data size is small (~130 kB to ~3.2 MB).

All three acquisition systems (NI virtual instrument, AEwin [121] and MultiPurpose TestWare® [138]) were synchronized with a 5 V pulse by the load frame controller (MTS FlexTest 60 [139]), at the start of each experiment to ensure the PSV, AE and loading data were acquired in unison.

5.7 Statistical methods

5.7.1.1 Linear Regression

Linear regression analysis [140] was computed using the MATLAB® `cftool` curve fitting tool [141], to investigate relationships between the predictor variable (cumulative No. AE events) and response variable (cumulative No. PSV events). The linear regression results presented in this thesis have p-values < 0.05, indicating that there is 95 % chance of the relationship between predictor being valid. The r^2 value represents the goodness of fit of the regression line, i.e. the variation from a linear relationship between cumulative number of AE and PSV events.

5.7.1.2 Parametric data testing

A Jarque-Bera goodness [142] of fit test computed by the `jbtest` MATLAB® function [143] was used to examine if data sets matched a normal distribution.

5.7.1.3 Linear Correlation

A non-parametric Spearman linear correlation [140] computed by the `corr` MATLAB® function [144] was used to investigate linear relationships, between two normally distributed variables. This method measures the strength of association between the two variables, where the correlation coefficient (R) represents the degree of correlation. R = 1 is an absolute linear correlation, R = 0 is the weakest linear correlation and R = -1 is an absolute inverse linear correlation between the two variables.

5.7.1.4 Cross-correlation

Cross-correlation [145] analysis computed by the `xcorr` MALAB® function [146], was used to measure similarity between time series data, as a function of the lead/lag relative to the each other.

Multiple linear correlation coefficients are calculated between one data set and a time shifted version of the other data set. The correlation coefficients can then be plotted against the corresponding lead or lag times between the two data sets. As with linear correlation, a cross-correlation coefficient of 1 indicates an absolute correlation, 0 indicates the minimum linear correlation and -1 an absolute inverse correlation. A cross-correlation between two identical time series data (autocorrelation), would result in a lag time of 0 and cross-correlation coefficient of 1.

In this thesis, the RMS voltage produced in either piezo transducer associated with each AE events was normalized and used for cross-correlation analysis, with the normalized differential measurement of RMS PSV from the rock. The maximum linear correlation is referred to as the cross-correlation coefficient. If its associated lag time is negative this indicates AE events lag behind PSV activity, if the lag time is positive this indicates PSV activity lags behind AE events and a lag time of 0 indicates PSV and AE data occur simultaneously.

5.7.1.5 Multi comparison statistics

To test if there are significant differences between groups, i.e. environmental conditions or stages of loading, an appropriate statistical test was chosen. If the groups were non-parametric a Kruskal–Wallis one-way analysis of variance test [140] was used, via the `kruskalwallis` MATLAB® function [147]. For parametric data a one-way analysis of variance test (ANOVA) [140] was used, via the `anova1` MATLAB® function [148]. If the resulting p-value was less than the significance value ($p<0.005$) a follow up multiple comparison test using the Dunn and Sidák's approach [149], via the MATLAB® function `multcompare` [150] was used to determine which groups were statistically different.

5.8 Aluminium control test

A cylindrical aluminium sample (50 mm diameter and 100 mm length) was tested using a cyclic loading profile, as a control experiment. Because aluminium is a metal conductor it should not hold charge and should not produce any self-potential (i.e. PSV).

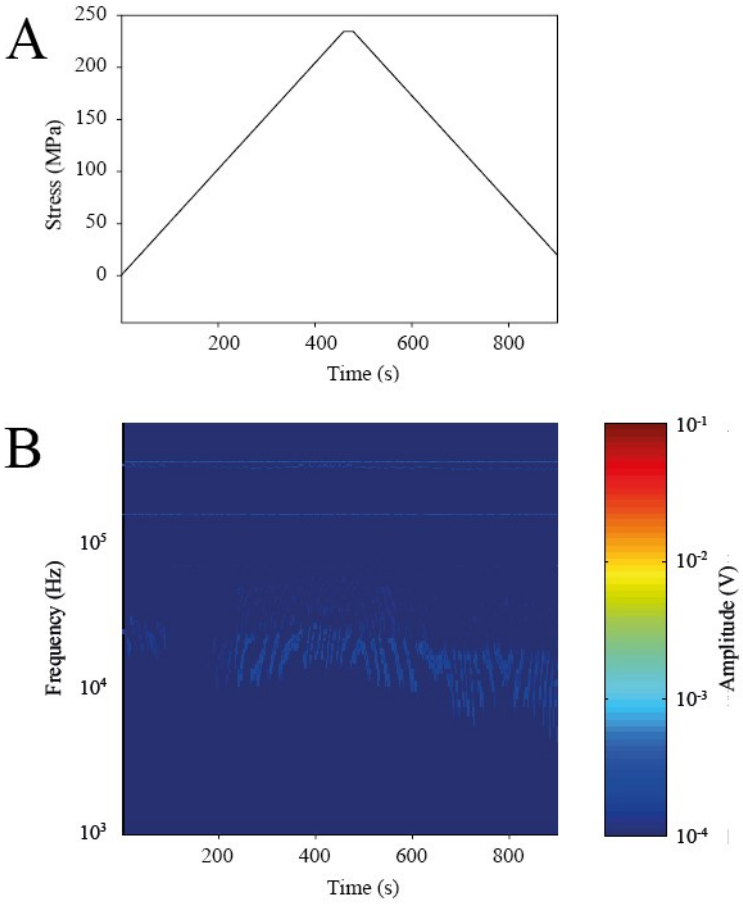

Figure 5-5 Auminium control test. *A) Applied load to the cyclidicral aluminium control sample; B) resulting PSV spectrogram differential measurement from two EPS placed dimetrically opposide eachother on the specemin.*

Figure 5-5 shows the PSV spectrogram and loading data from the aluminium control test. The load was increases at constant rate of 1 kNs^{-1} up until a load of 234.4 MPa was reached, the load was held for 20 s and then released at a constant rate of 1 kNs^{-1}. It is clear from the EPS spectrogram that there are no PEPS or TEPS produced, as with the rock and manmade materials experiments shown in chapters 6 and 7. However, there are low amplitude high frequency bands of noise, produced from surrounding electrical equipment (not expected to interfere with PSV measurement). The results of the aluminium control experiment, show PSV signals originate from the insulting materials tested (rocks, glass ceramic and concrete) and do not originate from the testing apparatus.

6 UNIAXIAL COMPRESSIVE STRESS TESTING OF ROCKS IN DIFFERENT ENVIRONMENTAL CONDITIONS USING CAPACITIVELY COUPLED EPSS

This chapter begins by stating the motivations behind the experiments carried out in this results chapter (section 6.1). A selection of results pages containing detailed observations of pressure stimulated voltage (PSV), acoustic emissions (AEs), stress and strain and statistical relationships between each measurement quantity, are provided in section 6.2. The results are then compared and discussed in the last part of the chapter (section 6.3).

6.1 Introduction

Work by others [17, 82-84], has shown pressure stimulated electromagnetic emissions (PSEs) in rock exist, using laboratory electrometers and electromagnetic emissions (EME) antennas. However, this phenomenon has only been observed in a limited number of rock lithology and the generation mechanism/s is/are still uncertain. In addition, both detection methods are not practical for field use outside of the laboratory setting, as described in section 3.3.

This thesis the first study attempting to characterise PSEs 1) over a wide range of different rock lithology, 2) in different environmental conditions and 3) using a field capable technology i.e. the electric potential sensor (EPS). The experiments that were carried out and presented in this chapter, were undertaken with the aim of answering the following research questions:

Are PSVs present in a wide range of rock lithology, including rocks with no piezoelectric minerals?

Are PSVs produced by rocks related to acoustic events?

Can the detection of PSVs be used as an indication of the structural health or the current stage of deformation in rock?

Is the electric potential sensor (EPS) a suitable technology for the wide scale monitoring of PSVs in rock?

6.2 Results

6.2.1 Experimental procedure

Cylindrical specimens of various rock lithology were instrumented with two axial strain gauges, a circumferential strain gauge, two piezo-transducers and two capacitively coupled EPS. Each rock specimen was subjected to a ramp to destruction (RTD) uniaxial loading using a servo controlled load frame. The full details of the testing procedure are shown in chapter 5 of this thesis. Specimens were tested in different environmental conditions, including oven dried, air dried, water saturated and saline saturated; detailed information about specimen preparation is presented in section 5.1.

For each lithology, a constant strain or force rate was chosen, to induce material failure in ~5 – 10 minutes; the loading rates are presented in section 5.4 for each RTD experiment. The results presented in this chapter show the resulting stress, strain, AE and PSV emitted from rock specimens during loading and up to fracture and the statistical correlations between AE and PSV.

All of the experiments listed in Table 6-1 are presented in this thesis chapter, in the same order as they occur in the table.

Material	Environmental condition	Figure number
Quartzite	Oven dried	Figure 6-1
Halite	Oven dried	Figure 6-2
Syenogranite	Oven dried	Figure 6-3
Syenogranite	Air dried	Figure 6-4
Syenogranite	Water saturated	Figure 6-5
Sandstone	Oven dried	Figure 6-6
Sandstone	Air dried	Figure 6-7
Sandstone	Water saturated	Figure 6-8
Sandstone	Saline saturated	Figure 6-9
Granite	Oven dried	Figure 6-10
Granite	Water saturated	Figure 6-11
Granite	Saline saturated	Figure 6-12
Marble	Oven dried	Figure 6-13
Marble	Air dried	Figure 6-14
Marble	Water saturated	Figure 6-15
Marble	Saline saturated	Figure 6-16
Schist	Oven dried	Figure 6-17
Schist	Air dried	Figure 6-18
Schist	Water saturated	Figure 6-19
Gabbro	Oven dried	Figure 6-20
Gabbro	Water saturated	Figure 6-21

Table 6-1 List of RTD experiments. *An index for all of the uniaxial compression RTD experiments carried out, presented and discussed in this thesis chapter.*

The amplitudes of the PSV and AE discussed in this thesis chapter, are referred to the input (RTI) of the EPS and piezo transducers respectively. Both the AE and PSV amplitudes are graphed in part 1) of each figure listed in Table 6-1 have been normalised, for ease of comparison and for cross-correlation analysis. All of the PSV values presented are differential measurements between the two ground referenced EPS, mounted diametrically opposite each other, on the material specimen. The AE data presented in this chapter is a combination of detectable events from both piezo transducers, mounted in acoustic platens above and below the material specimen.

6.2.2 Defining the stages of material deformation

For the all of the RTD experiments the stress strain curves were divided into five recognized stages of deformation [132-134], to investigate the correlations between PSV and AE during different deformation modes. A detailed description including an example of typical rock deformation properties in terms of a stress strain curve and resulting AEs graph, is contained in section 5.5.

Stage 1) pre-existing microcrack and pore closure: characterized by strain-hardening behaviour (concave up) and an increase in AE event rate.

Stage 2) recoverable elastic deformation: characterized by linear axial and volumetric deformation with very little or no AE activity (low event rate).

Stage 3) partially recoverable elastic deformation and stable microcrack propagation: characterized by linear axial deformation, onset of volumetric dilatency and an increase in AE activity, in terms of amplitude and event rate.

Stage 4) non-recoverable pre-peak inelastic deformation, resulting from unstable microcrack propagation and coalescence: characterized by strain-hardening behaviour (concave down), rapid volumetric dilation and acceleration in AE rate and amplitude.

Stage 5) non-recoverable post-peak inelastic deformation, resulting from unstable macrocrack and shear plane development: characterized by strain-softening behaviour (concave down), surge in volumetric dilation and AE activity.

6.2.3 Oven dried quartzite RTD experimental results summary

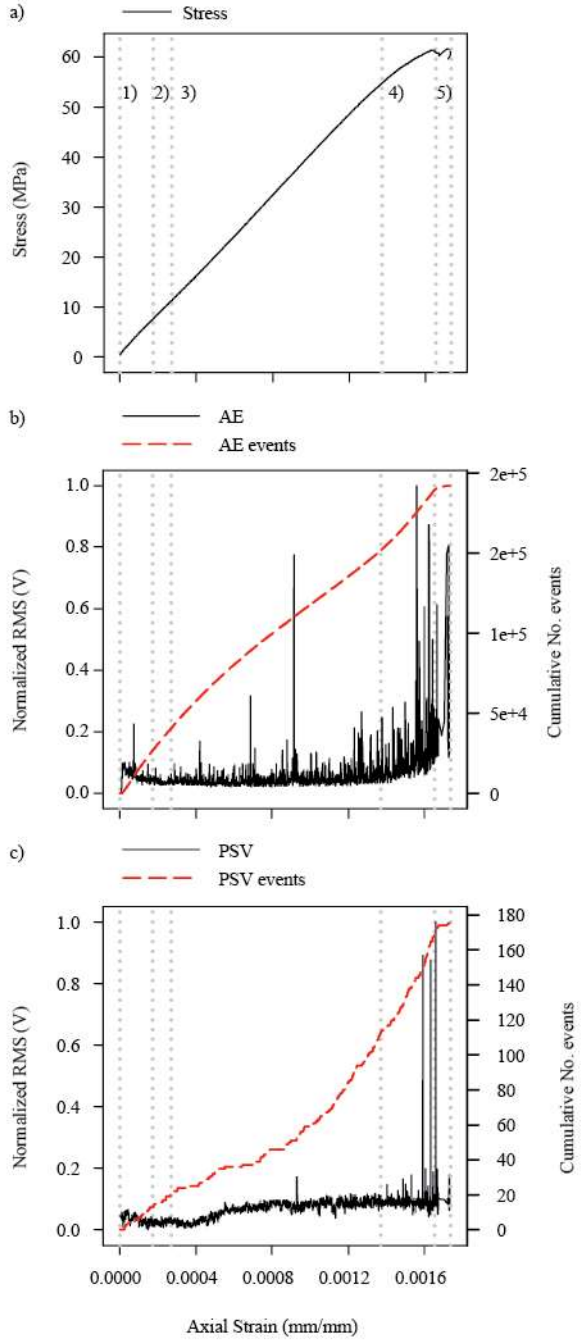

Part 1 – Strain based RTD loading data: *a) applied stress; b) normalized piezoelectric transducer RMS voltage and cumulative number of AE events; and c) normalized PSV RMS voltage and cumulative number of PSV events. Loading stages 1 to 5 are defined in chapter 5.5.*

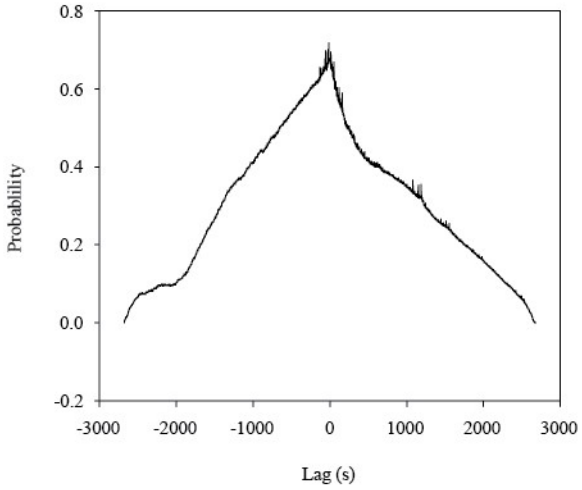

Part 2 – Overall cross-correlation: *Probability of correlation between PSV and AE events at varying lag times. A positive lag time indicates PSV lags behind AE and negative lag time indicates AE lags behind PSV.*

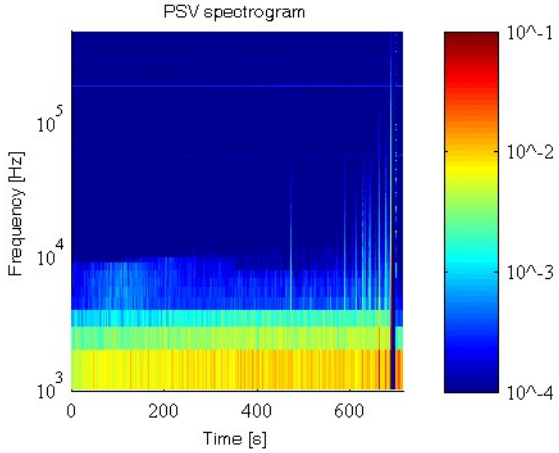

Part 3 – PSV spectral density.

Linear regression	$r^2 = 0.90$
Max Strength	61.60 MPa
Average PSV amplitude	0.75 mV
Average AE amplitude	64.46 dB

Part 4 – loading and statistical data: *The linear regression r^2 is computed between cumulative PSV and AE events.*

Cross-correlation between PSV and AE events						
Loading stage	1	2	3	4	5	Entire test
Coefficient	0.90	0.93	0.79	0.72	0.59	0.72
Lag time (s)	-5	0	-3.5	-3.5	-3.25	-3.25

Part 5– cross-correlation data: *A negative lag time indicates AE events lag behind PSV events and a positive lag time indicates PSV events lag behind AE events at the maximum probability of correlation (coefficient).*

Figure 6-1 Oven dried quartzite results summary. *Part 1) strain based stress, PSV and AE plot; Part 2) overall cross-correlation; Part 3) PSV spectrogram; Part 4) loading data; Part 5) cross-correlation results summary per stage of loading.*

The uniaxial RTD loading data for an oven dried quartzite specimen, is shown in Figure 6-1. The applied stress, AE event amplitude, cumulative number of AE events, PSV event amplitude and cumulative number of PSV events with respect to axial strain is shown in Part 1 of the figure. The PSV spectrogram in Part 3 shows persistent electric potential signals (PEPS) throughout the experiment and the onset of transient electric potential signals (TEPS), towards the end of the experiment up to material failure. The cross-correlation between PSV and AE events is high and PSV activity precedes AE activity, as shown in Part 5. There is a well-defined single peak in cross-correlation probability, shown in Part 2, indicating that the lag time between PSV and AE shows little variability. The linear regression between cumulative number of AE and PSV events is also high, as shown in Part 4.

During Stage 1 of loading there is an increase in the AE and PSV event rate and the baseline AE amplitude, there is also a small increase in PSV amplitude. The cross-correlation probability is high and PSV activity precedes AE activity.

Over the course of Stage 2 the AE event amplitude drops and the event rate declines compared to Stage 1; as expected with recoverable elastic deformation. The PSV amplitude is relatively low during this stage and the event rate drops compared to the previous stage. The cross-correlation probability is highest during this stage and PSV and AE activity occur simultaneously.

The AE and PSV event rate continues to reduce up until the midpoint of Stage 3, in which there is a high amplitude AE event and PSV event at ~0.93×10^{-3} mm/mm. After this point the AE and PSV event rate begins to increase, however the PSV increases more rapidly. The amplitude of the AE and PSV events increases throughout this stage. The cross-correlation probability is high and PSV activity precedes AE activity.

During Stage 4 the AE and PSV amplitudes continue to increase and there are distinct high amplitude spikes. The AE event rate increase further as does the PSV event rate and there is a surge in PSV and AE amplitude, towards the end of the stage. The cross-correlation probability is high and PSV precedes AE activity.

Prior to failure during Stage 5, the AE and PSV peak amplitudes reduce and the event rates decline. There is a distinct spike in AE and PSV amplitude at the point of material failure at the end of the experiment. The cross-correlation probability is lowest during this stage and PSV precedes AE activity.

6.2.4 Oven dried halite RTD experimental results summary

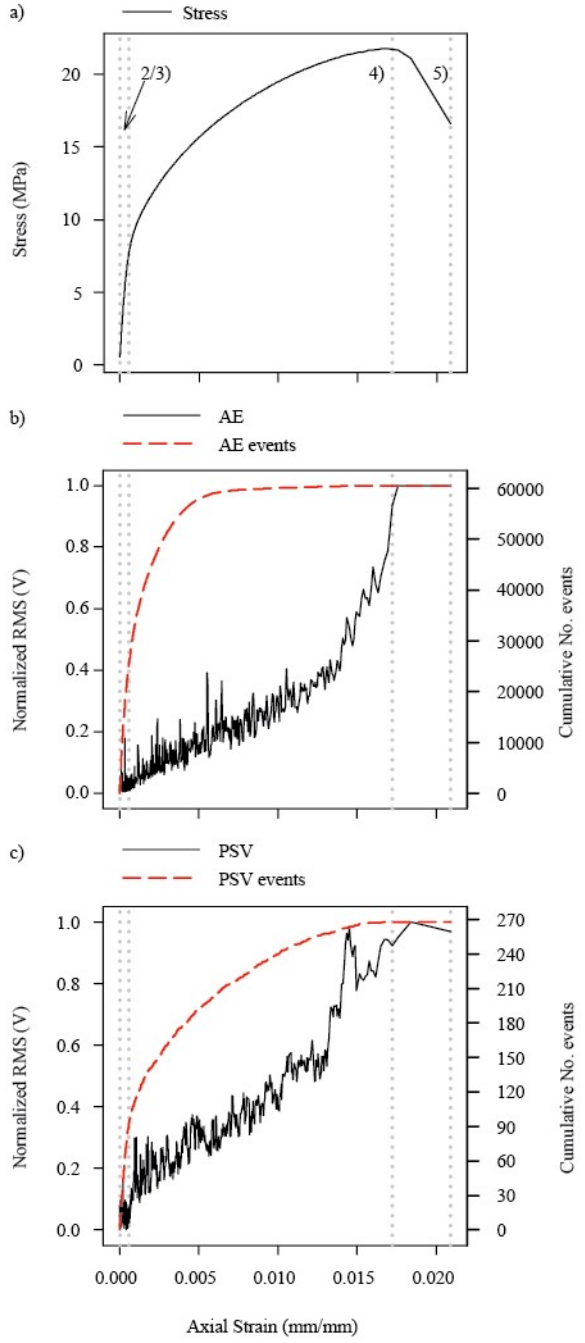

Part 1 – Strain based RTD loading data: *a) applied stress; b) normalized piezoelectric transducer RMS voltage and cumulative number of AE events; and c) normalized PSV RMS voltage and cumulative number of PSV events. Loading stages 1 to 5 are defined in chapter 5.5.*

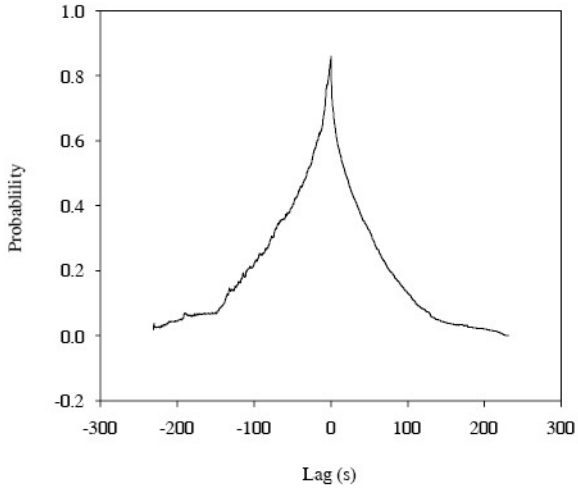

Part 2 – Overall cross-correlation: *Probability of correlation between PSV and AE events at varying lag times. A positive lag time indicates PSV lags behind AE and negative lag time indicates AE lags behind PSV.*

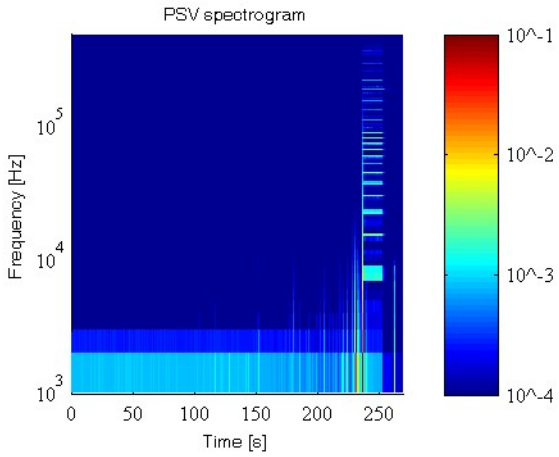

Part 3 – PSV spectral density.

Linear regression	$r^2 = 0.95$
Max Strength	21.75 MPa
Average PSV amplitude	0.322 mV
Average AE amplitude	125.4 dB

Part 4 – loading and statistical data: *The linear regression r^2 is computed between cumulative PSV and AE events.*

Cross-correlation between PSV and AE events						
Loading stage	1	2	3	4	5	Entire test
Coefficient	Undefined	0.6186		0.97	Insufficient	0.86
Lag time (s)	stage	-4		0	No. data	0

Part 5 – cross-correlation data: *A negative lag time indicates AE events lag behind PSV events and a positive lag time indicates PSV events lag behind AE events at the maximum probability of correlation (coefficient).*

Figure 6-2 Oven dried halite results summary. *Part 1) strain based stress, PSV and AE plot; Part 2) overall cross-correlation plot; Part 3) PSV spectrogram; Part 4) experimental data; Part 5) cross-correlation results summary per stage of loading.*

The uniaxial RTD loading data for an oven dried halite specimen is shown in Figure 6-2. The applied stress, AE event amplitude, cumulative number of AE events, PSV event amplitude and cumulative number of PSV events, with respect to axial strain is shown in Part 1 of the figure. The PSV spectrogram in Part 3 shows PEPS throughout the experiment and the onset of TEPS towards the end of the experiment, up to material failure. The cross-correlation probability is high and PSV and AE activity occur simultaneously, as shown in Part 5. There is a well-defined single peak in cross-correlation probability, as shown in Part 2, indicating that the lag time between PSV and AE shows little variability. The linear regression between cumulative number of AE and PSV events, is also high as shown in Part 4.

Stage 1 is not observed in the halite specimen and thus there is no correlation data for this stage.

Stage 2 and 3 have been combined because the volumetric and axial stress strain relationships, deviate from linearity almost simultaneously. In Stage 2/3 low amplitude AE and PSV activity is observed up until the end of the stage ($0.56x10^{-3}$ mm/mm). The PSV and AE events rates are high and the cross-correlation probability high with PSV occurring before AE activity.

There is a small sharp increase in PSV at the beginning of Stage 4 and a steady increase in AE and PSV event amplitude, up until ~$13.13x10^{-3}$ mm/mm, at this point there is a sudden surge in amplitude for the rest of the stage. The frequency of AE and PSV events decreases throughout Stage 4 and 5, although AE shows a more exponential rate of decline than PSV. The cross-correlation is highest during this stage and PSV and AE activity occur simultaneously.

The AE event amplitude continues to increase towards its maximum level and the PSV event amplitude is consistently high throughout Stage 5. This stage occurs over a short time frame and thus there are not enough data points for cross-correlation analysis.

6.2.5 Oven dried syenogranite RTD experimental results summary

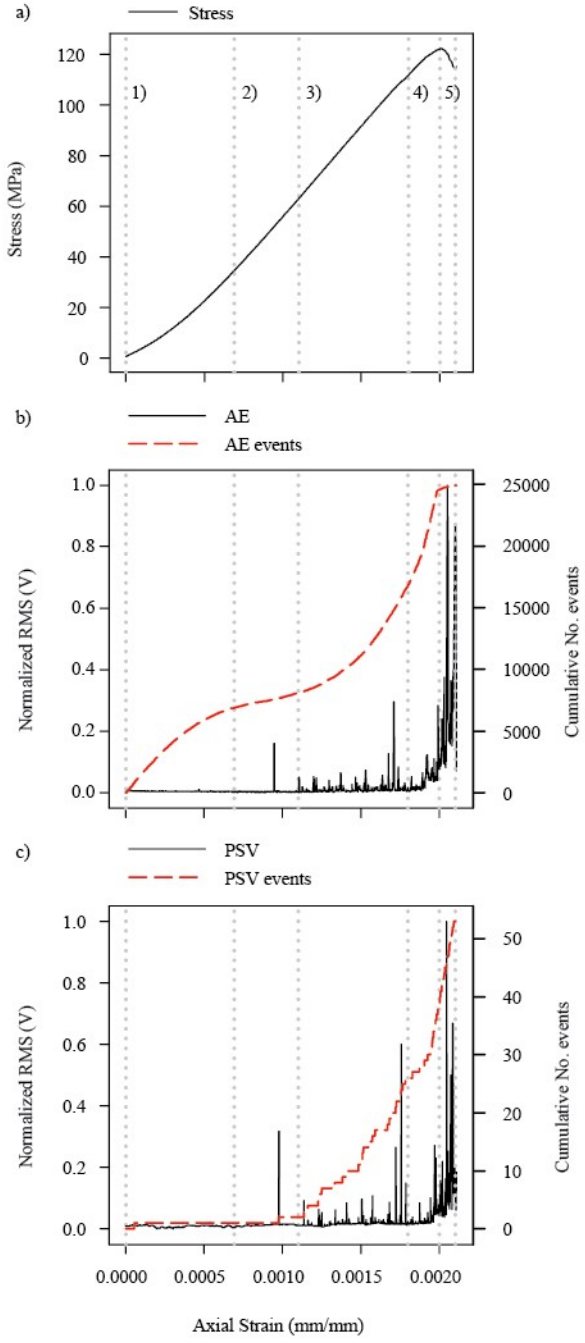

Part 1 – Strain based RTD loading data: *a) applied stress; b) normalized piezoelectric transducer RMS voltage and cumulative number of AE events; and c) normalized PSV RMS voltage and cumulative number of PSV events. Loading stages 1 to 5 are defined in chapter 5.5.*

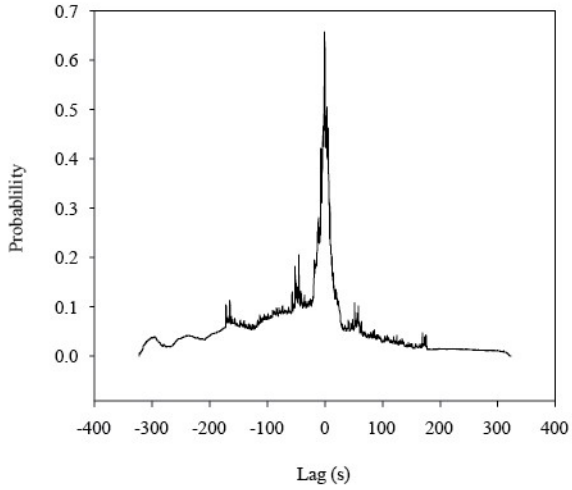

Part 2 – Overall cross-correlation: *Probability of correlation between PSV and AE events at varying lag times. A positive lag time indicates PSV lags behind AE and negative lag time indicates AE lags behind PSV.*

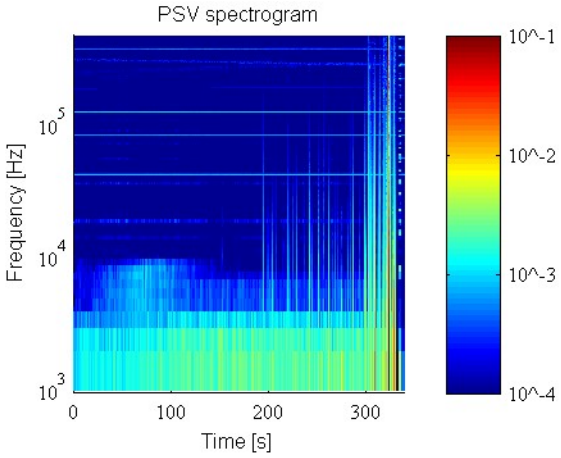

Part 3 – PSV spectral density.

Linear regression	$r^2 = 0.91$
Max Strength	123.3 MPa
Average PSV amplitude	1.557 mV
Average AE amplitude	65.43 dB

Part 4 – loading and statistical data: *The linear regression r^2 is computed between cumulative PSV and AE events.*

Cross-correlation between PSV and AE events						
Loading stage	1	2	3	4	5	Entire test
Coefficient	No	0.73	0.72	0.71	0.73	0.66
Lag time (s)	correlation	4.25	7.25	-3.25	-0.75	-0.75

Part 5 – cross-correlation data: *A negative lag time indicates AE events lag behind PSV events and a positive lag time indicates PSV events lag behind AE events at the maximum probability of correlation (coefficient).*

Figure 6-3 Oven dried syenogranite results summary. *Part 1) strain based stress, PSV and AE plot; Part 2) overall cross-correlation plot; Part 3) PSV spectrogram; Part 4) experimental data; Part 5) cross-correlation results per stage of loading.*

The uniaxial RTD loading data for an oven dried syenogranite specimen is shown in Figure 6-3. The applied stress, AE event amplitude, cumulative number of AE events, PSV event amplitude and cumulative number of PSV events, with respect to axial strain is shown in Part 1 of the figure. The PSV spectrogram in Part 3, shows a wide frequency band of PEPS throughout the experiment. An increase in PEPS frequency occurs in between 25 s – 100 s and the onset of TEPS towards the end of the experiment, up to material failure. The cross-correlation probability is highest out of the syenogranite experiments and AE activity occurs after PSV activity as shown in Part 5. There is a well-defined single peak in cross-correlation probability, shown in Part 2, indicating that the lag time between PSV and AE shows little variability. The linear regression between cumulative number of AE and PSV events is also high, as shown in Part 4.

During Stage 1 there is an increase in the AE event rate, however the AE events are relatively small as expected with this loading stage and there is little to no PSV activity. As there was little to no PSV activity the a cross-correlation was not calculated.

In Stage 2 there is little to no AE or PSV activity, with the exception of a single high magnitude event at ~0.95×10^{-3} mm/mm in the AE and at ~0.98×10^{-3} mm/mm in the PSV. The AE event rate is lower than the previous stage, the cross-correlation probability is high and AE activity precedes PSV activity.

There is a simultaneous increase in both the AE and PSV amplitude, at the beginning of Stage 3. The frequency of both the AE and PSV events increase until the end of the stage. The magnitude of the events is consistent at the beginning of the stage and then begins to noticeably increase from ~1.676×10^{-3} mm/mm for the AE and PSV. The cross-correlation probability is high, with AE activity preceding PSV.

During Stage 4 the pattern from the previous stage initially continues, before a clear increase in both the frequency and magnitude of both the AE and PSV events, from ~1.94×10^{-3} mm/mm is detected. The cross-correlation probability is high and PSV precedes AE activity.

The PSV events rate is high throughout Stage 5, however the AE event rate begins to decrease. The highest frequency and magnitude of the AE and PSV events are observed during this stage and the cross-correlation probability is high, with PSV preceding AE activity.

6.2.6 Air dried syenogranite RTD experimental results summary

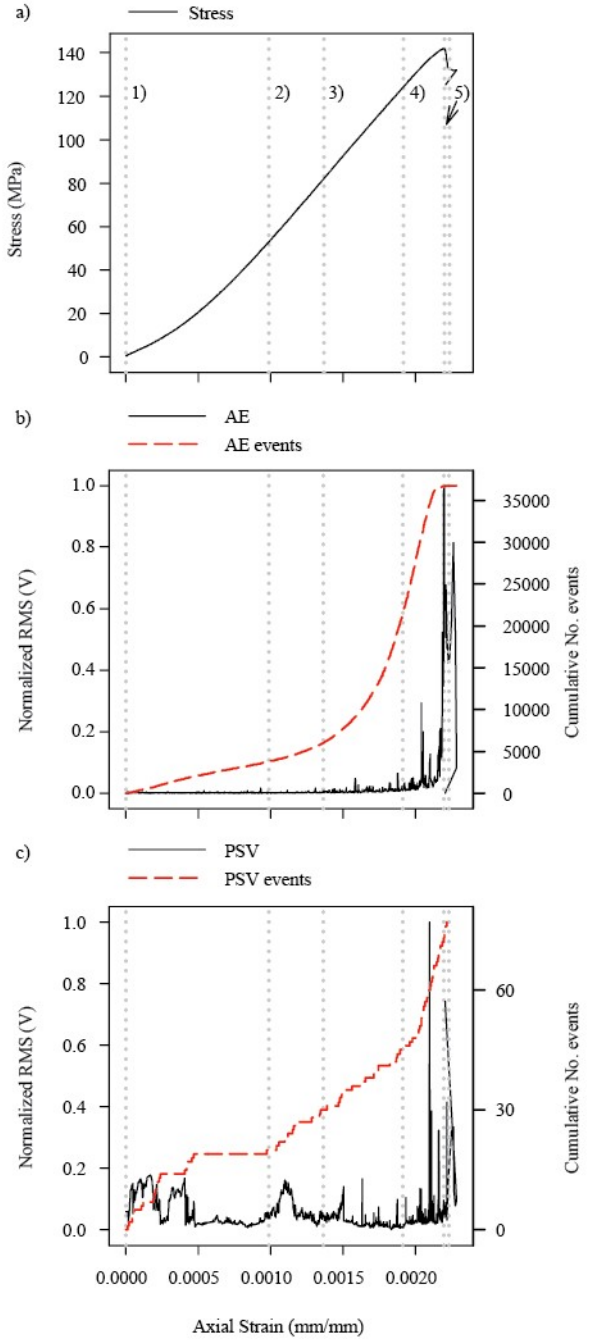

Part 1 – Strain based RTD loading data: *a) applied stress; b) normalized piezoelectric transducer RMS voltage and cumulative number of AE events; and c) normalized PSV RMS voltage and cumulative number of PSV events. Loading stages 1 to 5 are defined in chapter 5.5.*

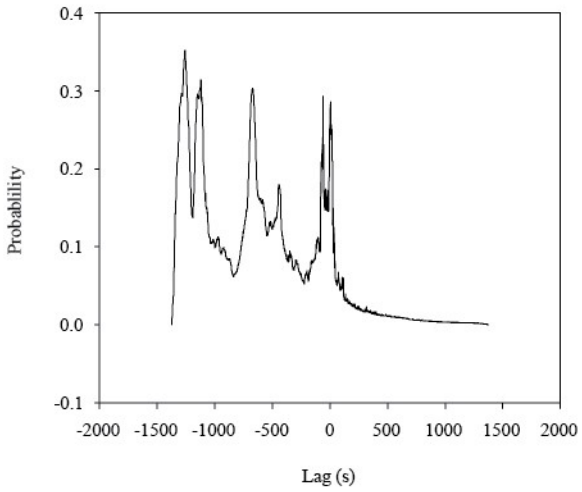

Part 2 – Overall cross-correlation: *Probability of correlation between PSV and AE events at varying lag times. A positive lag time indicates PSV lags behind AE and negative lag time indicates AE lags behind PSV.*

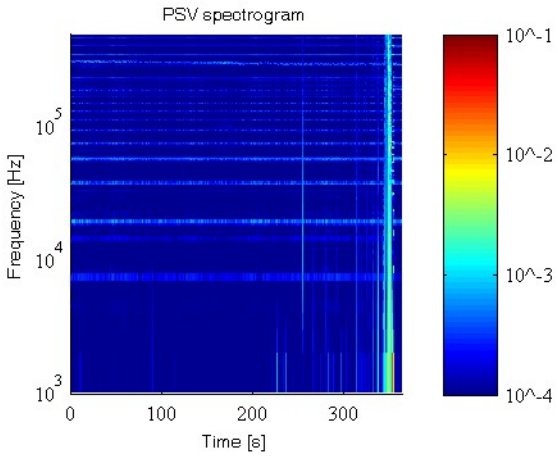

Part 3 - PSV ***spectral density.***

Linear regression	$r^2 = 0.89$
Max Strength	141.78 MPa
Average PSV amplitude	1.4 mV
Average AE amplitude	68.67 dB

Part 4 – loading and statistical data: *The linear regression r^2 is computed between cumulative PSV and AE events.*

Cross-correlation between PSV and AE events						
Loading stage	1	2	3	4	5	Entire test
Coefficient	0.66	0.72	0.56	0.58	0.672	0.28
Lag time (s)	-0.75	-0.25	-12.75	9	0	4

Part 5 – cross-correlation data: *A negative lag time indicates AE events lag behind PSV events and a positive lag time indicates PSV events lag behind AE events at the maximum probability of correlation (coefficient).*

Figure 6-4 Air dried syenogranite results summary. *Part 1) strain based stress, PSV and AE plot; Part 2) overall cross-correlation plot; Part 3) PSV spectrogram; Part 4) experimental data; Part 5) cross-correlation results per stage of loading.*

The uniaxial RTD loading data for an air dried syenogranite specimen is shown in Figure 6-4. The applied stress, AE event amplitude, cumulative number of AE events, PSV event amplitude and cumulative number of PSV events with respect to axial strain, is shown in Part 1 of the figure. The PSV spectrogram in Part 3 shows little to no PEPS throughout the experiment, however high amplitude TEPS events happen prior to failure after ~220 s. Whereas, the oven dried experiment (Figure 6-3) had greater PEPS and TEPS activity. The maximum cross-correlation probability is not valid, as the associated lag time lies outside of the excepted range of ±15 s, thus the maximum probability within the expected range was selected. The resulting cross-correlation probability is low, compared to the oven dried (Figure 6-3) and water saturated (Figure 6-5) experiments, with AE occurring before PSV activity. There is not a well-defined single peak in cross-correlation probability, indicating that there is a lot of variance in the cross-correlation. However, the linear regression between cumulative number of AE and PSV events is high, as shown in Part 4.

In Stage 1 there is only low amplitude AE activity and a small in increase in AE event rate. There is an increase in PSV amplitude and event rate until ~$0.5x10^{-3}$ mm/mm, after which there is little to no activity. The cross-correlation probability is high during this stage, with PSV activity preceding AE activity.

The trend continues in Stage 2, as AE activity remains low in amplitude and the event rate remains steady. However, at the onset of the stage there is a sharp increase in PSV event rate and amplitude fluctuations. The cross-correlation probability is highest during this stage, with AE events lagging PSV activity.

During Stage 3, the AE event rate increases in an exponential like manor and there is an increase in event amplitude. PSV activity increases in amplitude and so do the number of spikes in activity, although the PSV event rate remains almost constant. The cross-correlation probability is lower than the previous stages, with PSV occurring before AE activity

The AE events rate is high during Stage 4 and there are high amplitude spikes in activity, although the event rate decreases towards the end of the stage. The PSV event rate and amplitude increases during the stage. The cross-correlation coefficient is similar to the previous loading stage, with PSV activity occurring after AE activity.

Stage 5 occurs over a short time frame, however a number of high magnitude AE and PSV events were observed before failure. The AE event rate declines to a much lower rate, whereas the PSV event rate remains high. The cross-correlation probability is high during this stage, with AE and PSV events occurring simultaneously.

6.2.7 Water saturated syenogranite RTD experimental results summary

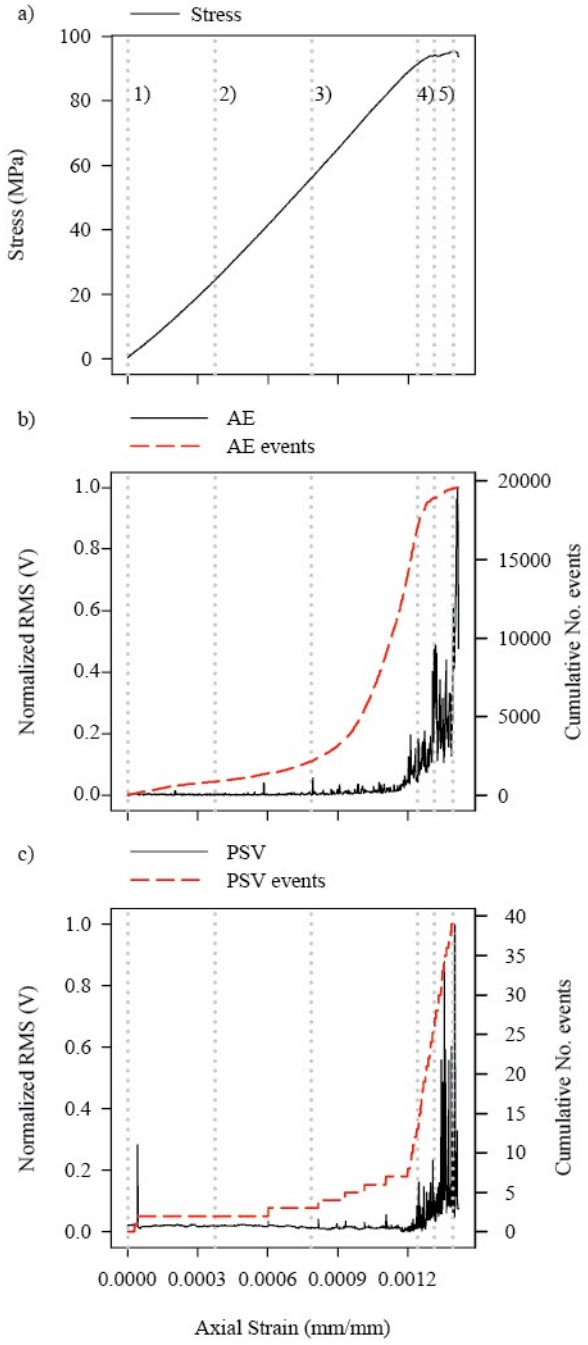

Part 1 – Strain based RTD loading data: *a) applied stress; b) normalized piezoelectric transducer RMS voltage and cumulative number of AE events; and c) normalized PSV RMS voltage and cumulative number of PSV events. Loading stages 1 to 5 are defined in chapter 5.5.*

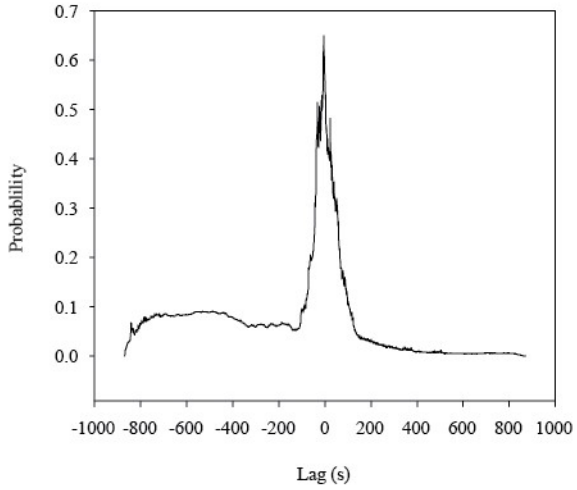

Part 2 – Overall cross-correlation: *Probability of correlation between PSV and AE events at varying lag times. A positive lag time indicates PSV lags behind AE and negative lag time indicates AE lags behind PSV.*

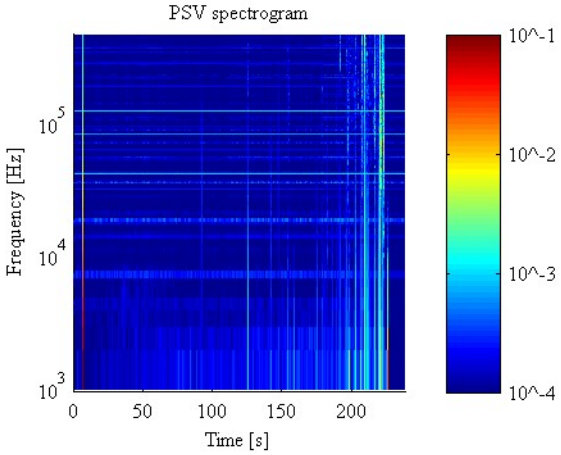

Part 3 – PSV spectral density.

Linear regression	$r^2 = 0.79$
Max Strength	95.32 MPa
Average PSV amplitude	1.56 mV
Average AE amplitude	65.43 dB

Part 4 – loading and statistical data: *The linear regression r^2 is computed between cumulative PSV and AE events.*

Cross-correlation between PSV and AE events						
Loading stage	1	2	3	4	5	Entire test
Coefficient	0.70	0.6564	0.55	0.78	0.63	0.65
Lag time (s)	1.75	0	1	-1	-0.5	5.75

Part 5 – cross-correlation data: *A negative lag time indicates AE events lag behind PSV events and a positive lag time indicates PSV events lag behind AE events at the maximum probability of correlation (coefficient).*

Figure 6-5 Water saturated syenogranite results summary. *Part 1) strain based stress, PSV and AE plot; Part 2) overall cross-correlation; Part 3) PSV spectrogram; Part 4) experimental data; Part 5) cross-correlation results per stage of loading.*

The uniaxial RTD loading data for a water saturated syenogranite specimen is shown in Figure 6-5. The applied stress, AE event amplitude, cumulative number of AE events, PSV event amplitude and cumulative number of PSV events, with respect to axial strain, is shown in Part 1 of the figure. The PSV spectrogram in Part 3, shows little to no PEPS activity throughout the experiment. However, TEPS events occur after ~120 s and their frequency and amplitude increases as failure approaches. There is more TEPS activity compared to the air dried experiment (Figure 6-4). PSV occurs after AE activity and there is a single peak in cross-correlation probability, indicating there is little variance. The overall cross-correlation data is similar to the oven dried experiment (Figure 6-3) and has a better correlation coefficient than the air dried experiment. The linear regression r^2 value between cumulative number of AE and PSV events is high as shown in Part 4.

The PSV and AE amplitude are relatively low during Stage 1 of loading, apart from a single PSV event. The AE event rate increases slightly and the cross-correlation probability is high during this stage, with PSV activity lagging behind AE activity.

The PSV and AE amplitude remains low during Stage 2, apart from a single AE at event at ~$0.6x10^{-3}$ mm/mm, after which the AE and PSV event rate begins to increase. The AE-PSV cross-correlation is high, however the coefficient is lower than the previous stage and PSV occurs simultaneously.

During Stage 3, there is a surge in AE event rate and the amplitude of events begins to increase. The PSV event amplitude increases, with multiple spikes occurring throughout the stage and the PSV event rate is almost constant. The cross-correlation between AE and PSV activity is weakest during this stage and PSV activity lags AE activity.

The AE event rate begins to decline during Sage 4. However, just before Stage 4 commences, there is a sharp increase in PSV event rate, which remains consistent throughout the stage. The cross-correlation probability is highest during this stage, with PSV occurring before AE activity.

The largest amplitude PSV and AE events happen in the final stage of loading, before material failure. The AE event rate continues to decrease during this stage, however the PSV event rate remains high. The cross-correlation probability is high and PSV activity precedes AE activity.

6.2.8 Oven dried sandstone RTD experimental results summary

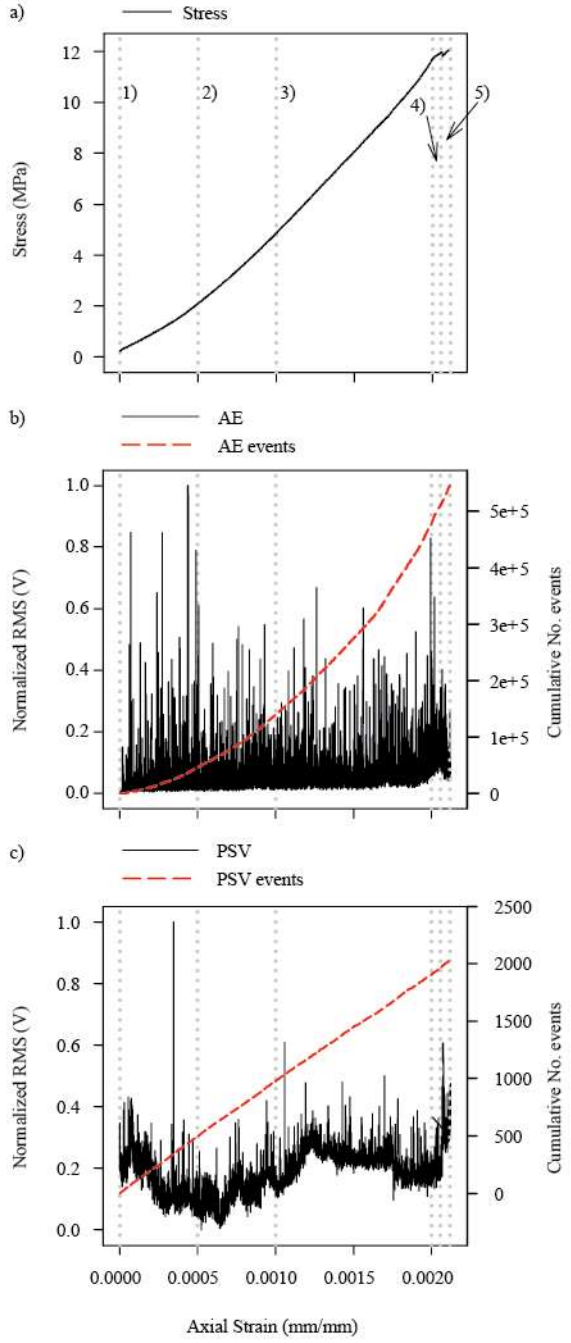

Part 1 – Strain based RTD loading data: *a) applied stress; b) normalized piezoelectric transducer RMS voltage and cumulative number of AE events; and c) normalized PSV RMS voltage and cumulative number of PSV events. Loading stages 1 to 5 are defined in chapter 5.5.*

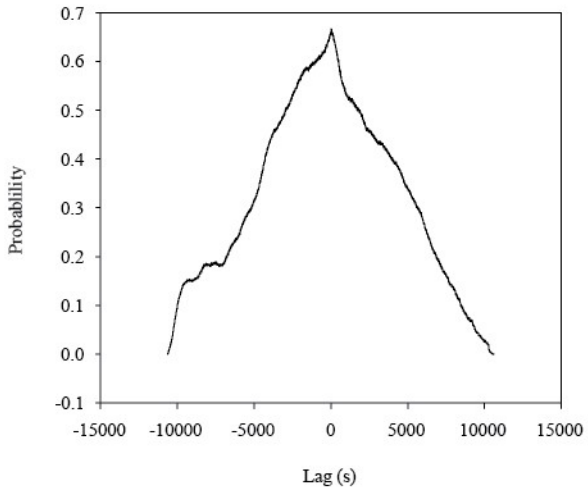

Part 2 – Overall cross-correlation: *Probability of correlation between PSV and AE events at varying lag times. A positive lag time indicates PSV lags behind AE and negative lag time indicates AE lags behind PSV.*

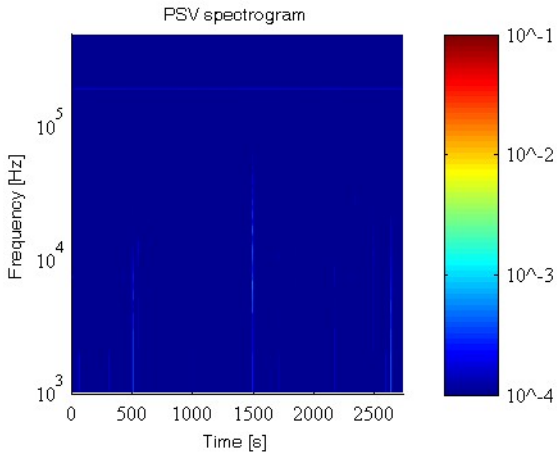

Part 3 – PSV spectral density.

Linear regression	$r^2 = 0.95$
Max Strength	12.10 MPa
Average PSV amplitude	0.43 mV
Average AE amplitude	88.44 dB

Part 4 – loading and statistical data: *The linear regression r^2 is computed between cumulative PSV and AE events.*

	Cross-correlation between PSV and AE events					
Loading stage	1	2	3	4	5	Entire test
Coefficient	0.4334	0.65	0.73	0.89	0.84	0.67
Lag time (s)	4	7	-4	0	2	5.75

Part 5 – cross-correlation data: *A negative lag time indicates AE events lag behind PSV events and a positive lag time indicates PSV events lag behind AE events at the maximum probability of correlation (coefficient).*

Figure 6-6 Oven dried sandstone results summary. *Part 1) strain based stress, PSV and AE plot; Part 2) overall cross-correlation plot; Part 3) PSV spectrogram; Part 4) experimental data; Part 5) cross-correlation results per stage of loading.*

The uniaxial RTD loading data for an oven dried sandstone specimen, is shown in Figure 6-6. The applied stress, AE event amplitude, cumulative number of AE events, PSV event amplitude and cumulative number of PSV events, with respect to axial strain, is shown in Part 1 of the figure. The PSV spectrogram in Part 3 shows little to no PEPS, however there are some low amplitude TEPS over the course of the experiment. The cross-correlation probability is higher than the air dried (Figure 6-7) and water saturated (Figure 6-8) experiments and AE occurs before PSV activity; there is a single peak in probability indicating little variance. The linear regression between cumulative number of AE and PSV events is also high, as shown in Part 4.

There is AE and PSV activity during Stage 1, the baseline PSV amplitude peaks at the start of the stage and subsequently reduces in amplitude. There is a single high amplitude PSV event and the largest amplitude AE events occur during this stage. The AE event rate increases, however the PSV event rate remains almost constant over the course of the stage. The cross-correlation probability is lowest during this stage, with AE preceding PSV activity.

The AE events rate continues to increase over Stage 2 and the PSV event rate remains consistent. There is PSV and AE activity throughout the stage and the cross-correlation probability high, with PSV activity lagging AE activity.

During Stage 3 there is AE and PSV activity throughout, as with the previous stages, however there is an increase in the baseline PSV amplitude. The AE event rate continues to increase and the PSV event rate remains almost constant. The cross-correlation probability is high and PSV occurs before AE activity.

In Stage 4 the AE and PSV activity is continually active and there is a surge in AE baseline amplitude. The AE event rate continues to increase, whilst the PSV event rate remains constant. The cross-correlation probability is highest during this stage and AE and PSV occur simultaneously.

A surge in PSV amplitude occurs during Stage 5 of loading and the AE events remain high in amplitude. The AE event rate increases up to material failure, whilst the PSV remains steady. The cross-correlation probability is high, as with the previous stage and PSV activity occurs after AE activity.

6.2.9 Air dried sandstone RTD experimental results summary

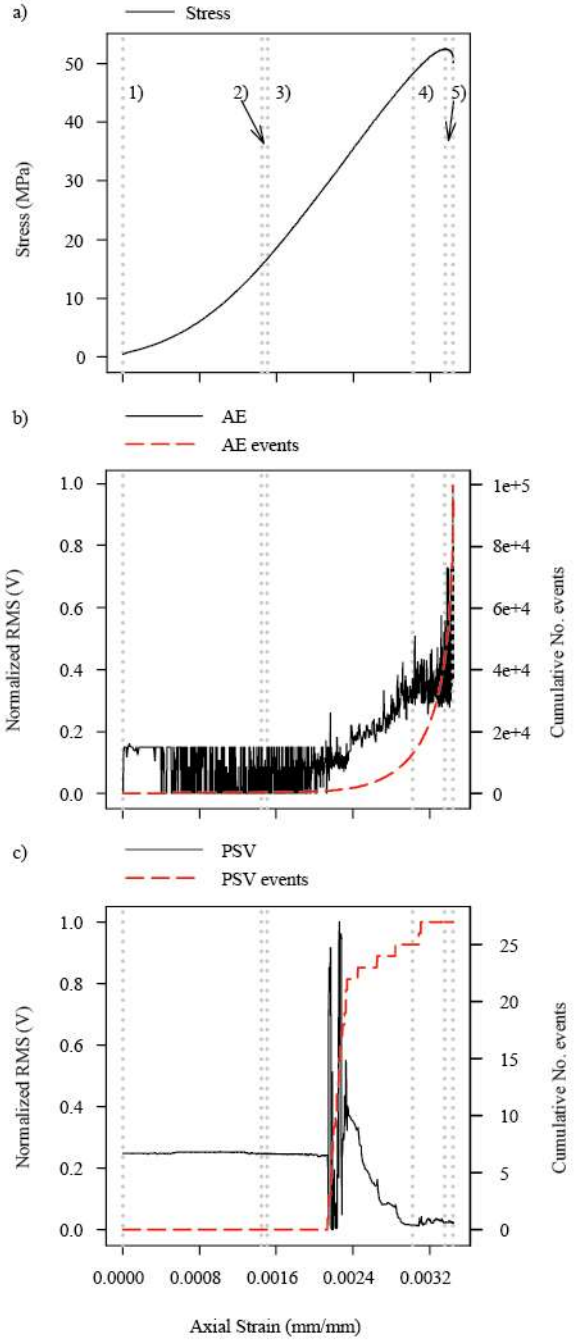

Part 1 – Strain based RTD loading data: *a) applied stress; b) normalized piezoelectric transducer RMS voltage and cumulative number of AE events; and c) normalized PSV RMS voltage and cumulative number of PSV events. Loading stages 1 to 5 are defined in chapter 5.5.*

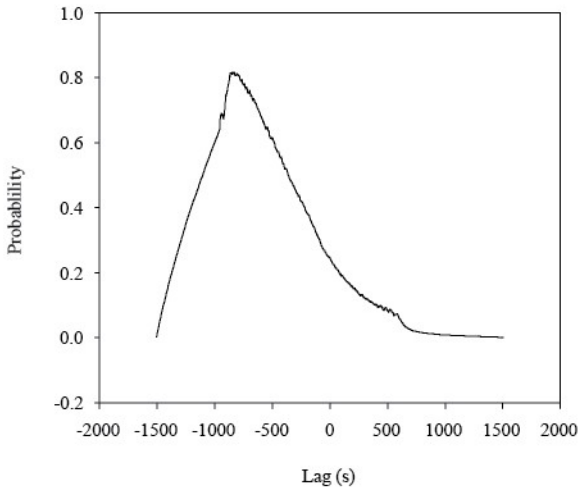

Part 2 – Overall cross-correlation: *Probability of correlation between PSV and AE events at varying lag times. A positive lag time indicates PSV lags behind AE and negative lag time indicates AE lags behind PSV.*

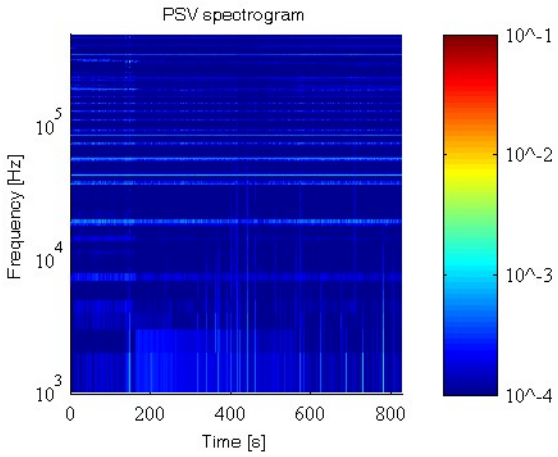

Part 3 - Time frequency PSV data.

Linear regression	$r^2 = 0.54$
Max Strength	52.42 MPa
Average PSV amplitude	1.026 mV
Average AE amplitude	62.86 dB

Part 4 – loading and statistical data: *The linear regression r^2 is computed between cumulative PSV and AE events.*

	Cross-correlation between PSV and AE events					
Loading stage	1	2	3	4	5	Entire test
Coefficient	0.71	0.52	0.66	0.96	0.96	0.27
Lag time (s)	-0.25	0	-15	0	0	-15

Part 5 – cross-correlation data: *A negative lag time indicates AE events lag behind PSV events and a positive lag time indicates PSV events lag behind AE events at the maximum probability of correlation (coefficient).*

Figure 6-7 Air dried sandstone results summary. *Part 1) strain based stress, PSV and AE plot; Part 2) overall cross-correlation plot; Part 3) PSV spectrogram; Part 4) experimental data; Part 5) cross-correlation results per stage of loading.*

The uniaxial RTD loading data for an air dried sandstone specimen is shown in Figure 6-7. The applied stress, AE event amplitude, cumulative number of AE events, PSV event amplitude and cumulative number of PSV events, with respect to axial strain, is shown in Part 1 of the figure. The PSV spectrogram in Part 3 shows little to no PEPS, however there are more TEPS events compared to the oven dried experiment (Figure 6-6). The cross-correlation peak in probability is not valid, as the peak probability occurs out of the expected lag time window of ±15 s, thus the closest valid maximum probability was used for analysis. The resulting cross-correlation probability is low compared to the oven dried (Figure 6-6) and saline saturated (Figure 6-9) experiments and PSV precedes AE activity. The linear regression between PSV and AE cumulative events is low, as shown in Part 4.

During Stages 1 and 2 there is little to no PSV activity and only low amplitude AE activity. The cross-correlation probability is high for Stage 1 and AE lags PSV activity. The correlation is lower for Stage 2 and AE and PSV activity occur simultaneously.

The trend continues during the initial part of Stage 3, however at ~$2.1x10^{-3}$ mm/mm begins an exponential like increase in AE event rate and the baseline amplitude increases throughout the stage. At the same point (~$2.1x10^{-3}$ mm/mm), there is a spike in PSV amplitude and event rate, momentarily up until ~$2.3x10^{-3}$ mm/mm, after which the amplitude and event rate reduces for the rest of the stage. The cross-correlation probability is high and PSV activity occurs before AE activity.

The AE amplitude continues to increase throughout Stage 4 and the event rate continues on its exponential like increase. The PSV amplitude continues to decrease to a level lower than its initial amplitude at the start of the experiment and the event rate gradually reduces. The cross-correlation probability is highest during this stage and PSV and AE activity occur simultaneously.

During Stage 5 the AE amplitude increases in amplitude and the event rate is very high before failure occurs. The PSV amplitude remains constant and low in amplitude, negative in comparison to the initial PSV amplitude at the start of the experiment and the event rate is very low. The cross-correlation probability is highest during this stage and the previous stage, with PSV and AE events occur simultaneously.

6.2.10 Water saturated sandstone RTD experimental results summary

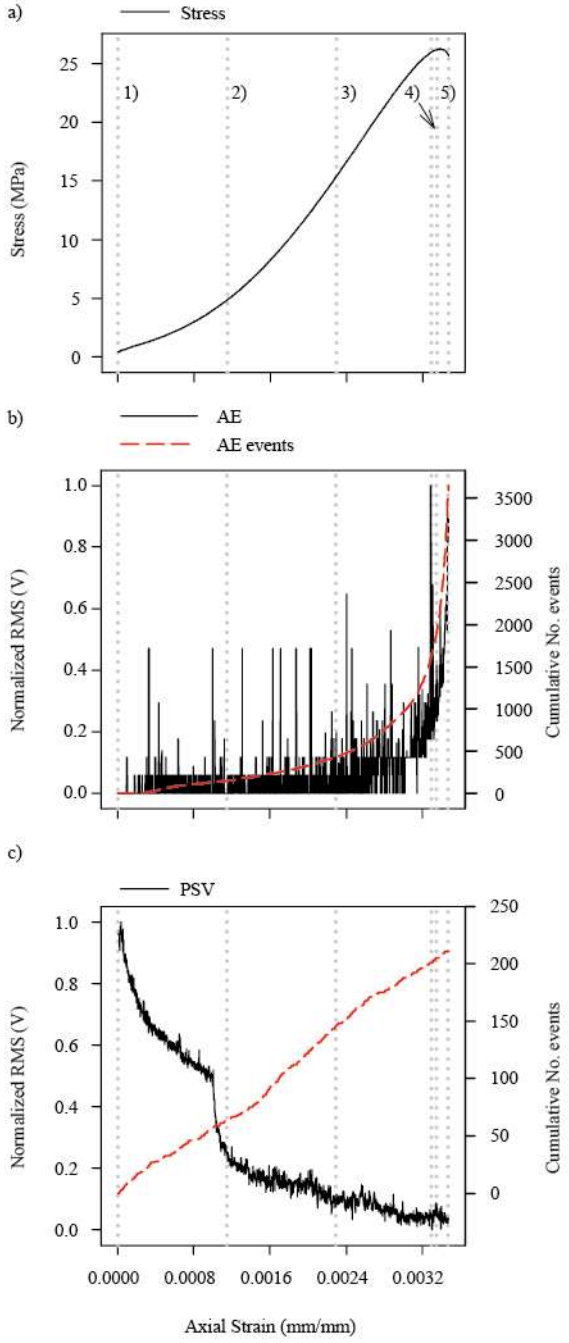

Part 1 – Strain based RTD loading data: *a) applied stress; b) normalized piezoelectric transducer RMS voltage and cumulative number of AE events; and c) normalized PSV RMS voltage and cumulative number of PSV events. Loading stages 1 to 5 are defined in chapter 5.5.*

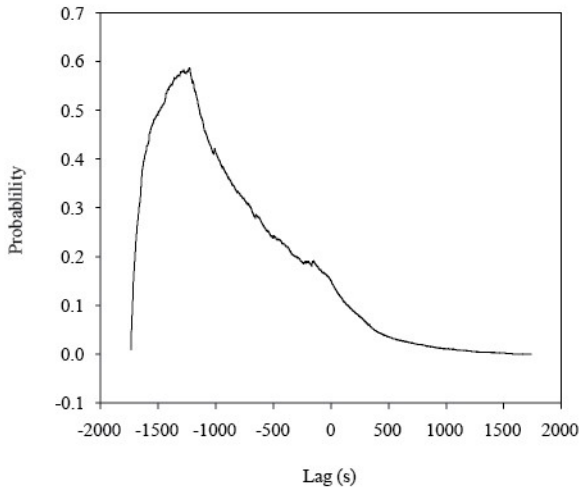

Part 2 – Overall cross-correlation: *Probability of correlation between PSV and AE events at varying lag times. A positive lag time indicates PSV lags behind AE and negative lag time indicates AE lags behind PSV.*

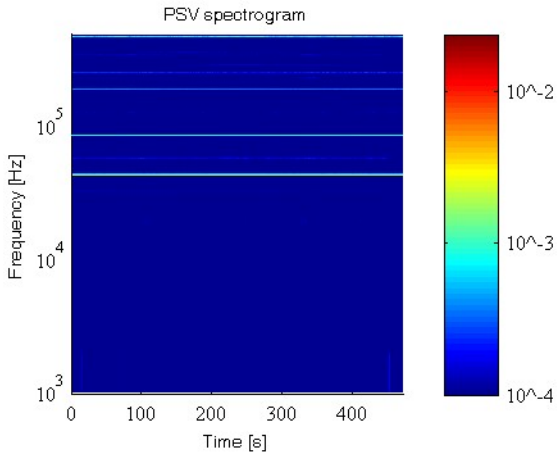

Part 3 – PSV spectrogram

Linear regression	$r^2 = 0.65$
Max Strength	26.24 MPa
Average PSV amplitude	1.36 mV
Average AE amplitude	47.53 dB

Part 4 – loading and statistical data: *The linear regression r^2 is computed between cumulative PSV and AE events.*

Cross-correlation between PSV and AE events						
Loading stage	1	2	3	4	5	Entire test
Coefficient	0.35	0.51	0.45	0.61	0.86	0.17
Lag time (s)	-11.5	-1	-3.75	-13.75	0	-15

Part 5 – cross-correlation data: *A negative lag time indicates AE events lag behind PSV events and a positive lag time indicates PSV events lag behind AE events at the maximum probability of correlation (coefficient).*

Figure 6-8 Water saturated sandstone results summary. *Part 1) strain based stress, PSV and AE plot; Part 2) overall cross-correlation plot; Part 3) PSV spectrogram; Part 4) experimental data; Part 5) cross-correlation results per stage of loading.*

The uniaxial RTD loading data for a water saturated sandstone specimen, is shown in Figure 6-8. The applied stress, AE event amplitude, cumulative number of AE events, PSV event amplitude and cumulative number of PSV events, with respect to axial strain, is shown in Part 1 of the figure. The PSV spectrogram in Part 3 shows little to no PEPS or TEPS activity compared to the oven dried (Figure 6-6) and air dried (Figure 6-7) experiments. The cross-correlation peak in probability is not valid, as the peak probability occurs out of the expected lag time window of ±15 s; the maximum probability within the expected range was selected for analysis. The resulting cross-correlation probability is lowest out of all of the sandstone experiments and PSV precedes AE activity. The linear regression between PSV and AE cumulative events is high, as shown in Part 4.

During Stage 1 there is an increase in AE event rate and there is AE activity throughout the stage. The PSV amplitude decreases up to ~0.11×10^{-3} mm/mm, after which the amplitude decreases at a higher rate and the event rate is constant. The cross-correlation probability is lowest during this stage and PSV precedes AE activity.

The AE event rate continues to increase during Stage 2 and there is AE activity throughout with multiple higher amplitude AE events. The PSV amplitude continues to decrease at a constant rate and the PSV remains steady. The cross-correlation probability is higher than the previous stage and PSV occurs before AE activity.

Over Stage 3 there is a surge in AE event rate and the baseline amplitude begins to increase in the latter half of the stage. The PSV amplitude continues to decrease and the PSV event rate remains constant. The cross-correlation probability is low, with PSV occurring before AE activity.

Throughout Stage 4 and 5 the AE event rate continues to increase and there is a surge in AE event amplitude. The PSV amplitude continues to decrease and the event rate remains stable. The probability of correlation for Stage 4, is higher than the previous stages and PSV precedes AE activity. The cross-correlation probability for Stage 5, is the highest and PSV and AE occur simultaneously.

6.2.11 Saline saturated sandstone RTD experimental results summary

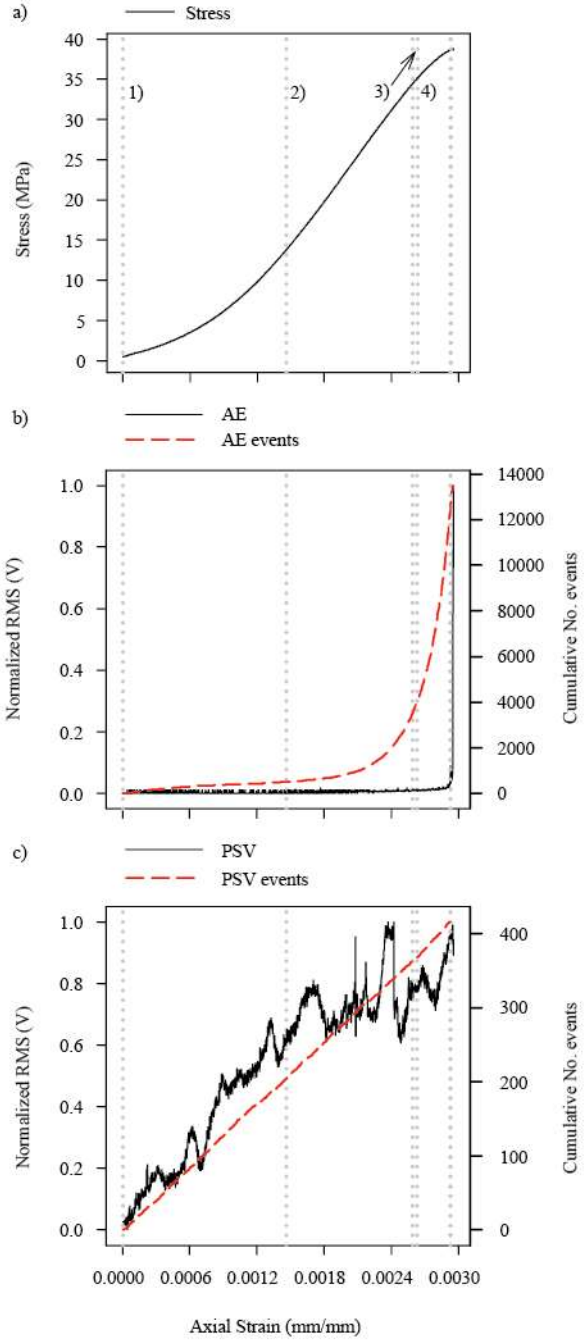

Part 1 – Strain based RTD loading data: *a) applied stress; b) normalized piezoelectric transducer RMS voltage and cumulative number of AE events; and c) normalized PSV RMS voltage and cumulative number of PSV events. Loading stages 1 to 5 are defined in chapter 5.5.*

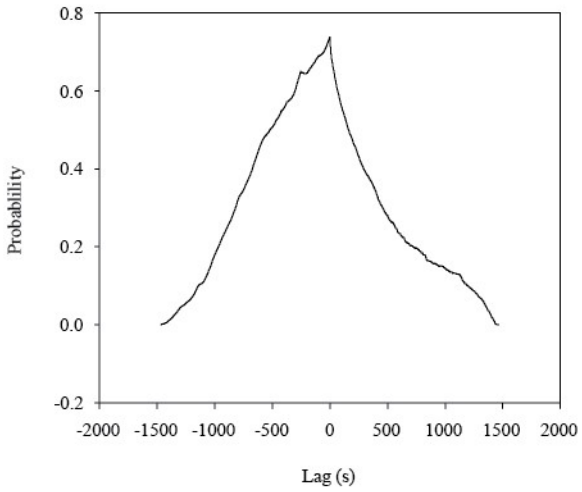

Part 2 – Overall cross-correlation: *Probability of correlation between PSV and AE events at varying lag times. A positive lag time indicates PSV lags behind AE and negative lag time indicates AE lags behind PSV.*

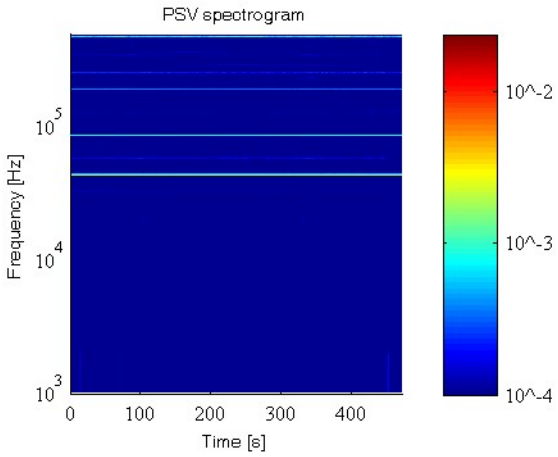

Part 3 – PSV spectral density.

Linear regression	$r^2 = 0.49$
Max Strength	38.78 MPa
Average PSV amplitude	0.92 mV
Average AE amplitude	53.591 dB

Part 4 – loading and statistical data: *The linear regression r^2 is computed between cumulative PSV and AE events.*

Cross-correlation between PSV and AE events						
Loading stage	1	2	3	4	5	Entire test
Coefficient	0.65	0.48	0.85	0.96	Stage	0.74
Lag time (s)	7.75	0.25	-0.25	0	undefined	0

Part 5 – cross-correlation data: *A negative lag time indicates AE events lag behind PSV events and a positive lag time indicates PSV events lag behind AE events at the maximum probability of correlation (coefficient).*

Figure 6-9 Saline saturated sandstone results summary. *Part 1) strain based stress, PSV and AE plot; Part 2) overall cross-correlation plot; Part 3) PSV spectrogram; Part 4) experimental data; Part 5) cross-correlation results per stage of loading.*

The uniaxial RTD loading data for a saline saturated sandstone specimen is shown in Figure 6-9. The applied stress, AE event amplitude, cumulative number of AE events, PSV event amplitude and cumulative number of PSV events, with respect to axial strain, is shown in Part 1 of the figure. The PSV spectrogram in Part 3 shows little to no PEPS or TEPS activity, as with the water saturated experiment (Figure 6-8). The maximum cross-correlation probability is the highest out of the sandstone experiments, with PSV and AE activity occurring simultaneously. However, there is some variability in the cross-correlation, as shown in part 2. The linear regression between PSV and AE cumulative events is low, as shown in Part 4.

During Stage 1 there is low amplitude AE activity and the AE event rate begins to increase; the PSV amplitude increases during the stage and the event rate is constant. The cross-correlation probability is high and PSV occurs after AE activity.

The AE event rate begins to increase in an exponential like fashion throughout Stage 2 and the amplitude remains low. The PSV amplitude continues to increase at a slower rate and there is more variation in its amplitude; the PSV event rate remains constant. The cross-correlation probability is lower than the previous stage and AE occurs before PSV activity.

Over Stages 3 and 4 the AE event rate continues to increase and there are relatively low amplitude AE events, apart from one high amplitude event prior to material failure. The PSV amplitude increases up to the failure occurrence, however the events rate remains almost constant. The cross-correlation probability is high for Stage 3, but Stage 4 has the highest correlation. PSV occurs before AE in Stage 3 and PSV and AE occur simultaneously in Stage 4.

Stage 5 is undefined for this experiment, because there is not a defined post peak stress region of the stress strain curve.

6.2.12 Oven dried granite RTD experimental results summary

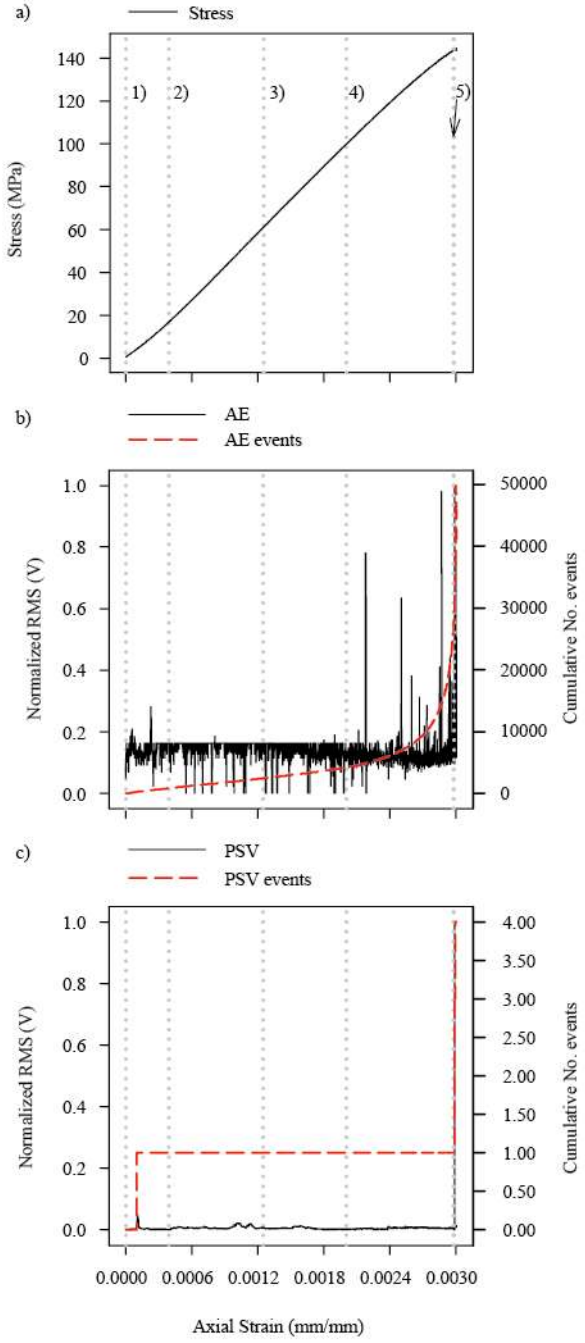

Part 1 – Strain based RTD loading data: *a) applied stress; b) normalized piezoelectric transducer RMS voltage and cumulative number of AE events; and c) normalized PSV RMS voltage and cumulative number of PSV events. Loading stages 1 to 5 are defined in chapter 5.5.*

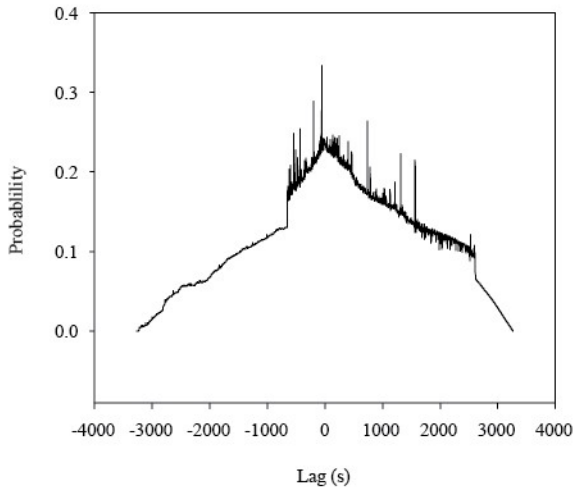

Part 2 – Overall cross-correlation: *Probability of correlation between PSV and AE events at varying lag times. A positive lag time indicates PSV lags behind AE and negative lag time indicates AE lags behind PSV.*

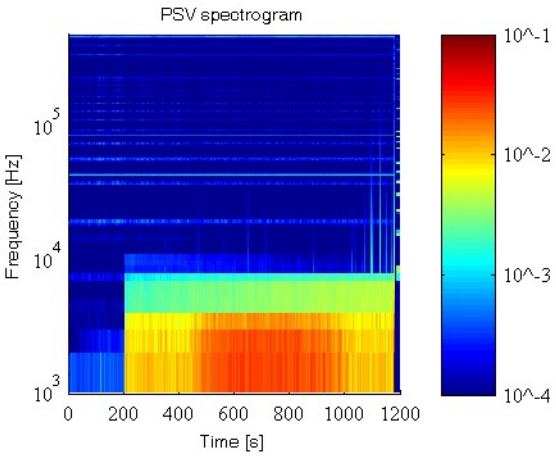

Part 3 – PSV spectral density.

Linear regression	r^2 = NA
Max Strength	144.29 MPa
Average PSV amplitude	0.59 mV
Average AE amplitude	41.09 dB

Part 4 – loading and statistical data: *The linear regression r^2 is computed between cumulative PSV and AE events.*

Cross-correlation between PSV and AE events						
Loading stage	1	2	3	4	5	Entire test
Coefficient	0.47	0.86	0.83	0.32	0.92	0.33
Lag time (s)	-11.75	0	-0.5	-14.75	0	-14.75

Part 5 – cross-correlation data: *A negative lag time indicates AE events lag behind PSV events and a positive lag time indicates PSV events lag behind AE events at the maximum probability of correlation (coefficient).*

Figure 6-10 Oven dried granite results summary. *Part 1) strain based stress, PSV and AE plot; Part 2) overall cross-correlation plot; Part 3) PSV spectrogram; Part 4) experimental data; Part 5) cross-correlation results per stage of loading.*

The uniaxial RTD loading data for an oven dried granite specimen is shown in Figure 6-10. The applied stress, AE event amplitude, cumulative number of AE events, PSV event amplitude and cumulative number of PSV events, with respect to axial strain, is shown in Part 1 of the figure. The PSV spectrogram in Part 3, shows a wide frequency band of high amplitude PEPS starting at ~200 s and distinct TEPS events after ~1000 s, prior to failure. There is much more activity in the PSV spectrogram compared to the water (Figure 6-11) and saline (Figure 6-12) saturated granite experiments. The maximum probability of correlation is not valid, as the lag time lies outside of the expected lag time range of ±15 s, as shown in Part 2; thus the next largest peak within the desired range was chosen. The resulting cross-correlation probability is highest out of the granite experiments and PSV occurs before AE activity. There were not enough detectable PSV events for an accurate linear regression, between cumulative PSV and AE events.

There is an increase in AE event rate and the event amplitude is relatively low during Stage 1 and there is little to no PSV activity, apart from a single event occurring at ~$0.2x10^{-3}$ mm/mm. The cross-correlation probability is low, with PSV occurring before AE events.

During Stage 2 and 3 there is little to no PSV activity and there are relatively low amplitude AE events throughout the stage. The AE event rate remains almost constant and the cross-correlation probability is high for both stages; PSV and AE activity occur simultaneously for Stage 2 and PSV occurs before AE activity for Stage 3.

The AE event rate begins to increase in an exponential like manor and there are relatively high amplitude AE events over the course of Stage 4. The PSV amplitude remains low, as with the previous stages and the event rate is also low. The cross-correlation probability is lowest during this stage and PSV occurs before AE activity.

Over Stage 5 the AE and PSV event rate is very high and the highest amplitude PSV and AE events occur prior to failure. The cross-correlation probability is highest during this stage and AE and PSV events occur simultaneously.

6.2.13 Water saturated granite RTD experimental results summary

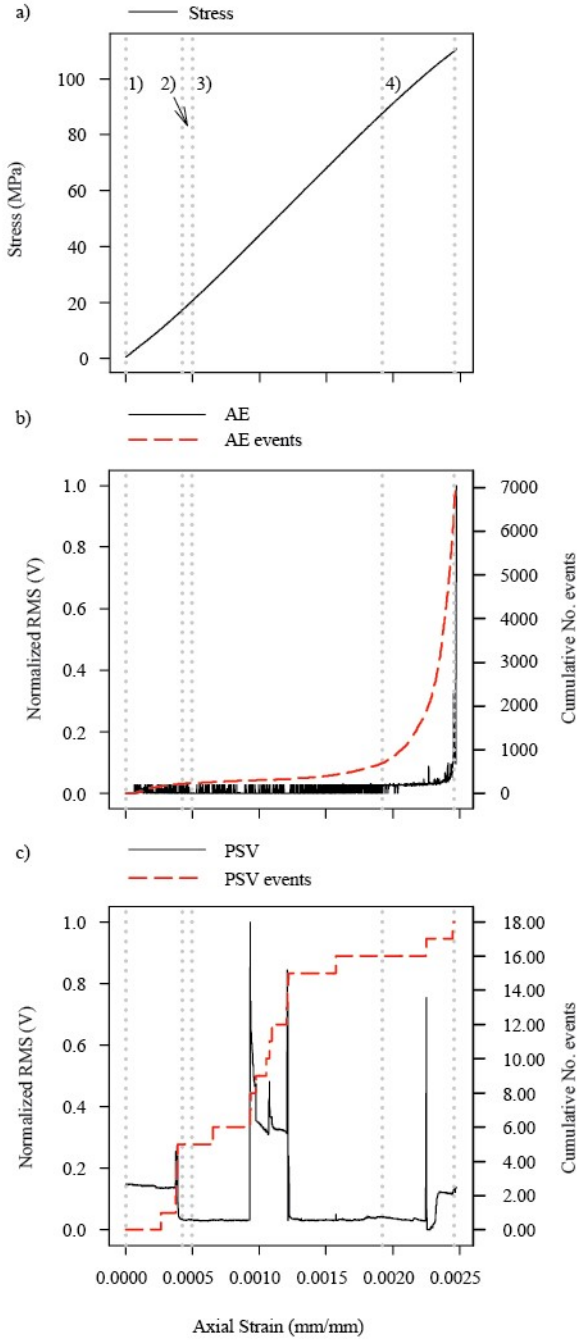

Part 1 – Strain based RTD loading data: *a) applied stress; b) normalized piezoelectric transducer RMS voltage and cumulative number of AE events; and c) normalized PSV RMS voltage and cumulative number of PSV events. Loading stages 1 to 5 are defined in chapter 5.5.*

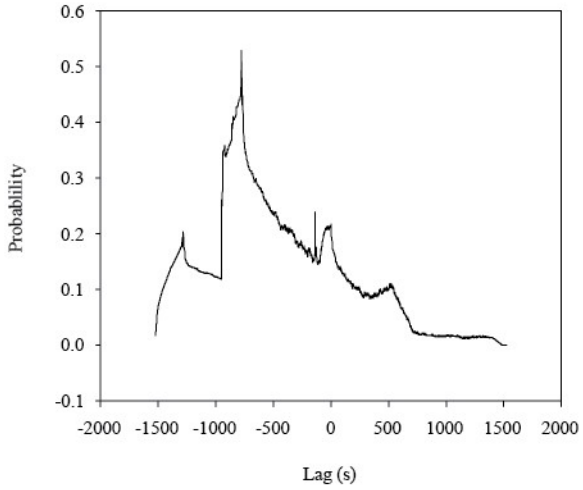

Part 2 – Overall cross-correlation: *Probability of correlation between PSV and AE events at varying lag times. A positive lag time indicates PSV lags behind AE and negative lag time indicates AE lags behind PSV.*

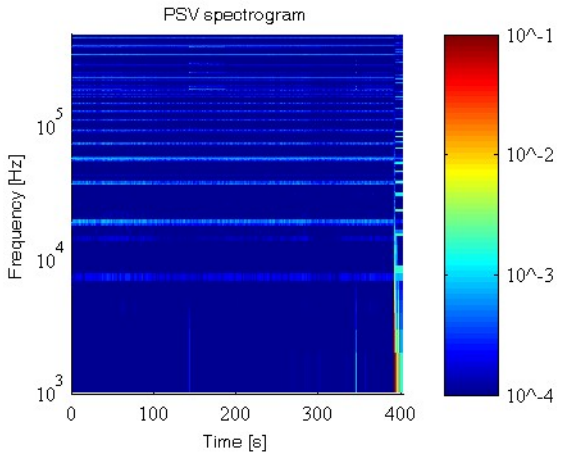

Part 3 – PSV spectral density.

Linear regression	$r^2 = 0.24$
Max Strength	110.73 MPa
Average PSV amplitude	0.96 mV
Average AE amplitude	33.17 dB

Part 4 – loading and statistical data: *The linear regression r^2 is computed between cumulative PSV and AE events.*

Cross-correlation between PSV and AE events						
Loading stage	1	2	3	4	5	Entire test
Coefficient	0.60	0.43	0.25	0.70	Stage	0.28
Lag time (s)	0.75	-1.5	-14.25	0	undefined	-6.5

Part 5 – cross-correlation data: *A negative lag time indicates AE events lag behind PSV events and a positive lag time indicates PSV events lag behind AE events at the maximum probability of correlation (coefficient).*

Figure 6-11 Water saturated granite results summary. *Part 1) strain based stress, PSV and AE plot; Part 2) overall cross-correlation plot; Part 3) PSV spectrogram; Part 4) experimental data; Part 5) cross-correlation results per stage of loading.*

The uniaxial RTD loading data for a water saturated granite specimen is shown in Figure 6-11. The applied stress, AE event amplitude, cumulative number of AE events, PSV event amplitude and cumulative number of PSV events with respect to axial strain, is shown in Part 1 of the figure. The PSV spectrogram in Part 3 shows little to no PEPS or TEPS, apart from prominent high amplitude TEPS events prior to failure (~400 s). There is considerably less activity in the PSV spectrogram, compared to the oven dried experiment (Figure 6-10). The maximum probability of correlation is not valid, as the lag time lies outside of the expected lag time range of ±15 s, as shown in Part 2; thus, the next largest peak within the desired range was chosen. The resulting cross-correlation probability is lower than the oven dried specimen (Figure 6-10) and PSV occurs before AE activity. The linear regression between cumulative AE and PSV events is also low, as shown in Part 4.

During Stage 1 and 2 there is an increase in AE event rate and relatively low amplitude AE events occur. The PSV amplitude remains almost constant, apart from a positive spike in amplitude at the end of Stage 1, after which the amplitude drops down to a lower value for the duration of Stage 2. The cross-correlation probability is high and AE events occurred before PSV activity for Stage 1; the cross-correlation probability is lower for Stage 2 and PSV events occurred before AE events.

The AE event amplitude stays relatively low as with the previous stages, however the event rate begins to increase after ~$1.2x10^{-3}$ mm/mm, during Stage 3. The PSV amplitude remains at a low amplitude for the duration of the stage, apart from between ~$0.9x10^{-3}$ mm/mm to ~$1.3x10^{-3}$ mm/mm, in which there is a relatively large increase in PSV amplitude. The cross-correlation probability is low, with PSV activity occurring before AE activity.

The AE event rate continues to increase over Stage 4, in an exponential like manor up until failure occurs and the baseline amplitude increases towards the failure occurrence. The PSV event amplitude remains low at the beginning of the stage, at ~$2.25x10^{-3}$ mm/mm there is a relatively large spike in PSV, followed by a more gradual increase up until failure. The cross-correlation probability is highest during this stage and PSV and AE activity occurs simultaneously.

Stage 5 is undefined, because there is no post stress peak region for the stress strain curve.

6.2.14 Saline saturated granite RTD experimental results summary

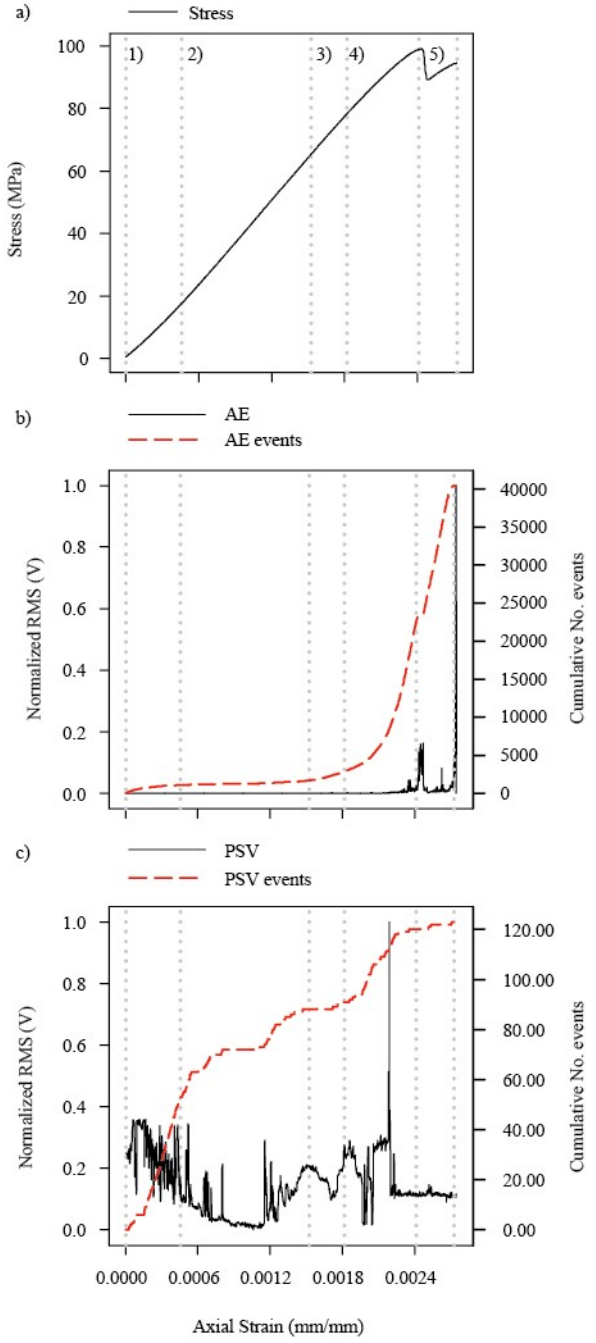

Part 1 – Strain based RTD loading data: *a) applied stress; b) normalized piezoelectric transducer RMS voltage and cumulative number of AE events; and c) normalized PSV RMS voltage and cumulative number of PSV events. Loading stages 1 to 5 are defined in chapter 5.5.*

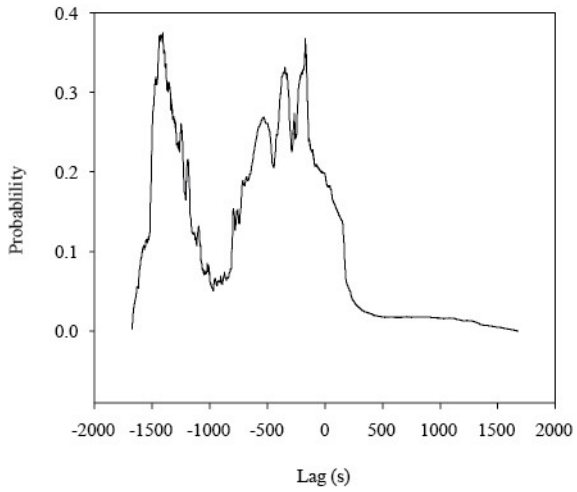

Part 2 – Overall cross-correlation: *Probability of correlation between PSV and AE events at varying lag times. A positive lag time indicates PSV lags behind AE and negative lag time indicates AE lags behind PSV.*

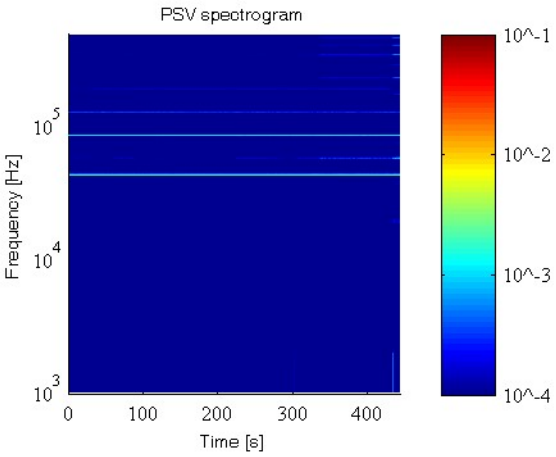

Part 3 – PSV spectral density.

Linear regression	$r^2 = 0.41$
Max Strength	99.04 MPa
Average PSV amplitude	0.75 mV
Average AE amplitude	64.63 dB

Part 4 – loading and statistical data: *The linear regression r^2 is computed between cumulative PSV and AE events.*

Cross-correlation between PSV and AE events						
Loading stage	1	2	3	4	5	Entire test
Coefficient	0.92	0.55	0.81	0.41	0.56	0.21
Lag time (s)	0	-4	-0.25	-14.25	0	-13.25

Part 5 – cross-correlation data: *A negative lag time indicates AE events lag behind PSV events and a positive lag time indicates PSV events lag behind AE events at the maximum probability of correlation (coefficient).*

Figure 6-12 Saline saturated granite results summary. *Part 1) strain based stress, PSV and AE plot; Part 2) overall cross-correlation plot; Part 3) PSV spectrogram; Part 4) experimental data; Part 5) cross-correlation results per stage of loading.*

The uniaxial RTD loading data for a saline saturated granite specimen is shown in Figure 6-12. The applied stress, AE event amplitude, cumulative number of AE events, PSV event amplitude and cumulative number of PSV events with respect to axial strain, is shown in Part 1 of the figure. The PSV spectrogram in Part 3, shows little to no PEPS or TEPS compared to the oven dried experiment (Figure 6-10). The maximum cross-correlation probability is the lowest out of the granite experiments and PSV occurs before AE activity. The cross-correlation plot does not have a single peak in probability, thus there is variation in the lag time, as shown in Part 2. The linear regression between cumulative AE and PSV events is low as shown in Part 4.

In Stage 1, there are relatively low amplitude AE events but the AE event rate increases. The PSV amplitude shows variation and decreases in amplitude over the course of the stage and the event rate is high. The cross-correlation probability is highest during this stage and PSV and AE activity occur simultaneously.

The PSV amplitude and event rate continues to decrease in Stage 2 up to ~1.1×10^{-3} mm/mm, after which the amplitude and event rate begins to increase up the end of the stage and there is variation in the PSV amplitude. The AE activity follows a similar trend to the previous stage, with the amplitude and rate remaining low. The cross-correlation probability is lower than the previous stage and PSV precedes AE activity.

During Stage 3 the PSV amplitude increases, although there is a lot of variation and the event rate is low. The AE event rate begins to increase in an exponential like manor, however the AE event amplitude remains relatively low. The cross-correlation probability is high, with PSV activity occurring before AE events.

Over Stage 4 the AE event rate increases rapidly and then becomes almost constant, towards the end of the stage there is a surge in amplitude. The PSV shows variation and increases in amplitude and event rate up to ~2.1×10^{-3} mm/mm, after which the amplitude and event rate drops. The cross-correlation probability is lowest during this stage and PSV activity occurs before AE events.

The final stage shows PSV activity remaining at a low amplitude and the event rate shows much less variation compared to the previous stages. The AE event rate remains constant and there is a surge in AE event amplitude prior to the failure occurrence. The cross-correlation probability is higher than the previous stage and AE and PSV activity occur simultaneously.

6.2.15 Oven dried marble RTD experimental results summary

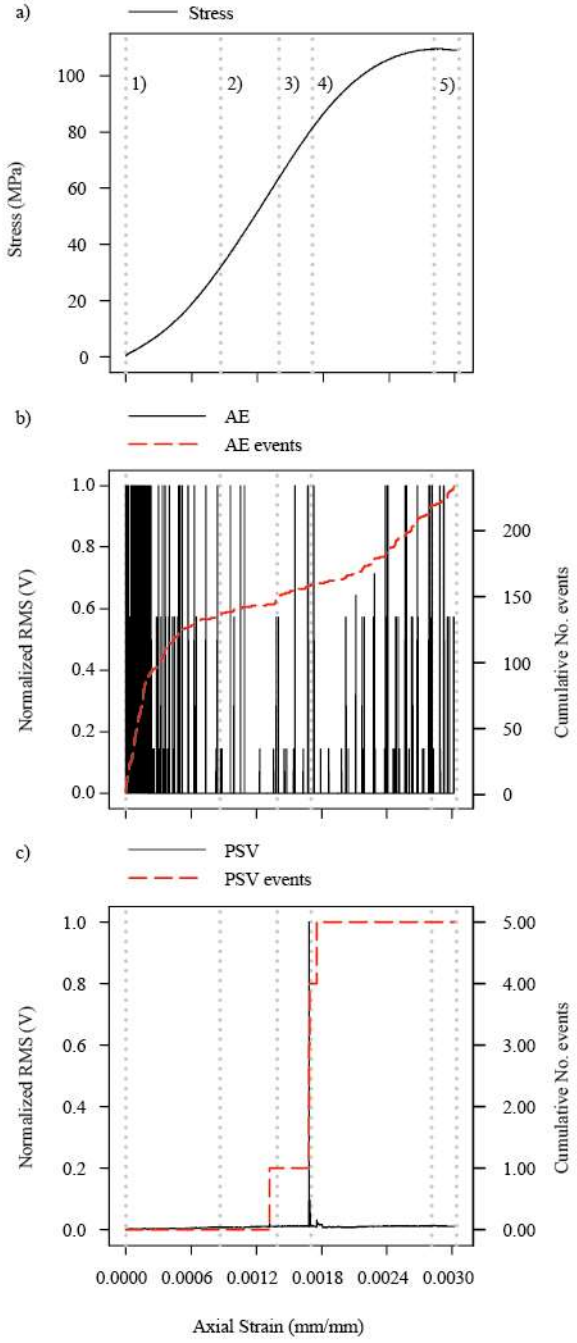

Part 1 – Strain based RTD loading data: *a) applied stress; b) normalized piezoelectric transducer RMS voltage and cumulative number of AE events; and c) normalized PSV RMS voltage and cumulative number of PSV events. Loading stages 1 to 5 are defined in chapter 5.5.*

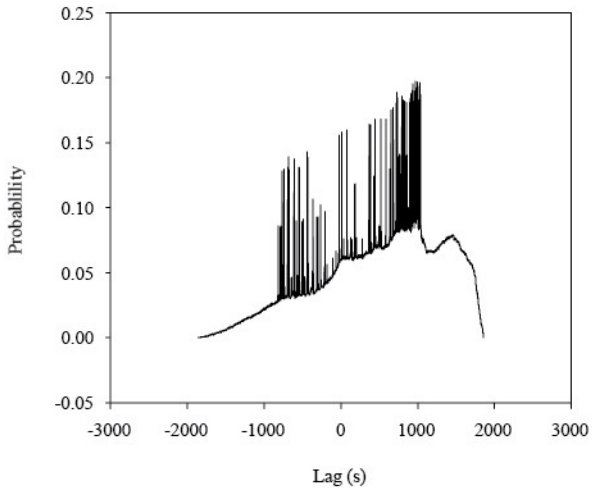

Part 2 – Overall cross-correlation: *Probability of correlation between PSV and AE events at varying lag times. A positive lag time indicates PSV lags behind AE and negative lag time indicates AE lags behind PSV.*

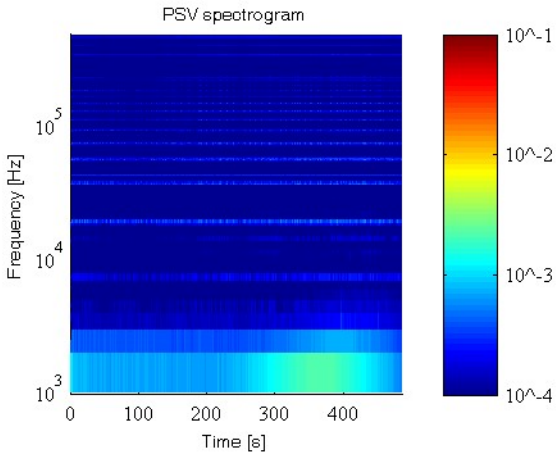

Part 3 – PSV spectral density.

Linear regression	r^2 = NA
Max Strength	109.42 MPa
Average PSV amplitude	0.47 mV
Average AE amplitude	5.72 dB

Part 4 – loading and statistical data: *The linear regression r^2 is computed between cumulative PSV and AE events.*

Cross-correlation between PSV and AE events						
Loading stage	1	2	3	4	5	Entire test
Coefficient	0.26	0.13	0.61	0.22	0.25	0.16
Lag time (s)	9.25	14.5	1.75	-3.25	0	1.75

Part 5 – cross-correlation data: *A negative lag time indicates AE events lag behind PSV events and a positive lag time indicates PSV events lag behind AE events at the maximum probability of correlation (coefficient).*

Figure 6-13 Oven dried marble results summary. *Part 1) strain based stress, PSV and AE plot; Part 2) overall cross-correlation plot; Part 3) PSV spectrogram; Part 4) experimental data; Part 5) cross-correlation results per stage of loading.*

The uniaxial RTD loading data for an oven dried marble specimen is shown in Figure 6-13. The applied stress, AE event amplitude, cumulative number of AE events, PSV event amplitude and cumulative number of PSV events with respect to axial strain, is shown in Part 1 of the figure. The PSV spectrogram in Part 3, shows a wide frequency band of low amplitude PEPS; its amplitude increases between 300 s and 400 s. The maximum cross-correlation probability lies outside of the expected lag time range of ±15 s, thus a valid maximum probability was chosen within the range for analysis. The chosen cross-correlation probability is the lowest out of all of the marble experiments and AE events occur before PSV activity. There were not enough detectable PSV events for a valid linear regression, between cumulative number of PSV and AE events.

Throughout Stages 1, 2 and 3 there are AE events and little to no PSV activity. The frequency of the AE events increases during Stage 1 and subsequently reduces during Stage 2 and 3. The cross-correlation is lowest during Stage 2, Stage 1 is higher and Stage 3 has the highest correlation coefficient. In all stages PSV activity lags behind AE events.

At the onset of Stage 4 there is a relatively large amplitude PSV event, after which the PSV amplitude reduces back to its baseline level, as observed in the previous stages. There are AE events occurring almost simultaneously with the PSV event and the AE event rate increases during this stage. The cross-correlation probability is low, with PSV activity occurring before AE events.

During Stage 5 the AE event rate is high and there are numerous AE events and little to no PSV activity is observed. The cross-correlation probability is low with AE and PSV activity occurring simultaneously.

6.2.16 Air dried marble RTD experimental results summary

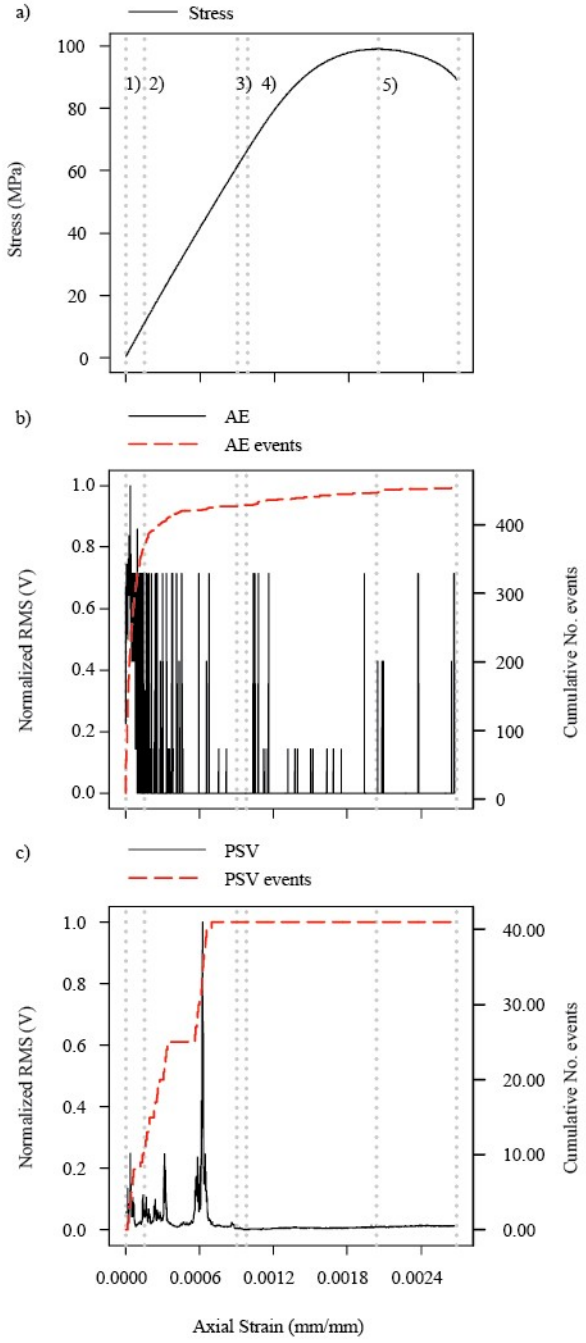

Part 1 – Strain based RTD loading data: *a) applied stress; b) normalized piezoelectric transducer RMS voltage and cumulative number of AE events; and c) normalized PSV RMS voltage and cumulative number of PSV events. Loading stages 1 to 5 are defined in chapter 5.5.*

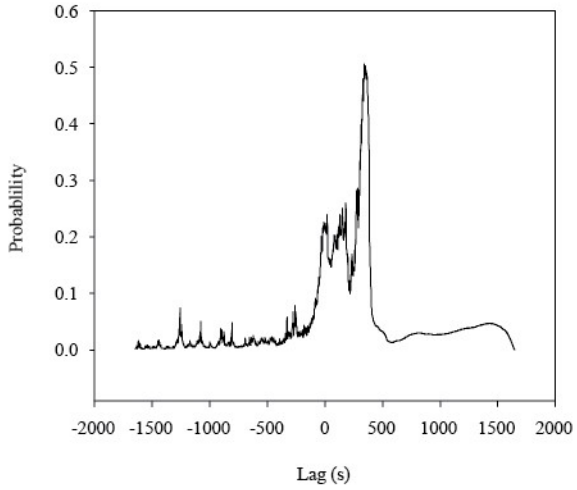

Part 2 – Overall cross-correlation: *Probability of correlation between PSV and AE events at varying lag times. A positive lag time indicates PSV lags behind AE and negative lag time indicates AE lags behind PSV.*

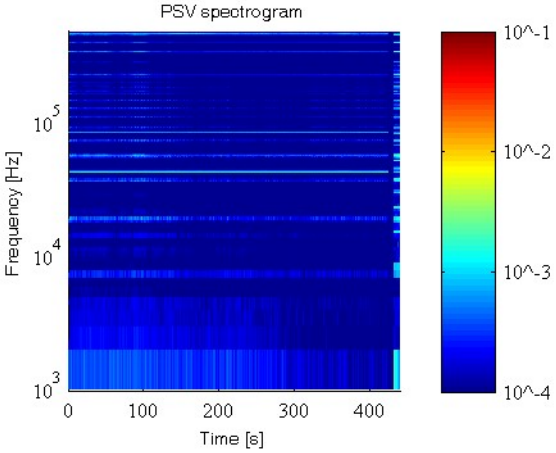

Part 3 – PSV spectral density.

Linear regression	$r^2 = 0.65$
Max Strength	99.13 MPa
Average PSV amplitude	0.69 mV
Average AE amplitude	6.15 dB

Part 4 – loading and statistical data: *The linear regression r^2 is computed between cumulative PSV and AE events.*

Cross-correlation between PSV and AE events						
Loading stage	1	2	3	4	5	Entire test
Coefficient	0.75	0.1762	0.18	0.10	0.11	0.2415
Lag time (s)	0.75	4.75	7.25	8.75	-1	4.75

Part 5 – cross-correlation data: *A negative lag time indicates AE events lag behind PSV events and a positive lag time indicates PSV events lag behind AE events at the maximum probability of correlation (coefficient).*

Figure 6-14 Air dried marble results summary. *Part 1) strain based stress, PSV and AE plot; Part 2) overall cross-correlation plot; Part 3) PSV spectrogram; Part 4) experimental data; Part 5) cross-correlation results per stage of loading.*

The uniaxial RTD loading data for an air dried marble specimen is shown in Figure 6-14. The applied stress, AE event amplitude, cumulative number of AE events, PSV event amplitude and cumulative number of PSV events with respect to axial strain, is shown in Part 1 of the figure. The PSV spectrogram in Part 3 shows low amplitude PEPS throughout and low amplitude TEPS prior to failure. The maximum probability of correlation is not valid, as the lag time lies outside of the expected lag time range of ±15 s, as shown in Part 2, thus the next largest peak within the desired range is chosen. The resulting cross-correlation probability is lower than the water (Figure 6-15) and saline (Figure 6-16) saturated marble experiments and AE occurs before PSV activity. The linear regression for cumulative AE and PSV events is high.

Over the course of Stage 1 there is relatively low amplitude PSV activity and relatively large AE events. The AE and PSV event rate is high, in addition cross-correlation probability is highest during this stage and AE events occur before PSV activity.

There are multiple spikes in PSV activity during Stage 2 and high amplitude events occur at ~$0.6x10^{-3}$ mm/mm after which the PSV amplitude declines. The PSV event rate remains high throughout the stage, apart from a period of inactivity between ~$0.35x10^{-3}$ mm/mm to ~$0.5x10^{-3}$ mm/mm. The AE event rate reduces down to a lower rate and there are multiple relatively high amplitude AE events, throughout the stage up to ~$0.6x10^{-3}$ mm/mm, after which the amplitude and reduces. The cross-correlation probability is low, with AE events occurring before PSV events.

Little to no PSV or AE activity occurs during Stage 3 and the amplitudes and event rates are low. The cross-correlation probability is low, with AE events occurring before PSV activity.

During Stage 4 the AE event rate remains constant and relatively high in amplitude, AE events occur at the start of the stage followed by lower amplitude events. The PSV activity remains low throughout the stage, in terms of amplitude and event rate. The cross-correlation probability is lowest during this stage and AE events occurring before PSV activity.

Little to no PSV activity occurs over Stage 5, however there are multiple high amplitude AE events and the AE event rate remains constant. The cross-correlation probability is low, with PSV activity occurring before AE events.

6.2.17 Water saturated marble RTD experimental results summary

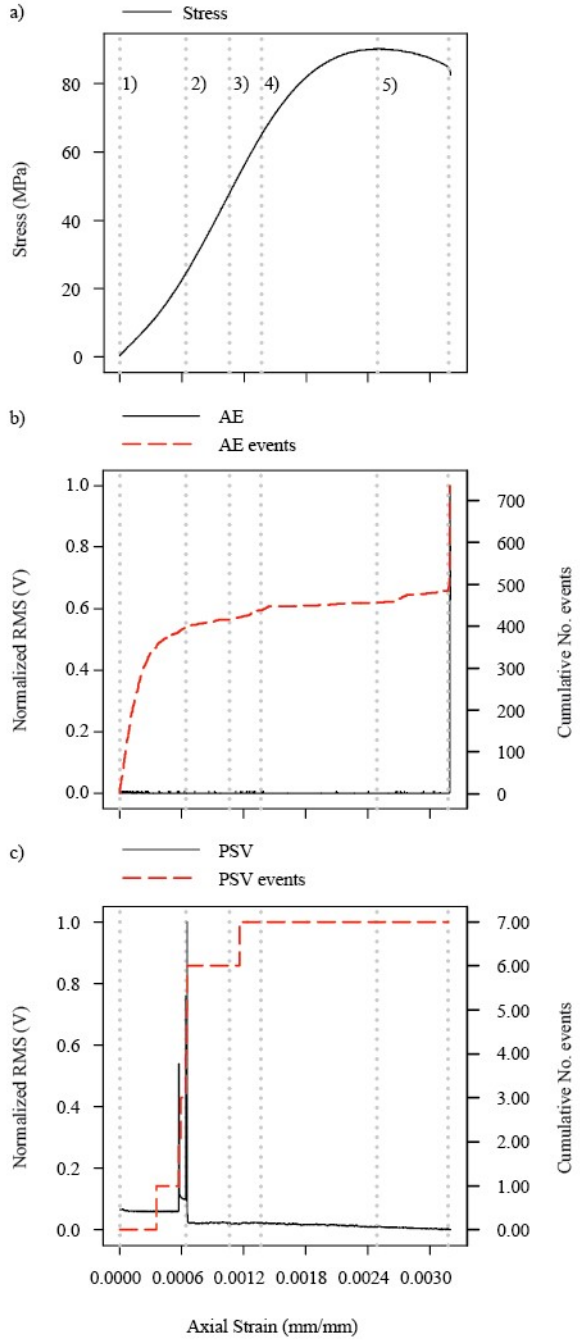

Part 1 – Strain based RTD loading data: *a) applied stress; b) normalized piezoelectric transducer RMS voltage and cumulative number of AE events; and c) normalized PSV RMS voltage and cumulative number of PSV events. Loading stages 1 to 5 are defined in chapter 5.5.*

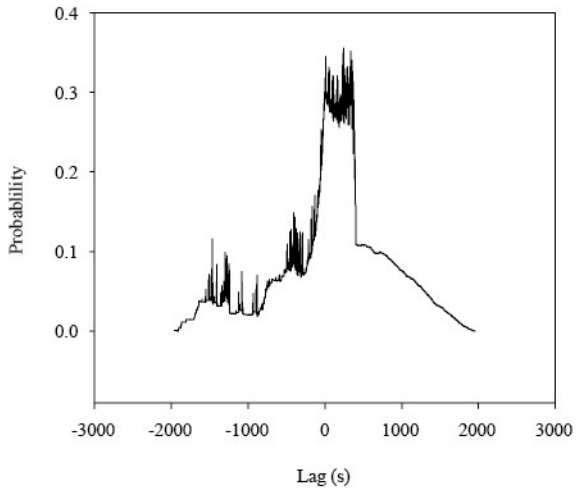

Part 2 – Overall cross-correlation: *Probability of correlation between PSV and AE events at varying lag times. A positive lag time indicates PSV lags behind AE and negative lag time indicates AE lags behind PSV.*

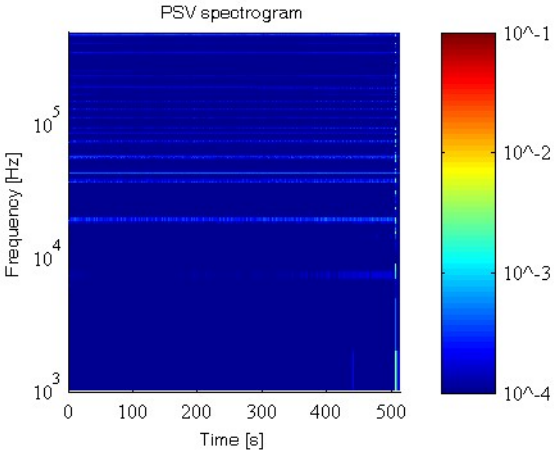

Part 3 – PSV spectral density.

Linear regression	r^2 = NA
Max Strength	90.12 MPa
Average PSV amplitude	0.64 mV
Average AE amplitude	11.53 dB

Part 4 – loading and statistical data: *The linear regression r^2 is computed between cumulative PSV and AE events.*

Cross-correlation between PSV and AE events						
Loading stage	1	2	3	4	5	Entire test
Coefficient	0.54	0.39	0.27	0.12	0.2033	0.3454
Lag time (s)	0	-11.75	3.5	4.75	-14.75	2.25

Part 5 – cross-correlation data: *A negative lag time indicates AE events lag behind PSV events and a positive lag time indicates PSV events lag behind AE events at the maximum probability of correlation (coefficient).*

Figure 6-15 Water saturated marble results summary. *Part 1) strain based stress, PSV and AE plot; Part 2) overall cross-correlation plot; Part 3) PSV spectrogram; Part 4) experimental data; Part 5) cross-correlation results per stage of loading.*

The uniaxial RTD loading data for a water saturated marble specimen is shown in Figure 6-15. The applied stress, AE event amplitude, cumulative number of AE events, PSV event amplitude and cumulative number of PSV events with respect to axial strain, is shown in Part 1 of the figure. The PSV spectrogram in Part 3, shows little to no PEPS or TEPS, apart from TEPS prior to failure at ~500 s. The PSV spectrogram shows less activity comparted to the oven dried (Figure 6-13) and air dried (Figure 6-14) specimens. The cross-correlation probability is higher than the oven and air dried marble experiments and AE occurs before PSV activity; the cross-correlation graph shows variability in the lag time, as shown in Part 2. There are only seven detected PSV events occurring at ~$0.6x10^{-3}$ mm/mm and thus no reliable linear regression value for cumulative AE and PSV events could be calculated.

During Stages 1 and 2 there is little to no PSV or AE activity, apart from high amplitude PSV events occurring at ~$0.6x10^{-3}$ mm/mm. However, the AE event rate increases during Stage 1 and then reduces to a lower rate, for the duration of Stage 2. The cross-correlation probability for Stage 1, is the highest compared to other the stages and AE and PSV occur simultaneously. For Stage 2 the probability is lower and AE events lag behind PSV activity.

Over Stages 3, 4 and 5 there is little no to PSV or AE activity, apart from a high amplitude AE event at the point of material failure. The AE event rate remains constant throughout the stages; however, the event rate becomes very high nearing the point of material failure. The cross-correlation probability for Stage 4, is the lowest followed by Stage 5 then Stage 3. AE events occur before PSV activity in Stages 3 and 4 and PSV activity occurs before AE events during Stage 5.

6.2.18 Saline saturated marble RTD experimental results summary

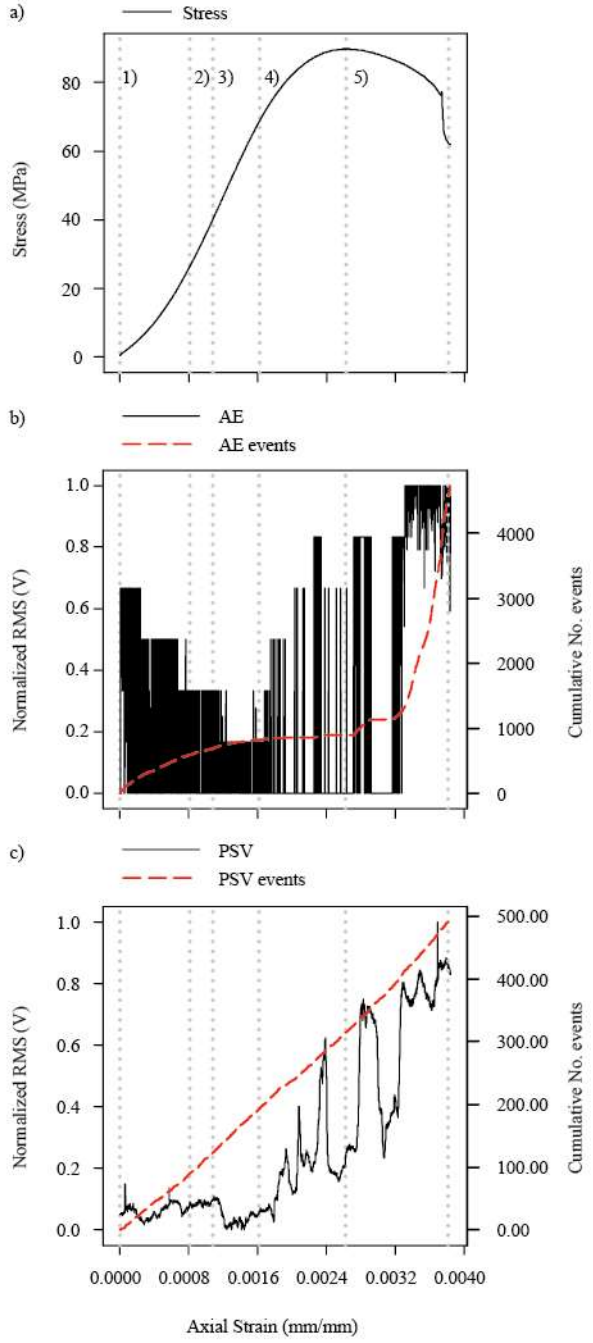

Part 1 – Strain based RTD loading data: *a) applied stress; b) normalized piezoelectric transducer RMS voltage and cumulative number of AE events; and c) normalized PSV RMS voltage and cumulative number of PSV events. Loading stages 1 to 5 are defined in chapter 5.5.*

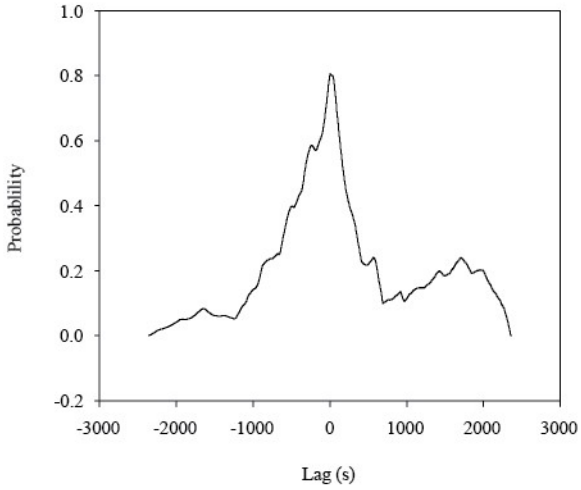

Part 2 – Overall cross-correlation: *Probability of correlation between PSV and AE events at varying lag times. A positive lag time indicates PSV lags behind AE and negative lag time indicates AE lags behind PSV.*

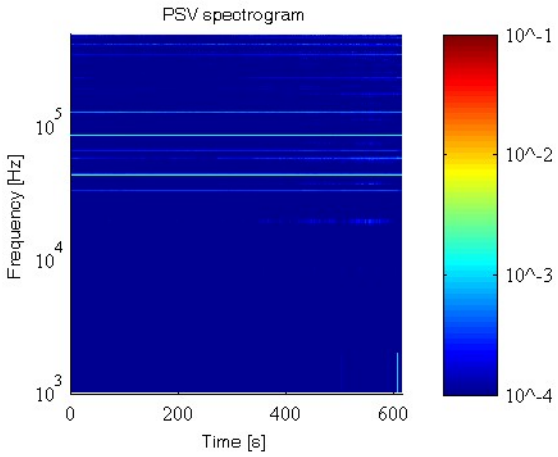

Part 3 – PSV spectral density.

Linear regression	$r^2 = 0.62$
Max Strength	89.69 MPa
Average PSV amplitude	2.40 mV
Average AE amplitude	9.51 dB

Part 4 – loading and statistical data: *The linear regression r^2 is computed between cumulative PSV and AE events.*

Cross-correlation between PSV and AE events						
Loading stage	1	2	3	4	5	Entire test
Coefficient	0.72	0.62	0.59	0.45	0.89	0.80
Lag time (s)	-0.25	-2	-0.5	8.75	0	0

Part 5 – cross-correlation data: *A negative lag time indicates AE events lag behind PSV events and a positive lag time indicates PSV events lag behind AE events at the maximum probability of correlation (coefficient).*

Figure 6-16 Saline saturated marble results summary. *Part 1) strain based stress, PSV and AE plot; Part 2) overall cross-correlation plot; Part 3) PSV spectrogram; Part 4) experimental data; Part 5) cross-correlation results per stage of loading.*

The uniaxial RTD loading data for a saline saturated marble specimen is shown in Figure 6-16. The applied stress, AE event amplitude, cumulative number of AE events, PSV event amplitude and cumulative number of PSV events with respect to axial strain, is shown in Part 1 of the figure. The PSV spectrogram in Part 3 shows little to no PEPS or TEPS compared to the oven (Figure 6-13) and air dried (Figure 6-14) specimens. The maximum probability of correlation is the highest out of the marble experiments and PSV and AE activity occur simultaneously. There is a single well defined peak in probability indicating little variance, as shown in Part 2. The linear regression between PSV and AE cumulative events is significant, as shown in Part 4.

Initially during Stage 1, there is an increase in AE event rate and there are relatively high amplitude AE events. The amplitude and event rates reduce towards the end of the stage and throughout Stages 2 and 3. The PSV amplitude remains relatively low throughout Stages 1, 2 and 3, although there is some variation in the PSV amplitude, in addition the PSV event rate remains constant throughout Stages 1, 2 and 3. The cross-correlation probability for Stage 1, is high and decreases over Stages 2 and 3; for all three stages PSV occurs before AE activity.

During Stages 4 and 5 the PSV and AE amplitudes increase up until the failure occurrence. There is a surge in AE event rate, at the onset of Stage 5 and the PSV event rate remains constant. The cross-correlation probability for Stage 4, is the lowest and AE events occur before PSV activity; for Stage 5 the probability is the highest and AE and PSV activity occur simultaneously.

6.2.19 Oven dried schist RTD experimental results summary

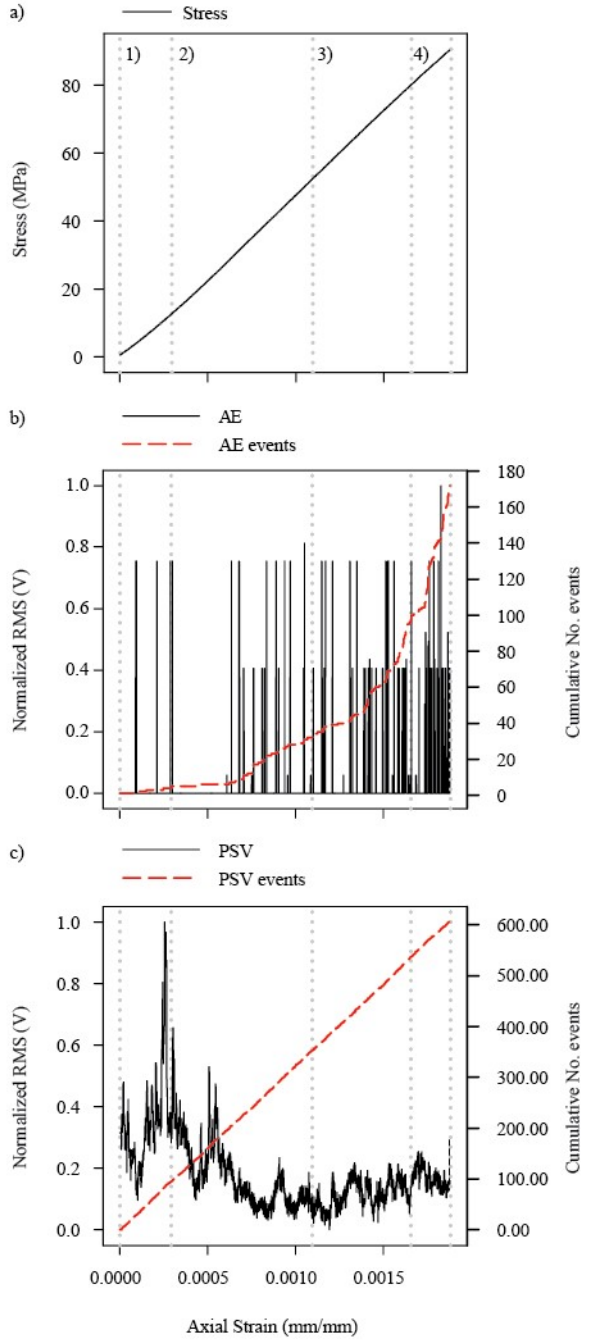

Part 1 – Strain based RTD loading data: *a) applied stress; b) normalized piezoelectric transducer RMS voltage and cumulative number of AE events; and c) normalized PSV RMS voltage and cumulative number of PSV events. Loading stages 1 to 5 are defined in chapter 5.5..*

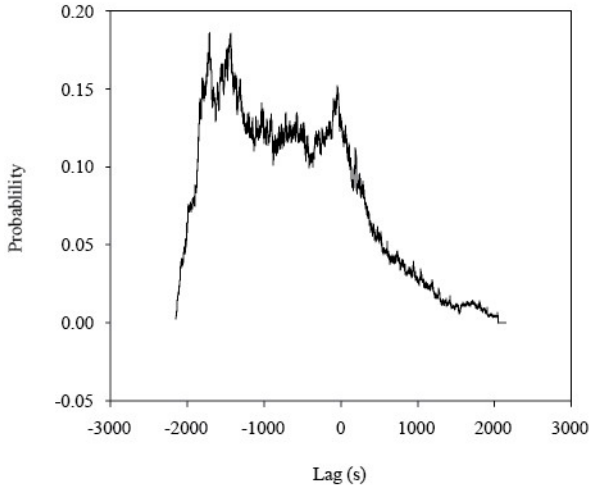

Part 2 – Overall cross-correlation: *Probability of correlation between PSV and AE events at varying lag times. A positive lag time indicates PSV lags behind AE and negative lag time indicates AE lags behind PSV.*

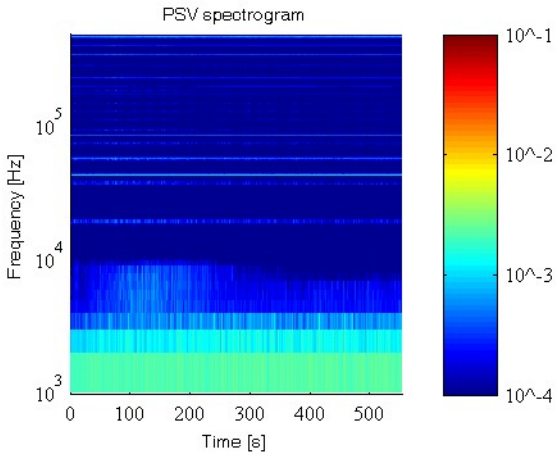

Part 3 – PSV spectral density.

Linear regression	$r^2 = 0.80$
Max Strength	120.38 MPa
Average PSV amplitude	0.64 mV
Average AE amplitude	4.39 dB

Part 4 – loading and statistical data: *The linear regression r^2 is computed between cumulative PSV and AE events.*

Cross-correlation between PSV and AE events						
Loading stage	1	2	3	4	5	Entire test
Coefficient	0.13	0.10	0.24	0.34	Stage	0.13
Lag time (s)	-9	0.5	1.5	-8.25	undefined	-12.5

Part 5 – cross-correlation data: *A negative lag time indicates AE events lag behind PSV events and a positive lag time indicates PSV events lag behind AE events at the maximum probability of correlation (coefficient).*

Figure 6-17 Oven dried schist results summary. *Part 1) strain based stress, PSV and AE plot; Part 2) overall cross-correlation plot; Part 3) PSV spectrogram; Part 4) experimental data; Part 5) cross-correlation results per stage of loading.*

The uniaxial RTD loading data for an oven dried schist specimen is shown in Figure 6-17. The applied stress, AE event amplitude, cumulative number of AE events, PSV event amplitude and cumulative number of PSV events with respect to axial strain, is shown in Part 1 of the figure. The PSV spectrogram in Part 3 shows a wide frequency band of high amplitude PEPS throughout the experiment and there is an increase in the PEPS frequency, between ~50 s to ~200 s. There is more PSV activity in the spectrogram compared to the water saturated specimen (Figure 6-19). The maximum probability of correlation lies outside of the expected lag time window of ±15 s; thus, a maximum probability was selected within the expected range. The resulting cross-correlation probability is low, with PSV occurring before AE activity, as shown in Part 2. The linear regression between PSV and AE cumulative events is high, as shown in Part 4.

During Stage 1 there are multiple high amplitude AE events and a slight increase in AE event rate. The PSV reaches it maximum amplitude, towards the end of the stage and the event rate is constant. The cross-correlation probability is low, with PSV occurring before AE activity.

Over Stage 2 the baseline PSV amplitude decreases, although there is variation in its amplitude and the event rate is constant throughout the stage. The AE event rate begins to increase in an exponential like manor and the AE event amplitude is high. The cross-correlation probability is lowest during this stage and PSV occurs after AE activity.

The PSV amplitude increases slightly over the course of Stage 3, although there is variation in the amplitude and the event rate remains constant. The AE event rate continues to increase and there are multiple high amplitude events. The cross-correlation probability is low, with AE events occurring before PSV events.

The baseline PSV amplitude continues to gradually increase during Stage 4, although there is variation in its amplitude and the event rate remains constant. There are larger amplitude AE events during this stage and the AE event rate increases. The cross-correlation probability highest during this stage and AE events occur after PSV events.

Stage 5 is undefined because there is no post maximum stress peak region of the stress strain curve.

6.2.20 Air dried schist RTD experimental results summary

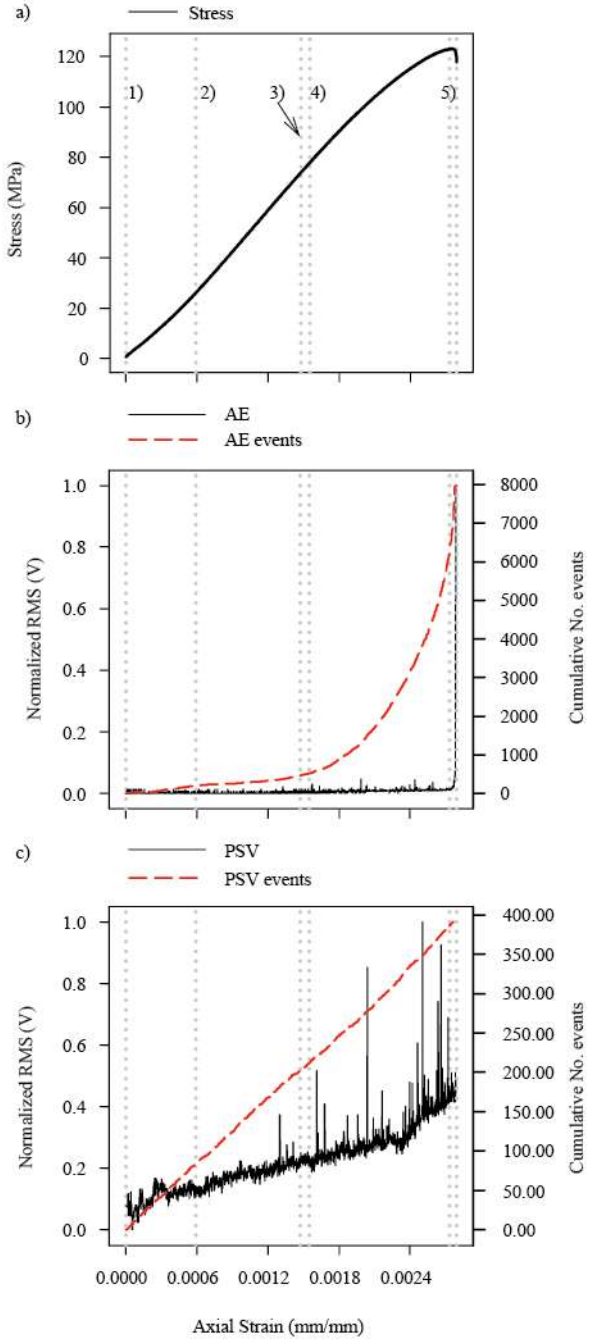

Part 1 – Strain based RTD loading data: *a) applied stress; b) normalized piezoelectric transducer RMS voltage and cumulative number of AE events; and c) normalized PSV RMS voltage and cumulative number of PSV events. Loading stages 1 to 5 are defined in chapter 5.5.*

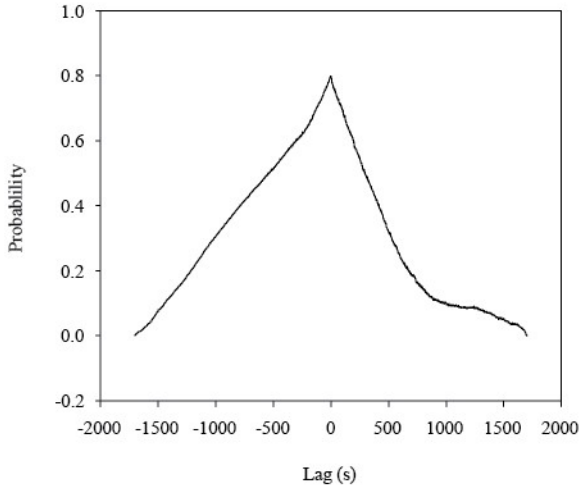

Part 2 – Overall cross-correlation: *Probability of correlation between PSV and AE events at varying lag times. A positive lag time indicates PSV lags behind AE and negative lag time indicates AE lags behind PSV.*

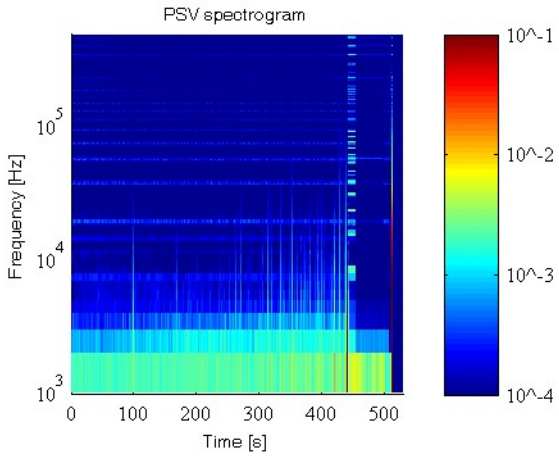

Part 3 - PSV spectral density.

Linear regression	$r^2 = 0.70$
Max Strength	123.07 MPa
Average PSV amplitude	0.43 mV
Average AE amplitude	40.35 dB

Part 4 – loading and statistical data: *The linear regression r^2 is computed between cumulative PSV and AE events.*

Cross-correlation between PSV and AE events						
Loading stage	1	2	3	4	5	Entire test
Coefficient	0.42	0.45	0.70	0.88	0.97	0.80
Lag time (s)	0.5	-1.25	0	1	0	0

Part 5 – cross-correlation data: *A negative lag time indicates AE events lag behind PSV events and a positive lag time indicates PSV events lag behind AE events at the maximum probability of correlation (coefficient).*

Figure 6-18 Air dried schist results summary. *Part 1) strain based stress, PSV and AE plot; Part 2) overall cross-correlation plot; Part 3) PSV spectrogram; Part 4) experimental data; Part 5) cross-correlation results per stage of loading.*

The uniaxial RTD loading data for an air dried schist specimen is shown in Figure 6-18. The applied stress, AE event amplitude, cumulative number of AE events, PSV event amplitude and cumulative number of PSV events with respect to axial strain, is shown in Part 1 of the figure. The PSV spectrogram in Part 3 shows a wide frequency band of high amplitude PEPS, throughout the experiment and multiple TEPS that increase in amplitude towards failure. The is more PSV activity in the spectrogram compared to the water saturate experiment (Figure 6-19). The cross-correlation probability is the highest out of the schist experiments and PSV and AE activity occur simultaneously. There is a single well defined peak in cross-correlation probability, indicating little variation, as shown in Part 2. The linear regression between PSV and AE cumulative events is also high, as shown in Part 4.

During Stage 1 there is little to no AE activity, however the AE event rate increases slightly. The PSV amplitude increases over the course of the stage and there is some variation in its amplitude; the event rate remains constant. The cross-correlation probability is lowest during this stage and PSV occurs after AE activity.

The AE event amplitude remains low over the course of Stage 2 and the AE event rate is constant. The PSV amplitude continues to increase throughout the stage, and the event rate remains constant. The cross-correlation probability slightly higher than the previous stage and PSV occurs before AE activity.

The AE event rate begins to increase at an exponential like rate during Stage 3 and the PSV event rate remains stable. The amplitude of the PSV continues to increase and the cross-correlation probability is high, with AE and PSV activity occurring simultaneously.

Over Stage 4 the AE amplitude remains relatively low and the AE event rate continues to increase, however the PSV event rate remains constant. Overall the PSV amplitude increases, however there are multiple large amplitude spikes in variation. The cross-correlation is higher than the previous stage and AE occurs before PSV activity.

Stage 5 contains the highest amplitude AE events occurring prior to failure and the AE event rate is at its highest value. The PSV amplitude continues increasing, however there are smaller spike variations compared to the previous stage and the event rate is stable. The cross-correlation probability is highest during this stage and PSV and AE events occur simultaneously.

6.2.21 Water saturated schist RTD experimental results summary

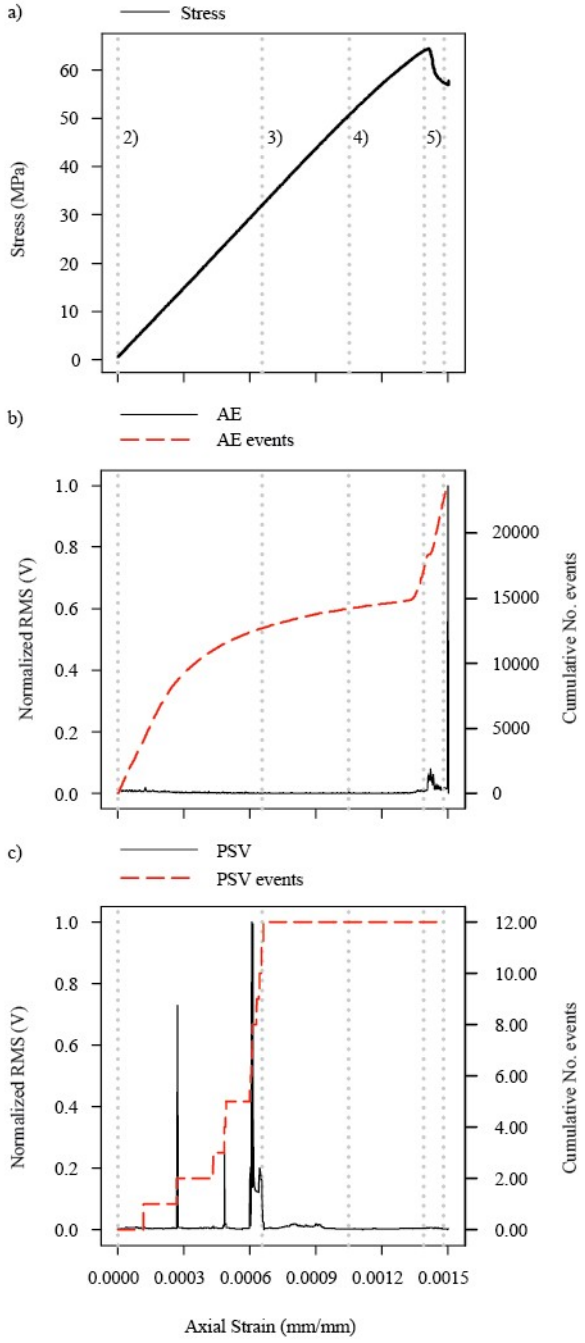

Part 1 – Strain based RTD loading data: *a) applied stress; b) normalized piezoelectric transducer RMS voltage and cumulative number of AE events; and c) normalized PSV RMS voltage and cumulative number of PSV events. Loading stages 1 to 5 are defined in chapter 5.5.*

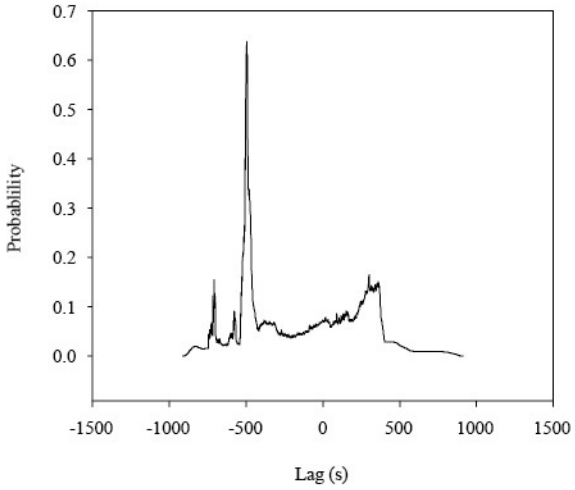

Part 2 – Overall cross-correlation: *Probability of correlation between PSV and AE events at varying lag times. A positive lag time indicates PSV lags behind AE and negative lag time indicates AE lags behind PSV.*

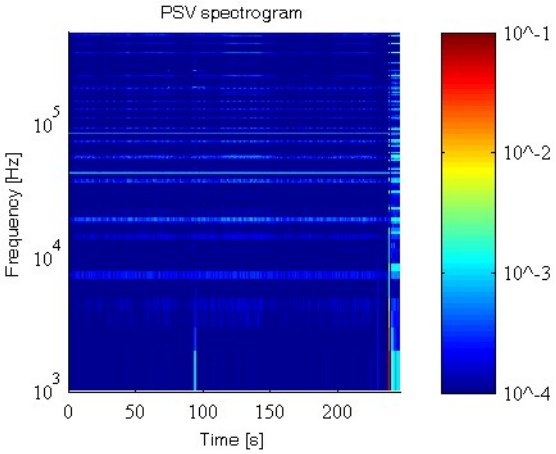

Part 3 – PSV spectral density.

Linear regression	r^2 = NA
Max Strength	64.25 MPa
Average PSV amplitude	0.58 mV
Average AE amplitude	83.30 dB

Part 4 – loading and statistical data: *The linear regression r^2 is computed between cumulative PSV and AE events.*

Cross-correlation between PSV and AE events						
Loading stage	1	2	3	4	5	Entire test
Coefficient	Stage	0.1448	0.43	0.79	0.83	0.08
Lag time (s)	undefined	8.75	-5.75	0	-0.25	4.25

Part 5 – cross-correlation data: *A negative lag time indicates AE events lag behind PSV events and a positive lag time indicates PSV events lag behind AE events at the maximum probability of correlation (coefficient).*

Figure 6-19 Water saturated schist results summary. *Part 1) strain based stress, PSV and AE plot; Part 2) overall cross-correlation plot; Part 3) PSV spectrogram; Part 4) experimental data; Part 5) cross-correlation results per stage of loading.*

The uniaxial RTD loading data for a water saturated schist specimen is shown in Figure 6-19. The applied stress, AE event amplitude, cumulative number of AE events, PSV event amplitude and cumulative number of PSV events, with respect to axial strain, is shown in Part 1 of the figure. The PSV spectrogram in Part 3, shows a little to no PEPS, however there are TEPS at ~90 s and prior to material failure. There is considerably less activity in the PSV spectrogram compared to the oven dried specimen (Figure 6-17). The cross-correlation lag time lies outside of the expected lag range of ±15 s, thus the maximum probability within the range was chosen. The resulting cross-correlation probability is lowest out of the schist experiments and PSV occurs after AE activity, as shown in Part 2. The linear regression between PSV and AE cumulative number of events is not valid, because there are very few detectable PSV events.

The stress strain curve does not have a defined pore closure region and thus Stage 1 is not represented in this test.

Over Stage 2 there are relatively small AE events and the AE event rate increases, however after ~$0.4x10^{-3}$ mm/mm the event rate begins to reduce. There are four large spikes in PSV activity, with the largest occurring at the end of the stage. The cross-correlation probability is lowest during this stage and AE occurs before PSV activity.

Throughout Stage 3 the PSV and AE amplitudes are relatively low and the AE event rate continues to decrease. The cross-correlation probability is higher than the previous stage and PSV events occur before AE events.

The amplitude of the PSV and AE remains low and the AE event rate decreases further over Stage 4. However, the cross-correlation probability is high during this stage and AE and PSV occur simultaneously.

During Stage 5 there are multiple high amplitude AE events, with the largest happening around the occurrence of material failure, however the PSV activity remains relatively low throughout the stage. The cross-correlation probability is highest during this stage and PSV occurs before AE events.

6.2.22 Oven dried gabbro RTD experimental results summary

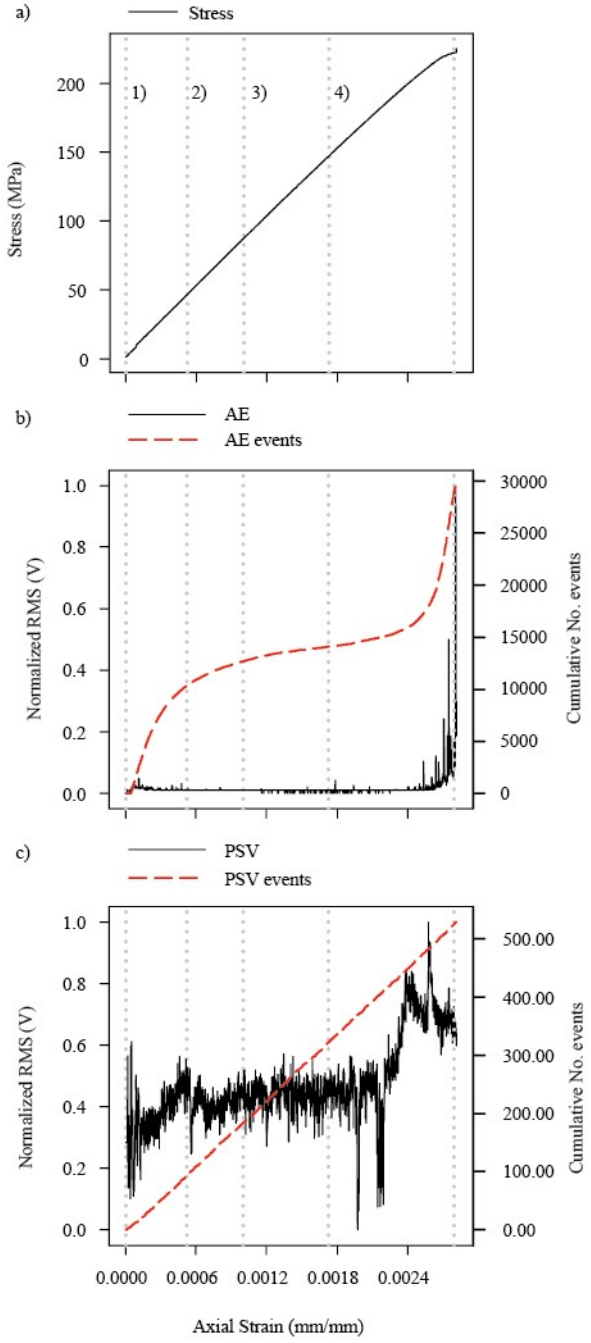

Part 1 – Strain based RTD loading data: *a) applied stress; b) normalized piezoelectric transducer RMS voltage and cumulative number of AE events; and c) normalized PSV RMS voltage and cumulative number of PSV events. Loading stages 1 to 5 are defined in chapter 5.5.*

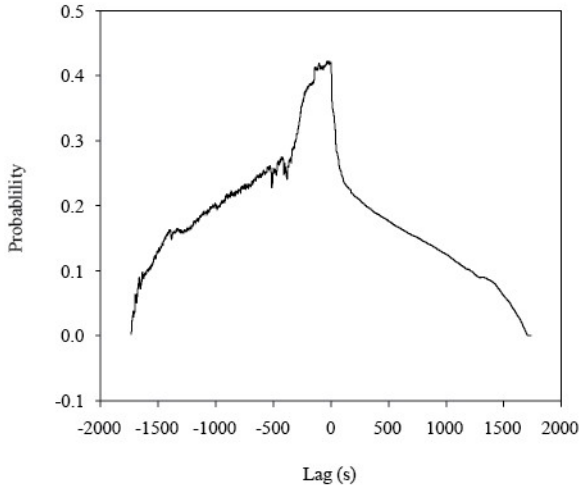

Part 2 – Overall cross-correlation: *Probability of correlation between PSV and AE events at varying lag times. A positive lag time indicates PSV lags behind AE and negative lag time indicates AE lags behind PSV.*

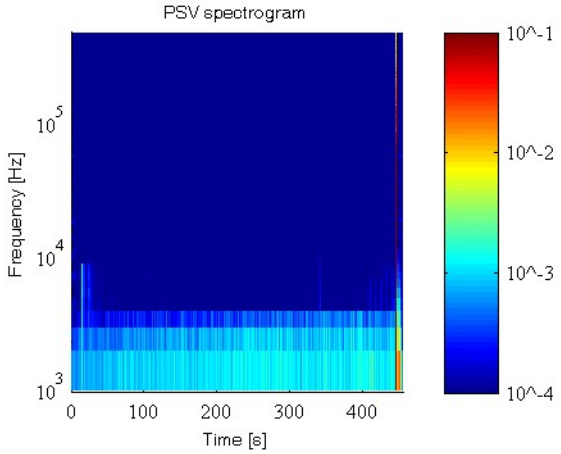

Part 3 – PSV spectral density.

Linear regression	$r^2 = 0.77$
Max Strength	222.33 MPa
Average PSV amplitude	0.36 mV
Average AE amplitude	64.81 dB

Part 4 – loading and statistical data: *The linear regression r^2 is computed between cumulative PSV and AE events.*

Cross-correlation between PSV and AE events						
Loading stage	1	2	3	4	5	Entire test
Coefficient	0.88	0.99	0.95	0.40	Stage	0.42
Lag time (s)	-0.25	0	0	-8.5	Undefined	-8.5

Part 5 – cross-correlation data: *A negative lag time indicates AE events lag behind PSV events and a positive lag time indicates PSV events lag behind AE events at the maximum probability of correlation (coefficient).*

Figure 6-20 Oven dried gabbro results summary. *Part 1) strain based stress, PSV and AE plot; Part 2) overall cross-correlation plot; Part 3) PSV spectrogram; Part 4) experimental data; Part 5) cross-correlation results per stage of loading.*

The uniaxial RTD loading data for an oven dried gabbro specimen is shown in Figure 6-20. The applied stress, AE event amplitude, cumulative number of AE events, PSV event amplitude and cumulative number of PSV events, with respect to axial strain is shown in Part 1 of the figure. The PSV spectrogram in Part 3, shows PEPS throughout the experiment and high amplitude TEPS before material failure. The spectrogram shows more PSV activity compared to the water saturated experiment (Figure 6-21). The cross-correlation probability slightly lower than the water saturated experiment and PSV occurs before AE activity. There is a defined peak in cross-correlation probability with some variation, as shown in Part 2. The linear regression between PSV and AE cumulative events is high, as shown in Part 4.

The AE events are relatively small during Stage 1, however there is an increase in event rate initially and then the rate reduces throughout the rest of the stage. The PSV amplitude increases overall, although there is variation in its amplitude, with the largest variation occurring at the start of the stage. The PSV event rate is constant. The cross-correlation probability is high, with PSV events occurring before AE events.

During Stage 2 and 3 the AE event rate continues to decline and there are relatively low amplitude AE events. The PSV baseline amplitude remains stable although there are some variations in its amplitude and the event rate is constant. The cross-correlation probability is highest during Stage 2 and slightly lower over Stage 3; for both stages PSV and AE activity occur simultaneously.

There is a surge in AE amplitude after ~2.4×10^{-3} mm/mm, during Stage 4 and the event rate increases simultaneously. The PSV amplitude also begins to increase during Stage 4, there are multiple spikes like variations in amplitude and the PSV event rate remains constant; however, prior to failure the PSV amplitude drops. The cross-correlation probability is lowest during this stage, with PSV occurring before AE activity

Stage 5 is undefined because there is not an identifiable post peak stress area of the stress strain curve.

6.2.23 Water saturated gabbro RTD experimental results summary

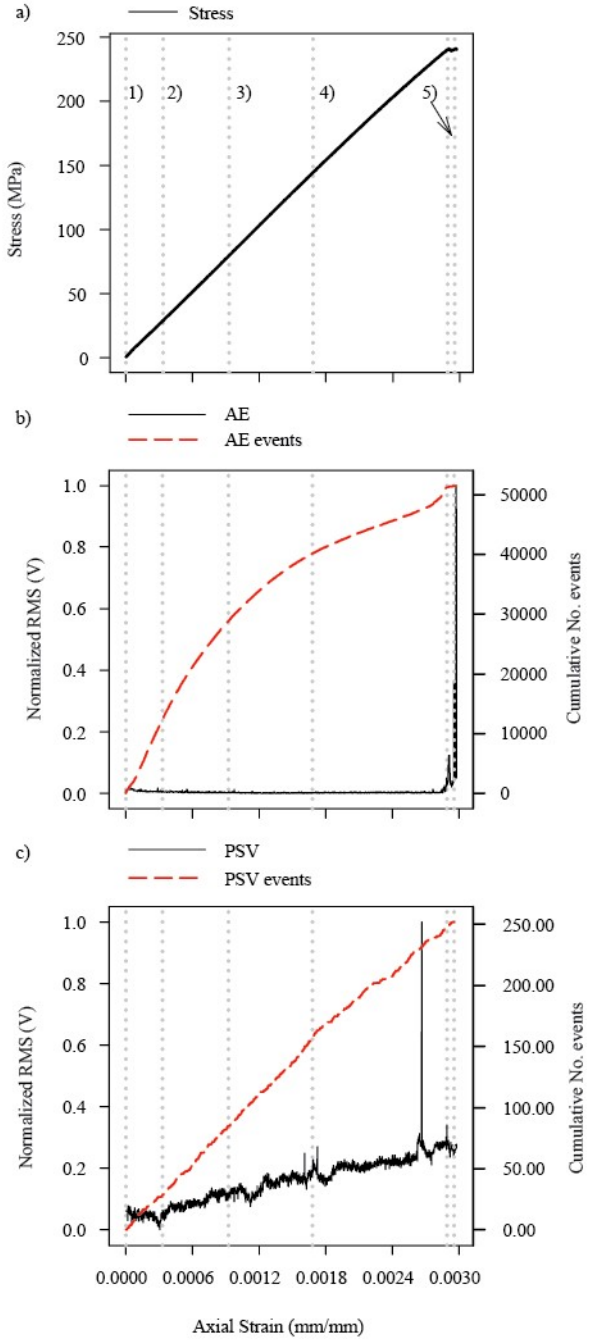

Part 1 – Strain based RTD loading data: *a) applied stress; b) normalized piezoelectric transducer RMS voltage and cumulative number of AE events; and c) normalized PSV RMS voltage and cumulative number of PSV events. Loading stages 1 to 5 are defined in chapter 5.5.*

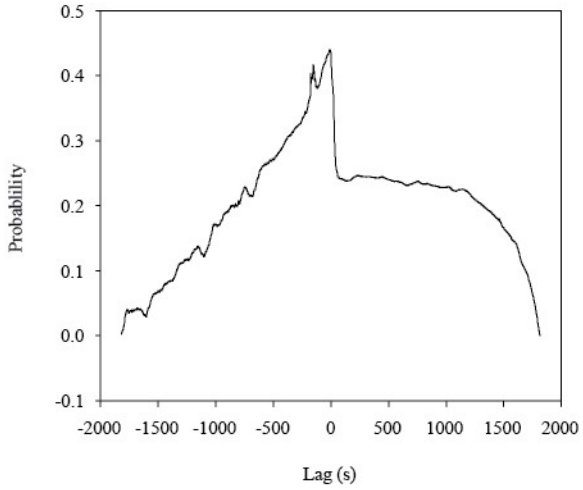

Part 2 – Overall cross-correlation: *Probability of correlation between PSV and AE events at varying lag times. A positive lag time indicates PSV lags behind AE and negative lag time indicates AE lags behind PSV.*

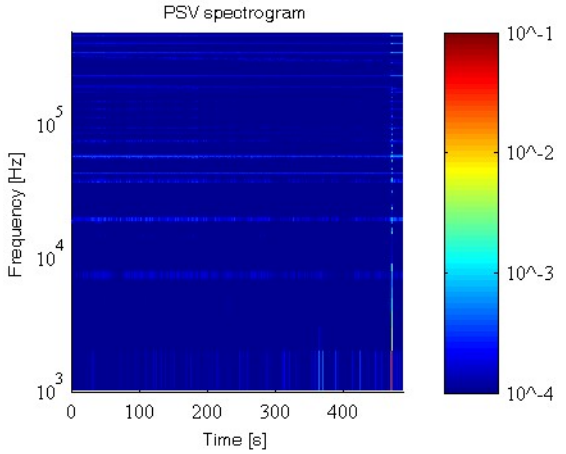

Part 3 – PSV spectral density.

Linear regression	$r^2 = 0.93$
Max Strength	240.58 MPa
Average PSV amplitude	0.69 mV
Average AE amplitude	82.40 dB

Part 4 – loading and statistical data: *The linear regression r^2 is computed between cumulative PSV and AE events.*

Cross-correlation between PSV and AE events						
Loading stage	1	2	3	4	5	Entire test
Coefficient	0.92	0.88	0.88	0.72	0.83	0.44
Lag time (s)	0	0	0	0	0	-2.75

Part 5 – cross-correlation data: *A negative lag time indicates AE events lag behind PSV events and a positive lag time indicates PSV events lag behind AE events at the maximum probability of correlation (coefficient).*

Figure 6-21 Water saturated gabbro results summary. *Part 1) strain based stress, PSV and AE plot; Part 2) overall cross-correlation plot; Part 3) PSV spectrogram; Part 4) experimental data; Part 5) cross-correlation results per stage of loading.*

The uniaxial RTD loading data for a water saturated gabbro specimen is shown in Figure 6-21. The applied stress, AE event amplitude, cumulative number of AE events, PSV event amplitude and cumulative number of PSV events with respect to axial strain, is shown in Part 1 of the figure. The PSV spectrogram in Part 3, shows low amplitude PEPS, however there are high amplitude TEPS before material failure. There is considerably less activity in the PSV spectrogram, compared to the oven dried specimen (Figure 6-20). The cross-correlation probability is slightly higher than the oven dried specimen and PSV occurs before AE activity. There is a single defined peak in cross-correlation probability as shown in Part 2. The linear regression for cumulative AE and PSV events is high as shown in Part 4.

During Stage 1, initially there is an increase in AE event rate which then reduces over the course of the stage and the PSV event rate is constant. The AE and PSV amplitudes are both relatively low, the cross-correlation probability is highest during this stage and AE and PSV occur simultaneously.

The AE event rate continues to decline over the course of Stages 2 and 3 and the AE event amplitude remains relatively low. However, the PSV amplitude increases throughout Stages 2 and 3 and the event rate remains constant. The cross-correlation probability is slightly lower than Stage 1 for both stages and AE and PSV events occur simultaneously.

The AE event rate begins to increase at the onset of Stage 4 and reduces during Stage 5, before material failure. There are relatively high amplitude AE events at the end of Stage 4 and during Stage 5. The PSV amplitude continues to increase throughout Stage 4 and 5 and the PSV event rate is constant up until material failure. The cross-correlation probability during Stage 4 and 5 is lower than the previous stages and PSV and AE activity occur simultaneously, for both Stage 4 and 5.

6.3 Discussion

6.3.1 Detected PSVs for all rock lithologies regardless of quartz content, environmental condition or loading stage

For the RTD experiments presented in this chapter, PSV signals were detected in the range of millivolts for all rock lithologies and in all environmental condition. as shown in Figure 6-22. The plotted voltages are referred to the input (RTI) of the EPS. The signal to noise ratio for measuring PSV is much better than measuring the associated PSC; work by others has shown PSC to be in the range of Pico amps in marble and cement mortar specimens [15, 151]. This data indicates PSV generation cannot be solely produced by the piezo electric effect of quartz, as marble, halite and gabbro specimens contain no quartz. In fact, the largest PSV amplitude was produced by a quartz devoid saline saturated marble specimen.

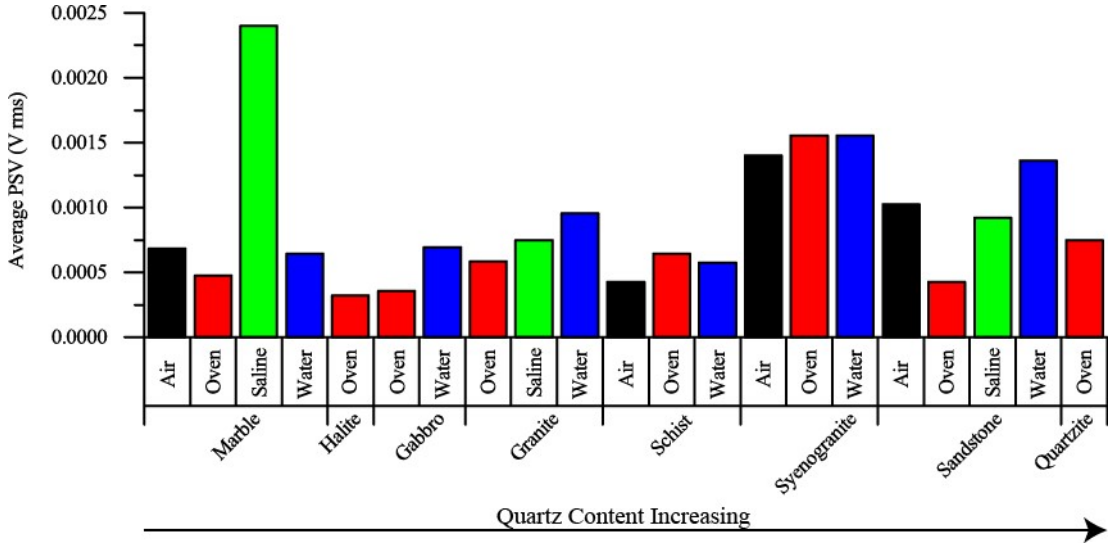

Figure 6-22 Average PSV amplitudes resulting from RTD experiments*. Environmental conditions include oven dried, air dried, water saturated and saline saturated. The amplitudes are plotted in order of quartz content from lowest to highest.*

Saline saturated specimens produced the highest PSV amplitudes, followed by water saturated and air dried specimens. The lowest PSV amplitudes were produced by oven dried specimens, as shown in Figure 6-23.

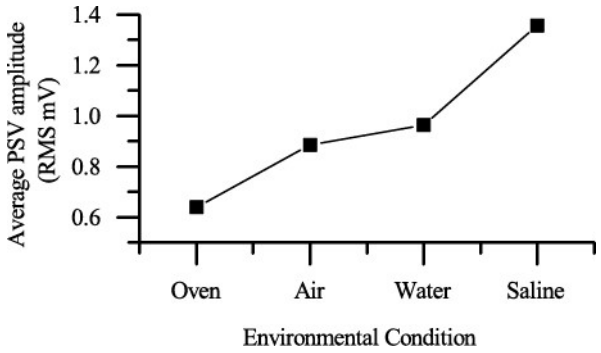

Figure 6-23 Mean PSV amplitude for each environmental condition*.*

6.3.2 Cross-correlations between PSVs and AEs and the PSV event detection procedure.

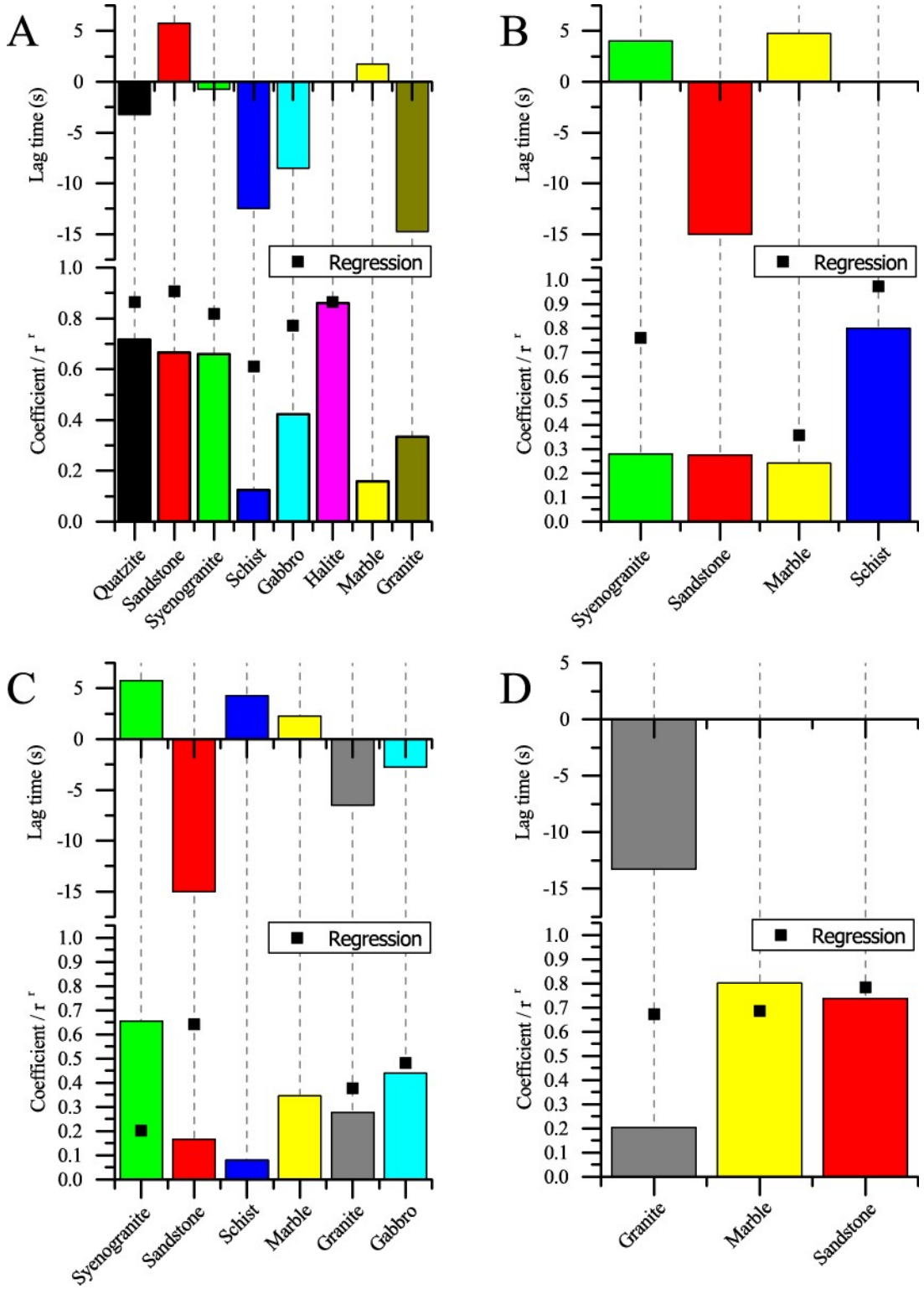

Figure 6-24 PSV and AE statistical relationship summary. *The vertical bars represent the cross-correlation probability and lag time. A negative lag time indicates PSV activity occurs before AE activity and vice versa. The black line and symbol plot represents the r^2 value for the linear regression between AE and PSV cumulative events. A) oven dried specimens, B) air dried specimens, C) water saturated specimens and D) saline saturated specimens.*

The results presented in Figure 6-24, show the maximum overall cross-correlation coefficients and associated lag times (represented by the vertical bars) for AE and PSV amplitude time series data. Additionally, the overall r^2 values (represented by the line symbol plots) for the linear regression between cumulative AE events and cumulative PSV events, are shown in the figure.

For all environmental conditions (Oven dried, air dried, water saturated and saline saturated) there is some degree of correlation between changes in PSV and AE amplitude, regardless of the rock lithology. The highest cross-correlation coefficient is for an oven dried Halite specimen (0.86) and the lowest coefficient was a water saturated schist specimen (0.079). A cross-correlation coefficient of 0 indicates no correlation, a value of 1 indicates perfect correlation and a value of -1 indicates a perfect inverse correlation.

All linear regression results for AE and PSV cumulative events have a p-values < 0.05, indicating that the relationship between the predictor variable (AE) and the response variable (PSV) is statistically significant. The r^2 value represents the goodness of the regression line, i.e. the variation from a linear relationship between cumulative AE and PSV events. The lowest r^2 value is for a water saturated syenogranite specimen (0.20) and the highest r^2 value is for an air dried schist specimen (0.97). These statistical results show that there is a relationship between PSV and AE event rates.

There is a linear correlation between overall cross-correlation coefficients and overall linear regression r^2 values for all of the rocks tested. The cross-correlation coefficients were not normally distributed, thus a non-parametric Spearman linear correlation [140] was used. The linear correlation coefficient is 0.6529, where 1 would be a perfect positive linear correlation, 0 would indicate no relationship and -1 would be a perfect negative correlation. The p-value (0.0075) is less than 0.01, providing evidence to reject the null hypothesis of AE and PSV cumulative event regression and AE and PSV amplitude cross-correlation not being related. This statistical result shows the novel PSV event detection method described in section 4.7.1, that was used to calculate the PSV cumulative events, is a reliable method for data reduction.

6.3.3 The effects of environmental condition and loading deformation stage on cross-correlation between PSV and AE activity

To test if there are significant differences between groups, i.e. environmental conditions or stages of loading an appropriate statistical test was chosen. If the groups were non-normally distributed, a Kruskal–Wallis [140] one-way analysis of variance test was used and for parametric data, a one-way analysis of variance test (ANOVA) was used [140]. If the resulting p-value was less than the significance value ($p<0.005$), a follow up multiple comparison test using the Dunn and Sidák's approach [150] was used, to determine which groups were statistically different.

The overall cross-correlation coefficients and overall cross-correlation lag times were grouped by environmental condition, to test for significant differences between the groups. The resulting p-values (coefficients: $p = 0.54$, lag times: $p = 0.90$) showed the overall cross-correlation coefficients and overall

cross-correlation lag times for all rocks tested, were not significantly different between oven dry, air dry, water saturated and saline saturated environmental conditions.

The overall linear regression r^2 values were grouped by environmental condition, to investigate any differences between the groups. The resulting p-value (0.0036), indicates a significant difference between groups. A follow up multiple comparison test, reveals the linear regression between cumulative PSV an AE events is significantly lower for water saturated specimens, compared to oven dried specimens.

The cross-correlation coefficients and lag times for all stages of loading, were grouped by environmental condition and loading stage, to test if there were any significant differences between the groups. The resulting p-values (coefficients: p = 0.24, lag times: p=0.56) for environmental condition groups, indicate that there is not a significant difference between oven dried, air dried, water saturated and saline saturated rock specimens. In addition, the p-values (coefficients: p = 0.23, lag times: p=0.75) for loading stage groups reveal, that there is not a significant difference between the stages of loading.

Due to the relatively small data set, the analysis of variance tests used may not show any significant differences, between environmental conditions and stages of loading deformation. Simply comparing the average cross-correlation coefficients and lag times per loading stage and environmental condition may provide more information, as shown in Figure 6-25.

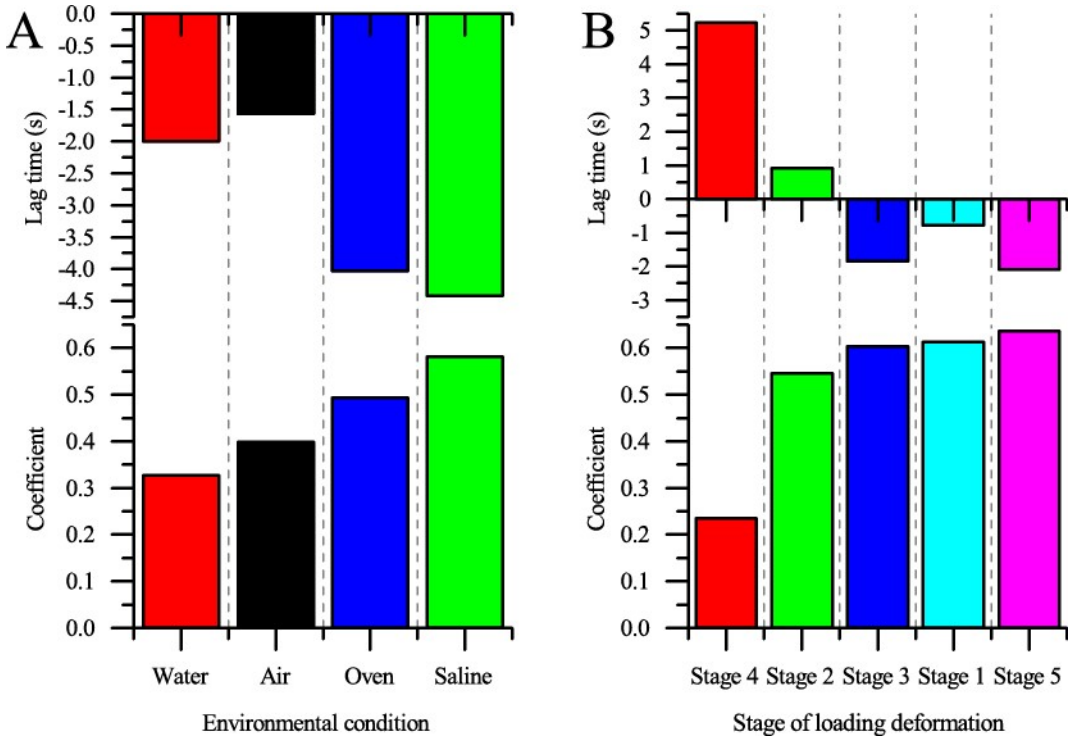

Figure 6-25 Average cross-correlation data summary*. A) shows the average overall cross-correlation data, grouped by environmental condition. B) shows the average cross –correlation data, grouped by loading stage. The data is plotted in ascending order of cross-correlation coefficient.*

Saline saturated specimens have the highest cross –correlation coefficients, followed my oven dried and air dried specimens and water saturated specimens have the lowest cross-correlation coefficients. The average lag times for all environmental conditions are negative, meaning that PSV activity occurs before AE activity. The lag time appears to follow a similar trend in terms of relative magnitude, to the cross-correlation coefficient, however water saturated specimens have a larger lag time than air dried specimens. This data confirms that there is a correlation between PSV and AE activity, in all environmental conditions. The degree of correlation and the lag time between PSV and AE activity, is effected by varying degrees of water saturation (oven dry, air dry and water saturated) and saline saturation (saline saturated).

My hypothesis is that PSV emissions are related to the movement and separation of fresh charged fracture surfaces and increasing levels of water or saline saturation may prevent charge build up and thus PSV-AE correlation. This is because water (474 μS) and saline (56.58 mS) are more electrically conductive than air which would normally be in the pores of dry rocks. Furthermore, saline is more electrically conductive than water and thus I would expect PSV-AE correlations to be lowest for saline saturated specimens. The PSV-AE cross-correlation coefficients do support this hypothesis, apart from the mean coefficient for the saline saturated specimens. I suspect that the mean coefficient for the saline saturated specimens may be an anomalous result, for the following reasons. Firstly, the number of samples tested in the saline category is lowest out of all environmental conditions (oven, air, water saturated and saline saturated) and thus the mean value is more vulnerable to outliers. Secondly, the concrete specimens tested support my hypothesis as shown in chapter 7.

The highest correlation between AE activity and PSV occurs during Stage 5 of loading, this indicates that there is a relatively strong correlation between PSV and non-recoverable post-peak inelastic deformation, resulting from unstable macrocrack and shear plane development. There are also relatively strong correlations between PSV and pre-existing microcrack and pore closure occurring in Stage 1 and partially recoverable elastic deformation and stable microcrack propagation occurring in Stage 3. The correlation is lower during Stage 2, where recoverable elastic deformation occurs. However, there is a relatively low correlation between PSV and non-recoverable pre-peak inelastic deformation, resulting from unstable microcrack propagation and coalescence, during Stage 4. PSV activity occurs before AE activity on average during Stage 1, 3 and 5 and PSV activity occurs after AE activity for lower correlating Stages 2 and 4. This data reveals differences in cross-correlation coefficient and lag time are linked to the deformation process in rocks.

6.3.4 Rock lithology and cross-correlation between AE and PSV activity

The overall cross-correlation for all lithology types tested is shown in Figure 6-26. All specimens presented are oven dried, to negate the effect of water and saline saturation and thus the effect of lithology type is prominent.

There is not a significant relationship between quartz content and the degree of correlation between PSV and AE activity. The linear regression between cross-correlation coefficient and quartz content rank gave a low r^2 value of 0.1435. Rock lithologies, Halite, Gabbro and Marble all contain no quartz minerals and have higher cross-correlation coefficients than some of the quartz bearing rocks, with halite having the highest cross-correlation coefficient. This data suggests the piezoelectric effect of quartz, is not solely responsible for the correlations between AE activity and PSV activity; other minerals may have an effect as well as the rock type. Table 6-2 shows a summary of the rock type and mineralogy, alongside correlations between AE and PSV activity.

The lowest correlations occurred in metamorphic rocks (schist and marble), the middle correlations occurred in igneous rocks (granite, gabbro and syenogranite) and the highest correlations occurred in sedimentary rocks (sandstone and halite). The exception to this rule is the quartzite specimen which has a relatively high correlation between AE and PSV activity, but is metamorphic rock type.

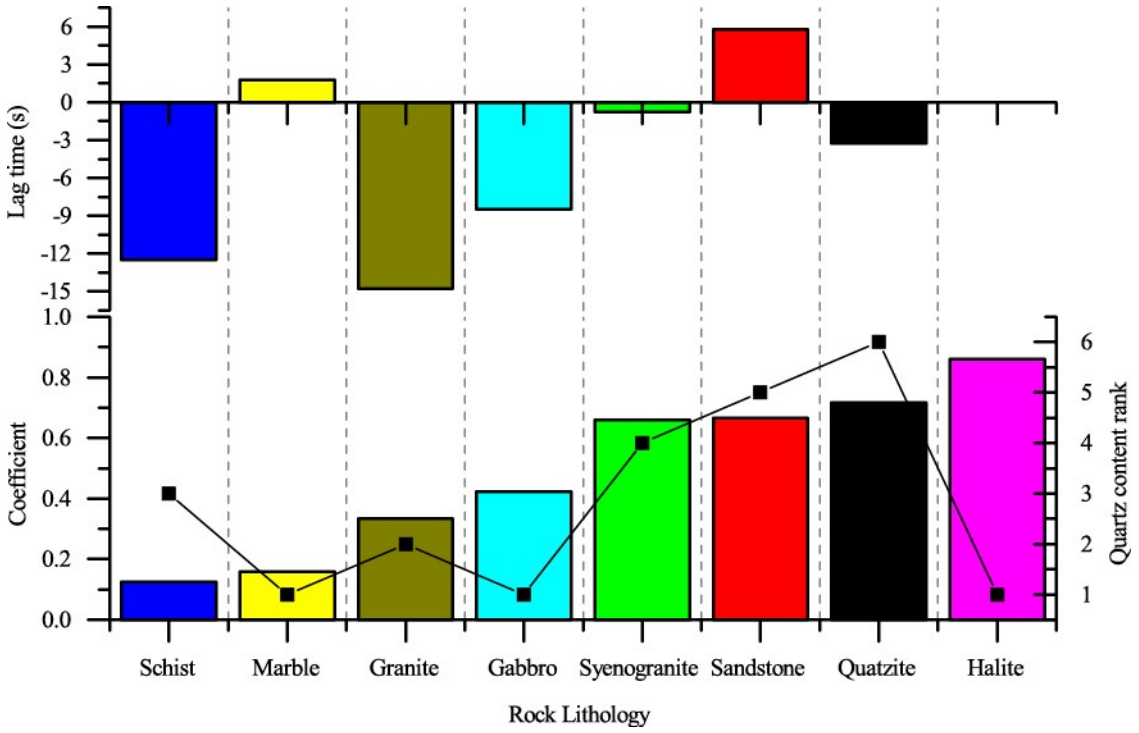

Figure 6-26 Overall cross-correlation data for all rock lithologies tested. *All of the experiments presented in the graph are oven dried specimens. The bars represent the cross-correlation coefficients and lag times, where a negative lag time indicates PSV activity occurring before AE activity and vice versa. The line symbol plot represents the quartz content ranking of each rock lithology where a rank of 1 is the lowest and a rank of 6 is the highest quartz content.*

There does not appear to be any relationship between the mineral content of each rock type and the correlation between AE and PSV activity. Excluding quartz none of the minerals are not considered to have piezoelectric or pyroelectric properties. Therefore, the generation of PSVs and their correlation with AE, must be related to the AE generation mechanisms. Work by others has suggested that electrical emissions are related to movement and separation of fresh charged fracture surfaces [83], i.e. microcrack closure (Stage 1), microcrack propagation (Stage 3) and marcrocrack propagation (Stages 4-5) and sheer

plane movement (Stage 5). The data presented here supports this pressure stimulated electrical emission generation theory.

On the contrary as described section 6.3.3 there was a relatively strong correlation between PSV and AE during linear elastic deformation (Stage 2), which generally produces very little AE activity and thus little fresh charged facture surfaces. An explanation for this, is both AE and PSV activity is generally low during this stage and thus a relatively strong cross-correlations occur.

Rock lithology	**Rock type**	**Rock mineralogy**	**Cross-correlation**	
			coefficient	**lag time (s)**
Halite	Sedimentary	Halite – 62 % Anhydrites/clays – 38 %	0.86	0
Quartzite	Metamorphic	Mono quartz – 83 % Poly quartz – 5 % Alkali feldspar – 6 % Plagioclase – 1 % Lithic – 3 % Altered grain – 2 %	0.72	-3.25
Sandstone	Sedimentary	Mono quartz – 66 % Poly quartz -14 % Alkali feldspar – 9 % Lithic – 7 % Altered grain – 4 %	0.67	5.75
Syenogranite	Igneous	Quartz – 45 % Alkal feldspar – 36 % Plagioclase – 17 % Sericite – 1 % Muscovite - <1 %	0.66	-0.75
Gabbro	Igneous	Plagioclase – 66 % Opaques – 14 % Chlorite – 9 % CPX – 7 % Sericite – 4 % Zircon - <1 %	0.42	-8.5
Granite	Igneous	Quartz – 26 % Alkali feldspar – 27 % Plagioclase – 17 % Muscovite – 12 % Biotite – 6 % Chlorite – 1 % Sericite – 11 % Zircon - <1 %	0.33	-14.25
Marble	Metamorphic	Calcite – 100 %	0.16	1.75
Schist	Metamorphic	Biotite – 43 % Alkali feldspar - 15% Sillimanite - 5 % Plagioclase - 4 % Andalusite - 3 % Opaques - 2 %	0.13	-12.5

Table 6-2 Rock type and mineral composition summary. *Rocks specimens are listed in order of cross-correlation coefficient, with the first specimen having the highest correlation between AE and PSV activity and the following specimens are in descending order. A positive lag time indicates AE events occurred before PSV events and a negative lag time indicates PSV events occurred before AE events.*

6.3.5 Research question conclusions

Are PSVs present in a wide range of rock lithology, including rocks with no piezoelectric minerals?

For the RTD experiments presented in this chapter, PSV signals were detected in the range of millivolts for all rock lithologies and in all environmental conditions as shown in Figure 6-22. This data indicates PSV generation cannot be solely produced by the piezoelectric effect of quartz, as marble, halite and gabbro specimens contain no quartz. In fact, the largest PSV amplitude was produced by a quartz devoid saline saturated marble specimen.

Are PSVs produced by rocks related to acoustic events?

For all environmental conditions (Oven dried, air dried, water saturated and saline saturated) there is some degree of correlation between changes in PSV and AE amplitude, regardless of the rock lithology. Therefore, high frequency (25.5 mHz to 750 kHz) PSV events detected by the capacitively coupled EPS are likely related to AE events.

Can the detection of PSVs be used as an indication of the structural health or the current stage of deformation in rock?

The loading deformation stages of the materials influenced the PSV-AE cross-correlations. The type of material deformation affected not only the degree of correlation between PSV and AE events, but also the lead/lag time between PSV event and AE events. It could be possible to use capacitively coupled EPS and piezo transducers simultaneously in SHM applications, to analyse PSV-AE lag times and determine the deformation stage in a structure. For instance, irreversible damage occurring beyond loading Stage 3 could be avoided in structures using a PSV-AE monitoring technique.

Is the electric potential sensor (EPS) a suitable technology for the wide scale monitoring of PSVs in rock?

PSVs were detected in all rock lithology and in all environmental conditions in the range of millivolts. Therefore, the signal to noise ratio for measuring PSV is much better than measuring the associated PSC; work by others has shown PSC to be in the range of Pico amps in marble and cement mortar specimens [15, 151]. Because Faraday shielding of the experiment is not necessary (good signal to noise ratio) and the sensor is a compact, portable and cost effective solution as described in Section 4.5, EPS lends itself to the possible wide scale monitoring of PSVs outside of the laboratory setting.

7 UNIAXIAL COMPRESSIVE STRESS TESTING OF MANMADE MATERIALS IN DIFFERENT ENVIRONMENTAL CONDITIONS USING CAPACITIVELY COUPLED EPSS

This chapter describes the motivations behind the experiments carried out and presented in this results chapter, in section 7.1. Followed by a selection of results pages, containing detailed observations of pressure stimulated voltage (PSV), acoustic emissions (AE), stress and strain, for each material specimen tested and statistical relationships between each measurement quantity (section 7.2). Finally, all of the experimental results for each material specimen are compared and discussed in section 7.3.

7.1 Introduction

Work by others has shown pressure stimulated electrical emissions exist in a small number of different rock lithologies [18, 83] and cement mortar [15], however the generation mechanism/s is/are still uncertain. The current measurement technologies, including laboratory electrometers and electromagnetic emissions (EME) antennas, are not suitable for detection of pressures stimulated electric emissions (PSEs) outside of the laboratory setting. In addition, there have not been any studies investigating PSEs in concrete, which is one of the most widely used and versatile modern building materials.

This is the first study: 1) attempting to measure PSEs in concrete, 2) attempting to characterise PSEs with AE and mechanical properties in concrete, 3) monitoring PSE emissions using a field capable technology i.e. the electric potential sensor (EPS). The experiments that were carried out and presented in this chapter, were undertaken with the aim of answering the following research questions:

Are PSVs present in concrete specimens when subjected to uniaxial loading?

Are PSVs produced by concrete related to AE?

Can the detection of PSVs be used as an indication of the structural health or the current stage of deformation in concrete?

Is EPS technology suitable for the wide scale field monitoring of PSVs over concrete structures?

7.2 Results

7.2.1 Experimental procedure

Four cylindrical specimens of concrete were tested, each in different environmental conditions including, oven dried, air dried, water saturated and saline saturated. In addition, a cylindrical specimen of glass ceramic (Macor ®) was tested. Refer to section 5.1 for detailed information about material composition and preparation for each environmental condition.

Specimens were loaded in a uniaxial compressive load frame at a constant strain rate, in ordered to induce material failure with ~5-10 minutes. Each specimen was instrumented with two piezoelectric transducers, two EPS, two axial strain gauges and a circumferential strain gauge to measure AE, PSV, axial strain and circumferential strain respectively. In addition, a load cell was used to monitor the applied force. Details about the testing procedure are described in detail in chapter 5 and the loading rates are listed in section 5.4. The Macor ® experiment was designed to investigate if PSVs are present in a manmade material, that contains zero quartz and is humongous in nature.

Table 7-1 shows a list of all the experiments carried out; the experimental data is presented in this thesis chapter in the same order in which they appear in the table.

Material	Environmental condition	Figure number
Macor ®	Oven dried	Figure 7-1
Concrete	Oven dried	Figure 7-2
Concrete	Air dried	Figure 7-3
Concrete	Water saturated	Figure 7-4
Concrete	Saline saturated	Figure 7-5

Table 7-1 A list of manmade material specimens tested and presented in this thesis chapter.

The PSV emissions discussed and presented in this chapter, are referred to the input (RTI) of the EPS i.e. the rock surface. The AEs are referred to the input of the piezo transducers and the piezo transducer voltages are referred to the output of the piezo transducers before the 40dB amplification stage.

All PSV data is the result of a differential measurement, between the two EPS mounted diametrically opposite each other on the material specimen. The AE data is the combination of AE events from both piezo transducers mounted on steel platens, above and below the material specimen.

7.2.2 Defining the stages of material deformation

For the all of the ramp to destruction (RTD) experiments, the stress strain curves were divided into five recognized stages of deformation [132-134], to investigate the correlations between PSV and AE during different deformation modes. A detailed description of the stages of loading, including an example stress-strain curve and resulting AEs activity graph, is shown in section 5.5.

Stage 1) pre-existing microcrack and pore closure: characterized by strain-hardening behaviour (concave up) and an increase in AE event rate.

Stage 2) recoverable elastic deformation: characterized by linear axial and volumetric deformation with very little or no AE activity (low event rate).

Stage 3) partially recoverable elastic deformation and stable microcrack propagation: characterized by linear axial deformation, onset of volumetric dilatency and an increase in AE activity, in terms of amplitude and event rate.

Stage 4) non-recoverable pre-peak inelastic deformation, resulting from unstable microcrack propagation and coalescence: characterized by strain-hardening behaviour (concave down), rapid volumetric dilation and acceleration in AE rate and amplitude.

Stage 5) non-recoverable post-peak inelastic deformation, resulting from unstable macrocrack and shear plane development: characterized by strain-softening behaviour (concave down), surge in volumetric dilation and AE activity.

7.2.3 Oven dried glass ceramic (Macor ®) RTD experimental results summary

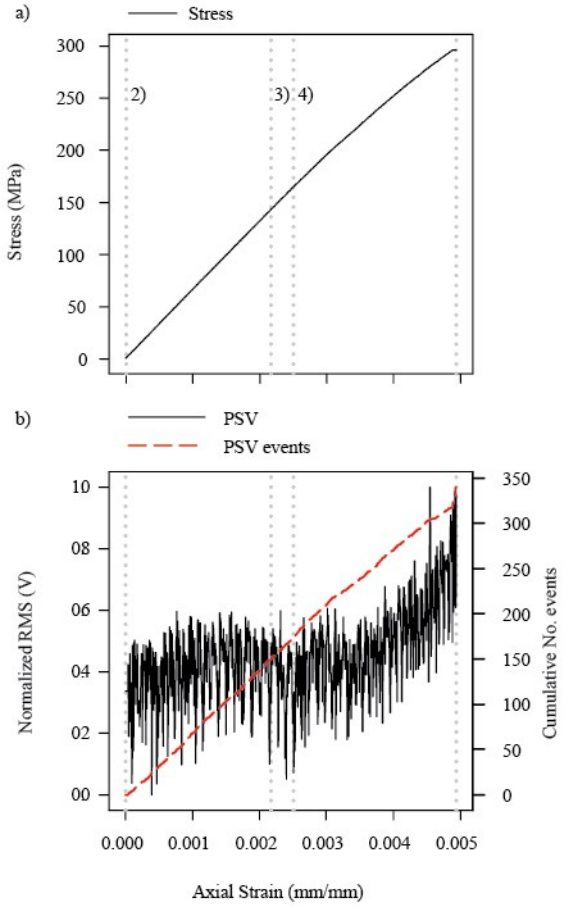

Part 1 – Strain based RTD loading data: *a) applied stress; b) normalized PSV RMS voltage and cumulative number of PSV events. Loading stages 1 to 5 are defined in chapter 5.5.*

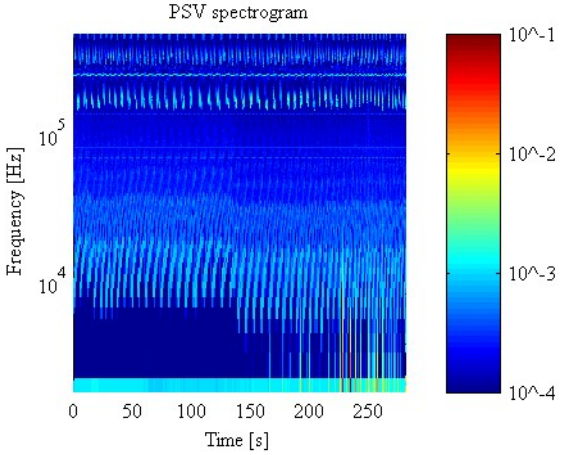

Part 2 – PSV spectral density.

Max Strength	296 MPa
Max PSV amplitude	3.90 mV

Part 3 – Loading data.

Figure 7-1 Oven dried glass ceramic (Macor ®) results summary. *Part 1) strain based stress and PSV plot; Part 2) PSV spectrogram; Part 3) experimental data.*

The uniaxial RTD loading data for an oven dried glass ceramic specimen is shown in Figure 7-1. Part 1 of the figure shows the PSV and applied stress data, plotted against axial strain. The PSV spectrogram in Part 2 of the figure shows low frequency and amplitude PEPS throughout the experiment and high amplitude TEPS towards the end of the experiment. The activity contained in higher frequency bands, can be regarded as noise, as detailed in section 4.7.1. Part 3 of the figure shows the maximum applied stress and maximum PSV amplitude during the experiment. The specimen was not instrumented with piezo transducers for this loading experiment and thus correlations between PSV and AE were not investigated.

The stress-strain relationship is linear at the start of the loading ramp and thus there is no defined pre-existing microcrack and pore closure stage of loading (Stage 1).

There is PSV activity throughout the experiment and the baseline amplitude increases slightly and then declines during Stage 2 of loading. During Stage 3 and 4 there is a larger increase in amplitude, up until the end of the experiment. The PSV event rate remains constant, apart from an increase in event rate at the end of the experiment.

There is not a defined Stage 5 of loading (non-recoverable post-peak inelastic deformation), because the maximum compressive strength of glass ceramic is very high and experts at the British Geological Survey (BGS) deemed it too dangerous to load until catastrophic failure occurred.

7.2.4 Oven dried concrete RTD experimental results summary

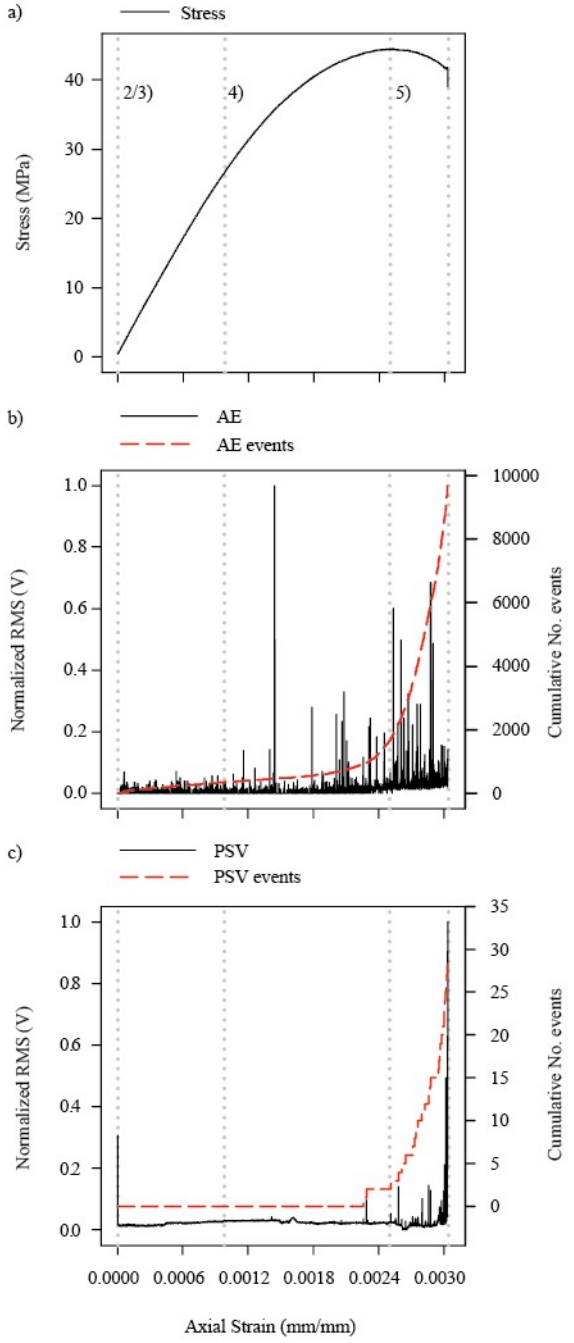

Part 1 *– Strain based RTD loading data: a) applied stress; b) normalized piezoelectric transducer RMS voltage and cumulative number of AE events; and c) normalized PSV RMS voltage and cumulative number of PSV events. Loading stages 1 to 5 are defined in chapter 5.5.*

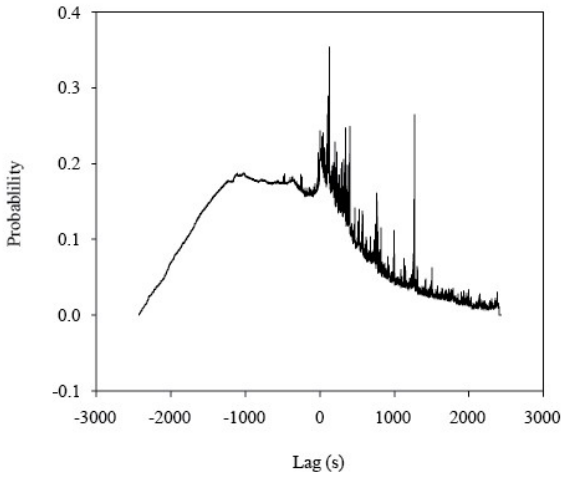

Part 2 – Overall cross-correlation: *Probability of correlation between PSV and AE events at varying lag times. A positive lag time indicates PSV lags behind AE and negative lag time indicates AE lags behind PSV.*

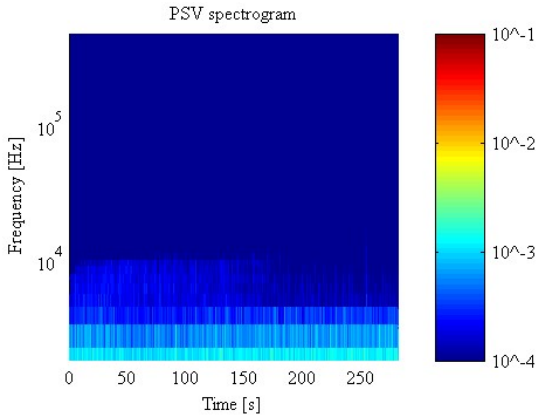

Part 3 – PSV spectral density.

Linear regression	$r^2 = 0.98$
Max Strength	44.44 MPa
Max PSV amplitude	0.797 mV
Max AE amplitude	94 dB

Part 4 – loading and statistical data: *The linear regression r^2 is computed between cumulative PSV and AE events.*

Cross-correlation between PSV and AE events				
Loading stage	2/3	4	5	Entire test
Coefficient	0.47	0.27	0.24	0.24
Lag time (s)	-0.25	-4.75	0	0

Part 5– cross-correlation data: *A negative lag time indicates AE evens lag behind PSV events and a positive lag time indicates PSV events lag behind AE events at the maximum probability of correlation (coefficient).*

Figure 7-2 Oven dried concrete results summary. *Part 1) strain based stress, PSV and AE plot; Part 2) overall cross-correlation plot; Part 3) PSV spectrogram; Part 4) experimental data; Part 5) cross-correlation summary per stage of loading.*

The uniaxial RTD loading data for an air dried concrete specimen is shown in Figure 7-2. The applied stress, AE event amplitude, cumulative number of AE events, PSV event amplitude and cumulative number of PSV events with respect to axial strain, is shown in Part 1 of the figure. The PSV spectrogram in Part 3 shows low amplitude PEPS throughout the experiment and the PEPS frequency decreases from ~175 s towards the end of the experiment. There is considerably more PSV activity visible in the spectrogram compared to the air dried (Figure 7-3) and saline saturated (Figure 7-5) concrete experiments, but not the water saturated (Figure 7-4) experiment. The maximum cross-correlation coefficient lies outside of expected lag time range of ±15 s, thus the highest coefficient within the expected range was chosen for analysis. The resulting cross-correlation between PSV and AE is higher than the water (Figure 7-4) and saline (Figure 7-5) saturated experiments and PSV and AE activity occur simultaneously, as shown in Part 5. There are multiple peaks in in the cross-correlation probability, as shown in Part 2, indicating that the lag time between PSV and AE shows variability. However, the linear regression between cumulative number of AE and PSV events is high, as shown in Part 4.

There is a small increase in AE event rate at the beginning of Stage 2/3, after which the rate remains constant and the event amplitude is relatively low throughout the stage. There is little to no PSV activity throughout the stage, apart from a spike in PSV amplitude at the beginning. The highest correlation between PSV and AE occurs during Stage 2/3 and PSV activity occurs before AE activity.

Over the course of Stage 4 the AE amplitude increases, there are multiple spikes in activity and the largest amplitude event occurs at ~1.4×10^{-3} mm/mm. The AE event rate remains stable initially, however after ~1.9×10^{-3} mm/mm the event rate begins to increase throughout the rest of the stage. The PSV amplitude is relatively low during this stage, however there are spikes in PSV amplitude nearing the end of the stage and an increase in event rate. The cross-correlation probability is lower than the previous stage and PSV events occur before AE events.

During the final stage of loading there is a surge in both AE a PSV event rate, and the amplitude of PSV and AE events increases towards material failure. The largest PSV amplitudes occur during this stage, however this is not the case with regards to the AE amplitude. This stage has the lowest cross-correlation probability and PSV and AE events occur simultaneously.

7.2.5 Air dried concrete RTD experimental results summary

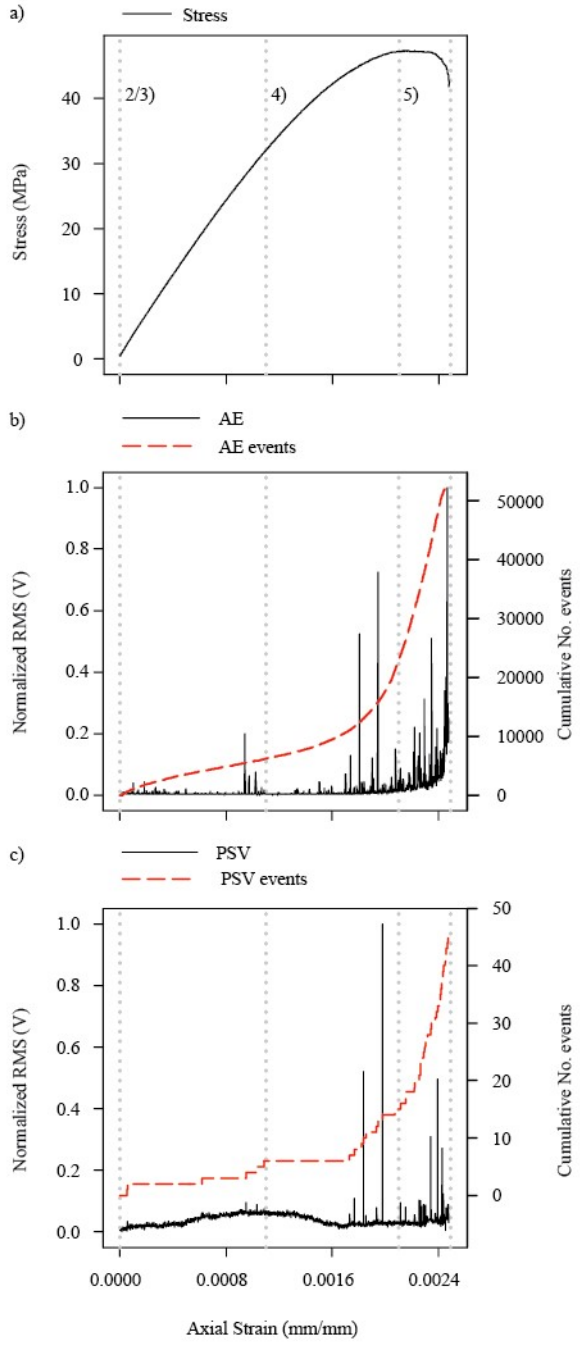

Part 1 – Strain based RTD loading data: *a) applied stress; b) normalized piezoelectric transducer RMS voltage and cumulative number of AE events; and c) normalized PSV RMS voltage and cumulative number of PSV events. Loading stages 1 to 5 are defined in chapter 5.5.*

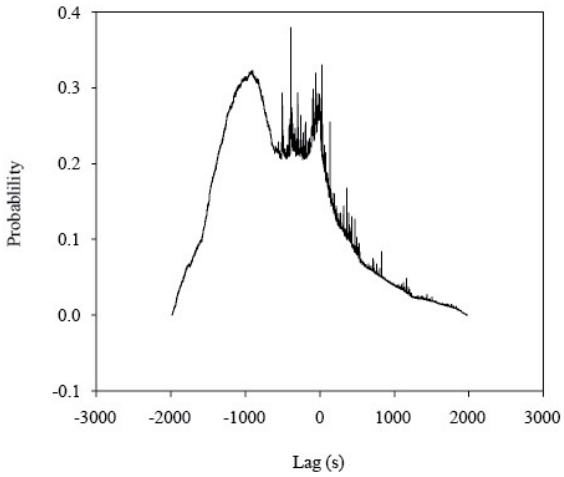

Part 2 – Overall cross-correlation: *Probability of correlation between PSV and AE events at varying lag times. A positive lag time indicates PSV lags behind AE and negative lag time indicates AE lags behind PSV.*

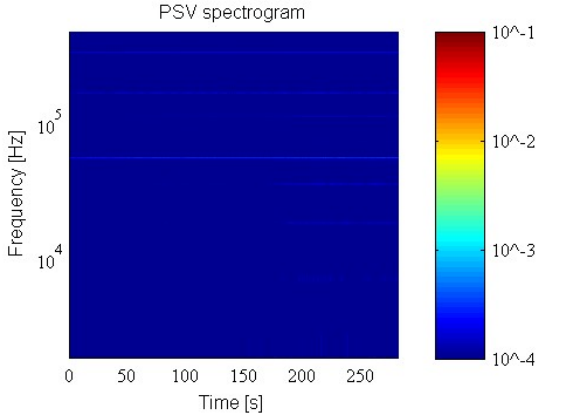

Part 3 *– PSV spectral density.*

Linear regression	$r^2 = 0.9785$
Max Strength	47.25 MPa
Max PSV amplitude	0.47 mV
Max AE amplitude	72 dB

Part 4 – loading and statistical data: *The linear regression r^2 is computed between cumulative PSV and AE events.*

Cross-correlation between PSV and AE events				
Loading stage	2/3	4	5	Entire test
Coefficient	0.53	0.49	0.61	0.33
Lag time (s)	1.75	7	-14.25	7

Part 5– cross-correlation data: *A negative lag time indicates AE evens lag behind PSV events and a positive lag time indicates PSV events lag behind AE events at the maximum probability of correlation (coefficient).*

Figure 7-3 Air dried concrete results summary. *Part 1) strain based stress, PSV and AE plot; Part 2) overall cross-correlation plot; Part 3) PSV spectrogram; Part 4) experimental data; Part 5) cross-correlation results summary per stage of loading.*

The uniaxial RTD loading data for an air dried concrete specimen, is shown in Figure 7-3. The applied stress, AE event amplitude, cumulative number of AE events, PSV event amplitude and cumulative number of PSV events, with respect to axial strain, is shown in Part 1 of the figure. The PSV spectrogram in Part 3 shows little to no PSV activity throughout the experiment compared to the oven dried experiment (Figure 7-2). The maximum cross-correlation coefficient lies outside if expected lag time range of ± 15 s, thus the highest coefficient within the expected range was chosen for analysis. The resulting cross-correlation between PSV and AE is highest out of the concrete experiments and PSV occurs after AE activity as shown in Part 5. There are multiple peaks in in the cross-correlation probability as shown in Part 2, indicating that the lag time between PSV and AE shows variability. However, the linear regression between cumulative number of AE and PSV events is high as shown in Part 4.

At the beginning of Stage 2/3 there is an increase in AE event rate, however the AE and PSV event amplitudes are relatively small. When the strain reaches ~$0.5x10^{-3}$ mm/mm, there is a steady increase in PSV amplitude up until the end of the stage. There is a spike in AE activity at ~$0.9x10^{-3}$ mm/mm, that appears to coincide with the peak in PSV amplitude. The AE event rate increases at an almost linear rate throughout the rest of stage and there is an increase PSV event rate nearing the end of Stage 2/3. During this stage there is a correlation between AE activity and PSV activity and AE events occur before PSV activity.

In the beginning of Stage 4, there is a steady decline in PSV amplitude and the AE event amplitude is relatively low. The AE event rate remains steady up until ~$1.75x10^{-3}$ mm/mm, after which there is a surge in both AE and PSV event rate towards the end of the stage. There are two distinct high amplitude PSV and AE events in the latter half of Stage 4, along with a number of lower amplitude spikes. The cross-correlation probability is lowest during this stage and AE events occur before PSV activity.

Throughout Stage 5 there is an exponential surge in both AE amplitude and event frequency, but towards the end of the stage the AE event rate reduces. A similar exponential increase in PSV event rate can be observed throughout this stage. The PSV amplitude increases initially and then declines prior to material failure at the end of Stage 5. This stage has the highest correlation between AE and PSV activity and PSV events occur before AE events.

7.2.6 Water Saturated concrete RTD experimental results summary

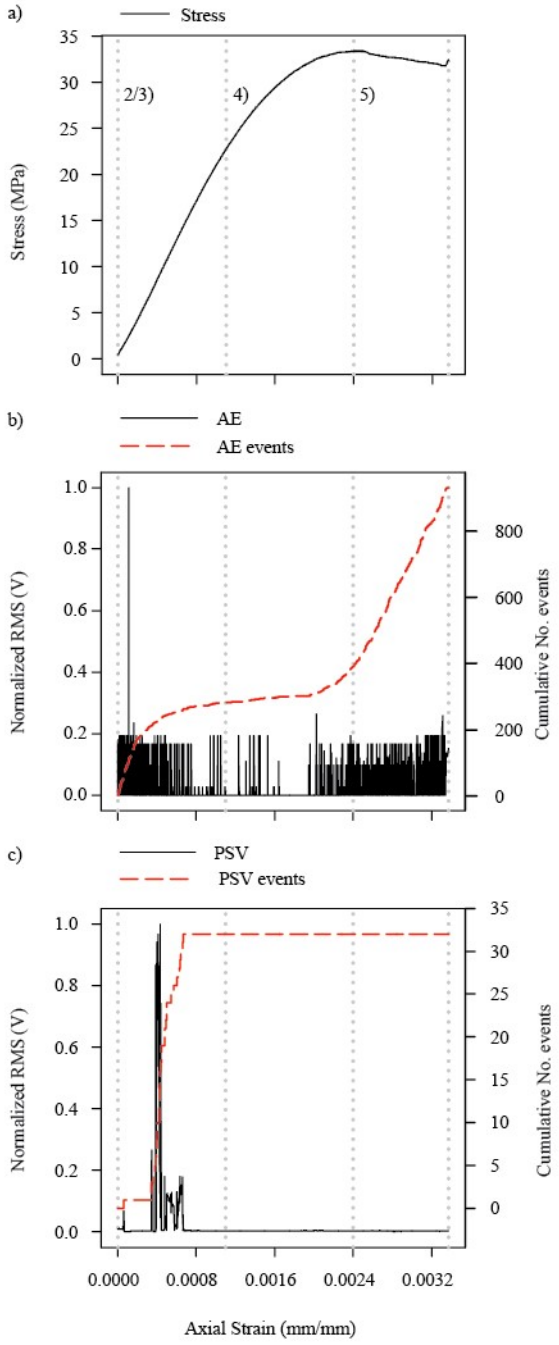

Part 1 – Strain based RTD loading data: *a) applied stress; b) normalized piezoelectric transducer RMS voltage and cumulative number of AE events; and c) normalized PSV RMS voltage and cumulative number of PSV events. Loading stages 1 to 5 are defined in chapter 5.5.*

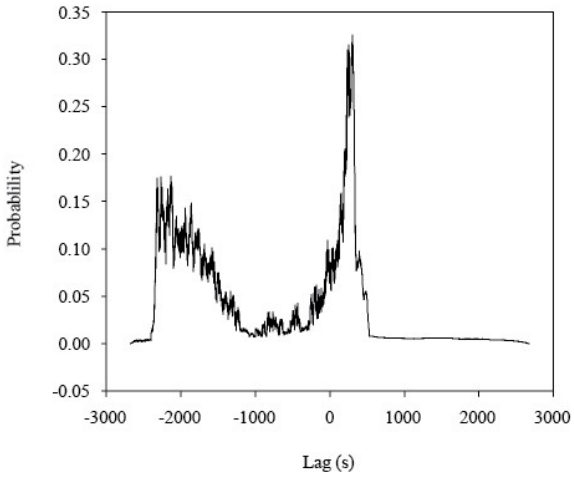

Part 2 – Overall cross-correlation: *Probability of correlation between PSV and AE events at varying lag times. A positive lag time indicates PSV lags behind AE and negative lag time indicates AE lags behind PSV.*

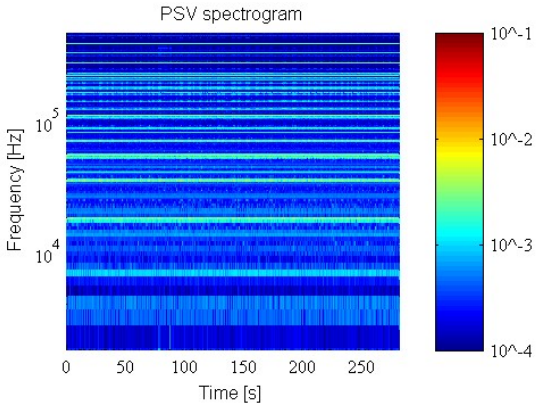

Part 3 – PSV spectral density.

Linear regression	$r^2 = 0.23$
Max Strength	33.39 MPa
Max PSV amplitude	4.30 mV
Max AE amplitude	78.5 dB

Part 4 *– loading and statistical data: The linear regression r^2 is computed between cumulative PSV and AE events.*

Cross-correlation between PSV and AE events				
Loading stage	2/3	4	5	Entire test
Coefficient	0.14	0.22	0.54	0.11
Lag time (s)	-8.25	-14	0	-8.25

Part 5– cross-correlation data: *A negative lag time indicates AE evens lag behind PSV events and a positive lag time indicates PSV events lag behind AE events at the maximum probability of correlation (coefficient).*

Figure 7-4 Water saturated concrete results summary. *Part 1) strain based stress, PSV and AE plot; Part 2) overall cross-correlation plot; Part 3) PSV spectrogram; Part 4) experimental data; Part 5) cross-correlation results summary.*

The uniaxial RTD loading data for a water saturated concrete specimen, is shown in Figure 7-4. The applied stress, AE event amplitude, cumulative number of AE events, PSV event amplitude and cumulative number of PSV events with respect to axial strain, is shown in Part 1 of the figure. The PSV spectrogram in Part 3, shows relatively high amplitude PEPS in different frequency bands throughout the entire measured bandwidth. The maximum cross-correlation coefficient lies outside of the expected lag time range of ±15 s, thus the maximum coefficient within the expected range was chosen for analysis. The resulting cross-correlation between PSV and AE is lowest out of the concrete experiments and PSV occurs before AE activity, as shown in Part 5. There are multiple peaks in the cross-correlation probability, as shown in Part 2, indicating that the lag time between PSV and AE shows variability. In addition, the linear regression r^2 value between PSV and AE cumulative events is low, as shown in Part 4.

At the start of Stage 2/3 there is little to no PSV activity, apart from a single relatively low amplitude PSV event at ~$0.69x10^{-3}$ mm/mm. In contrast, there is a sharp increase in the frequency of AE events and the amplitude of these events stays constant, apart from a single high amplitude AE event occurring at ~$0.011x10^{-3}$ mm/mm. The AE event rate begins to decline to a lower stable rate from ~$0.34x10^{-3}$ mm/mm for the rest of the stage. As the AE event rate is beginning to decline, there is a surge of high amplitude PSV activity, with the highest amplitude event occurring at ~$0.43x10^{-3}$ mm/mm. Subsequently, the PSV activity rapidly declines to the base line level from ~$0.7x10^{-3}$ mm/mm, onwards. Toward the end of stage 2/3 the PSV remains at its baseline amplitude; there are relatively low amplitude AE events followed by mean amplitude events and the AE event frequency remains low. The correlation between AE and PSV is lowest during this stage and AE activity occurs after PSV activity.

Throughout Stage 4 there are AE events and the PSV remains at its baseline level, throughout the stage. There is an absence of AE events from the beginning of Stage 4 up to ~$1.2x10^{-3}$ mm/mm and in the middle of the stage from ~$1.63x10^{-3}$ mm/mm to ~$1.9x10^{-3}$ mm/mm; after which, a single larger AE event occurs at ~$2.0x10^{-3}$ mm/mm. The AE event rate remains constant until a strain of ~$2.0x10^{-3}$ mm/mm is reached, after which there is a large increase in AE event frequency. The cross-correlation probability is higher than the previous stage and PSV activity occurs before AE events.

The number of AE events increases linearly up to the point of material fracture, at the end of Stage 5. However, the AE event amplitude remains fairly constant at around ~0.2 V_{norm}, but from ~$3.0x10^{-3}$ mm/mm to the end of Stage 5 there is an increase in AE amplitude. There is little to no PSV activity during this stage. The correlation between PSV and AE activity is highest during this stage, with PSV and AE activity occurring simultaneously.

7.2.7 Saline Saturated concrete RTD experimental results summary

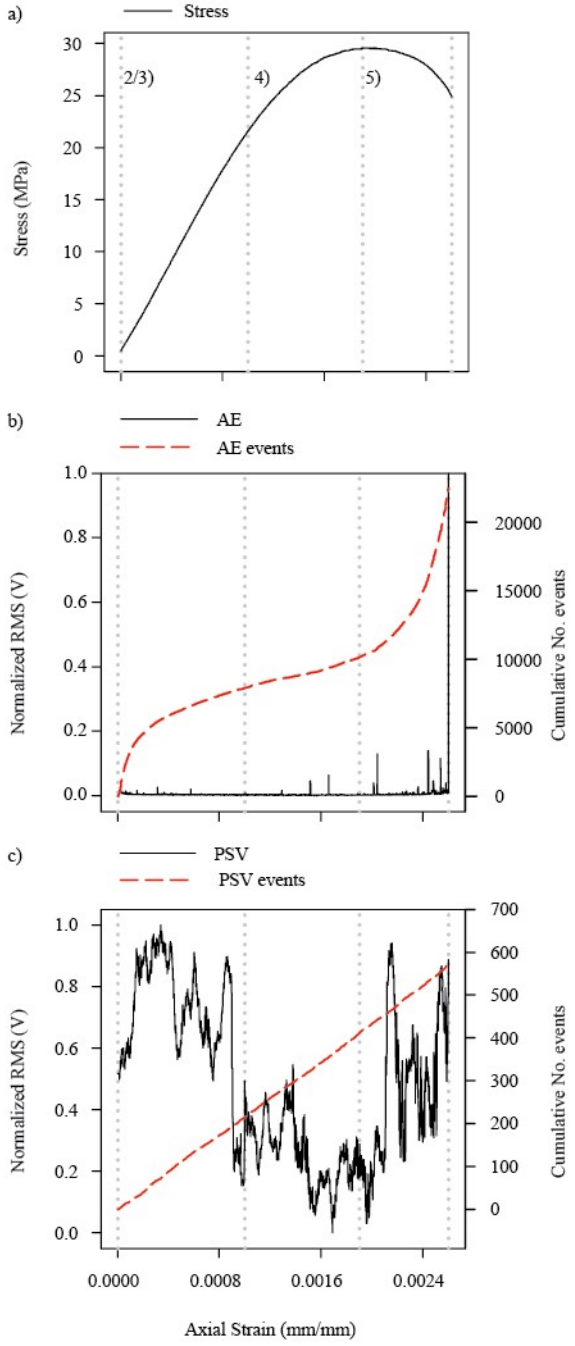

Part 1 – Strain based RTD loading data: *a) applied stress; b) normalized piezoelectric transducer RMS voltage and cumulative number of AE events; and c) normalized PSV RMS voltage and cumulative number of PSV events. Loading stages 1 to 5 are defined in chapter 5.5.*

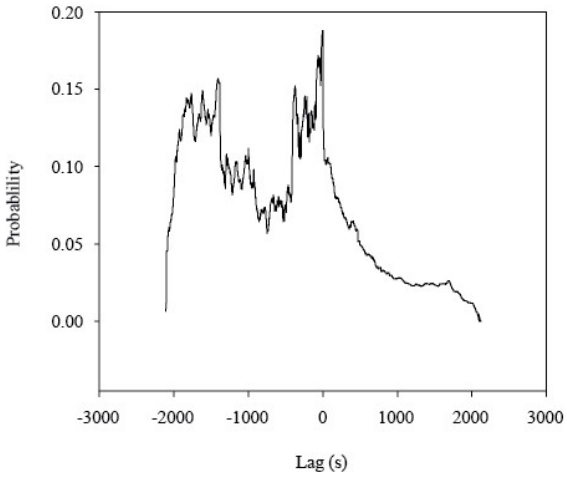

Part 2 – Overall cross-correlation: *Probability of correlation between PSV and AE events at varying lag times. A positive lag time indicates PSV lags behind AE and negative lag time indicates AE lags behind PSV.*

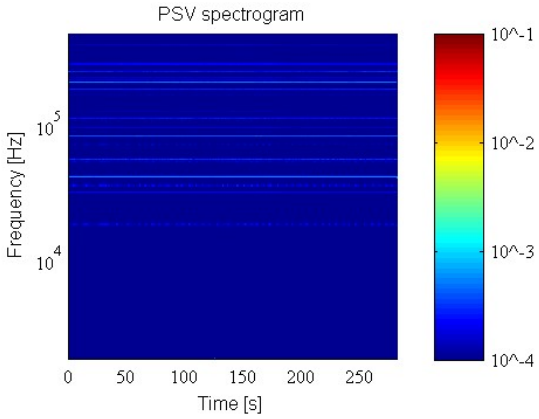

Part 3 – PSV spectral density.

Linear regression	r^2 = 0.8281
Max Strength	29.6 MPa
Max PSV amplitude	1.27 mV
Max AE amplitude	88.5 dB

Part 4 – loading and statistical data: *The linear regression r^2 is computed between cumulative PSV and AE events.*

Cross-correlation between PSV and AE events				
Loading stage	2/3	4	5	Entire test
Coefficient	0.81	0.45	0.26	0.19
Lag time (s)	0	-4.75	-0.75	-0.75

Part 5– cross-correlation data: *A negative lag time indicates AE evens lag behind PSV events and a positive lag time indicates PSV events lag behind AE events at the maximum probability of correlation (coefficient).*

Figure 7-5 Saline saturated concrete results summary. *Part 1) strain based stress, PSV and AE plot; Part 2) overall cross-correlation plot; Part 3) PSV spectrogram; Part 4) experimental data; Part 5) cross-correlation results summary.*

The uniaxial RTD loading data for a saline saturated concrete specimen is shown in Figure 7-5. The applied stress, AE event amplitude, cumulative number of AE events, PSV event amplitude and cumulative number of PSV events with respect to axial strain, is shown in Part 1 of the figure. The PSV spectrogram in Part 3, shows little to no PSV activity compared to the oven dried (Figure 7-2) concrete experiment. The cross-correlation between PSV and AE is lower than the oven dried (Figure 7-2) and air dried (Figure 7-3) experiments and PSV occurs before AE activity, as shown in Part 5. There are multiple peaks in the cross-correlation probability, as shown in Part 2, indicating that the lag time between PSV and AE shows variability. However, the PSV and AE cumulative regression r^2 is relatively high, as shown in Part 4.

Initially, during Stage 2/3 the AE event frequency increases sharply until ~0.057x10^{-3} mm/mm, subsequently the frequency of events declines until a stable rate is reached which then continues throughout the rest of the stage. At the beginning of the stage there are distinct relatively low amplitude spikes in AE activity. The PSV amplitude varies from ~0.14 V_{norm} to ~1 V_{norm} over the course of Stage 2/3. The correlation between PSV and AE activity is highest during this stage, with AE and PSV occurring simultaneously.

At the onset of Stage 4 the AE event rate remains stable and there is relatively low amplitude AE activity throughout. There are three distinct higher amplitude AE events during the stage, occurring at ~1.3x10^{-3} mm/mm, ~1.5x10^{-3} mm/mm and ~1.7x10^{-3} mm/mm, increasing in amplitude with each occurrence. The AE event rate begins to increase after the third high amplitude AE event. The PSV activity rapidly declines in amplitude just before the end of Stage 4 and ranges between ~0 V_{norm} and ~0.54 V_{norm}. The cross-correlation probability is lower than the previous stage and AE occurs after PSV activity.

During Stage 5, the AE event rate increase exponentially throughout the stage. At ~2.0x10^{-3} mm/mm there are a number of high amplitude AE events that appear to coincide with a large increase in PSV activity. Throughout the rest of the stage, there is a surge in baseline AE event amplitude along with transient high amplitude events, prior to the fracture point at the end of the stage. The PSV activity remains relatively high throughout Stage 5, varying between around ~0.03 V_{norm} to ~0.91 V_{norm}. During the final stage of loading the correlation between PSV and AE is lowest, with PSV occurring before AE activity.

7.3 Discussion

7.3.1 PSVs in concrete specimens for different environmental conditions

PSVs were observed in all concrete specimens in the range of millivolts, this provides a much better signal to noise ratio than measuring the associated PSCs, which has been shown to be the range of Pico amps in rock [82, 151] and cement mortar specimens [15]. Figure 7-6 shows the average PSV amplitude for concrete RTD experiments, in different environmental conditions. All amplitudes are referred to the input of the EPS (i.e. the rock surface) and are in a similar range to the rocks lithologies tested in chapter 6.

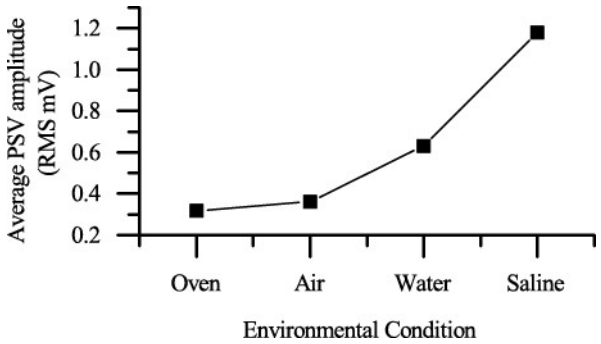

Figure 7-6 PSV average amplitude for concrete specimens in each environmental condition.

The average PSV amplitude increases with higher water saturation of the concrete specimens; the water saturated specimen has a high PSV amplitude followed by air dried then the oven dried specimen. The saline saturated concrete sample has the highest average PSV amplitude. The same phenomena occurred with the rock RTD experiments, detailed in chapter 6.3.1.

Oven dried and air died concrete specimens emitted transient spikes in PSV, that appear to be related to AE events during Stage 4 and 5 of loading. However, a different behaviour was observed in Stage 2/3 of loading, where the amplitude of PSV is reduced and lower frequency fluctuations in amplitude are observed. This observation suggests that relatively higher amplitude transient spikes in PSV are related to unstable microcracking and macrocracking events and the lower amplitude PSV observed in Stage 2/3 are related to stable microcracking events in the concrete structure. Previous research has only observed PSC emissions beyond the elastic limit (Stage 2) of loading in marble samples [18].

The PSV behaviour is drastically altered when the concrete is saturated with water. The mean amplitude of PSV is higher than that of the oven and air dried samples. In addition, the PSV activity is relatively low apart from a large surge in PSV activity during Stage 1, which could be associated with the electrokinetic effect of water movement. A solid-liquid charged interface known as the electrical double layer (EDL), could be formed between concrete grains and the water saturated in the pores of concrete. When a pressure gradient is produced (i.e. from pore closure during Stage 1) a potential difference across the sample could be created, in agreement with theory [11, 74].

The PSV behaviour is again changed by saline saturation of the concrete. The mean PSV amplitude for the saline saturated concrete (1.18 mV RMS) is also higher than water saturated and air dry concrete. Saline solution (56.58 mS) is considerably more electrically conductive than reverse osmosis (RO) purified water (474 uS). This could be responsible for the higher mean PSV amplitude of the saline saturated concrete, compared to water saturated concrete and the lack of a surge in PSV during pore closure in Stage 1 of the saline saturated sample.

PSV was also detected in the glass ceramic (Macor ®), a non-piezo homogeneous specimen. The PSV average amplitude was 3.7 millivolts RMS which is larger in amplitude than the quartz rich concrete specimens. This indicates PSV emissions in manmade materials cannot be generated purely by the piezoelectric effect of quartz, other mechanism/s must be involved.

7.3.2 The effect of environmental condition on cross-correlation between PSV and AE activity in concrete

As shown in Figure 7-7 there is some degree of correlation between AE and PSV activity in all samples, however environmental condition does have an effect on the correlation.

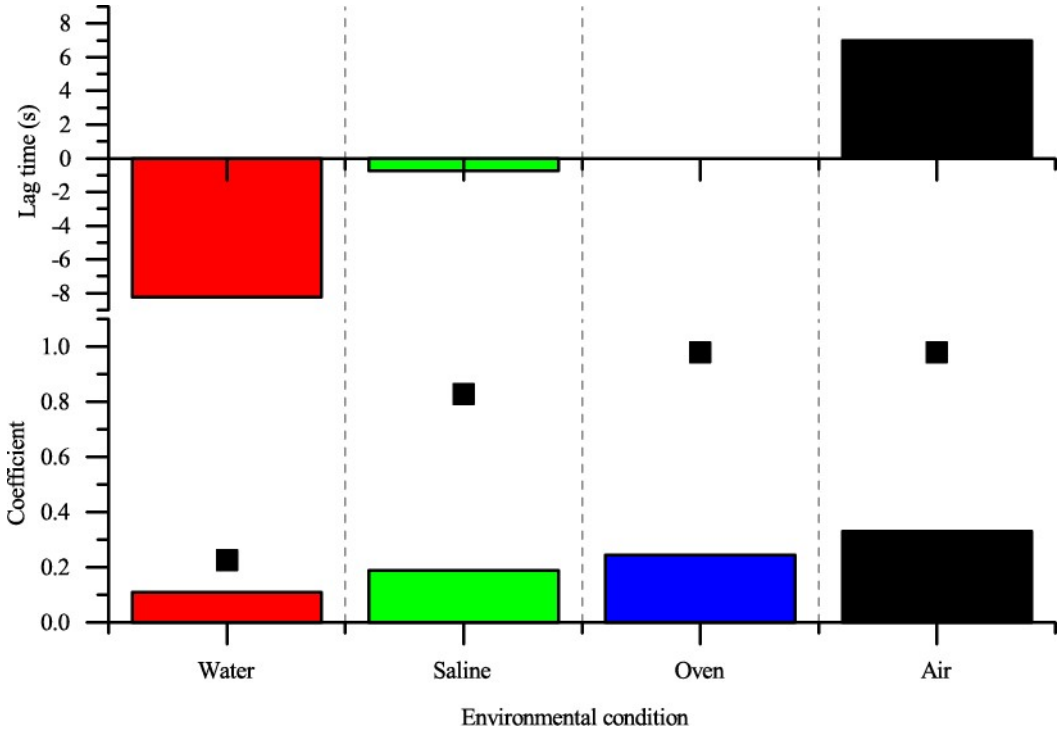

Figure 7-7 Overall cross-correlation data summary. *The graph shows the overall cross-correlation data grouped by environmental condition, the data is plotted in ascending order of cross-correlation coefficient. A negative lag time indicates AE lags behind AE activity and positive lag time indicates PSV lags behind AE activity. The scatter graph represents the linear regression r^2 values for cumulative PSV and AE events.*

The lowest correlation between AE and PSV activity occurred in the water saturated sample, followed by the saline saturated sample; the highest correlation is present in the air dried sample, followed by the oven dried. For water and saline saturated samples, the PSV activity occurred before AE activity; for oven dried, the PSV and AE activity occurred simultaneously and for air dried AE activity occurred before PSV activity.

As stated in the previous results chapter (section 6.3.3) my hypothesis is that increasing levels of water or saline saturation could discharge PSV generated by micro/macro cracking events and thus reduce PSV-AE correlation. This is because water and saline are more electrically conductive than air and thus as the pores of the concrete or rocks become more saturated with these liquids the discharging effect is increased. For example, air has an electrical conductivity of 3 fS to 8 fS, whereas the purified water and saline solution used in thesis study have conductance's of 474 µS and 56.58 mS respectively. Therefore, you would expect the oven dried specimens to have the best PSV-AE correlation followed by the air dried, water saturated and saline saturated specimens to have the worst correlations. The concrete specimens tested in this results chapter support this hypothesis as shown in Figure 7-7.

All linear regression results for AE and PSV cumulative events have a p-values < 0.05 indicating the relationship between the predictor variable (AE) and the response variable (PSV) is statistically significant. The r^2 value represents the goodness of fit for the regression line, i.e. the variation from a linear relationship between cumulative AE and PSV events. For all samples tested, there is a linear relationship between AE and PSV events rate, although the variation from linearity is affected by environmental condition. The r^2 values follow a similar tend to the cross-correlation coefficients, with water saturated having the lowest r^2, the only difference being the oven dried specimen having a higher r^2 value than the air dried specimen.

A linear correlation exists between cross-correlation coefficients and the linear regression r^2 values. The data is normally distributed and thus a Pearson linear correlation [140] was used, yielding a coefficient of 0.86; where a value of 1 would indicate a perfect correlation, 0 no correlation and -1 perfect inverse correlation. This information indicates that the novel PSV event detection method used, is effective for data reduction and can be used to monitor the relationship between PSV and AE activity. The cumulative number of AE and PSV events linear regression analysis. supports the conclusions drawn from established statistic methods used on the raw data, i.e. cross-correlation. However, the p-value (0.14) for the linear correlation was not significant. Therefore, there is a chance the null hypothesis of no correlation between cumulative number of AE and PSV event regression and AE and PSV cross-correlation being true. A larger run of experiments would be needed to verify the suitability of the PSV event detection method in concrete.

7.3.3 Effect of deformation stage on the cross-correlation between PSV and AE activity

The cross-correlation data per stage is shown in Figure 7-8 there are differences in coefficient and lag time between stages of deformation. For the over dried specimen the strongest correlation is between PSV and stable microcrack propagation during Stage 2/3 with PSV occurring before microcracking events. The correlation between PSV and unstable microcrack propagation is lower than the previous stage with PSV occurring before microcracking events. The lowest correlation occurs between PSV and unstable macrocrack propagation and sheer plain development during Stage 5 with PSV occurring after macrocracking and sheer plain development events.

The correlations between PSV and AE activity in the air dried specimen, show less variation in terms of coefficient, but there is greater variation in the lag times. The lowest correlation happens between PSV and unstable microcrack propagation during Stage 4, followed by the correlation between PSV and recoverable stable microcrack propagation during Stage 2/3. For both stages, PSV activity occurs after microcrack events. The highest correlation happens between PSV and unstable macrocrack propagation and sheer plain development during Stage 5, with PSV activity occurring before AE activity.

The lowest correlation for the water saturated specimen occurs between PSV and stable microcrack propagation during Stage 2/3, followed by the correlation between PSV and unstable microcrack propagation during Stage 4. The highest correlation happens between PSV and unstable macrocrack propagation and sheer plain development during Stage 5. PSV activity occurs before stable microcrack propitiation and unstable macrocracking propagation events and occurs simultaneously with unstable macrocrack and sheer plain development events.

The saline saturated specimen has the strongest correlation between PSV and stable microcrack propagation during Stage 2/3, followed by the correlation between PSV and unstable microcrack propagation occurring during Stage 4. The lowest correlation is between PSV and unstable macrocrack propitiation and sheer plane development over Stage 5. PSV and stable microcrack propagation events occur simultaneously, PSV is a precursor to unstable microcrack and macrocrack propagation and sheer plane development.

A likely reason for the difference in lag times between PSV and AE, is that multiple generation mechanisms exist and the dominance of each mechanism changes whilst transitioning through the stages of loading. For instance, the main sources of AE during Stage 2/3 are from stable microcrack propagation, Stage 4 unstable microcrack propagation and coalescence and Stage 5 unstable macrocrack propagation and sheer plane development [132-134]. As for PSV generating mechanism there appears to be at least two mechanisms one that precedes cracking and another in which PSV events occur after cracking.

PSV events that occur after cracking may be a result of charge redistribution due to the formation of new charged fracture surfaces [83]. I propose that charge redistribution may be associated with an accumulation of microcracking/macrocracking events and thus there is not an instantaneous relationship between PSV and cracking events. PSV events that precede AE events may be due stress accumulation before the development of fresh charged fracture surfaces resulting from microcracking, macrocracking and sheer plane development. This would be in agreement with the theory of moving charge dislocations [152].

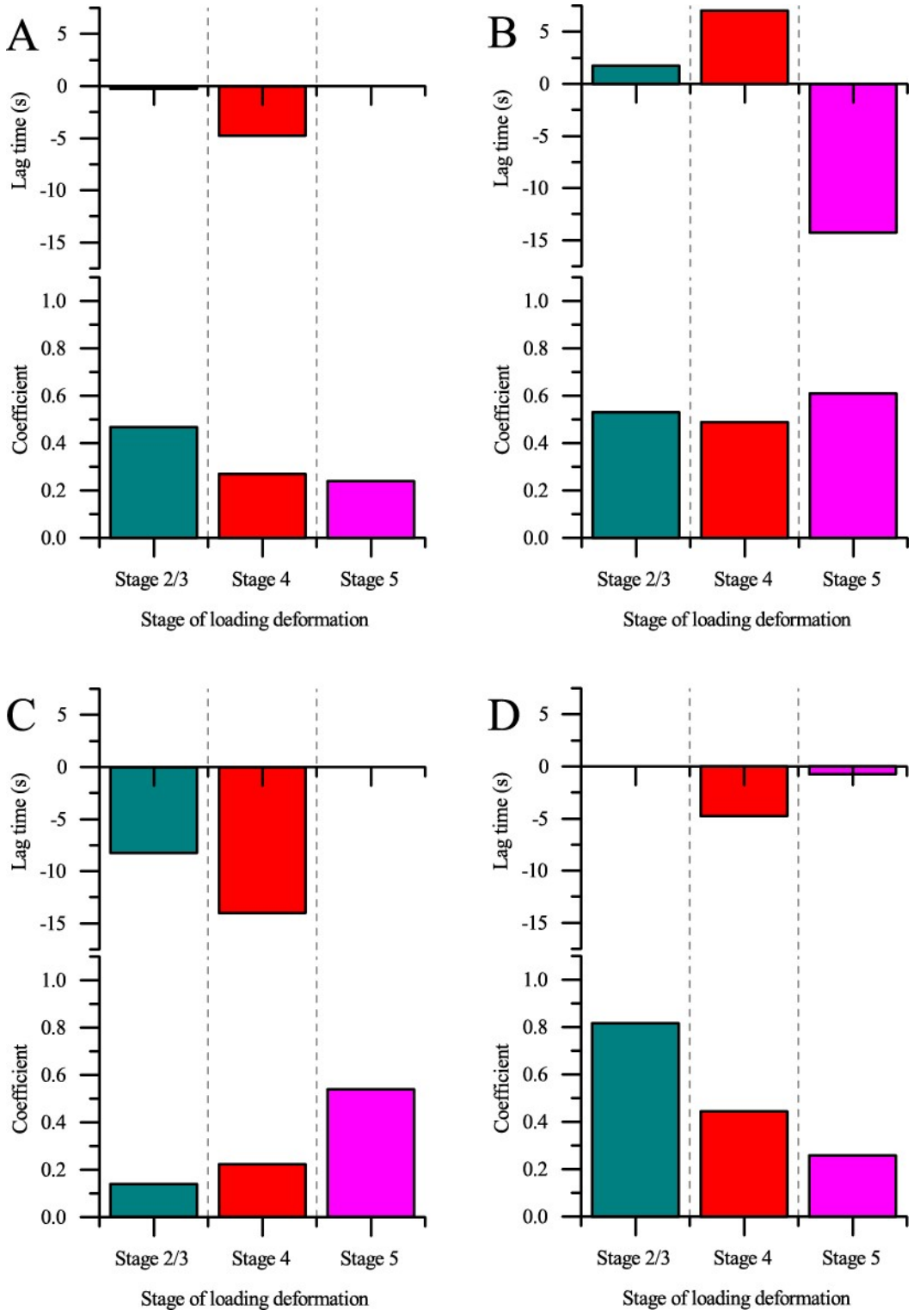

Figure 7-8 Cross-correlation data summary per stage of loading. *The graphs represent the cross-correlation coefficient and lag time per stage of deformation for each specimen tested, where a negative lag time indicates PSV occurs before AE activity and a positive lag time indicates AE occurs before PSV activity., A) Oven dried concrete, B) air dried concrete, C) water saturated concrete and D) saline statured concrete.*

7.3.4 Research question conclusions

Are PSVs present in concrete specimens when subjected to uniaxial loading?

PSVs were observed in all concrete specimens in the range of millivolts, there have been no other studies observing PSE in concrete to date. The PSV-concrete experiments show a much better signal to noise ratio than measuring the associated PSCs, which has been shown to be the range of Pico amps in cement mortar specimens [15].

Are PSVs produced by concrete related to AE?

There was some degree of correlation between PSV and AE in concrete in all environmental conditions (oven dried, air dried, water saturated and saline saturated). Therefore, PSV emissions in concrete are likely associated with AE, however in general the PSV-AE correlations are lower than that of most rock lithologies discussed in the previous chapter.

Can the detection of PSVs be used as an indication of the structural health or the current stage of deformation in concrete?

The deformation loading state had an effect of the PSV-AE cross-correlation in concrete specimens, in terms of cross-correlation coefficient and lag time. A likely reason for the difference in correlation coefficients and lag times between PSV and AE, is that multiple generation mechanisms exist and the dominance of each mechanism changes, whilst transitioning through the stages of loading. Therefore, EPS and piezo transducers could be used to monitor structures simultaneously to identify different stages of deformation by analysing differences in the PSV-AE cross-correlation.

Is EPS technology suitable for the wide scale field monitoring of PSVs over concrete structures?

This is the first study observing PSE in concrete, additionally PSVs were detected in the range of millivolts and thus Faraday shielding of the experiments was not necessary. The aforementioned points and the fact that the EPS lends itself to field use and array formats due the compact size, cost effective and portable nature of the device, indicates that EPS could be used for the wide scale SHM of concrete.

8 UNIAXIAL COMPRESSIVE CYCLIC STRESS TESTING OF MATERIALS IN DIFFERENT ENVIRONMENTAL CONDITIONS USING CAPACITIVELY COUPLED EPSS

In this chapter, an introduction to the Kaiser and Felicity effect of acoustic emissions (AE) and the motivations behind the experiments carried out and presented in this chapter, are presented in section 8.1. Followed by a selection of results pages (section 8.2), showing observations of pressure stimulated voltages (PSV), acoustic emission (AE) and stress for each material specimen tested. Each of the results pages presented shows a truth table, indicating the presence of various effects observed in the PSV and AE activity. The results of each material specimen tested are compared and discussed in section 8.3 at the end of the chapter.

8.1 Introduction

The Kaiser effect in rocks [52, 53] and concrete [54] is a well understood phenomenon with regards to the behaviour of AEs. However, there has not been a great deal of research with regards to the associated electrical emissions, apart from cyclic loading studies of pressure stimulated current (PSC) emissions in marble [18, 82] and granite [81] samples. The Kaiser effect is the absence of AEs at loads not exceeding the previous maximum load (PML) during cyclic loading [52]. The Felicity effect reduces the Kaiser effect, causing AE events to occur before the PML [52]. For more information refer to Figure 2-9 in section 2.4.2, which contains detailed information about Kaiser and Felicity effect and how they interact with each other.

This chapter presents the first study: 1) attempting to characterise PSV during cyclic loading of a wide range of rock lithology and concrete, 2) investigating the Kaiser effect in both PSV emissions and AEs simultaneously in concrete and 3) using a field capable technology i.e. the electric potential sensor (EPS). The experiments carried out and presented in this chapter were undertaken with the aim of answering the following research questions:

Do PSV emissions exhibit a work hardening effect synonymous to the Kaiser effect of acoustic emissions, during cyclic uniaxial loading, in a wide range of rock lithologies and concrete?

Can the detection of PSV during cyclic loading be used as an indication of damage in rocks and concrete?

Is EPS suitable for monitoring PSV during cyclic loading and is it a viable technology for field use?

8.2 Results

8.2.1 Experimental procedure

Oven dried cylindrical specimens of various rock lithology were instrumented with two axial strain gauges, a circumferential strain gauge, two piezo-transducers and two capacitively coupled EPS. Each rock specimen was subjected to a cyclic ramp to destruction (RTD) uniaxial loading, using a servo controlled load frame. The full details of the testing procedure are shown in chapter 5. For each material specimen tested, a constant strain loading rate was chosen and the maximum applied stress was increased for each successive loading cycle, until catastrophic material failure occurred within 4-6 loading cycles.

The results presented in this chapter show the applied stress and resulting AEs and PSV activity during loading thus indicating the Kaiser effect of AEs and any relationship this may have with PSV emissions. A new phenomenon observed in this results chapter, coined the 'Initial loading effect' is an increase in PSV events at the onset of a loading cycle, before the onset of Kaiser effect and thus an absence of PSV events.

The experiments are presented in the same order as shown in Table 8-1, for this thesis chapter. The AE events discussed in this chapter, are a combination of events detected by two piezo transducers mounted on steel platens above and below the material specimen. The PSV events are calculated from the differential signal of two EPS mounted diametrically opposite each other on the material specimen. A detailed explanation of the PSV event detection method is described in section 4.7.

Material	Environmental condition	Figure number
Syenogranite	Oven dried	Figure 8-1
Sandstone	Oven dried	Figure 8-2
Marble	Oven dried	Figure 8-3
Schist	Oven dried	Figure 8-4
Gabbro	Oven dried	Figure 8-5
Concrete	Oven dried	Figure 8-6

Table 8-1 List of experiments presented in results chapter 8. *The experiments appear in the table in the same order as they are presented in this thesis chapter.*

8.2.2 Oven dried syenogranite cyclic RTD experimental results summary

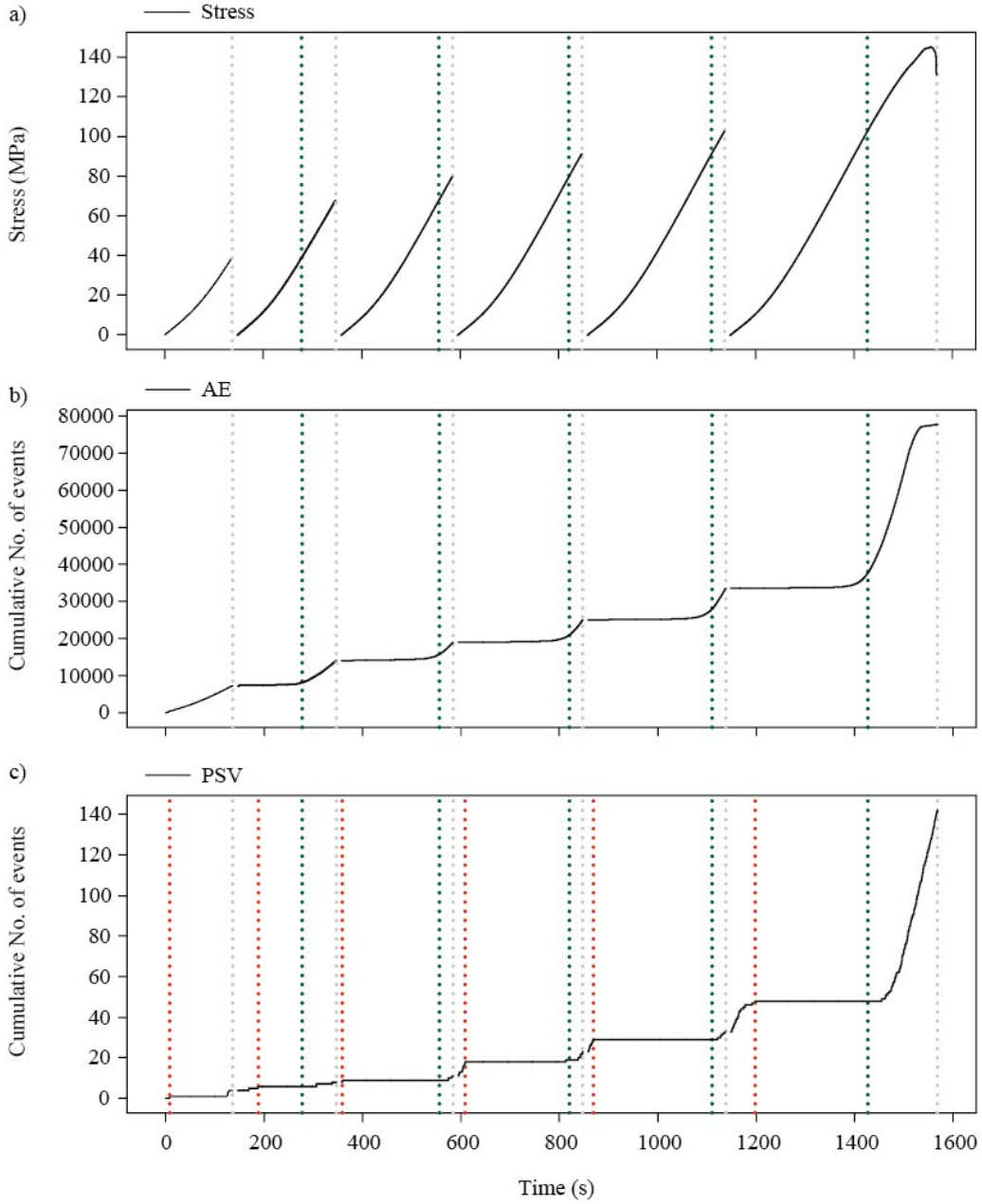

***Part 1 time based cyclic RTD loading data**: a) Applied stress (MPa), b) cumulative number of AE events and c) cumulative number of PSV events. The grey vertical lines represent the end of each loading cycle, green lines represent the PML threshold and the red lines indicate the end of the initial loading effect in the PSV activity.*

	PSV			AE	
	Initial Loading	**Kaiser**	**Felicity**	**Kaiser**	**Felicity**
Cycle 1	✓	NA	NA	NA	NA
Cycle 2	✓	✓	✗	✓	✓
Cycle 3	✓	✓	✗	✓	✓
Cycle 4	✓	✓	✗	✓	✓
Cycle 5	✓	✓	✗	✓	✓
Cycle 6	✓	✓	✗	✓	✓

***Part 2 Effects truth table:** the table indicates if the following effects associated with PSV and AEs are present for each loading cycle: Kaiser effect, Felicity effect and initial loading effect.*

***Figure 8-1 Oven dried syenogranite results summary**. Part 1) time based stress, PSV cumulative number of events and AE cumulative number of events plot; Part 2) table indicating the presence of Kaiser, Felicity and initial loading effect.*

The cyclic RTD loading of an oven dried syenogranite specimen is shown in Figure 8-1. The maximum strength of the material was 145.15 MPa and the resulting maximum PSV and AE amplitudes were 2.87 mV and 98.2 dB respectively. The Felicity effect of AEs is observed during all cycles of loading, but is more prominent in the latter cycles. The Felicity effect is not observed in the PSV, as the event activity does not increase until after the PML threshold, apart from a momentary increase of events resulting from the initial loading effect at the onset of each loading cycle.

During the first loading cycle there is an increase in the number of AE events throughout loading. There is a single PSV event at the start of loading (initial loading effect), no further events occur from ~9.35 s to ~117.25 s, after which there is an increase in the number of PSV events.

The AE event rate is low during the second loading cycle (Kaiser effect), until just before the PML threshold at ~ 233.25 s, after which there is an increase in AE activity (Felicity effect). At the start of the loading cycle there is a small increase in PSV events (initial loading effect), no further events occur until after the PML threshold is reached from ~188.25 s to ~ 306.75 s (Kaiser effect), after which the PSV event rate increases.

Cycle 3 shows a relatively low AE event rate before the PML threshold (Kaiser effect) and a significantly increased rate before the threshold (Felicity effect) at ~521.5 s. At the start of the loading cycle there is a single PSV event (initial loading effect), followed by an absence of events between ~363.75 s and ~571.25 s (Kaiser effect) and the PSV event rate increases after the PML.

At the beginning of Cycle 4 the initial loading effect is observed in the PSV, followed by a period of inactivity (Kaiser effect) from ~610.75 s to ~814 s and after the PML threshold is reached there is an increase in event rate. The AE event rate is relatively low initially (Kaiser effect), however at ~772.25 s (which is before the PML threshold) the AE event rate increases (Felicity effect).

The initial loading effect is observed during Cycle 5 in the PSV, followed by a period of inactivity until after the PML threshold (Kaiser effect); once the PML is exceeded the PSV event rate increases. The AE event rate is low initially (Kaiser effect) and increases before the PML threshold is reached at ~1056.25 s (Felicity effect).

The initial loading effect is most prominent during the last loading cycle, resulting in a large number of PSV events, followed by a period of inactivity from ~1198.5 s to ~1453 s (Kaiser effect); once the PML threshold is reached there is a relatively large increase in PSV event rate. The AE event rate is initially low (Kaiser effect) and begins to increase from ~1380.75 s (which is before the PML threshold), indicating Felicity effect is present.

8.2.3 Oven dried sandstone cyclic RTD experimental results summary

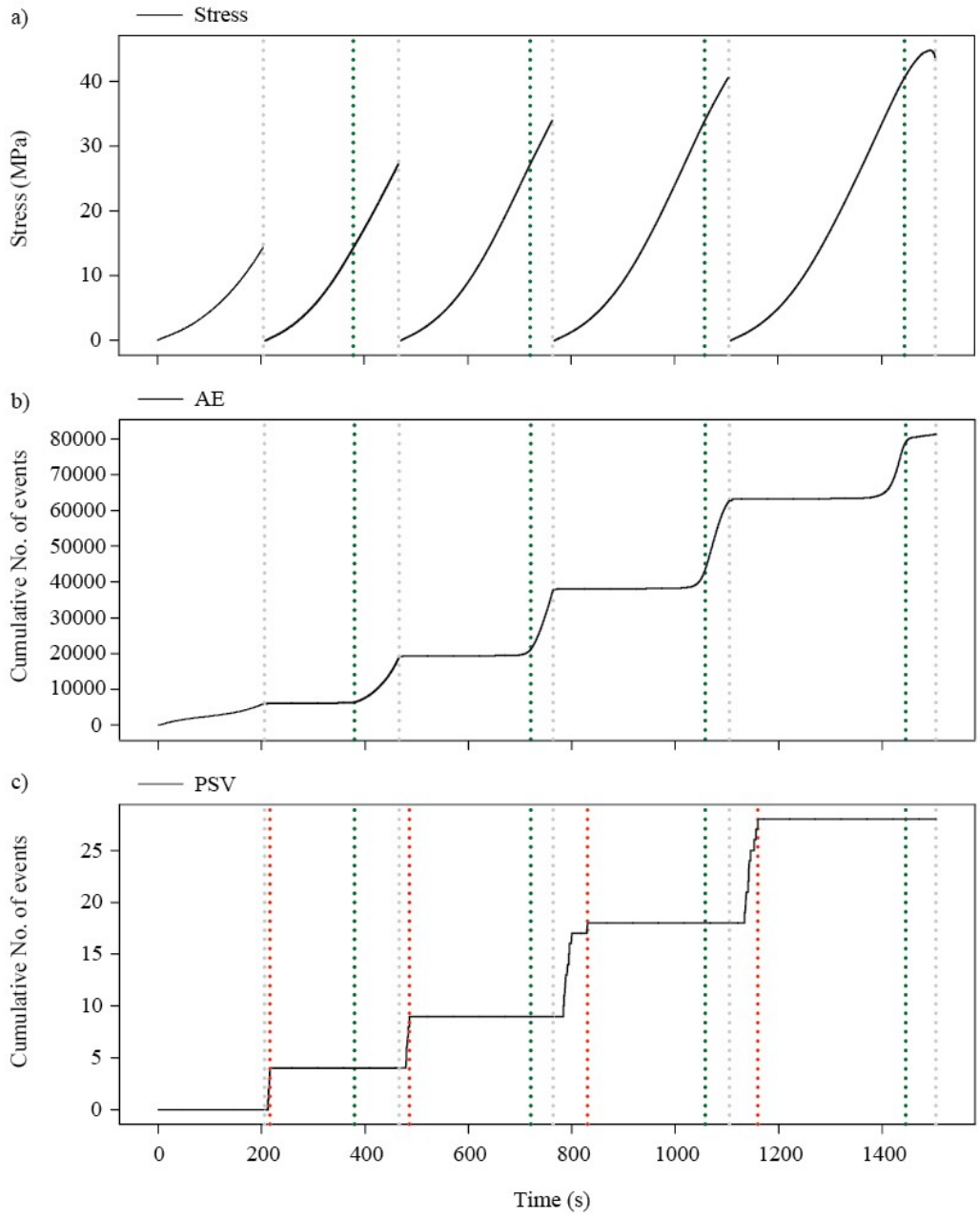

***Part 1 time based cyclic RTD loading data**: a) Applied stress (MPa), b) cumulative number of AE events and c) cumulative number of PSV events. The grey vertical lines represent the end of each loading cycle, green lines represent the PML threshold and the red lines indicate the end of the initial loading effect in the PSV activity.*

	PSV			AE	
	Initial Loading	**Kaiser**	**Felicity**	**Kaiser**	**Felicity**
Cycle 1	✗	NA	NA	NA	NA
Cycle 2	✓	✗	✗	✓	✗
Cycle 3	✓	✗	✗	✓	✓
Cycle 4	✓	✗	✗	✓	✓
Cycle 5	✓	✗	✗	✓	✓

***Part 2 Effects truth table:** the table indicates if the following effects associated with PSV and AEs are present for each loading cycle: Kaiser effect, Felicity effect and initial loading effect.*

***Figure 8-2 Oven dried sandstone results summary**. Part 1) time based stress, PSV cumulative number of events and AE cumulative number of event plot; Part 2) table indicating the presence of Kaiser, Felicity and initial loading effect.*

The cyclic RTD loading of an oven dried sandstone specimen is shown in Figure 8-2. The maximum strength of the specimen was 44.82 MPa, the maximum AE event amplitude was 95.8 dB and the maximum PSV amplitude was 16.15 mV. The Kaiser effect occurs during all loading cycles for the AEs as does the Felicity effect, apart from during loading Cycle 2. With regards to PSV activity, the Felicity and Kaiser effect are not observed for any of the loading cycles, however the initial loading effect is present for Cycles 2 to 5.

Over Cycle 1 there are no PSV events, however there is an increase in the number of AE events up to the point of unloading. The AE event rate is lowest compared to the subsequent cycles post PML threshold events rates.

At the beginning of Cycle 2 the PSV event rate is high (initial loading effect), however after this initial spike in activity there are no further PSV evens for the rest of the stage. The AE event rate is low before the PML threshold, but just before and threshold at ~363.25 s there in an increase in AE event rate for the rest of the loading cycle, indicating the Kaiser and Felicity effect are present.

Over Cycle 3 there are no PSV events, apart from a momentary increase in events at the beginning of the loading cycle, associated with the initial loading effect. The AE event rate is low before the PML threshold and just before the threshold is reached at ~676.5 s there is an increase in AE event rate, providing evidence of Kaiser and Felicity effect.

The AE event rate is very low to begin with during Cycle 4 (Kaiser effect), however the event rate increases before the PML is reached at ~988.75 s (Felicity effect). There are no PSV events during Cycle 4, apart from a momentary spike in the number PSV events at the start of loading, associated with the initial loading effect.

The final loading cycle has the largest increase in the number of PSV events at the start of the cycle, resulting from the initial loading effect, after which there are no more PSV events for the duration the loading cycle. The AE event rate is relatively low to start with, however before the PML threshold is reached at ~1370 s the AE event rate begins to increase. The Kaiser effect is present in the AEs and the Felicity effect is most prominent for this loading cycle.

8.2.4 Oven dried marble cyclic RTD experimental results summary

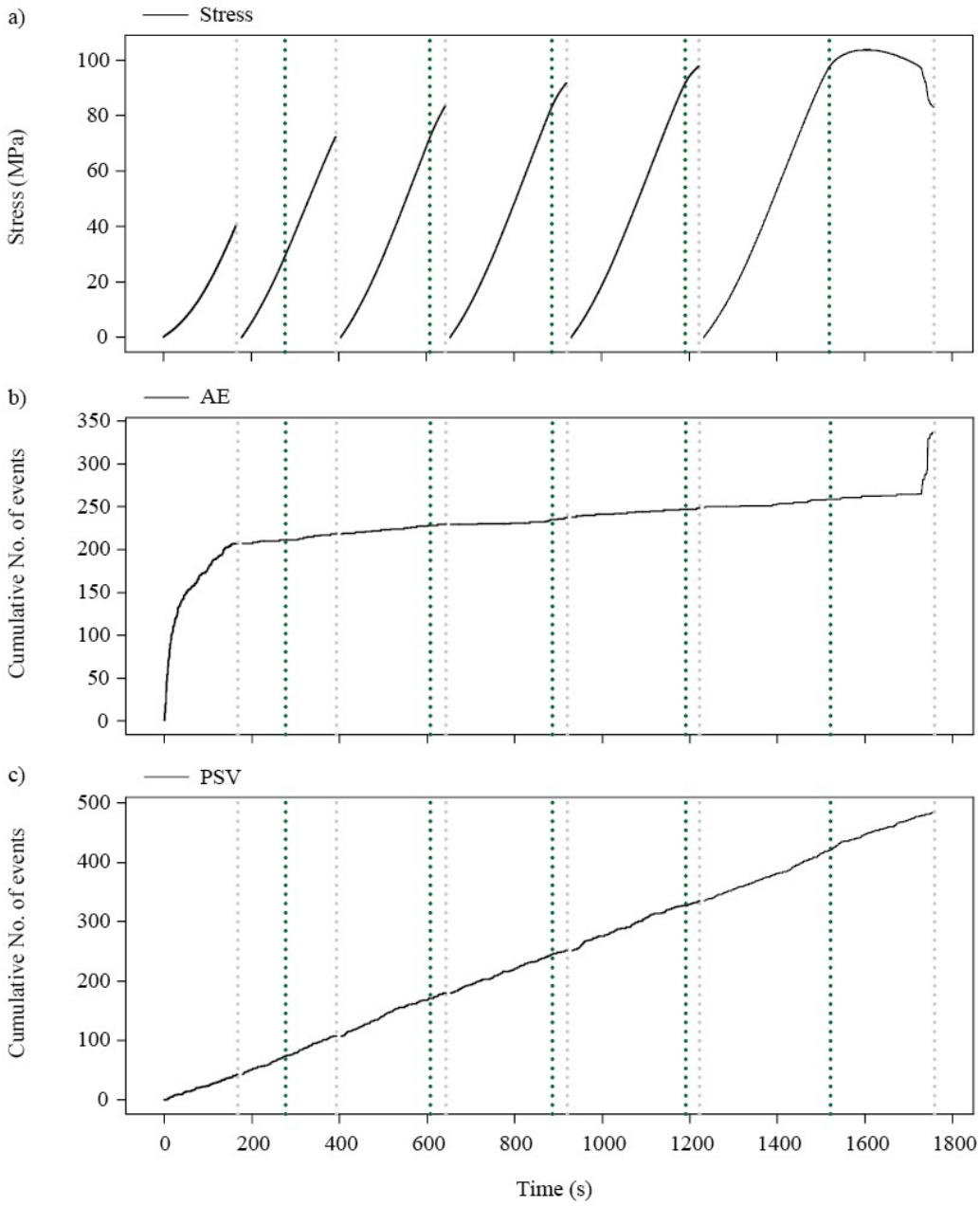

***Part 1 time based cyclic RTD loading data**: a) Applied stress (MPa), b) cumulative number of AE events and c) cumulative number of PSV events. The grey vertical lines represent the end of each loading cycle, green lines represent the PML threshold and the red lines indicate the end of the initial loading effect in the PSV activity.*

	PSV			AE	
	Initial Loading	**Kaiser**	**Felicity**	**Kaiser**	**Felicity**
Cycle 1	✗	NA	NA	NA	NA
Cycle 2	✗	✗	✗	✗	✗
Cycle 3	✗	✗	✗	✗	✗
Cycle 4	✗	✗	✗	✗	✗
Cycle 5	✗	✗	✗	✗	✗

***Part 2 Effects truth table:** the table indicates if the following effects associated with PSV and AEs are present for each loading cycle: Kaiser effect, Felicity effect and initial loading effect.*

***Figure 8-3 Oven dried marble results summary.** Part 1) time based stress, PSV cumulative number of events and AE cumulative number of event plot; Part 2) table indicating the presence of Kaiser, Felicity and initial loading effect.*

The cyclic RTD loading of an oven dried marble specimen, is shown in Figure 8-3. The maximum strength of the spaceman was 103.77 MPa, the maximum AE event amplitude was 67 dB and the maximum PSV amplitude was 0.69 mV. The Kaiser and Felicity effect is not observed in the AEs or the PSV activity.

The highest AE event rate occurs during loading Cycle 1. The PSV event rate is more or less constant, however the AE event rate is initially high and then begins to decline towards the end of the loading cycle. The initial loading effect of PSV emissions is not present during this loading cycle.

Although there are small fluctuations in PSV and AE event rates, they remain constant throughout loading Cycles 2 to 5. The Kaiser effect and Felicity effect are not observable in the AEs and PSV activity during these loading cycles and the initial loading effect of PSV emissions is also not present.

The AE and PSV event rates remain almost constant over the course for the final loading cycle. However, there is an increase in AE event rate after the PML threshold at ~1712.75 s, most likely associated with a post peak inelastic deformation indicated by strain-softening behaviour. The Kaiser effect and Felicity effect are not present in the AE or PSV activity, neither is the initial loading effect of PSV emissions during this loading cycle.

8.2.5 Oven dried schist cyclic RTD experimental results summary

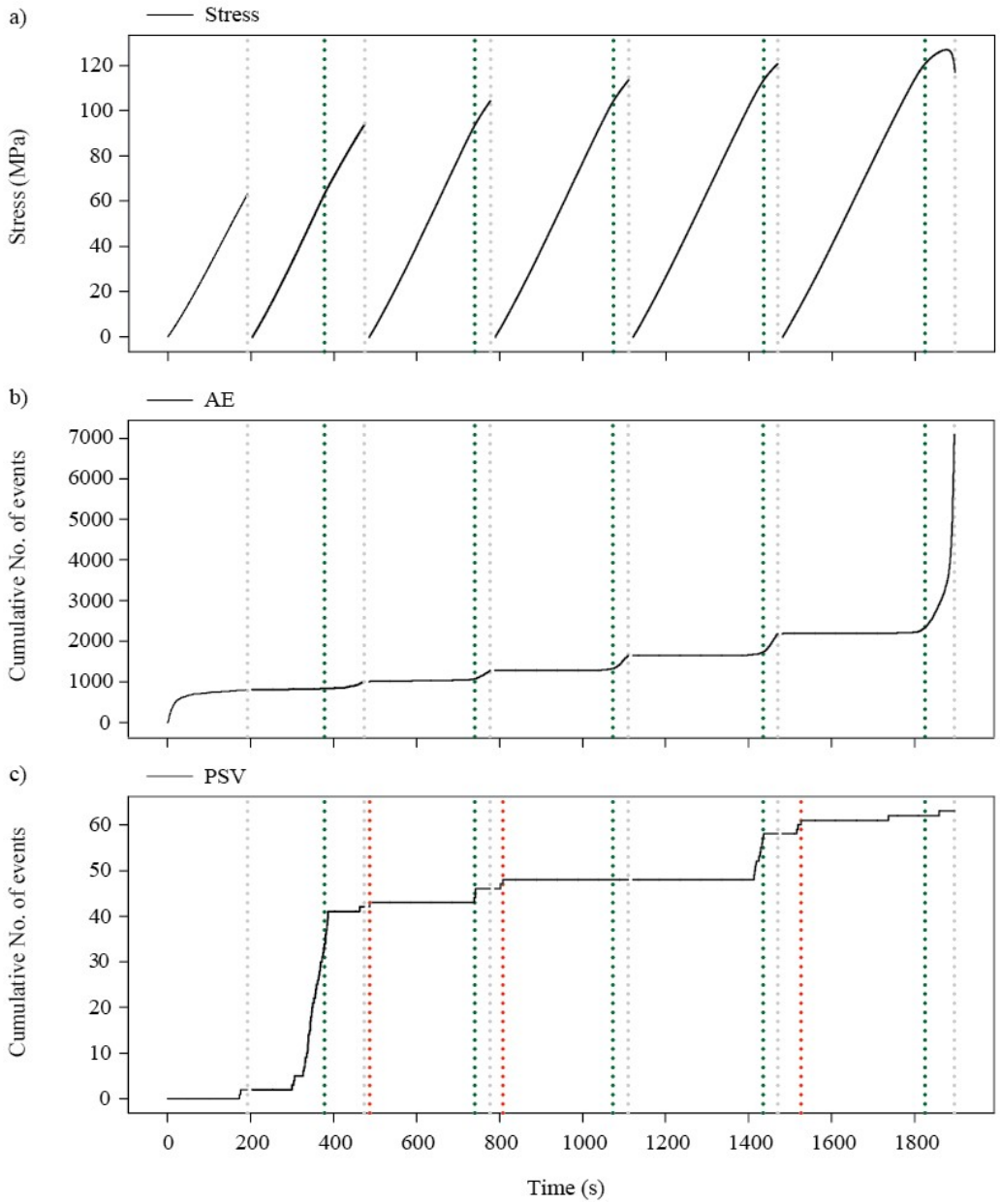

***Part 1 time based cyclic RTD loading data**: a) Applied stress (MPa), b) cumulative number of AE events and c) cumulative number of PSV events. The grey vertical lines represent the end of each loading cycle, green lines represent the PML threshold and the red lines indicate the end of the initial loading effect in the PSV activity.*

	PSV			AE	
	Initial Loading	**Kaiser**	**Felicity**	**Kaiser**	**Felicity**
Cycle 1	✗	NA	NA	NA	NA
Cycle 2	✗	✓	✓	✓	✗
Cycle 3	✓	✓	✗	✓	✓
Cycle 4	✓	✗	✗	✓	✓
Cycle 5	✗	✓	✓	✓	✓
Cycle 6	✓	✓	✓	✓	✓

***Part 2 Effects truth table:** the table indicates if the following effects associated with PSV and AEs are present for each loading cycle: Kaiser effect, Felicity effect and initial loading effect.*

***Figure 8-4 Oven dried schist results summary.** Part 1) time based stress, PSV cumulative number of events and AE cumulative number of event plot; Part 2) table indicating the presence of Kaiser Felicity and initial loading effect.*

The cyclic RTD loading of an oven dried schist specimen is shown in Figure 8-4. The maximum strength of the specimen was 127.06 MPa, the maximum AE event amplitude was 79.33 dB and the maximum PSV amplitude was 3.5 mV. The Felicity effect is present in the AEs for all loading cycles, apart from Cycle 2 and it is more prominent during higher loads. The Felicity effect is also present in the PSV emissions during loading Cycles 2,5 and 6. The Kaiser effect is observed in the AEs and PSV for all of the loading cycles, apart from Cycle 4 for the PSV. The initial loading effect is observed in the PSV emissions during Cycles 3,4 and 6.

There is a rapid increase in AE events rate at the beginning of Cycle 1, however the event rate then reduces for the rest of the cycle. There are no PSV events until near the end of Cycle 1 at ~173.25 s, after which there is an increase in event rate.

The AE event rate over Cycle 2 is low to begin with (Kaiser effect), at the PML threshold the event rate increases. A similar behaviour is observed in the PSV emissions, however PSV event rate increases before the PML threshold indicating that Kaiser effect and Felicity effect are present. A although, there is a more extreme increase in PSV event rate at ~301.5 s compared to the AEs.

During Cycle 3 the AE and PSV events rates are low initially (Kaiser effect), apart from an increase in PSV event rate at the beginning of the loading cycle (initial loading effect). In the AE activity there is an increase in event rate just before the PML threshold (Felicity effect).

Over the course of Cycle 4 the PSV and AE events rates are low to begin with. Before the PML threshold is reached at ~1058.5 s the AE event rate begins to increase, however the PSV event rate remains low. Kaiser and Felicity effect are present in the AEs, but not in the PSV emissions; there is a small increase in PSV activity at the onset of the cycle (initial loading effect).

The AE and PSV event rates are low at the start of Cycle 5 (Kaiser effect), however just before the PML threshold is reached at ~1416.75 s the event rates begins to increase (Felicity effect).

During the final loading cycle, the AE event rate is low at the start (Kaiser effect), then the event rate begins to increase before the PML threshold is reached at ~1759.5 s (Felicity effect). The highest AE event rate is observed after the threshold. There is an initial increase in PSV activity at the beginning of the loading cycle (initial loading effect), followed by a period of inactivity (Kaiser effect) and the PSV event rate begins to increase before the PML threshold at ~1719.5 s (Felicity effect).

8.2.6 Oven dried gabbro cyclic RTD experimental results summary

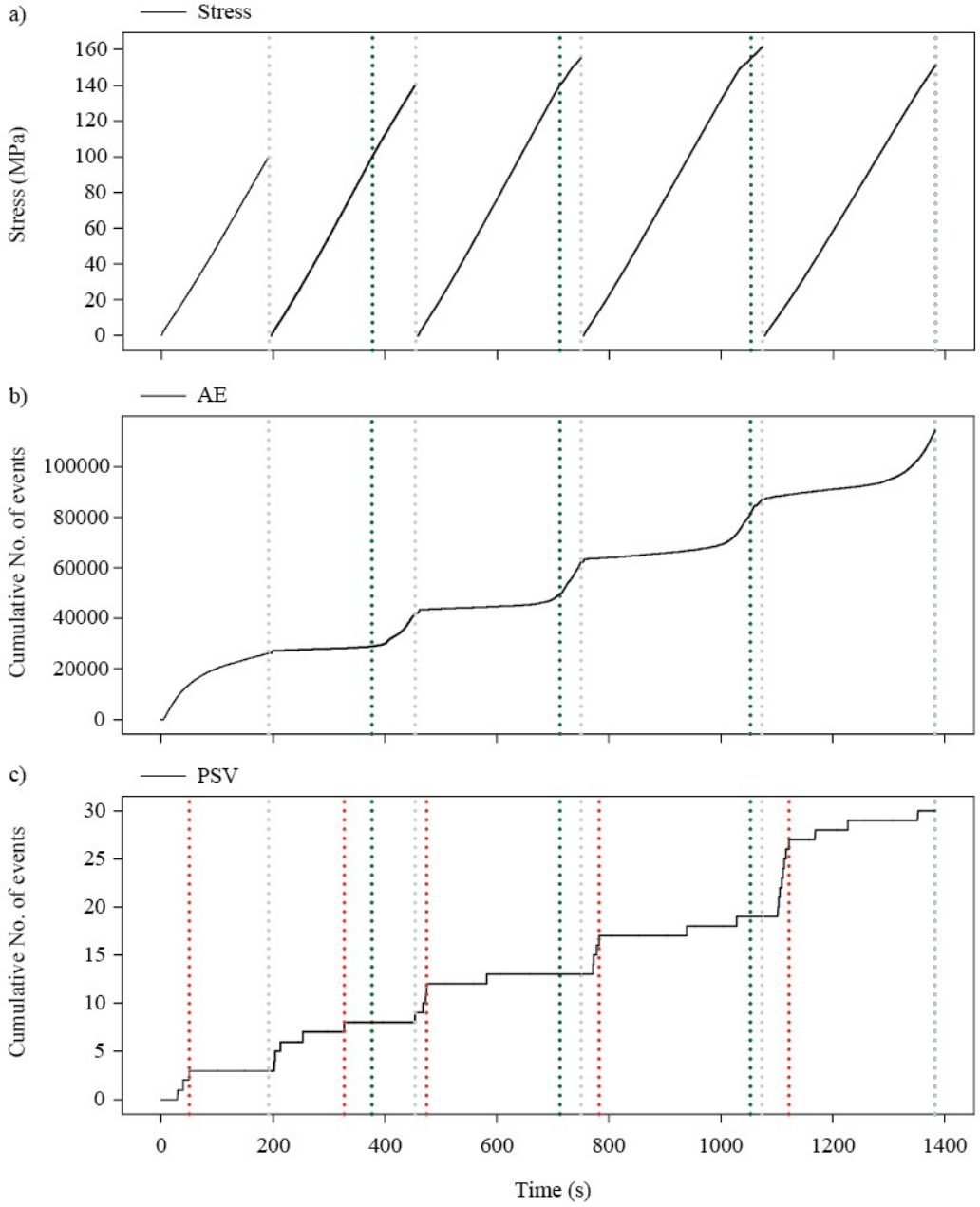

***Part 1 time based cyclic RTD loading data**: a) Applied stress (MPa), b) cumulative number of AE events and c) cumulative number of PSV events. The grey vertical lines represent the end of each loading cycle, green lines represent the PML threshold and the red lines indicate the end of the initial loading effect in the PSV activity.*

	PSV			AE	
	Initial Loading	**Kaiser**	**Felicity**	**Kaiser**	**Felicity**
Cycle 1	✓	NA	NA	NA	NA
Cycle 2	✓	✗	✗	✓	✗
Cycle 3	✓	✓	✓	✓	✓
Cycle 4	✓	✓	✓	✓	✓
Cycle 5	✓	✓	✓	✓	✓

***Part 2 Effects truth table:** the table indicates if the following effects associated with PSV and AEs are present for each loading cycle: Kaiser effect, Felicity effect and initial loading effect.*

***Figure 8-5 Oven dried gabbro results summary**. Part 1) time based stress, PSV cumulative number of events and AE cumulative number of event plot; Part 2) table indicating the presence of Kaiser, Felicity and initial loading effect.*

The cyclic RTD loading of an oven dried gabbro specimen is shown in Figure 8-5. The maximum strength of the specimen was 161.33 MPa, the maximum AE event amplitude was 97.25 dB and the maximum PSV amplitude was 0.532 mV. The Kaiser effect is present in the AE activity during all loading cycles; the Felicity effect is observable in all loading cycles apart from Cycle 2, and it is more prominent during higher loads. The initial loading effect can be seen at the onset of each loading cycle, however the Kaiser effect is not observable in the PSV emissions apart from during Cycle 3,4 and 5.

During loading Cycle 1 there is an increase in AE event rate, however the rate begins to decline after ~30 s for the rest of the cycle. The PSV event rate also increases at the beginning of the loading cycle (initial loading effect), after which there are no new PSV events for the rest of the loading cycle.

At the onset of loading Cycle 2 the AE event rate is low (Kaiser effect), when the PML threshold is reached the AE event rate increases for the remainder of the loading cycle. The PSV event rate increases to begin with (initial loading effect), after which there is a period of inactivity for the remainder of the loading cycle.

During loading Cycle 3 there is an increase in the number of PSV events initially (initial loading effect), then a period of inactivity (Kaiser effect) and at ~583.75 s there is an increase in event rate (Felicity effect). The AE event rate is initially low (Kaiser effect) and before the PML is reached at ~643.75 s the AE event rate begins to increase (Felicity effect).

The number of PSV events increases at the beginning of loading Cycle 4 (initial loading effect), followed by a period of inactivity from ~785.25 s to 925.5 s (Kaiser effect), after which there is an increase in PSV event rate before the PML threshold (Felicity effect). The AE event rate is initially low (Kaiser effect), but higher than the previous cycles; before the PML threshold is reached at ~972.5 s the AE event rate increases (Felicity effect).

There is a large increase in PSV event rate at the onset of loading Cycle 5 (initial loading effect), followed by a period of lower event rate up until material failure (Felicity effect). The AE event rate is relatively low at the beginning of the loading cycle (Kaiser effect) and it begins to increases before the PML threshold is reached at ~1287.75 s (Felicity effect). In fact, during the last loading cycle the rock specimen fails before the PML threshold is reached.

8.2.7 Oven dried concrete cyclic RTD experimental results summary

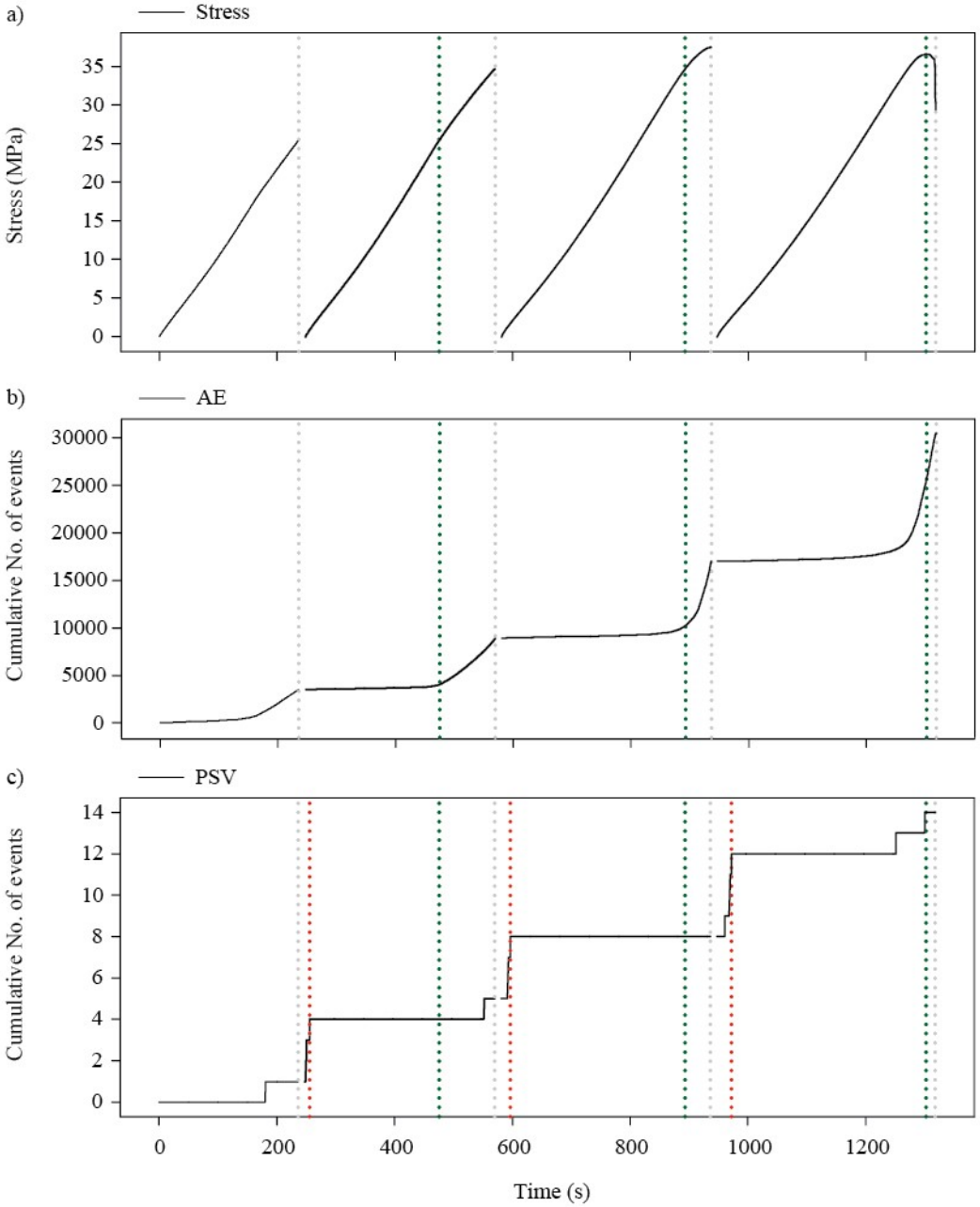

***Part 1 time based cyclic RTD loading data**: a) Applied stress (MPa), b) cumulative number of AE events and c) cumulative number of PSV events. The grey vertical lines represent the end of each loading cycle, green lines represent the PML threshold and the red lines indicate the end of the initial loading effect in the PSV activity.*

	PSV			AE	
	Initial Loading	**Kaiser**	**Felicity**	**Kaiser**	**Felicity**
Cycle 1	✗	NA	NA	NA	NA
Cycle 2	✓	✓	✗	✓	✓
Cycle 3	✓	✗	✗	✓	✓
Cycle 4	✓	✓	✓	✓	✓

***Part 2 Effects truth table:** the table indicates if the following effects associated with PSV and AEs are present for each loading cycle: Kaiser effect, Felicity effect and initial loading effect.*

***Figure 8-6 Oven dried concrete results summary**. Part 1) time based stress, PSV cumulative number of events and AE cumulative number of event plot; Part 2) table indicating the presence of Kaiser, Felicity and initial loading effect.*

The cyclic RTD loading of an oven dried concrete specimen, is shown in Figure 8-6. The maximum strength of the spaceman was 37.52 MPa, the maximum AE event amplitude was 65 dB and the maximum PSV amplitude was 1.49 mV. The Kaiser effect is present in the AE activity for all loading cycles and also the Felicity effect. However, the Kaiser effect is only present during loading Cycles 2 and 4 in the PSV activity and for Felicity only during loading Cycle 4.

The AE and PSV event rates are initially low during Cycle 1, however the event rate in the AEs begins to increases at ~132.5 s and there is a single PSV event at ~180.5 s.

At the beginning of Cycle 2 there is an increase in PSV events (initial loading effect), followed by a period of inactivity from ~245 s to ~530 s (Kaiser effect), after which there is an increase in PSV activity after the PML threshold. The AE event rate is low to begin with (Kaiser effect) and before the PML threshold at ~ 428 s there is an increase in AE event rate for the rest of the loading cycle (Felicity effect).

Over the course of loading Cycle 3 the AE event rate is low initially (Kaiser effect), just before the PML threshold at ~ 829.5 s there in an increase in AE event rate (Felicity effect). The PSV event rate increases to begin with (initial loading effect), after this there are no new PSV events for the remainder of the loading cycle.

During the final loading cycle there is a relatively large number of PSV events produced at the beginning of the cycle (initial loading effect), followed by a period of inactivity from ~972.5 s to ~1235.75 s (Kaiser effect), after which the PSV event rate increases prior to the PML threshold (Felicity effect). The AE event rate is relatively low initially (Kaiser effect), however the AE event rate begins to increase before the PML threshold (~1186 s) is reached (Felicity effect).

8.3 Discussion

8.3.1 The initial loading effect of PSV emissions

The initial loading effect is classified as a momentary increase in PSV event rate at the beginning of a loading cycle. The initial loading effect region is defined as the time from the start of the loading cycle to the end of the momentary increase in PSV event rate (usually the start of the low PSV event rate Kaiser effect region).

The initial loading effect of PSV emissions was observed in all rock lithologies (excluding marble) and concrete, as shown in Figure 8-7. The marble specimens PSV event rate behaved in a similar manor to the AE event rate, as it remained constant throughout the loading cycles and there was no evidence of initial loading effect, Kaiser effect or Felicity effect.

The effect was present during all loading cycles of syenogranite and gabbro specimens; this is also true for sandstone and concrete specimens excluding the first loading cycle. The schist specimen only shows evidence of the initial loading effect during Cycles 3, 4 and 6.

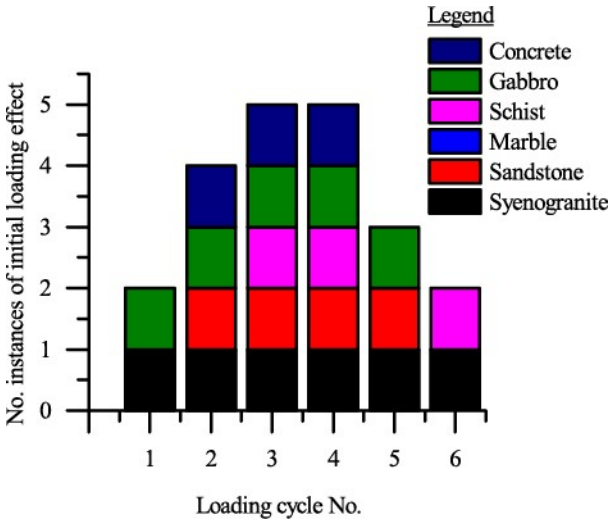

Figure 8-7 Initial loading effect occurrence summary. *The bar charts represent the number of occurrences of the initial loading effect for each material type per loading cycle in the PSV emissions.*

The initial loading effect region varies in length for different material types and for each loading cycle, as show in in Figure 8-8. The linear fit lines for the sandstone (r^2 =0.86), syenogranite (r^2 =0.09) and schist (r^2 =0.99) indicate a general increase in initial loading effect duration, with each successive loading cycle. The concrete (r^2 =0.51) and gabbro (r^2 =0.16) show a trend of decreasing initial loading effect duration with each successive loading cycle. However, there is not a strong relationship between loading cycle number and initial loading effect duration, for the gabbro and syenogranite samples.

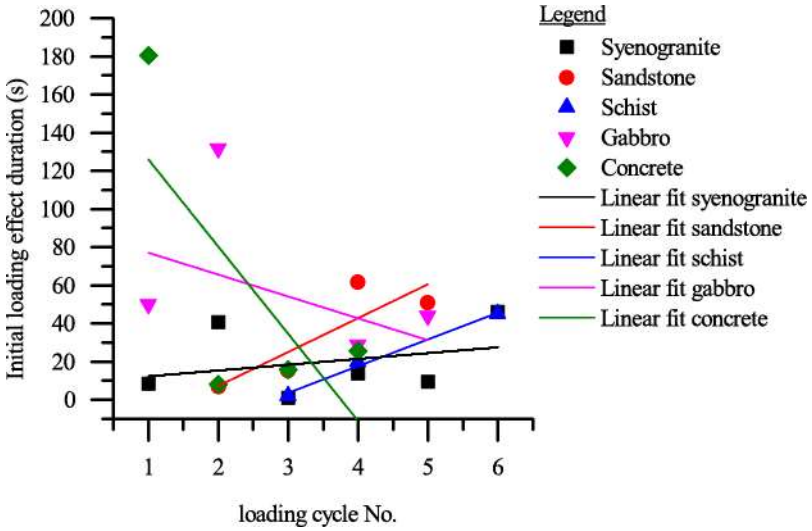

Figure 8-8 Initial loading effect duration summary. *The graph shows the scatter plots of the initial loading effect duration per cycle for each material type. A linear fit has been applied to the data for each material type.*

The initial loading effect is new phenomenon observed in PSV emissions and presented in this thesis for the first time; the mechanism/s for the initial momentary increase in PSV events is/are unknown. The effect was observed in quartz rich sandstone (66 % mono quartz, 14 % poly quartz) and quartz devoid gabbro specimens, indicating the PSV generation mechanism are not related to the piezo electric effect of quartz. The phenomenon was present in all material samples apart from marble (100 % calcite), thus calcite minerals do not play a role in the PSV generation mechanism/s related to initial loading effect. I hypothesise that PSV produced during the initial loading region is the result of an abrupt change in stress rate from unloading to loading; research by others has suggested that PSC emissions are linked to stress rate (specifically a change in Young's modulus) [151].

8.3.2 The Kaiser and Felicity effect

The Kaiser effect of AE was observed in all rock lithologies and concrete specimens and for all possible loading cycles, apart from in the marble specimen, as shown in Figure 8-9. The AE event rate for marble was consistent before and after the PML threshold indicating Kaiser effect not was in action; due to its relationship with Kaiser effect the Felicity effect is also not present in this experiment.

The Felicity effect was observed in all rock lithologies and concrete as shown in Figure 8-10, apart from the marble specimen as mentioned previously. The Felicity effect of AE was generally more prominent during higher loads and thus during the latter loading cycles, for each experiment. The Felicity effect was observed for all possible loading cycles for each material, however during the first possible instance (loading Cycle 2) for the sandstone, schist and gabbro experiments, the effect was not present.

The AE activity behaved as expected for all experiments in agreement with the well establish theories of Kaiser effect and Felicity effect [52, 53].

The Kaiser effect was also present in the PSV emissions for all materials tested, excluding the marble and sandstone specimens. The marble specimens PSV event rate has a similar trend to the AE, where

by the event rate remained more or less constant before and after the PML threshold, indicating Kaiser effect was not present. As for the sandstone specimen, the PSV event rate increased during the initial loading effect region then reduced to a null level before and after the PML threshold, indicating Kaiser effect was not present. For all possible loading cycles, the Kaiser effect was observed for the syenogranite specimen, this was also true for the schist, gabbro and concrete specimens except the effect was not present during loading Cycles 4, 2 and 3 respectively.

As Kaiser effect was observed in the PSV emissions of quartz rich syenogranite (45 % quartz) and quartz devoid gabbro, this suggests that the Kaiser effect of PSV emissions is not reliant on the piezo electric effect of quartz. Work by others [15, 83] has shown PSC and electromagnetic emissions are related to cracking events; in the previous results chapters of this thesis, I have demonstrated PSV emissions are related to acoustic events i.e. cracking in rock and concrete specimens. I hypothesise the Kaiser effect of PSV emissions is directly related to acoustic events in the sample and thus PSVs could be generated by the movement and separation of fresh charged fracture surfaces [13, 15, 80-83].

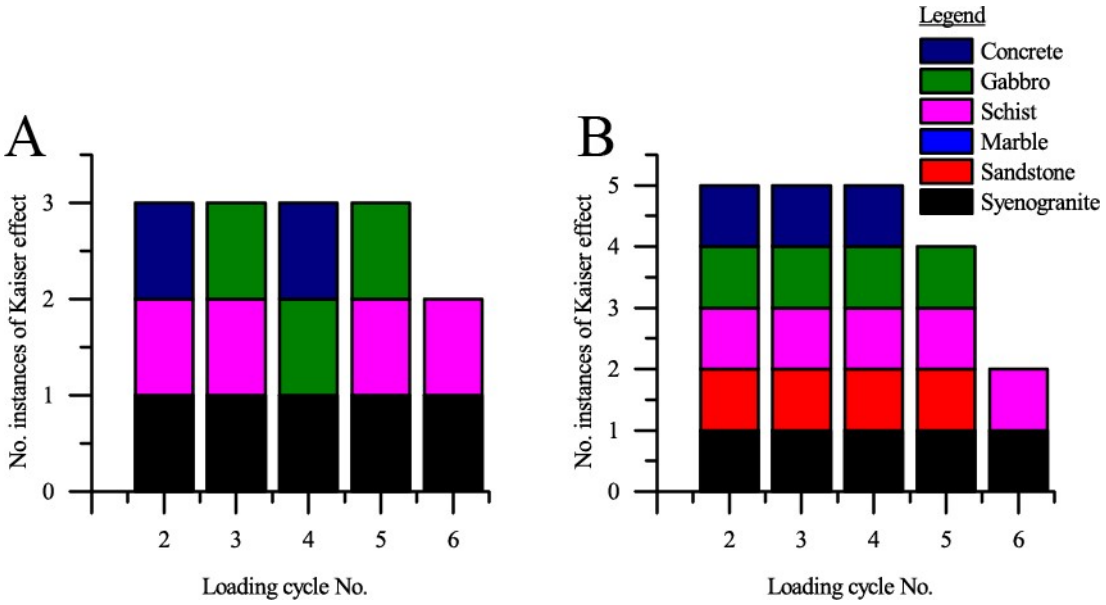

Figure 8-9 Kaiser effect occurrence summary. *The bar charts represent the number of occurrences of the Kaiser effect for each material type per loading cycle; A) PSV emissions and B) AEs.*

The Felicity effect is less prominent in the PSV than Kaiser effect as it was only observable in the gabbro, schist and concrete specimens and not for all loading cycles as shown in Figure 8-10.

Although Felicity effect is present in the AE for syenogranite and sandstone, it is not present in the PSV emissions. Felicity effect was observed during loading Cycles 2, 5 and 6 in the PSV emissions for the schist specimen, whereas the effect was present in all loading, excluding Cycle 2 for the AEs. The Felicity effect was observed during Cycles 3,4 and 5 in the PSV emissions and also in the AEs, for the gabbro specimen. Concrete however only had Felicity effect present in the PSV emissions during the final loading cycle (Cycle 4), but the effect was observable for all loading cycles in the AEs.

As for the absence of Felicity effect in the syenogranite and sandstone specimen, this could be a characteristic of the rock lithology/mineral composition. The theory of Felicity effect [53] of AEs states the effect is more prominent for higher loads, this is reflected in the PSV emissions as Felicity effect was observed during the final loading cycles of gabbro, schist and concrete.

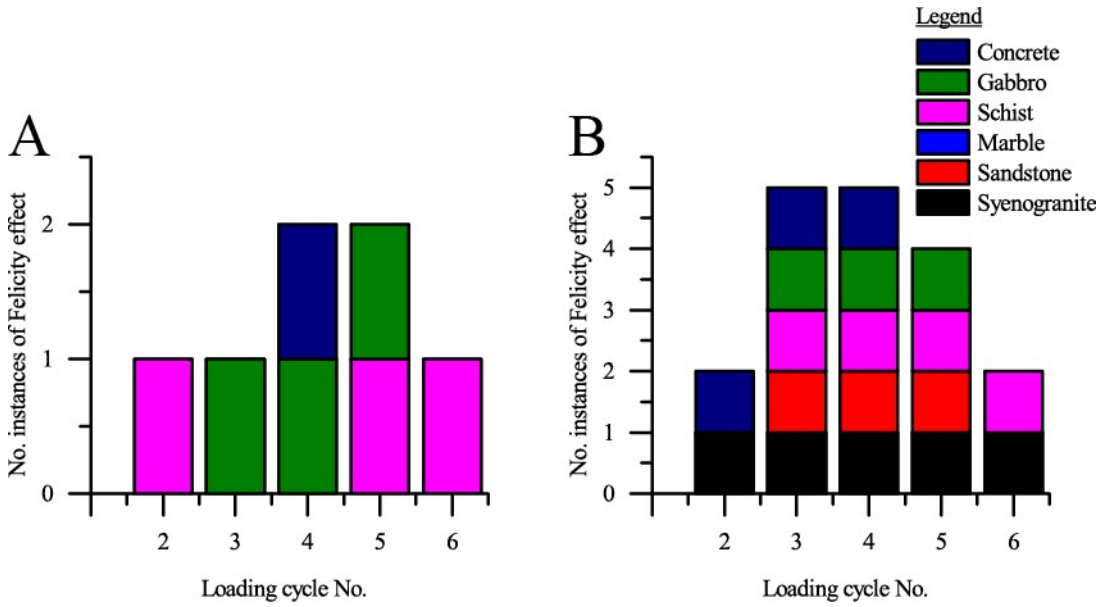

Figure 8-10 Felicity effect occurrence summary. *The bar charts represent the number of occurrences of the Felicity effect for each material type per loading cycle; A) PSV emissions and B) AE.*

There are many possible factors that could contribute to Kaiser and Felicity effect being present in AE but not in the PSV for the instances shown in Figure 8-9 and Figure 8-10. Including, lithology/mineralogy affecting the generation of PSV; piezoelectric affects in the quartz bearing materials; and the effect of deformation stage on PSV generation for different materials. Further experimentation would be necessary to give a definitive answer.

8.3.3 Research question conclusions

Do PSV emissions exhibit a work hardening effect synonymous to the Kaiser effect of acoustic emissions, during cyclic uniaxial loading, in a wide range of rock lithologies and concrete?

PSV emissions exhibit a work hardening effect similar to the Kaiser and Felicity effect of AEs. The Kaiser effect was observed in the PSV for all rock lithology and concrete apart from sandstone and marble specimens. The Felicity effect reduces Kaiser effect and was only observed in the PSV for gabbro, schist and concrete specimens. Although there have been studies by others [81, 82] observing Kaiser effect in PSE for granite and marble samples, this is the first study observing this effect in a wide range of rock lithology and concrete.

Can the detection of PSV during cyclic loading be used as an indication of damage in rocks and concrete?

The Kaiser and Felicity effect of AE's is already an establish method for detecting damage and monitoring its progression. The experiments presented in this thesis chapter suggest that PSVs exhibit a

work hardening effect similar to AEs and thus capacitively coupled EPS could be used to monitor damage in rocks and concrete.

Is EPS suitable for monitoring PSV during cyclic loading and is it a viable technology for field use?

The results of the cyclic loading experiments presented in this chapter and RTD loading experiments presented in chapters 6 and 7 show that PSV's are present in the range of millivolts. This yields a much better signal to noise ratio compared to the associated PSCs (Pico amps) observed by others [15, 151]. This means that EPS does not need Faraday shielding, a clear advantage over PSC measurement and is more advanced and cost effect than all current PSE technologies. All the aforementioned points make EPS amenable to field use.

9 UNIAXIAL COMPRESSIVE STEP LIKE STRESS TESTING OF ROCKS USING DIRECTLY COUPLED SMART EPSS

This chapter provides an introduction and motivations behind the experiments carried out and presented in this chapter, in section 9.1. Followed by a selection of results pages showing detailed observations of PSV and applied stress, for each material specimen tested (section 9.2) In addition, the results pages give details of statistical relationships between pressure stimulated voltage (PSV) and applied stress, for each material specimen. The last part of the chapter compares the results of all of the materials tested and discusses the outcomes (section 9.3).

9.1 Introduction

Currently there is no method for measuring in-situ stress in a cost effective and non-invasive manner in, manmade and geological structures. Traditional methods such as hydraulic, relief, jacking, strain recovery and borehole breakout [153] cause irreversible damage to the structure, in the process of taking the measurement, are expensive to implement and not appropriate for long term monitoring. One new technique in the structural health monitoring field (SHM) is the monitoring of pressure stimulated electrical emissions (PSEs).

Laboratory based studies measuring pressure stimulated currents (PSCs) and electromagnetic emissions (EME) have shown that they can be used to assess damage in rocks [18-20, 84]. Research has shown PSCs are present in marble samples subjected changes in stress, however the current relaxes to a baseline level shortly after the stress is applied [82, 151], thus only changes in stress can be observed by measuring PSC.

This is the first study: 1) attempting to characterise PSV with static stress, 2) using a field capable technology i.e. the electric potential sensor (EPS) and 3) using a new type of directly coupled EPS technology. The experiments that were carried out and presented in this chapter, were designed to address the following research questions:

Are low frequency PSVs related to static stress during the uniaxial loading of rock?

Can EPS be used to determine the in-situ stress state in rocks noninvasively by measuring low frequency PSV?

Is the directly coupled smart EPS suitable of measuring PSV outside of the laboratory setting?

9.2 Results

Four cylindrical rocks samples (two sandstone specimens and two calcite specimens) were subjected to step like stress (SLS) uniaxial loading profiles. Each specimen was instrumented with two axial strain gauges, one circumferential strain gauge and two directly coupled EPSs to measure the axial strain,

circumferential strain and PSV respectively during loading. In addition, a force transducer was used to measure the applied force and thus the applied stress could be determined.

An EPS input impedance calibration procedure was carried out before testing, as detailed in section 4.6. A bootstrap positive feedback of 87.12 % was optimal for both rock types, in order to give the maximum input resistance and thus lowest frequency sensitivity, whilst maintaining stable sensor operation.

9.2.1 Oven dried sandstone SLS experimental results summary

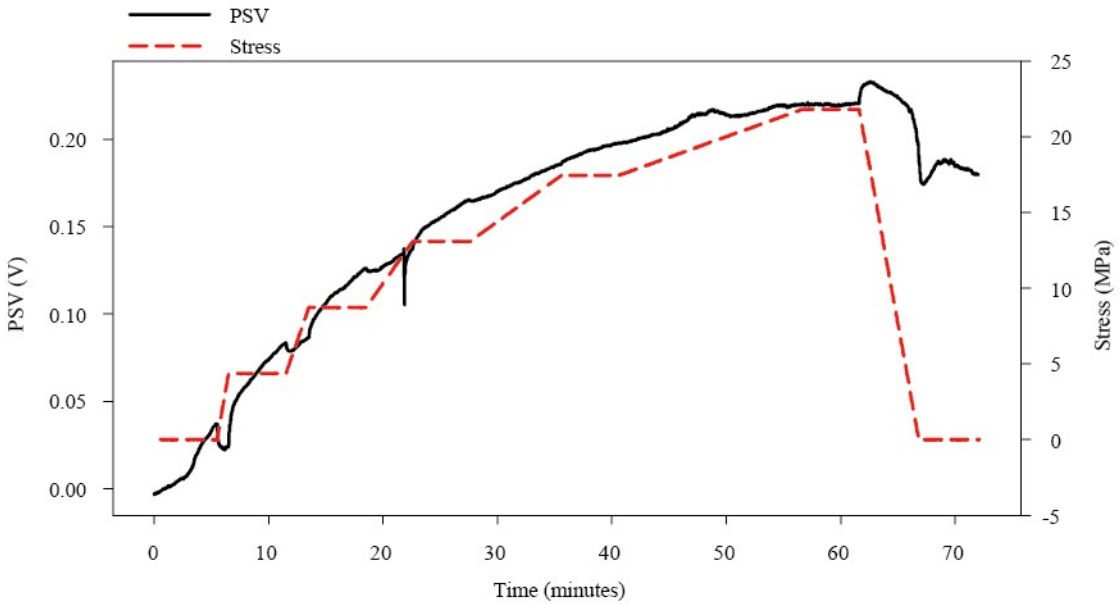

Part 1 Step like stress test plot: *The red dashed line represents the applied stress and the black line represents the resulting PSV. The material loading did not exceed the linear elastic region of deformation i.e. Stages 2/3.*

0.0

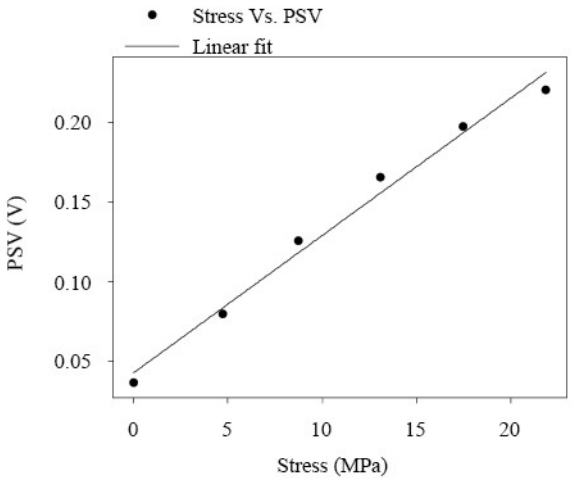

Part 2 Linear regression: *Data points at the end of each stress step were used for linear regression analysis, where dv/dt ≈ 0.*

Linear regression	$r^2 = 0.99$
Max stress	21.84 MPa
Max PSV	232.83 mV
Stress rate step 1	0.167 kNs^{-1}
Stress rate step 2	0.083 kNs^{-1}
Stress rate step 3	0.042 kNs^{-1}
Stress rate step 4	0.021 kNs^{-1}
Stress rate step 5	0.010 kNs^{-1}

Part 3 Summary of the loading data and statistics: *The linear regression r^2 value is for the relationship between applied stress and resulting PSV.*

Figure 9-1 Oven dried sandstone step like stress test results summary. *Part 1) applied stress and resulting PSV plot; Part 2) linear regression plot; and Part 3) loading and statistics data summary.*

Figure 9-1 shows an SLS test of an oven dried sandstone specimen. For each consecutive step the rate of stress increase was reduced, in order to investigate the effect of stress rate on PSV emissions. The PSV appears to increase in amplitude at a similar rate to the applied stress, the linear regression analysis confirms there is a linear relationship between PSV and applied stress (r^2 =0.99), as shown in Part 2 of the figure. At higher stress rates there are transient spikes in PSV at the transition from a positive stress rate (step slope) to null stress rate (step plateau); this effect is reduced by lowering the applied stress rate as shown in steps 4 and 5. The PSV amplitude relaxes by ~22 % when the stress is released at the end of the test.

9.2.2 Oven dried marble SLS experimental results summary

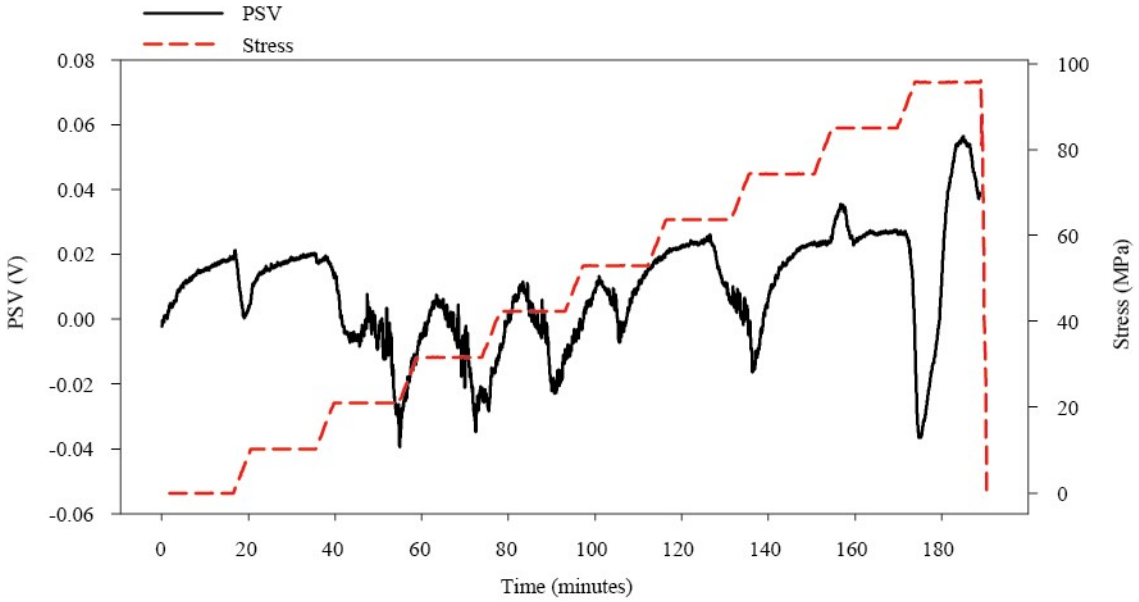

Part 1 Step like stress test plot: *The red dashed line represents the applied stress and the black line represents the resulting PSV. The material was loaded until catastrophic failure occurred.*

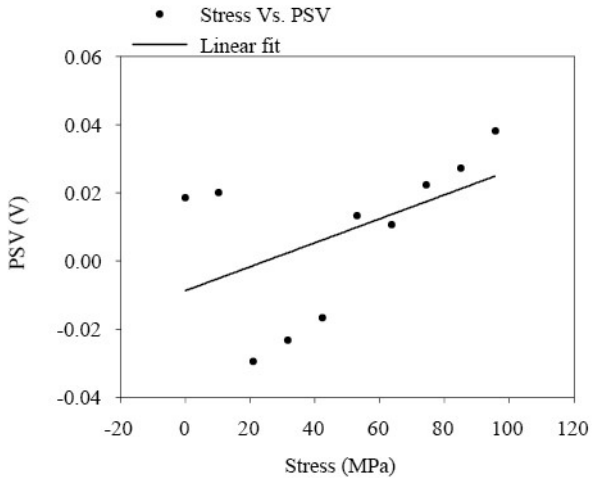

Part 2 Linear regression: *Data points at the end of each stress step were used for linear regression analysis, where $dv/dt \approx 0$.*

Linear regression	$r^2 = 0.24$
Max stress	96.1 MPa
Max PSV	53.61 mV
Stress rate	1 kNs^{-1}

Part 3 Summary of the loading data and statistics: *The linear regression r^2 value is for the relationship between applied stress and resulting PSV.*

Figure 9-2 Oven dried marble step like stress test results summary. *Part 1) applied stress and resulting PSV plot; Part 2) linear regression plot; and Part 3) loading and statistics data summary.*

Figure 9-2 shows the SLS loading of a calcite specimen. A constant loading rate of 1 kNs^{-1} was chosen for this experiment and preceding experiments, to optimise the experimental testing duration. The PSV amplitude varies between -43.4 mV and 53.61 mV during the test, this is a considerably smaller amplitude range compared to the sandstone testing (3.41 mV to 232.83 mV), as shown in Figure 9-1. There are abrupt polarity reversals in PSV at the transition between stress rate changes during each loading step, however there is not a strong linear relationship between PSV and applied stress, as shown in the linear regression results.

9.2.3 Oven dried sandstone cyclic SLS experimental results summary

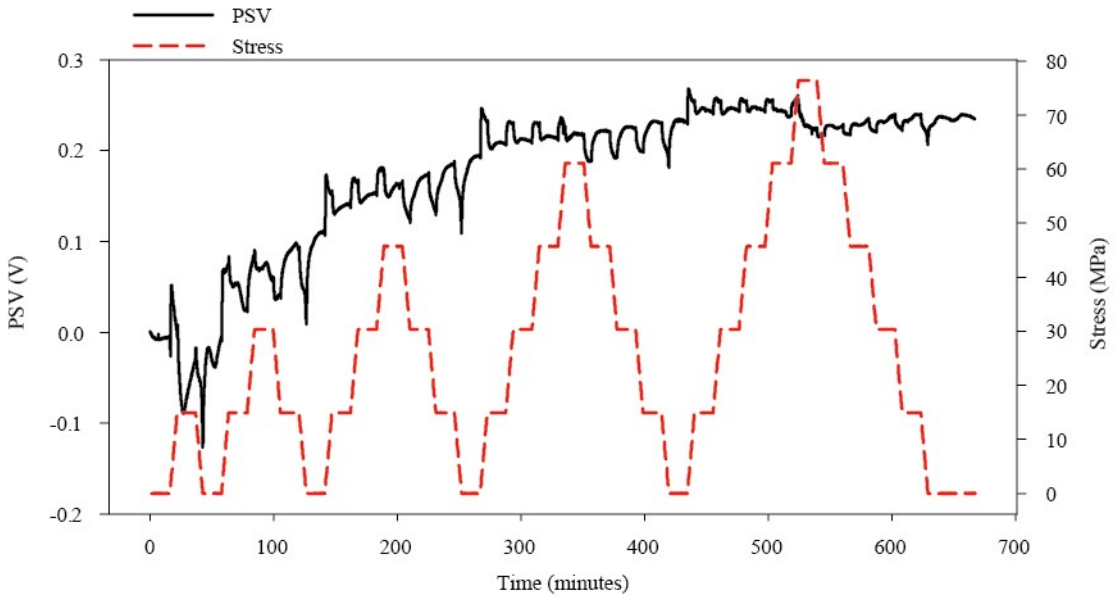

Part 1 Step like stress test plot: *The red dashed line represents the applied stress and the black line represents the resulting PSV. The maximum load was limited to 77 MPa which is within the linear elastic stage of deformation i.e. Stage 2/3.*

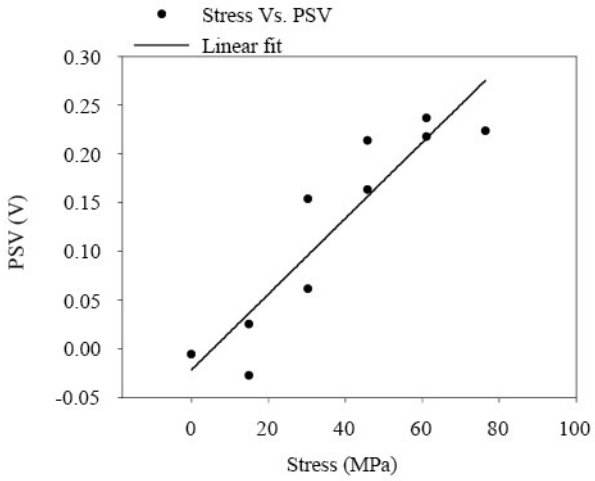

Part 2 Linear regression: *Data points at the end of each increasing stress step were used for linear regression analysis where dv/dt ≈ 0.*

Linear regression	$r^2 = 0.84$
Max stress	76.48 MPa
Max PSV	268.01 mV
Stress rate	1 kNs^{-1}

Part 3 Summary of the loading data and statistics: *The linear regression r^2 value is for the relationship between applied stress and resulting PSV.*

Figure 9-3 Oven dried sandstone cyclic step like stress test results summary. *Part 1) applied stress and resulting PSV plot; Part 2) linear regression plot; and Part 3) loading and statistics data summary.*

A cyclic SLS test was applied to a sandstone specimen, as shown in Figure 9-3, with a constant loading rate during each step. The PSV increases proportionally to the load, however the PSV does not reduce in amplitude whilst the specimen is being unloaded. There are transient spikes in PSV during stress rate transitions, for each step the polarity of the transients switches when transitioning from loading to unloading phases. After the specimen has been unloaded at the end of the experiment, the PSV initially relaxes slightly and then appears to stabilise at an amplitude of ~244.4 mV. The linear regression between applied stress and PSV is high ($r^2 = 0.84$), as shown in Part 2 of the figure.

9.2.4 Oven dried marble cyclic SLS experimental results summary

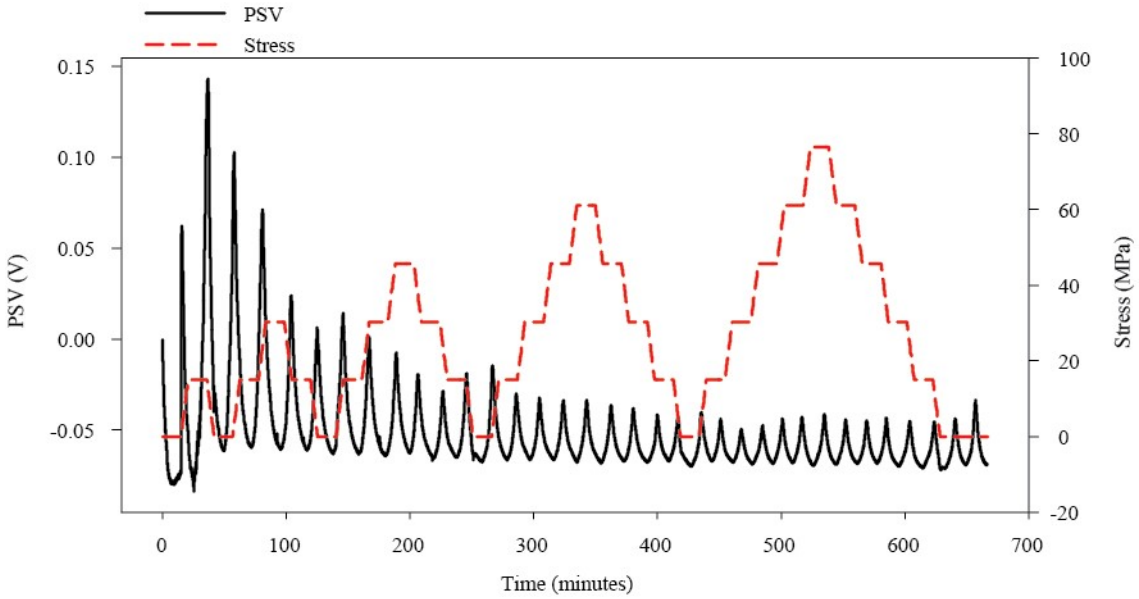

Part 1 Step like stress test plot: *The red dashed line represents the applied stress and the black line represents the resulting PSV. The maximum load was limited to 77 MPa which is within the linear elastic stage of deformation i.e. Stage 2/3.*

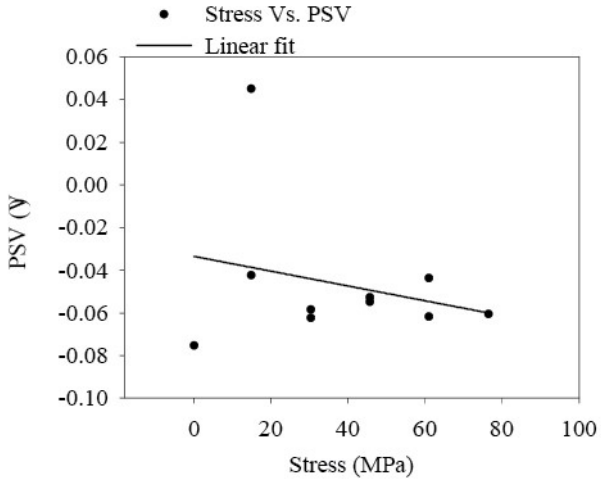

Part 2 Linear regression: *Data points at the end of each increasing stress step were used for linear regression analysis, where dv/dt ≈* 0.

Linear regression	$r^2 = 0.063$
Max stress	76.450 MPa
Max PSV	143.25 mV
Stress rate	1 kNs^{-1}

Part 3 Summary of the loading data and statistics: *The linear regression r^2 value is for the relationship between applied stress and resulting PSV.*

Figure 9-4 Oven dried marble cyclic step like stress test results summary. *Part 1) applied stress and resulting PSV plot; Part 2) linear regression plot; and Part 3) loading and statistics data summary.*

A calcite specimen was subjected to a cyclic SLS loading profile, as shown in Figure 9-4. There are transient spikes in PSV occurring at transitions in stress rate. The PSV transients increase in amplitude during loading cycles and decrease in amplitude whilst unloading. The amplitude of the transients appears to reduce in amplitude with each loading cycle and exhibits a work hardening phenomena, as observed in other studies [82]. There is not a strong relationship between applied stress and PSV amplitude, with regards to linear regression ($r^2 = 0.062$). The PSV amplitude ranges from -86.1 mV to 145.25 mV), which is lower than the cyclic loading sandstone experiment (-128.6 mV to 268.01 mV) shown in Figure 9-3.

9.3 Discussion

All linear regression results between applied stress and resulting PSV have a p-values < 0.05, indicating the relationship between the predictor variable (applied stress) and the response variable (PSV) is statistically significant. The r^2 value represents the goodness of fit for the regression line, i.e. the variation from a linear relationship between applied stress and PSV. The data point at the end of each stress step was chosen for linear regression analysis where dv/dt ≈ 0, thus giving PSV time to settle to a new DC level after a sudden transition of stress rate. As PSV amplitude is maintained during unloading cycles, subsequently increasing steps in stress were selected for linear regression analysis, for the cyclic SLS tests. There is a strong relationship between applied stress and resulting PSV in quartz bearing sandstone specimens, but not in the non-quartzose calcite specimens, as shown in Figure 9-5.

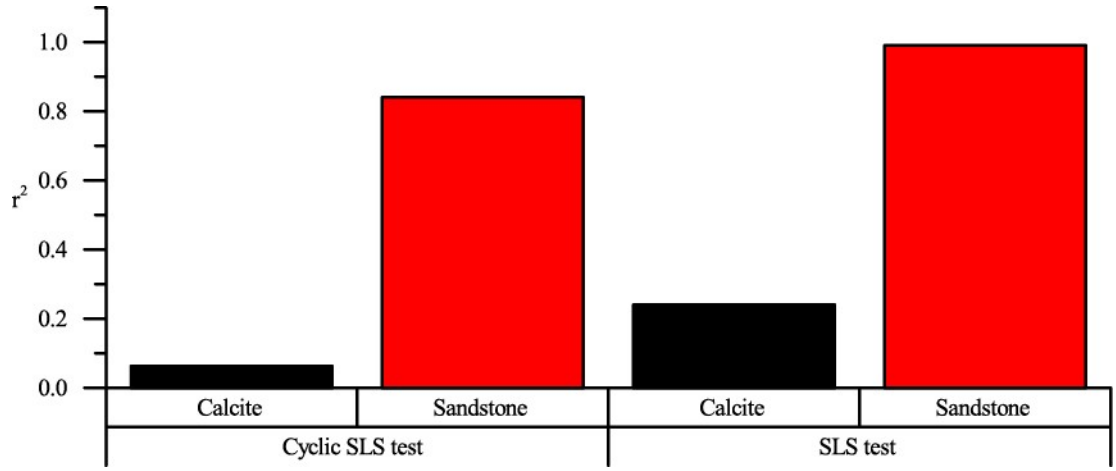

Figure 9-5 Applied stress and PSV linear regression summary. *The r^2 values for the SLS loading and cyclic SLS loading of oven dried sandstone and calcite specimens.*

The linear regression r^2 value is greater for the SLS tests compared to the cyclic SLS tests for both sandstone and marble specimens. It appears that cyclic loading of the material specimens reduces the PSV-stress linear relationship, this could be due to work hardening which is associated with repeated loading of materials.

There must be at least two different PSV generation mechanisms:

1) The piezoelectric effect of quartz, responsible for the DC shift in PSV amplitude, proportional to applied stress in the sandstone experiments. The theory of piezoelectricity states that the applied stress is proportional to the electric field produced in the piezo element [154].

2) Another mechanism responsible for transient spikes in PSV during abrupt changes in stress rate, present in both calcite and sandstone loading experiments

The transient PSV associated with the unknown mechanism changes polarity in the sandstone specimen, when transitioning from loading to unloading, this is a lithological effect as this phenomenon does not occur in the calcite specimen. Work by others studying piezo stimulated current in marble specimens (98 % calcite, 1.8 % other minerals, 0.2 % quartz) during step like cyclic loading profiles, observed

polarity changes in the current was proportional to the stress rate. However, in this study transient spikes in PSV did not show any polarity reversal when transitioning from loading steps to unloading steps, in the marble specimen (100 % calcite).

During the cyclic SLS tests for marble and sandstone specimens, the transient spikes in PSV reduce in amplitude with each successive stress step; although, this effect is more prominent in the marble specimen. This may be caused by a work hardening effect (Kaiser effect). Work by others has shown that transient spikes in PSC reduce in amplitude during progressive cyclic loading [82].

The amplitude of the transient spikes in PSV are related to the stress rate transitions, for example in the sandstone SLS test the spikes in PSV are more prominent during the higher stress rate steps, compared to the proceeding lower rate stress steps. This is in agreement with work by others, studying piezo stimulated currents in marble specimens [17].

For the calcite and sandstone cyclic SLS experiments, the maximum load was limited to the elastic region of deformation. The transient spikes in PSV associated with the unknown mechanism were observed in the linear elastic regions of the rocks. In this region there is not a change in Young's modulus occurring and yet there are still PSV signals produced; this is contradictory to studies by others showing that PSC emissions in non-quartzose marble specimens (98 % calcite, 1.8 % other minerals, 0.2 % quartz) are related a change in Young's modulus [151].

There is a significant difference in the maximum PSV amplitudes of the sandstone (268.01 mV) and calcite (143.25 mV) cyclic loading experiments, although they were subjected to identical loading profiles. This indicates the piezoelectric effect likely responsible for PSV activity in the sandstone, specimen produces higher amplitude PSV than the unknown mechanism, responsible for PSV activity in the non-quartzose calcite.

The results presented in this chapter provide evidence of directly coupled smart EPS being capable of determining the applied stress in quartzose rocks, i.e. sandstone. This is an inherent advantage over measuring PSC to determine the stress state, because only changes in stress can be determined using this method, as the measured current decays to a baseline level shortly after the stress is applied [82, 151]. This is not the case with regards to PSV measurement using directly coupled EPS technology.

9.3.1 Research question conclusions

Are low frequency PSVs related to static stress during the uniaxial loading of rock?

The experiments detailed in this results chapter, showed that there was a strong linear relationship between low frequency (DC to 250 Hz) PSV and applied stress in the SLS-RTD ($r^2 = 0.99$) and cyclic SLS ($r^2 = 0.84$) sandstone experiments. A weak relationship was observed in the marble specimens, for both the SLS-RTD ($r^2 = 0.24$) and the cyclic SLS ($r^2 = 0.063$) experiments. Therefore, I hypothesise that low frequency PSVs are related to static stress in quartz bearing rock due to the piezoelectric effect of

quartz; however, further experimentation is required to test this hypothesis on a wide range of rock lithology.

Can EPS be used to determine the in-situ stress state in rocks noninvasively by measuring low frequency PSV?

The PSV amplitude does not appear to decay back to its baseline level, after the sandstone specimens were unloaded. The PSV on surface of the rock could be an ultra-low frequency signal or a DC voltage could be maintained on the surface. The latter would enable the determination of in-situ-stress, at least in terms of stress field direction as one could compare the PSV amplitude of multiple sensors over a structure, to determine the maximum and minimum horizontal stress. The vertical stress is often determined by knowledge of the material properties and weight of overlaying material mass. The former would mean that only changes in in-situ stress could be determined, as the PSV corresponding to the stress level would not be maintained after it was applied. However, this would still be useful as one could apply load to a structure instrumented with an array of EPS to infer a stress map over the structure and thus identify weak spots.

Is the directly coupled smart EPS suitable of measuring PSV outside of the laboratory setting?

The novel directly coupled smart EPS sensor was a successful design, as it has the necessary high input impedance (resistance = 689 GΩ - 3.068 TΩ, capacitance = 0.67 pF) and low noise (31.68 nV√Hz at 1 kHz) characteristics for measuring PSV noninvasively, at low frequencies (DC-500 kHz). The implementation of this sensor allowed for relationships between applied stress and PSV to be studied without the use of Faraday shielding; thus, it is likely that the sensor will be suitable for SHM outside of the laboratory setting.

10 CONCLUSIONS AND FUTURE DIRECTIONS

The aim of this chapter is to conclude the findings of experiments presented in all results chapters 6, 7, 8 and 9 and explain future research objectives. Section 10.1 provides an overview and conclusions drawn from the ramp to destruction testing of manmade and geological material experiments, presented in chapters 6 and 7. The chapter continues in section 10.2, by presenting an overview and conclusions drawn from the cyclic loading of manmade and geological material experiments, presented in chapter 8. For the step like stress experiments presented in chapter 9, the overview and conclusions are detailed in section 10.3. Future directions for pressure stimulated voltage (PSV) research using electric potential sensor (EPS) technology are outlined in section 10.4; followed by comments on the viability of a PSV-EPS based structural health monitoring (SHM) tool, in section 10.5.

10.1 PSV emissions during ramp to destruction (RTD) testing of manmade and geological materials

10.1.1 Geological materials: rocks

The results of the experiments presented in chapter 6 showed that PSV emissions were detected in the range of millivolts, for all rock types and in all environmental conditions. This indicates that PSV emission are not solely generated by the piezo electric effect of quartz, because the marble, halite and gabbro specimens produce PSV and yet they contain no quartz minerals. Work by others has shown PSC can be generated in marble samples containing very low quartz content (~0.2 %), earlier work attributed PSC emissions to applied stress rate [16, 17], but later work suggested a change in Young's modulus [18, 151] is responsible. The results presented in chapter 6 show that PSV emissions are produced during the linear elastic region (Stage 2 and 3) where there is no a change in the Young's modulus, this contradictory to PSC research by others.

On average rocks with higher water concentrations produced the largest PSV amplitudes, with oven dried having the lowest, followed by air dried and then water saturated. Saline saturated rock specimens produce the highest average PSV amplitudes. However, water and saline saturation reduced PSV-AE correlations in the majority of materials. The electrokinetic effect of water movement appears to have an effect on the average PSV amplitude; such that increasing levels of absorbed water in rocks produces increasing PSV amplitudes. The saline solution may alter the zeta potential, i.e. the solid liquid charge interface electrical double layer (EDL) boundary between the oppositely charge saline solution and rock surface and produce larger PSVs. The value for the zeta potential is critical for electrokinetic phenomena [11].

For all rock lithology and in all environmental conditions, there was some degree of correlation between PSV and AEs, the highest cross-correlation coefficient was for an oven dried halite specimen (0.86) and the lowest was for a water saturated syenogranite specimen (0.079). In addition, linear regression

analysis was computed and for most specimens there was a linear relationship between cumulative number of AEs and PSV events. This shows that AE and PSV event rates are related in a wide range of rock lithology and in different environmental conditions. Work by others has shown statistical correlations between PSV and AE, but this has been limited to dry cement mortar [15].

The linear correlation coefficient calculated between the PSV-AE cross-correlation coefficients and the PSV-AE cumulative number of events linear regression r^2 values, for each material specimen was significant (p-value < 0.01) and had an r^2 value of 0.6529. This indicates that the event detection algorithm implemented, is a viable method for PSV event detection and data reduction. A PSV event detection system would be necessary for the long term monitoring of structures, because the PSV sampling rate needed (~1.5 MSs^{-1}) for crack detection is high and produces a large amount of redundant data during periods of inactivity.

The degree of correlation between AE and PSV events, are related to the water saturation of the rocks tested. On average the higher the water saturation the lower the cross-correlation coefficient; water saturated samples had the lowest correlations, followed by air dried and then oven dried samples. The highest degree of correlation between PSV and AE events occurred for the saline saturate specimens overall.

Oven dried (no absorbed water) specimens showed relatively high PSV-AE cross-correlation coefficients and thus PSV emissions are most likely related to cracking events. Increasing degrees of water saturation in the pores of the rocks, may prevent charge build-up from fresh charged fracture surfaces and thus the reduce PSV-AE correlation, because water is more electrically conductive than air. However, the average cross-correlation coefficients for the saline saturated specimens are the highest, even though saline is more electrically conductive then water, thus this contradicts the aforementioned hypothesis. The saline samples average cross-correlation coefficient could be an anomaly, because there are only three samples, or another unknown mechanism could be responsible.

On average the PSV-AE cross-correlation lag time for each environmental condition was negative, meaning that on average PSV events occur before AE events. This is concurrent with work by others observing relationships between PSC and AE emissions [15]. PSV emissions could a be used as a precursor signal to fracture events and material failure because on average PSV events occur before AE fracture events.

The loading deformation stages of the materials had an effect on the PSV-AE cross-correlations. On average Stage 5, had the highest degree of correlation between PSV and AE events, followed by Stages 1, 3, and 2, however the cross-correlation coefficient for Stage 4 was relatively low in comparison to the other stages. The PSV-AE cross-correlation lag times differed between loading stages, with PSV occurring before AEs during Stages 1, 3 and 5 and AEs occurring before PSV during Stages 2 and 4. The type of material deformation affected not only the degree of correlation between PSV and AE events, but also the lead/lag time between PSV events and AE events. It could be possible to use

capacitively coupled EPS and piezo transducers simultaneously in SHM applications, to analyse PSV-AE lag times and determine the deformation stage in a structure. For instance, irreversible damage occurring beyond loading Stage 3 could be avoided in structures using a PSV-AE monitoring technique.

Rock lithology has an effect on PSV-AE correlation. By analysing the overall cross-correlation data for all of the oven dried specimens, the effect of water and saline saturation level and deformation stages are negated and lithological effects are prominent. There does not appear to be a link between quartz content and the degree of AE-PSV correlation and thus the piezoelectric effect of quartz is not likely responsible. The lowest PSV-AE correlations occurred in metamorphic rocks, (schist and marble), the middle correlations occurred in igneous rocks (granite, gabbro and syenogranite) and the highest correlations occurred in sedimentary rocks (sandstone and halite). The exception to this rule is the quartzite specimen which has a relatively high correlation between AE and PSV activity, but is a metamorphic rock type. This data supports the theory that PSVs are generated by fresh charged fracture surfaces and thus there are correlations between PSV and AE in both piezo and non-piezoelectric rock types.

10.1.2 Manmade materials: concrete and glass ceramic

The results of the experiments presented in chapter 7 showed that PSV emissions were present in concrete specimens in all environmental conditions and in oven dried glass ceramic in the range of millivolts. As with the RTD rock testing experiments the signal to noise ratio of PSVs are better than the associate PSC (Pico amps) observed by others in rocks [16, 18, 82, 151] and cement mortar [15], which also required electrical shielding. Thus, PSV monitoring using EPS could be a more suitable method, for real world civil SHM applications for concrete structures. Although concrete does contain piezoelectric quartz minerals, the piezoelectric effect is not likely the sole generation mechanism, as glass ceramic (a homogenous man-made non-piezoelectric material) also produced PSV during loading.

Similar to the RTD rock testing experiments discussed previously in (section 10.1.1), higher water concentrations of the rocks produce larger average PSV amplitudes, with oven dry (i.e. no water) having the lowest amplitude, followed by air dry and water saturated concrete. Saline saturated concrete specimens had the highest average PSV amplitude. However, dry rocks generally have better PSV-AE correlations. As described the previously in section 10.1.1, the electrokinetic effect of water movement may be responsible for the increased average PSV amplitudes of the water saturated and saline saturated concrete specimens. Both specimens produced the highest PSV amplitude at the start of the loading cycle, where pores in the concrete are suspected to close and produce a pressure gradient in the fluid need for the electrokinetic effect to take place.

There was some degree of correlation between PSV and AE in concrete in all environmental conditions (oven dried, air dried, water saturated and saline saturated). Although, environmental conditions had an effect on the cross-correlations between AE and PSV events. The lowest overall cross-correlation coefficient between AE and PSV activity occurred in the water saturated sample (0.11), followed by the

saline saturated sample (0.19). The highest correlation is present in the air dried sample (0.33), followed by the oven dried (0.24). The concrete specimens AE-PSV correlation is generally lower than the majority of rock lithology, in their respective environmental conditions.

The lag time between PSV and AE also varied, on average water and saline specimens had PSV events occur before AE events; oven dried had PSV and AE events occurred simultaneously and for air dried AE events occurred before PSV events. The dryer (air dried and oven dried) concrete specimens appear to have stronger PSV AE correlations, compared to the water or saline saturated specimens. This was also the case with the RTD rock experiments discussed in section 10.1.1. However, on average saline saturated rocks had the highest PSV-AE correlation, but this could be an anomalous result due to small sample size, as explained previously.

A strong linear correlation exists between the PSV-AE cross-correlation coefficients and cumulative PSV and AE linear regression r^2 values. This indicates that the PSV event detection method may be a suitable method for data reduction, in concrete as well as rocks. However, further testing and development of the algorithm for "real time" event detection would be needed for a commercial system.

The deformation loading state also had an effect of the PSV-AE cross-correlation in concrete specimens, in terms of cross-correlation coefficient and lag time. A likely reason for the difference in correlation coefficients and lag times between PSV and AE, is that multiple generation mechanisms exist and the dominance of each mechanism changes, whilst transitioning through the stages of loading. For instance, the main sources of AE during Stage 2/3 are from stable microcrack propagation, Stage 4 unstable microcrack propagation and coalescence and Stage 5 unstable macrocrack propagation and sheer plane development.

As there were PSV-AE correlations in concrete (piezo) and glass ceramic (non-piezo). This data supports the theory [13, 15, 80-83] that PSVs are also generated by the movement and separation of fresh charged fracture surfaces, thus explaining the correlations between PSV and AEs.

10.1.3 Conclusions

- PSVs are present in a wide range of different rock lithology and concrete and for each environmental condition, in the range of millivolts. PSVs have a better single to noise ratio than their associated PSCs, work by others [11-13, 15-17, 80-86] have shown PSCs emitted are in the range of (Pico amps). An advantage of measuring PSV using EPS, is that it does not have to be carried out inside a Faraday shield and thus may be a more amenable for real world SHM applications.
- This is the first study observing PSE in concrete, providing evidence that monitoring PSV using EPS could be used for the SHM of civil structures.
- PSV emissions are present in quartz rich rocks and rocks containing no quartz. PSVs were also present in manmade materials including quartz rich concrete and non-quartzose glass ceramic.

Therefore, the generation mechanism/s behind PSV emissions in concrete and rock is/are not solely due to the piezoelectric effect of quartz.

- There was some degree of correlation between PSV and AE (i.e. cracking) in all rock lithology and concrete and in each environmental condition tested; although, PSV-AE correlations were generally lower in concrete specimens compared to rocks. Monitoring PSV using EPS technology could be a robust and more cost effective alternative/complimentary technology to piezo transducers, for detecting cracking events in geological and manmade structures.
- The PSV event detection algorithm implemented, was successful and there were linear relationships between cumulative number AE and PSV events in most rock lithology and concrete specimens tested. This algorithm demonstrates the principle for a more advanced PSV "real time" event detection algorithm needed for data reduction, for the long term monitoring of structures.
- Environmental conditions and the stage of uniaxial deformation of the rocks and concrete, have an effect on the PSV-AE cross-correlation, in terms of correlation coefficient and lead/lag time and will have to be taken into consideration for the SHM of structures using EPS. The general trend is that water saturation and saline saturation reduce the PSV-AE correlations.
- By monitoring PSV and AE simultaneously, it may be possible to determine changes in water or saline saturation and the deformation stage of the material; achieved by observing changes in AE-PSV cross-correlation coefficient and lead/lag time between AE and PSV events.
- The correlation and lag times between PSV and AE events is dependent on rock lithology and material type. Therefore, the electrical properties of rocks and concrete types will have to be taken into account for SHM applications using EPS, in order to monitor damage effectively.
- A likely generation mechanism for PSV-AE correlation is the movement and separation of fresh of charged facture surfaces.

10.2 PSVs during cyclic loading of geological materials using capacitively coupled EPS

The results of experiments presented in chapter 8 are concluded in this section. The initial loading effect of PSV emissions was observed in all rock lithology (excluding marble) and concrete. The effect was present during all loading cycles of syenogranite and gabbro specimens this is also true for sandstone and concrete specimens, excluding the first loading cycle. The schist specimen only shows evidence of the initial loading effect during Cycles 3, 4 and 6. The initial loading effect duration linearly increased with each successive cycle for the syenogranite, sandstone and schist specimens and linearly decreased in duration for the concrete and gabbro specimens. I hypothesise that PSV produced during the initial loading region, is the result of an abrupt change in stress rate from unloading to loading; research by others has suggested that PSC emissions are linked to stress rate [16, 17].

The Kaiser effect was observed in all rock lithology and concrete specimens and for all possible loading cycles, apart from in the marble cyclic loading experiment. A work hardening effect similar in nature to the Kaiser effect of AE, was also observed in all rock lithology, apart from marble and sandstone specimens. For all possible loading cycles, the Kaiser effect of PSV was observed for the syenogranite specimen, this was also true for the schist, gabbro and concrete specimens, except the effect was not present during loading Cycles 4, 2 and 3 respectively.

The Felicity effect of AE was observed in the syenogranite, gabbro, schist and concrete specimens but not for the marble specimen. The Felicity effect of PSV was only observed in the gabbro schist and concrete specimens; the absence of Felicity effect of PSV in the syenogranite and sandstone specimens could be a lithological effect. Felicity effect was observed during loading Cycles 2, 5 and 6 in the PSV emissions for the schist specimen, whereas the effect was present in all loading cycles excluding Cycle 2 for the AE. The Felicity effect was observed during Cycles 3,4 and 5 in the PSV emissions and AE for the gabbro specimen. Concrete however only had Felicity effect present in the PSV emissions during the final loading cycle (Cycle 4), but the effect was observable for all loading cycles in the AE.

The observations of Kaiser and Felicity effect of PSV emissions in rocks and concrete further support the theory that PSV emissions are related to movement and separation of charged fracture surfaces, as did the RTD experiments discussed section 10.1.

Kaiser effect is a measure of damage for materials subjected to load [53], in addition the Felicity ratio it can be used to monitor the progression of damage in materials [45]. Therefore, monitoring PSV using capacitively coupled EPS could be used to assess damage and its progression in rock and concrete structures.

10.2.1 Conclusions

- The initial loading effect observed in the PSV emissions in the cyclic RTD experiments has not been reported before in studies by others and may be useful for developing our understanding of PSV generation mechanism/s.
- PSV emissions exhibit an effect similar to the Kaiser and Felicity effect of AEs. Although there have been studies by others [81, 82] observing Kaiser effect in granite and marble samples, this is the first study observing this effect in a wide range of rock lithology and concrete.
- The observations of Kaiser and Felicity effect of PSV emissions in rocks and concrete, further support the theory that PSV emissions are related to movement and separation of charged fracture surfaces, as did the RTD experiments discussed section 10.1.
- Monitoring PSV using capacitively coupled EPS may allow for the detection of damage and damage progression monitoring in rock and concrete structures. The advantage of this is that EPS is a more advanced and cost effect technology than piezo transducers which are currently used for monitoring cracking events.

10.3 PSV emissions during step like stress (SLS) loading of geological materials using directly coupled EPSs

The experiments detailed in chapter 9, showed that there was a strong linear relationship between PSV and applied stress in the SLS-RTD ($r^2 = 0.99$) and cyclic SLS ($r^2 = 0.84$) sandstone experiments. A weak relationship was observed in the marble specimens, for both the SLS-RTD ($r^2 = 0.24$) and the cyclic SLS ($r^2 = 0.063$) experiments. In addition, there is a difference in the maximum PSV amplitudes of the sandstone (268.01 mV) and marble (143.25 mV) cyclic loading experiments, although they were subjected to identical loading profiles. The sandstone specimens contain high amounts of quartz whereas as the marble specimens contain none. Therefore, the piezoelectric effect of quartz is likely responsible for the DC changes in PSV amplitude, related to the applied stress steps. The theory of piezoelectricity states that the applied stress is proportional to the electric field produced in the piezo element [154].

The PSV amplitude does not appear to decay back to its baseline level, after the sandstone specimens were unloaded. The PSV on surface of the rock could be an ultra-low frequency signal or a DC voltage could be maintained on the surface. The latter would enable the determination of in-situ-stress, at least in terms of stress field direction as one could compare the PSV amplitude of multiple sensors over a structure, to determine the maximum and minimum horizontal stress. The vertical stress is often determined by knowledge of the material properties and weight of overlaying material mass. The former would mean that only changes in in-situ stress could be determined, as the PSV corresponding to the stress level would not be maintained after it was applied. However, this would still be useful as one could apply load to a structure instrumented with an array of EPS to infer a stress map over the structure and thus identify weak spots.

However, there were transient spikes in PSV amplitude in both the sandstone and marble experiments during abrupt changes in stress rate (i.e. from step to plateau to step). Another unknown generation mechanism must be responsible for this phenomenon, as the marble specimen contains no piezoelectric minerals.

It appears that the unknown mechanism is influenced by applied stress rate, as the transient spikes in PSV were greater during higher stress rates in the sandstone SLS-RTD experiment. This is in agreement with work by others, suggesting that PSC is related to stress rate [16, 17]. The polarity of the transient PSV spikes in sandstone changes when transitioning from loading to unloading cycles, this was also observed in studies by others [17] in marble samples containing small amounts of quartz minerals (<1 %). However, this phenomenon it did not occur in the quartz devoid marble (100 % calcite) specimens presented in this thesis. I hypothesise that the polarity reversals could be a lithological effect or possibly the piezoelectric effect of quartz is responsible. The transit spikes in PSV amplitude also exhibit a work hardening (Kaiser effect), as the PSV amplitude decrease with each successive loading cycle, although this is more prominent in the marble specimen. This could be useful for monitoring the damage progression in structures under repeated loading.

Both the sandstone and marble cyclic SLS experiments were not loaded beyond the materials linear elastic region (i.e. loading Stages 2 and 3), despite this, transient spikes were observed during the stress steps during rapid changes in stress rate. The is contradictory to work by others stating that PSCs are only detectable beyond the linear elastic region of marble specimens and are related to change in Young's modulus [18, 151]. I hypotheses that the measurement of PSV using EPS technology is more sensitive than monitoring PSCs using electrometers and this could be the reason for PSV detection in the linear elastic region.

10.3.1 Conclusions

- There is a linear relationship with applied static stress and PSV for quartz rich sandstone, but not for marble samples containing no quartz minerals. It is likely that the piezoelectric effect of quartz is responsible for the PSV-stress relationship.
- Transient PSV amplitude spikes are associated with stress step transitions, in both piezo rocks (i.e. sandstone) and non-piezo rocks (i.e. marble). The PSV generation mechanism/s behind this phenomenon is/are unknown, however it is expected to be related to abrupt changes in stress rate.
- The novel directly coupled smart EPS sensor was a successful design, as it has the necessary high input impedance (resistance = 689 GΩ - 3.068 TΩ, capacitance = 0.67 pF) and low noise (31.68 nV√Hz at 1 kHz) characteristics for measuring PSV noninvasively, at low frequencies (DC-500 kHz). The implementation of this sensor allowed for relationships between applied stress and PSV to be studied.
- An EPS-PSV system could be the first viable, non-invasive in-situ stress measurement tool. Current methods of in-situ stress measurement involve disturbing the rock mass and are costly to implement. As for other methods of PSE measurement such as EME antennas and electrometers, they are costly and/or not suitable for field use; EPS does not have these inherent disadvantages.

10.4 Future directions

A larger number of test runs of different rock lithology and concrete under different environmental conditions would be necessary to investigate variations. By doing multiple RTD, cyclic RTD and SLS loading experiments, variations in PSV-AE cross-correlation; initial loading, Kaiser and Felicity effects; and stress-PSV relationships could be accounted for. This would better characterise PSVs and create a more robust PSV-SHM tool, for real world applications. It may be necessary to characterise the spontaneous electrical properties of a materials, before the SHM monitoring of a structure made of the same material.

It would also be useful to complete a larger number of test runs for different types of concrete used in the construction of civil structures, to characterise PSV-AE and PSV-stress correlations for these materials and the degree of variation between material samples.

Civil structures are commonly made of reinforced concrete, in which steel rebar is embedded into the concrete to add strength. Loading experiments would have to be carried out to investigate the effect of the rebar, as it an electrically conductive medium that could have an effect on PSV measured at the surface of the concrete by EPS.

The development of "real time" PSV event detection system, in order to remove redundant data and enable long-term monitoring of structures, without using an excessive amounts of hard drive space. This system would most likely be a field programmable gate array (FPGA) based technology, as current AE event detection systems [48] utilise FPGAs for digitally controllable filtering and event detection of piezo transducer signals acquired at 5 MSs^{-1}.

Currently it is not known how long PSV is maintained on the surface of rocks during loading and after unloading. Future SLS loading experiments should investigate PSV relaxation time with specimens held at content loads for long durations (in the range of weeks or months). This would determine how long after a load is applied that it is still possible to monitor in-situ stress using PSV-EPS methods.

Work by others have used neural networks [155] and pattern recognition [27] for identifying precursory signals to damage in sensor data, a similar approach could be applied to PSV event data, for a more advanced method of detecting and monitoring damage in structures.

Scaling up the experiments to larger structures such as structural beams of rock or concrete, would be necessary to investigate the properties of PSV on a larger scale. Arrays of EPS and piezo transducers could be used to monitor the PSV and AE respectively, over different parts of the structure and could possibly be used for determining the source location of PSV and AE emissions.

Finally, the development of monolithic semiconductor integrated circuit (IC) version of the EPS, would be necessary for commercialisation. This would drive down the cost of the sensors to a significantly lower price point than piezo transducers for monitoring AE and in-situ stress monitoring technologies. In addition, a wide band restively coupled EPS could be developed so that high frequency transient PSV signals associated with AE and low frequency PSV signals associated with applied stress, could be monitored simultaneously.

10.5 On the measurement of PSV using EPS as a structural health monitoring tool

The work presented in this thesis demonstrates the viability of monitoring PSVs for the SHM of manmade and geological structures. The results show that PSV high frequency transient signals correlate with cracking events, in a wide variety of rock lithology and to a lesser extent in concrete. There was also a linear relationship between low frequency PSV signals and applied stress in quartz rich rocks (i.e. sandstone). In addition, monitoring PSV using EPS has inherent advantages to measuring PSC using

electrometers and EME antennas; such as better signal to noise ratio (i.e. no need for Faraday shielding) and more cost effective and portable compared to electrometers.

The work presented in this thesis advances the current understanding of PSE generation in man-made and geological materials. Work by others [15] have only shown statistical relationships between PSE and AE in cement mortar, however this thesis demonstrates that there are also correlations in a wide range of rock lithology and concrete and in different environmental conditions. Although research by others [18, 81, 82] has shown that PSE exhibits a Kaiser like effect in marble and granite, the work presented in this thesis shows the effect is present in a wide variety of rock lithology and concrete. In addition, PSC research by others [16, 17] has only shown relationships between stress rate and PSC, I suspect this is because the nature of current measurement discharges the material samples. Whereas work presented in this thesis shows that PSVs correlate with static stress; the PSV is not discharged by the measurement itself, as EPS is a non-invasive device. The work in this thesis also advances the understanding of PSE generation mechanisms. The results show a relationship between applied stress and PSV in only piezo materials, therefore the piezoelectric effect of quartz is most likely responsible for the low frequency/DC changes in PSV amplitude. There were correlations between PSV and AE in both piezo and non-piezo materials and thus the movement and separation of fresh charged fracture surfaces is likely responsible for the high frequency transient PSV signals (correlation with AEs).

The results are promising for the practical application of a PSV-EPS based tool in the SHM field. Although, relationships between PSV and mechanical properties of interest such as cracking events and applied stress are complex, as they are influenced by rock lithology, mineralogy, water and saline content, applied stress rate and previous structural damage (Kaiser and Felicity effect). Furthermore, there are multiple PSV generation mechanisms including the electrokinetic effect of water movement, the piezoelectric effect, contact and separation of fresh charged facture surfaces and the scientific community's theories of PSE generation mechanisms are often conflicting.

A EPS-PSV based measurement tool would be the first viable PSE monitoring method for real world SHM applications outside of the laboratory setting and have ubiquitous applications. EPS could be used as an alternative/complimentary technology to AE systems for monitoring fracture behaviour and fatigue detection; detecting faults and leaks in vessels and tanks; and monitoring the progression of corrosion. This would have useful applications in manufacturing processes; the SHM of civil and geological structures; and the aerospace industry [49]. EPS could be the first non-invasive in-situ stress monitoring tool, which would be of great importance for underground excavation and design for civil, mining, nuclear waste storage and petroleum engineering sectors [57]. The SHM process involves monitoring the frequency response function (FRF) of a structure in response to excitation [7]. The FRF of the structure is affected by damage such as crack formation and can be monitored with sensors such as piezo transducers. As PSVs are related to AE events it is likely that the PSV-FRF could also be used

to monitor damage progression in a structure. Although, this would have to be confirmed in future experiments; EPS could be more cost effective and advanced method than existing SHM technologies.

REFERENCES

[1] A. Barrias, J. R. Casas, and S. Villalba, "A Review of Distributed Optical Fiber Sensors for Civil Engineering Applications," *Sensors (Basel, Switzerland),* vol. 16, p. 748, 2016.

[2] P. C. Chang, A. Flatau, and S. C. Liu, "Review Paper: Health Monitoring of Civil Infrastructure," *Structural Health Monitoring,* vol. 2, pp. 257-267, 2003.

[3] S. Chase, "The role of smart structures in managing an aging highway infrastructure," presented at the Proceedings of the SPIE Conference, New Beach, CA, USA, 2001.

[4] Atkins Limited, "Structural Integrity monitoring: Review and appraisal of current technologies for offshore applications," Health and Safety Executive 2009.

[5] S. G. Evans, G. S. Mugnozza, A. Strom, and R. L. Hermanns, *Landslides from Massive Rock Slope Failure* vol. 49. Netherlands: Springer, 2006.

[6] B. Glisic, D. Inaudi, and N. Casanova, "SHM process as perceived through 350 projects," presented at the SPIE Smart Structures and Materials + Nondestructive Evaluation and Health Monitoring, San Diego, CA, USA, 2010.

[7] H. Sohn, C. R. Farrar, F. M. Hemez, D. D. Shunk, D. W. Stinemates, B. R. Nadler*, et al.*, "A Review of Structural Health Monitoring Literature: 1996–2001," Los Alamos National Laboratory2004.

[8] J. P. Lynch and K. J. Loh, "A summary review of wireless sensors and sensor networks for structural health monitoring," *Shock and Vibration Digest,* vol. 38, pp. 91-128, 2006.

[9] J. A. Rice, K. Mechitov, S.-H. Sim, T. Nagayama, S. Jang, R. Kim*, et al.*, "Flexible smart sensor framework for autonomous structural health monitoring," *Smart structures and Systems,* vol. 6.5-6, pp. 423-438, 2010.

[10] B. Glišić, D. Hubbell, D. H. Sigurdardottir, and Y. Yao, "Damage detection and characterization using long-gauge and distributed fiber optic sensors," *Optical Engineering,* vol. 52, pp. 087101-087101, 2013.

[11] D. Eccles, P. R. Sammonds, and O. C. Clint, "Laboratory studies of electrical potential during rock failure," *International Journal of Rock Mechanics and Mining Sciences,* vol. 42, pp. 933-949, 10// 2005.

[12] M. Ikeya, C. Yamanaka, T. Mattsuda, H. Sasaoka, H. Ochiai, Q. Huang*, et al.*, "Electromagnetic pulses generated by compression of granite rocks and animal behavior," *Episodes,* vol. 23, pp. 262-265, 2000.

[13] V. Hadjicontis, C. Mavromatou, and D. Ninos, "Stress induced polarization currents and electromagnetic emission from rocks and ionic crystals, accompanying their deformation," *Natural Hazards and Earth System Science,* vol. 4, pp. 633-639, 2004.

[14] R. Ulusay and J. A. Hudson, *The complete ISRM suggested methods for rock characterization, testing and monitoring : 1974-2006*: Commission on Testing Methods, International Society of Rock Mechanics, 2007.

[15] C. Stergiopoulos, I. Stavrakas, G. Hloupis, D. Triantis, and F. Vallianatos, "Electrical and Acoustic Emissions in cement mortar beams subjected to mechanical loading up to fracture," *Engineering Failure Analysis,* vol. 35, pp. 454-461, 12/15/ 2013.

[16] C. Anastasiadis, D. Triantis, I. Stavrakas, and F. Vallianatos, "Pressure Stimulated Currents (PSC) in marble samples," *Annals of Geophysics,* vol. 47, pp. 21-28, 2004.

[17] I. Stavrakas, C. Anastasiadis, D. Triantis, and F. Vallianatos, "Piezo Stimulated Currents in marble samples: Precursory and concurrent-with-failure signals," *Natural Hazards and Earth System Sciences,* vol. 3, pp. 243-47, 2003.

[18] I. Stavrakas, D. Triantis, Z. Agioutantis, S. Maurigiannakis, V. Saltas, F. Vallianatos*, et al.*, "Pressure stimulated currents in rocks and their correlation with mechanical properties," *Nat. Hazards Earth Syst. Sci,* vol. 4, pp. 563-567, 2004.

[19] A. Aydin, M. R. Dobbs, H. J. Reeves, M. P. Kirkham, and C. C. Graham, "Stress induced electric field measurements of different rock lithology using the Electric Potential Sensor," presented at the 47th US Rock Mechanics/Geomechanics Symposium, San Francisco , USA, 2013.

[20] A. Aydin, R. J. Prance, H. Prance, and C. J. Harland, "Observation of pressure stimulated voltages in rocks using an electric potential sensor," *Appl. Phys. Lett,* vol. 95, pp. 124102 - 124102-3, 2009.

[21] A. Rytter, "Vibrational Based Inspection of Civil Engineering Structures," PhD, Dept. of Building Technology and Structural Engineering, Aalborg University, 1993.

[22] P. Cawley, "Long range inspection of structures using low frequency ultrasound," presented at the DAMAS '97 (Euromech 365), 1997.

[23] C. Biemans, W. J. Staszewski, C. Boller, and G. R. Tomlinson, "Crack Detection in Metallic Structures Using Piezoceramic Sensors," presented at the Damage Assessment of Structures, Proceedings of the International Conference on Damage Assessment of Structures (DAMAS), Dublin, Ireland, 1999.

[24] S. W. Doebling and C. R. Farrar, "Using Statistical Analysis to Enhance Modal Based Damage Identification," presented at the Structural Damage Assessment Using Advanced Signal Processing Procedures, University of Sheffield, 1997.

[25] S. W. Smith, *The Scientist and Engineer's Guide to Digital Signal Processing* vol. 1: California Technical Pub., 1997.

[26] S.-F. Jiang, "Structural health monitoring - Intelligent information processing and application," *Gong Cheng Li Xue/Engineering Mechanics,* vol. 26, pp. 184-212, 2009.

[27] M. M. Reda Taha and J. Lucero, "Damage identification for structural health monitoring using fuzzy pattern recognition," *Engineering Structures,* vol. 27, pp. 1774-1783, 10// 2005.

[28] K. P. Chong and J. B. Scalzi, "NSF Programs in Nondestructive Evaluation of Civil Infrastructures " *Nondestructive Testing and Evaluation,* vol. 11, pp. 349-356, 1994/12/01 1994.

[29] M. Kaphle, "Analysis of acoustic emissions data for accurate damage assessment for structural health monitoring applications," Ph.D., School of Chemistry, Physics and Mechanical Engineering, Queensland University of Technology, Brisbane City, Australia, 2012.

[30] A. L. Window and G. S. Holister, "Introduction " in *Strain Gauge Technology*, ed: Applied Science Publishers LTD, 1982, p. 1.

[31] A. L. Window and G. S. Holister, "Basic Operating Principle " in *Strain Gauge Technology*, ed: Applied Science Publishers LTD, 1982, pp. 4-5.

[32] A. L. Window and G. S. Holister, "Gauge Construction," in *Strain Gauge Technology*, ed: Applied Science Publishers LTD, 1982, pp. 10-18.

[33] A. L. Window and G. S. Holister, "The Weatstone Bridge " in *Strain Gauge Technology*, ed: Applied Science Publishers LTD, 1982, pp. 140 - 141.

[34] H. Guo, G. Xiao, N. Mrad, and J. Yao, "Fiber Optic Sensors for Structural Health Monitoring of Air Platforms," *Sensors,* vol. 11, p. 3687, 2011.

[35] J. M. López-Higuera, L. R. Cobo, A. Q. Incera, and A. Cobo, "Fiber optic sensors in structural health monitoring," *J. Lightwave. Technol,* vol. 29 pp. 587–608, 2011.

[36] S. K. Abi Kaed Bey, T. Sun, and K. T. V. Grattan, "Simultaneous measurement of temperature and strain with long period grating pairs using low resolution detection," *Sensors and Actuators A: Physical,* vol. 144, pp. 83-89, 5/28/ 2008.

[37] K. T. V. Grattan and T. Sun, "Fiber optic sensor technology: an overview," *Sensors and Actuators A: Physical,* vol. 82, pp. 40-61, 5/15/ 2000.

[38] A. D. Kersey, "A Review of Recent Developments in Fiber Optic Sensor Technology," *Optical Fiber Technology,* vol. 2, pp. 291-317, 1996/07/01 1996.

[39] B. Lee, "Review of the present status of optical fiber sensors," *Optical Fiber Technology,* vol. 9, pp. 57-79, 2003/04/01 2003.

[40] S. K. T. Grattan, S. E. Taylor, T. Sun, P. A. M. Basheer, and K. T. V. Grattan, "Monitoring of Corrosion in Structural Reinforcing Bars: Performance Comparison Using In Situ Fiber-Optic and Electric Wire Strain Gauge Systems," *IEEE Sensors Journal,* vol. 9, pp. 1494-1502, 2009.

[41] H. N. Li, D. S. Li, and G. B. Song, "Recent applications of fiber optic sensors to health monitoring in civil engineering," *Engineering Structures,* vol. 26, pp. 1647-1657, 9// 2004.

[42] F. Surre, T. Sun, and K. T. Grattan, "Fiber Optic Strain Monitoring for Long-Term Evaluation of a Concrete Footbridge Under Extended Test Conditions," *IEEE Sensors Journal,* vol. 13, pp. 1036-1043, 2013.

[43] National Instruments. (2016, 08/08/2016). *FBG Optical Sensing: A New Alternative for Challenging Strain Measurements*. Available: http://www.ni.com/white-paper/12338/en/
[44] ASTM international, "ASTM E1316-07b Standard terminology for nondestructive examinations," West Conshohocken, PA, USA2007.
[45] A. Nair and C. S. Cai, "Acoustic emission monitoring of bridges: Review and case studies," *Engineering Structures,* vol. 32, pp. 1704-1714, 6// 2010.
[46] S. Jayant and C. Inderjit, "Fundamental Understanding of Piezoelectric Strain Sensors," *Intelligent Material Systems and Structures,* vol. 11, pp. 246-257, 2000.
[47] NDT Resource centre. (2016). *Introduction to Acoustic Emission Testing - Equiptment*. Available:https://www.ndeed.org/EducationResources/CommunityCollege/Other%20Methods/AE/AE_Equipment.php
[48] Physical Acoustics Cooperation, "PCI-2 BASED AE SYSTEM USER'S MANUAL Rev 3," 2007.
[49] S. Gholizadeh, Z. Leman, and B. T. H. T. Baharudin, "A review of the application of acoustic emission technique in engineering," *Structural Engineering and Mechanics An International Journal,* vol. 54, pp. 1075-1095, 2015.
[50] A. A. Pollock, "AE Signal Features: Energy, Signal Strength, Absolute Energy and RMS," 2014.
[51] J. F. Tressler, S. Alkoy, and R. E. Newnham, "Piezoelectric Sensors and Sensor Materials," *Journal of Electroceramics,* vol. 2, pp. 257-272, 1998.
[52] A. Lavrov, "The Kaiser effect in rocks: principles and stress estimation techniques," *International Journal of Rock Mechanics and Mining Sciences,* vol. 40, pp. 151-171, 2// 2003.
[53] C. Li and E. Nordlund, "Experimental verification of the Kaiser effect in rocks," *Rock Mechanics and Rock Engineering,* vol. 26, pp. 333-351, 1993.
[54] R. Vidya Sagar, B. K. Raghu Prasad, and R. K. Singh, "Kaiser effect observation in reinforced concrete structures and its use for damage assessment," *Archives of Civil and Mechanical Engineering,* vol. 15, pp. 548-557, 2// 2015.
[55] C. Rowland, L. Butler, and M. Preston, "Acoustic Emission Technique to Assist the Formula One Designer in Structural Design," in *26th European Conference on Acoustic Emission Testing*, Berlin, Germany, 2004.
[56] W. H. Prosser, *Nondestructive Evaluation: Theory, Techniques, and Applications*: CRC Press, 2002.
[57] S. Maleki, A. Moradzadeh, R. Ghavami Riabi, and F. Sadaghzadeh, "Comparison of Several Different Methods of in situ stress determination," *International Journal of Rock Mechanics and Mining Sciences,* vol. 71, pp. 395-404, 10// 2014.
[58] University of Idaho. (2013). *Advanced Structural Geology*. Available: http://webpages.uidaho.edu/~simkat/course_materials/geol542/PFfigs/06_14_15.jpg
[59] B. Amadei and O. Stephansson, "Methods of in situ Stress Measurement," in *Rock Stress and Its Measurement*, ed Dordrecht: Springer Netherlands, 1997, pp. 95-120.
[60] R. Z. Moayed, E. Izadi, and M. Fazlavi, "In-situ stress measurements by hydraulic fracturing method at Gotvand Dam site, Iran," *Turkish Journal of Engineering and Environmental Sciences,* vol. 36, pp. 179-194, 13/04/2011 2011.
[61] B. C. Haimson and F. H. Cornet, "ISRM suggested methods for rock stress estimation-part 3: Hydraulic fracturing (HF) and/or hydraulic testing of pre-existing fractures (HTPF)," *International Journal of Rock Mechanics and Mining Sciences,* vol. 40, pp. 1011-1020, 2003.
[62] W. Jing, W. P. Xue, P. W. Hao, L. W. Jing, and R. S. Yang, "Principle and method of sleeve fracturing method in testing in-situ stress," *Meitan Xuebao/Journal of the China Coal Society,* vol. 40, pp. 342-346, 2015.
[63] K. Sugawara and Y. Obara, "Measurement of in-situ rock stress by hemispherical-ended borehole technique," *Mining Science and Technology,* vol. 3, pp. 287-300, 1986/08/01 1986.
[64] J. Rutqvist and O. Stephansson, "A cyclic hydraulic jacking test to determine the in situ stress normal to a fracture," *International Journal of Rock Mechanics and Mining Sciences & Geomechanics Abstracts,* vol. 33, pp. 695-711, 1996/10/01 1996.
[65] W. Lin, M. Kwaśniewski, T. Imamura, and K. Matsuki, "Determination of three-dimensional in situ stresses from anelastic strain recovery measurement of cores at great depth," *Tectonophysics,* vol. 426, pp. 221-238, 10/30/ 2006.

[66] F. G. Strickland and N. K. Ren, "Use of Differential Strain Curve Analysis in Prediction In-situ Stress State for Deep Wells," *U.S. Symposium on Rock Mechanics,* pp. 523-532, 1980.
[67] T. Ogawa and H. Utada, "Electromagnetic signals related to incidence of a teleseismic body wave into a subsurface piezoelectric body," *Earth, Planets and Space,* vol. 52, pp. 253-260, 2000.
[68] A. Tzanis and F. Vallianatos, "A critical review of Electric Earthquake Precursors," *Annals of Geophysics,* vol. 44, 2001.
[69] H. Mizutani, T. Ishido, T. Yokokura, and S. Ohnishi, "Electrokinetic phenomena associated with earthquakes," *Geophysical Research Letters,* vol. 3, pp. 365-368, 1976.
[70] M. B. Gokhberg, V. A. Morgounov, T. Yoshino, and I. Tomizawa, "Experimental measurement of electromagnetic emissions possibly related to earthquakes in Japan," *Journal of Geophysical Research: Solid Earth,* vol. 87, pp. 7824-7828, 1982.
[71] J. W. Warwick, C. Stoker, and T. R. Meyer, "Radio emission associated with rock fracture: Possible application to the Great Chilean Earthquake of May 22, 1960," *Journal of Geophysical Research: Solid Earth,* vol. 87, pp. 2851-2859, 1982.
[72] Y. Fujinawa and K. Takahashi, "Electromagnetic radiations associated with major earthquakes," *Physics of the Earth and Planetary Interiors,* vol. 105, pp. 249-259, 1998.
[73] L. Jouniaux, J.-P. Pozzi, J. Berthier, and P. Massé, "Detection of fluid flow variations at the Nankai Trough by electric and magnetic measurements in boreholes or at the seafloor," *Journal of Geophysical Research: Solid Earth,* vol. 104, pp. 29293-29309, 1999.
[74] T. Ishido and H. Mizutani, "Experimental and theoretical basis of electrokinetic phenomena in rock-water systems and its applications to geophysics," *Journal of Geophysical Research: Solid Earth,* vol. 86, pp. 1763-1775, 1981.
[75] S. Pride, "Governing equations for the coupled electromagnetics and acoustics of porous media," *Physical Review B,* vol. 50, pp. 15678-15696, 12/01/ 1994.
[76] P. Mazur and J. T. G. Overbeek, "On electro-osmosis and streaming-potentials in diaphragms: II. General quantitative relationship between electro-kinetic effects," *Recueil des Travaux Chimiques des Pays-Bas,* vol. 70, pp. 83-91, 1951.
[77] C. Rosen, B. V. Hiremath, and R. Newnham, "Piezoelectricity," ed: American Inst. of Physics, 1992.
[78] X. Lv, Y. Pan, X. Xiao, and A. Wang, "Barrier formation of micro-crack interface and piezoelectric effect in coal and rock masses," *International Journal of Rock Mechanics and Mining Sciences,* vol. 64, pp. 1-5, 12// 2013.
[79] (06/01/2017). *Keithley Instruments, Inc.* Available: http://www.tek.com/keithley
[80] V. Frid, A. Rabinovitch, and D. Bahat, "Fracture induced electromagnetic radiation," *Journal of Physics D: Applied Physics,* vol. 36, p. 1620, 2003.
[81] Y. Mori, Y. Obata, J. Pavelka, J. Sikula, and T. Lokajicek, "AE Kaiser Effect and Electromagnetic Emission in the Deformation of Rock Sample," *Journal of Acoustic Emission,* vol. 22, pp. 90-101, 2004.
[82] C. Anastasiadis, D. Triantis, and C. Hogarth, "Comments on the phenomena underlying pressure stimulated currents in dielectric rock materials," *J. Mater. Sci,* vol. 42, pp. 2538-2542, 2007.
[83] I. Yamada, K. Masuda, and H. Mizutani, "Electromagnetic and acoustic emission associated with rock fracture," *Physics of the Earth and Planetary Interiors,* vol. 57, pp. 157-168, 10// 1989.
[84] T. Zhu, J. Zhou, and H. Wang, "Electromagnetic emissions during dilating fracture of a rock," *J. Asian, Earth. Sci,* vol. 73, pp. 252-262, 2013.
[85] F. Freund, "Charge generation and propagation in igneous rocks," *Journal of Geodynamics,* vol. 33, pp. 543-570, 5// 2002.
[86] J. J. Mellon, A. Takeuchi, B. W. Lau, R. Post, J. Keefner, and A. Al-Manaseer, "Electric Properties of Igneous Rock under Pre-Earthquake Conditions," Corvallis: Oregon State University, 2004.
[87] (06/01/2017). *Physical Acoustics Corporation*. Available: http://www.physicalacoustics.com/
[88] C. J. Harland, T. D. Clark, and R. J. Prance, "Electric potential probes - new directions in the remote sensing of the human body," *Measurement Science and Technology,* vol. 13, p. 163, 2002.

[89] R. J. Prance, S. T. Beardsmore-Rust, P. Watson, C. J. Harland, and H. Prance, "Remote detection of human electrophysiological signals using electric potential sensors," *Applied Physics Letters,* vol. 93, p. 033906, 2008.
[90] R. J. Prance, A. Debray, T. D. Clark, H. Prance, M. Nock, C. J. Harland*, et al.*, "An ultra-low-noise electrical-potential probe for human-body scanning," *Measurement Science and Technology,* vol. 11, p. 291, 2000.
[91] P. Watson, R. J. Prance, S. T. Beardsmore-Rust, and H. Prance, "Imaging electrostatic fingerprints with implications for a forensic timeline," *Forensic Science International,* vol. 209, pp. e41-e45, 6/15/ 2011.
[92] W. Gebrial, C. Antrobus, and R. J. Prance, "Non destructive testing of materials using a novel electric potential sensor," in *Proceedings of the 2006 IEEE Sensors Applications Symposium, 2006.*, 2006, pp. 115-118.
[93] S. Mukherjee, P. Watson, and R. J. Prance, "Non-contact measurement of local conductivity variations in carbon fibre based composite materials," *Journal of Physics: Conference Series,* vol. 307, p. 012034, 2011.
[94] R. J. Prance, T. D. Clark, H. Prance, and A. Clippingdale, "Non-contact VLSI imaging using a scanning electric potential microscope," *Measurement Science and Technology,* vol. 9, p. 1229, 1998.
[95] R. J. Prance and A. Aydin, "Acquisition of a nuclear magnetic resonance signal using an electric field detection technique," *Applied Physics Letters,* vol. 91, p. 044103, 2007.
[96] Plessey Semiconductors Ltd. (19/07/2016). *EPIC is Plessey's multi Award winning sensor*. Available: http://www.plesseysemiconductors.com/epic-plessey-semiconductors.php
[97] J. W. Archer, M. R. Dobbs, A. Aydin, H. J. Reeves, and R. J. Prance, "Measurement and correlation of acoustic emissions and pressure stimulated voltages in rock using an electric potential sensor," *International Journal of Rock Mechanics and Mining Sciences,* vol. 89, pp. 26-33, 11// 2016.
[98] Keithley Instruments Inc. (2014). *Low Level Measurements Handbook (7th ed.)*. Available: http://info.tek.com/KI-Low-Level-Measurements-Handbook-LP.html
[99] P. Horowitz and W. Hill, *The Art of Electronics 3rd Edition*: Cambridge University Press, 2015.
[100] M. H. Jones, "The emitter follower," in *A Practical Introduction to Electronic Circuits*, ed: MD Kelvin Hughes Ltd, 1995, p. 105.
[101] P. Grohe and Texas Instruments. (2011, 14/07/2016). Design femtoampere circuits with low leakage, part one. Available: http://www.edn.com/design/analog/4368681/Design-femtoampere-circuits-with-low-leakage-part-one
[102] Rogers Corporation. (2016, 14/07/2016). *Advanced Connectivity Solutions*. Available: https://www.rogerscorp.com/acs/index.aspx
[103] Texas Instruments. (2016, 14/072016). *LMC6081 Precision CMOS Single Operational Amplifier* Available: http://www.ti.com/product/LMC6081
[104] Number One Systems. (2016, 14/07/2016). *Easy-PC Ready To Use PCB Design Software*. Available: http://www.numberone.com/
[105] LPKF Laser & Electroncis. (2016, 14/07/2016). *LPKF CircuitPro PM*. Available: http://www.lpkf.com/products/rapid-pcb-prototyping/software/circuitpro-pm.htm
[106] LPKF Laser & Electronics. (2016, 14/07/2016). *LPKF ProtoMat S103*. Available: http://www.lpkf.com/products/rapid-pcb-prototyping/circuit-board-plotter/protomat-s103.htm
[107] LPKF Laser & Electronics. (2016, 14/07/2016). *LPKF ProtoFlow S*. Available: http://www.lpkf.com/products/rapid-pcb-prototyping/smd-assembly/soldering/smd-reflow-oven.htm
[108] (14/07/2016). *MATLAB*. Available: http://uk.mathworks.com/products/matlab/
[109] National Instruments. (2016, 14/07/2016). *NI PXIe-1071* Available: http://sine.ni.com/nips/cds/view/p/lang/en/nid/208933
[110] National Instruments. (2016, 14/07/2016). *NI PXIe-6124* Available: http://sine.ni.com/nips/cds/view/p/lang/en/nid/206514
[111] Texas Instruments. (2016, 14/07/2016). *UA78L05AIPK* Available: https://store.ti.com/UA78L05AIPK.aspx

[112] STMicroelectronics. (2016, 14/07/2016). *L79L Negative voltage regulators*. Available: http://www.st.com/content/ccc/resource/technical/document/datasheet/65/e7/d9/a9/61/68/43/be/CD00000539.pdf/files/CD00000539.pdf/jcr:content/translations/en.CD00000539.pdf
[113] Analog Devices. (2016, 14/07/2016). *Low Noise, Precision Operational Amplifier OP27*. Available: http://www.analog.com/media/en/technical-documentation/data-sheets/OP27.pdf
[114] Intersil. (2016, 14/07/2016). *ISL22313 Single Digitally Controlled Potentiometer* Available: https://www.intersil.com/content/dam/Intersil/documents/isl2/isl22313.pdf
[115] Texas Instruments. (2016, 14/07/2016). *LM4041-N-xx Precision Micropower Shunt Voltage Reference*. Available: http://www.ti.com/lit/ds/symlink/lm4041-n.pdf
[116] Altium. (2.16, 14/07/2016). *Altium Designer*. Available: http://www.altium.com/altium-designer/overview
[117] PCB Train. (2016, 14/07/2016). *PCB Train part of the Newbury Electronics group*. Available: http://www.pcbtrain.co.uk/?gclid=CjwKEAjw8Jy8BRCE0pOC9qzRhkMSJABC1pvJqhSP5E9be-q4XObJqMVBRP7JluAAGJ32hrdd6Q0JnxoCqA7w_wcB
[118] P.W.Circuits. (2016, 14/072016). *P.W.Circuits Ltd manufacturers of printed circuit boards*. Available: http://www.pwcircuits.co.uk/
[119] (14/07/2016). *Arduino*. Available: https://www.arduino.cc
[120] Maplin. (2016, 14/07/2016). *16x2 LCD Shield for Arduino*. Available: http://www.maplin.co.uk/p/16x2-lcd-shield-for-arduino-n07dh
[121] Physical Accoustics Cooperation. (2017). *AEwin™ - Real-time Data Acquisition and Replay Software*. Available: http://www.physicalacoustics.com/by-product/aewin/
[122] N. Yoder. (2015, 23/06/2016). *peakfinder(x0, sel, thresh, extrema, includeEndpoints, interpolate)*. Available: https://www.mathworks.com/matlabcentral/fileexchange/25500-peakfinder-x0--sel--thresh--extrema--includeendpoints--interpolate-
[123] M. R. Gillespie and M. T. Styles, "BGS Rock Classification Scheme Volume 1," British Geological Survey1999.
[124] C. R. Hallsworth and R. W. O. B. Knox, "BGS Rock Classification Scheme Volume 3," British Geological Survey1999.
[125] A. Streckeisen, "To each plutonic rock its proper name," *Earth-Science Reviews,* vol. 12, pp. 1-33, 3// 1976.
[126] Chemtronics. (23/06/2016). *CircuitWorks Conductive Epoxy*. Available: https://www.chemtronics.com/p-692-circuitworks-conductive-epoxy.aspx
[127] Physical Acoustics Cooperation. (2016, 15/07/2016). *WSa - 100-1000 kHz Wideband AE Sensor*. Available: http://www.physicalacoustics.com/by-product/sensors/WSa-100-1000-kHz-Wideband-AE-Sensor
[128] MTS Systems Corporation. (2016, 15/07/2016). *Extensometers* Available: http://www.mts.com/en/products/producttype/test-components/grips-fixtures-accessories/extensometers/index.htm
[129] E. A. Parr, *Industrial Control Handbook* vol. 3rd edition Industrial Press, Inc, 1999.
[130] MTS Systems Corporation. (2016, 15/07/2016). *Force Transducers (Load Cells)* Available: http://www.mts.com/en/products/producttype/test-components/grips-fixtures-accessories/load-cells-force-transducers/index.htm
[131] MTS Systems Corporation. (2016, 15/07/2016). *MTS Model 815 and 816 Rock Mechanics Test Systems*. Available: http://www.mts.com/ucm/groups/public/documents/library/mts_008000.pdf
[132] B. H. G. Brady and E. T. Brown, *Rock Mechanics for underground mining*: Springer Netherlands, 2004.
[133] I. W. Farmer, *Engineering Behaviour of Rocks*. London: Chapman and Hall Ltd, 1983.
[134] M. S. Paterson and T. F. Wong, *Experimental Rock Deformation –in the Brittle Field* Springer, Berlin, 2005.
[135] *National Instruments Corporation*. Available: http://www.ni.com
[136] C. U. Grosse and M. Ohtsu, *Acoustic Emission Testing* Springer, 2008.
[137] X.-l. Liu, X.-b. Li, L. Hong, T.-b. Yin, and M. Rao, "Acoustic emission characteristics of rock under impact loading," *Journal of Central South University,* vol. 22, pp. 3571-3577, 2015.

[138] MTS Systems Corporation. (2016, 15/07/2016). *MultiPurpose TestWare® Software*. Available: https://www.mts.com/ucm/groups/public/documents/library/dev_002042.pdf
[139] MTS Systems Corporation. (2017, 07/01/2017). *FlexTest® Controllers* Available: https://www.mts.com/en/products/producttype/test-components/controllers/flextest-controllers/index.htm
[140] R. E. Walpole, R. H. Myers, S. L. Myers, and K. E. Ye, *Probability and Statistics for Engineers and Scientists, 9th Edition*: Pearson, 2012.
[141] Mathworks. (2016, 25/06/2016). *Curve Fitting*. Available: http://uk.mathworks.com/help/curvefit/curvefitting-app.html
[142] R. Shanmugam and R. Chattamvelli, *Statistics for Scientists and Engineers*: Wiley, 2015.
[143] Mathworks. (2016, 25/06/2016). *jbtest*. Available: https://uk.mathworks.com/help/stats/jbtest.html
[144] Mathworks. (2016, 25/06/2015). *corr*. Available: http://uk.mathworks.com/help/stats/corr.html
[145] P. F. Dunn, *Measurement and Data Analysis for Engineering and Science, Second Edition*: CRC Press, 2010.
[146] Mathworks. (2016, 25/06/2016). *xcorr*. Available: https://uk.mathworks.com/help/signal/ref/xcorr.html
[147] Mathworks. (2016, 25/06/2015). *kruskalwallis*. Available: http://uk.mathworks.com/help/stats/kruskalwallis.html
[148] Mathworks. (2016, 25/03/2016). *anova1*. Available: http://uk.mathworks.com/help/stats/anova1.html
[149] J. Hsu, *Multiple Comparisons: Theory and Methods*: Chapman and Hall/CRC 1996.
[150] Mathworks. (2016, 25/06/2016). *multcompare*. Available: http://uk.mathworks.com/help/stats/multcompare.html
[151] D. Triantis, I. Stavrakas, C. Anastasiadis, A. Kyriazopoulos, and F. Vallianatos, "An analysis of pressure stimulated currents (PSC), in marble samples under mechanical stress," *Physics and Chemistry of the Earth, Parts A/B/C,* vol. 31, pp. 234-239, // 2006.
[152] F. Vallianatos and A. Tzanis, "Electric current generation associated with the deformation rate of a solid: Preseismic and coseismic signals," *Physics and Chemistry of the Earth,* vol. 23, pp. 933-938, // 1998.
[153] B. Amadei and O. Stephansson, *Rock Stress and Its Measurement*: Springer Netherlands, 1997.
[154] A. Arnau and D. Soares, "Fundamentals of Piezoelectricity," in *Piezoelectric Transducers and Applications*, A. A. Vives, Ed., ed Berlin, Heidelberg: Springer Berlin Heidelberg, 2008, pp. 1-38.
[155] A. Alexandridis, D. Triantis, I. Stavrakas, and C. Stergiopoulos, "A neural network approach for compressive strength prediction in cement-based materials through the study of pressure-stimulated electrical signals," *Construction and Building Materials,* vol. 30, pp. 294-300, 5// 2012.

APPENDICES

This chapter contains fully annotated software code used for key elements of work presented in this thesis, as well as descriptions of the code structure. Code for the following devices and procedures are presented: EPS control interface device firmware, automatic bootstrap calibration procedure and PSV event detection in Appendix. A, Appendix. B and Appendix. C respectively.

APPENDIX. A EPS Control Interface

The firmware code is written in C++ and is designed to run on the Arduino Uno [119] development board, based electric potential sensor (EPS) control interface as described in section 4.6.4 of this thesis. The EPS control interface is connected to the restively coupled smart EPS via a cable, using an I^2C serial bus to communicate with digital potentiometers on the EPS, that in turn set the EPS bootstrap feedback and DC offset of the sensor. The EPS control interface is connected to a personal computer (PC) via a communication port (COM) connection.

The firmware is a menu graphical user interface (GUI), giving the user the option to increment the resistivity coupled smart EPS's bootstrap feedback percentage (input resistance adjustment) and DC offset. In addition, the user has the option to enter the automatic bootstrap calibration mode, in which the optimum bootstrap feedback percentage can then be calculated by the MATLAB® [108] script (Appendix. B) on a PC, using a COM between the PC and EPS via the EPS control interface. A detailed description of the input-output (IO) connections between EPS, EPS control interface and PC are described in detail in section 4.6 of this thesis.

```
// include the library code:
#include <LiquidCrystal.h> // LCD library
#include <SoftwareSerial.h> // serial communication library (COM)
#include <Wire.h> // I2C library
#include <EEPROM.h> // EPROM library

// initialize the LCD connections
LiquidCrystal lcd(8, 9, 4, 5, 6, 7); //initialise LCD

// define global variables
int key_value = 0; // key pad analogue value
int x = 0; // keypad identifier
int y = 0; // increment exit variable
int z = 0; // menu exit variable
int pot_address=0; // pot address 8 bit
int save_address; // save address
byte pot_val_boot_ch1=0; // pot position 0-255
byte pot_val_offset_ch1=0; // pot position 0-255
byte incomingByte = 0; // for incoming serial data

//set up
void setup() //enter the setup subroutine
{
  //start the LCD and I2C
  lcd.begin(16, 2); // start the LCD
  Wire.begin(); // start the I^2C
```

```
  Serial.begin(9600); // opens serial port, sets data rate to 9600 bps

  pot_set(); // reset pot wiper to last saved values

  // print start up message on LCD
  lcd.print("SMART EPS"); // print a message to the LCD.
  delay(1000); // display message for 1 second
  lcd.clear(); // clear the LCD messages
}

// main Program
void loop() // enter main program loop
{
  if (x==2) // enter bootstrap adjustment mode if key pressed
  {
     x=0; // reset the keypad
      do
      {
          if (x==2) // increment bootstrap % if key pressed
          {
            pot_address=byte(B1010011); // load the pot address bootstrap
adjustment
            save_address=0; // select the bootstrap EPROM save address
            pot_val_boot_ch1=pot_increment_bootstrap(pot_val_boot_ch1); //
increment the pot wiper position
            pot_save(); // save the current wiper position to EPROM
          }
          if (x==1) // if key pressed initialise exit condition
          {
            z=1; // exit condition
          }
          keypad(); // detect if a button has been pressed
          lcd.clear(); // clear the LCD
          lcd.setCursor(0,0);  // set LCD the cursor position to column 0,
line 1
          lcd.print("Bootstrap Adj"); // print bootstrap adjustment message
to LCD
          delay(200); // display the message for 200 mS

          y=0; // reset pot increment exit integer
      }while(z != 1); // stay in bootstrap adjustment mode unless exit
condition it met
  }
  if (x==4) // enter Offset adjustment mode if key is pressed
  {
      x=0; // reset the keypad
      do
      {
          if (x==4) // increment DC offset if key pressed
          {
          pot_address=byte(B1010000); // load the pot address for offset
adjustment
          save_address=1; // load the address EPROM offset value storage
          pot_val_offset_ch1=pot_increment_offset(pot_val_offset_ch1); //
increment the pot wiper position
          pot_save(); // save the current wiper position to EPROM
          }
          if (x==1) // if key pressed enable exit condition
          {
            z=1; // exit condition
```

```
          }
          keypad();// detect if a button has been pressed

          lcd.clear(); // clear the LCD
          lcd.setCursor(0,0);  // set the LCD cursor to column 0, line 0
          lcd.print("Offset Adj"); // display message to LCD
          delay(200); // display message for 200ms

          y=0; // reset pot increment exit variable
      }while(z != 1); // remain in offset adjustment mode unless exit
condition enabled
  }
  if (x==3) // enter auto bootstrap calibration mode
  {
      x=0; // reset the keypad
      do
      {
          if (Serial.available() > 0) // if there is serial data available
from PC
          {
             pot_address=byte(B1010011); // load the pot address for
bootstrap adjustment
             serialRead (); // read the serial data from the PC
          }
          if (x==1) // if key is pressed enable the exit condition
          {
            z=1; // exit condition
          }
          keypad(); // detect if a button has been pressed

          lcd.clear(); // clear the LCD
          lcd.setCursor(0,0); // set the LCD cursor to column 0, line 0
          lcd.print("Calibrating..."); // display message on LCD
          delay(200);  // display the message for 200 ms

          y=0;// reset exit integer for the pot increment function
      }while(z != 1); // remain in automatic bootstrap calibration mode
unless exit variable initialised
  }
  keypad();// detect if a button has been pressed
  lcd.clear(); // clear the LCD
  lcd.setCursor(0,0);  // set the LCD cursor to column 0, line 0
  lcd.print("Boot:<  Offset:>"); // print message to LCD
  lcd.setCursor(0,1);  // set the LCD cursor to column 0, line 0
  lcd.print("Calibration:V"); // print message to LCD
  delay(200); // display LCD messages for 200ms

  z=0; // reset exit integer for main loop

} // end of main loop

// reads the desired pot wiper position from the serial port and sets the
bootstrap pot value
void serialRead () // start of subroutine
{
  // read the incoming byte and set pot wiper position
  incomingByte =  Serial.read();
  if (Serial.available() > 0) // if there is data available from PC
  {
    if ((incomingByte != 10)) // if the incoming byte does not = 10
    {
```

```
      Wire.beginTransmission(pot_address); // start transmission to
bootstrap pot
      Wire.write(byte(B11000000)); // sends instruction byte (write to ram)
      Wire.write(incomingByte); // sends potentiometer value byte
      Wire.endTransmission(); // stop transmitting

      // display the current bootstrap percentage
      float bootrap_percent; // value to display on LCD
      bootrap_percent = 70 + (incomingByte*0.15625); // bootstrap as a
percentage 70 + binary position*(110-70/255)
      lcd.setCursor(0,1); // set the cursor to column 0, line 1
      lcd.print("Boot:     %"); // display text on LCD
      delay(500); // display text for 0.5 s
      lcd.setCursor(6,1); // reset the LCD cursor position
      lcd.print(bootrap_percent,DEC); // display the bootstrap feedback %
on LCD
      delay(500); // display the messages for 0.5 seconds
    }
  }
}

// reads the current keypad status
void keypad(void) // start of subroutine
{
  int analog_val = analogRead(A0); // read the analogue pin corresponding
to key presses

   if (analog_val > 735  &&  analog_val < 750 ) // if select button pressed
        x = 1; // set keypad identifier variable
   else  if( analog_val > 500  &&  analog_val < 520 ) // if left button
Pressed
        x = 2; // set keypad identifier variable
   else  if(analog_val > 325  &&  analog_val < 340 ) // if down button
pressed
        x = 3; // set keypad identifier variable
   else  if(analog_val < 10) // if right button Pressed
        x = 4; // set keypad identifier variable
   else  if(analog_val > 140  &&  analog_val < 155  ) // if up button
Pressed
        x = 5; // set keypad identifier variable
   else // Return 0 if no button pressed
        x = 0; // set keypad identifier variable
}

// moves the pot wiper position of bootstrap pots
int pot_increment_bootstrap (byte p) // define byte = pot instruction byte
and p = potentiometer value
{
    do{
        lcd.clear(); // clear the LCD
        int bootstrap_val; // local bootstrap wiper position byte
        float bootrap_percent; // local bootstrap feedback percentage
floating point number
        if (x==3) // decrement pot wiper
        {
            bootstrap_val= p--; // reduce bootstrap value
            bootrap_percent = 70+ (p*0.16); // bootstrap as a percentage 70
+ binary position*(110-70/255)
            lcd.setCursor(0,1);  // set the cursor to column 0, line 1
            lcd.print(bootrap_percent); // display the bootstrap %
            lcd.setCursor(6,1);  // set the cursor to column 6, line 1
```

```
            lcd.print("%"); // display the message to the LCD
            delay(100); // display the message for 100ms

            Wire.beginTransmission(pot_address); // start transmission ch2
offset
            Wire.write(byte(B11000000)); // sends instruction byte (write
to ram)
            Wire.write(p); // sends potentiometer value byte
            Wire.endTransmission(); // stop transmitting

        }
        if (x==5) // increment pot wiper
        {
            bootstrap_val= p++; // increase bootstrap value
            bootrap_percent = 70+ (p*0.16); // bootstrap as a percentage 70
+ binary position*(40/255)
            lcd.setCursor(0,1);  // set the cursor to column 0, line 1
            lcd.print(bootrap_percent); // display the bootstrap % on LCD
            lcd.setCursor(6,1);  // set the cursor to column 6, line 1
            lcd.print("%"); // display the message on the LCD
            delay(100); // display the message for 100 ms

            Wire.beginTransmission(pot_address); // start transmission ch2
offset
            Wire.write(byte(B11000000)); // sends instruction byte (write
to ram)
            Wire.write(p); // sends potentiometer value byte
            Wire.endTransmission(); // stop transmitting
        }
        if (x==1) // save wiper position
        {
            lcd.clear(); // clear the LCD display
            lcd.setCursor(0,1);  // set the cursor to column 0, line 1
            lcd.print("Saving..."); // display the message on the LCD
            delay(1000); // display the message for 1 second
            pot_save(); // save the pot position to EPROM
            return bootstrap_val; // returns the binary value of the wiper
position to be remembered next time
            y=1; // enable subroutine exit variable
        }

        keypad(); // detect if a button has been pressed
        lcd.setCursor(0,0); // set the cursor to column 0, line 0
        lcd.print("Up:^ Down:v"); // display the message
        lcd.setCursor(0,1); // set the cursor to column 0, line 1
        lcd.print(bootrap_percent); // display the bootstrap percentage
        lcd.setCursor(6,1); // set the cursor to column 6, line 1
        lcd.print("%"); // display the message
        delay(100); // display for 100 ms

      }while(y != 1); // exit loop if exit variable enabled
}

// moves the wiper position of the offset pots
int pot_increment_offset (byte p) // define byte = pot instruction byte and
p = potentiometer value
{
    do{
        lcd.clear(); // clear the LCD
        int offset_val; // local wiper position byte
```

```
        float offset_voltage; //local wiper voltage level floating point
number
        if (x==3) // decrement pot wiper
        {
            offset_val= p++; // increase the wiper position
            offset_voltage =(offset_val-128)*-0.98; // (wiper position byte
-128) * (125mV/128)
            lcd.setCursor(0,1);  // set the cursor to column 0, line 1
            lcd.print(offset_voltage); // display the message on LCD
            lcd.setCursor(8,1);  // set the cursor to column 8, line 1
            lcd.print("mV"); // display the message on LCD
            delay(100); // display message for 100 ms

            Wire.beginTransmission(pot_address); // start transmission
offset
            Wire.write(byte(B11000000)); // sends instruction byte (write
to ram)
            Wire.write(p); // sends potentiometer value byte
            Wire.endTransmission(); // stop transmitting

        }
        if (x==5) // increment pot wiper
        {
            offset_val= p--; // decrease offset value
            offset_voltage =(offset_val-128)*-0.98; // (wiper position byte
-128) * (125mV/128)
            lcd.setCursor(0,1);  // set the cursor to column 0, line 1
            lcd.print(offset_voltage); // display message on LCD
            lcd.setCursor(8,1);  // set the cursor to column 8, line 1
            lcd.print("mV"); // display message on LCD
            delay(100); // delay for 100ms

            Wire.beginTransmission(pot_address); // start transmission ch2
offset
            Wire.write(byte(B11000000)); // sends instruction byte (write
to ram)
            Wire.write(p); // sends potentiometer value byte
            Wire.endTransmission(); // stop transmitting
        }
        if (x==1) // save wiper position
        {
            lcd.clear(); // clear the LCD
            lcd.setCursor(0,1);  // set the cursor to column 0, line 1
            lcd.print("Saving..."); // display the message on LCD
            delay(1000); // display message for 1 s
            pot_save(); // save the offset pot wipe reposition to EPROM
            return offset_val; // return the current wiper potion so value
can be loaded next time
            y=1; // enable the subroutine exit variable
        }

        keypad(); // detect if a button has been pressed
        lcd.setCursor(0,0); // set the cursor to column 0, line 0
        lcd.print("Up:^ Down:v");
        lcd.setCursor(0,1); // set the cursor to column 0, line 1
        lcd.print(offset_voltage);
        lcd.setCursor(8,1); // set the cursor to column 8, line 1
        lcd.print("mV"); // display message on LCD
        delay(100); // display message for 1 ms

      }while(y != 1); // increment offset unless exit variable is enabled
```

```
}
// save the pot position to EEPROM
void pot_save (void) // start of subroutine
{
  if(save_address==0){ // if the bootstrap save viable is enabled
  EEPROM.write(save_address,pot_val_boot_ch1);   // save bootstrap value to
EPROM
  }
  if(save_address==1){ // if the offset save variable is enabled
  EEPROM.write(save_address,pot_val_offset_ch1);   //save offset value to
EPROM
  }
}

// sets the value of the bootstrap and DC offset pots from saved values in
EPROM
void pot_set(void) // start of subroutine
{
  pot_val_boot_ch1= EEPROM.read(0); // retrieve the bootstrap value from
EPROM memory
  Wire.beginTransmission(byte(B1010011)); // start transmission boot
  Wire.write(byte(B11000000)); // sends instruction byte (write to ram)
  Wire.write(pot_val_boot_ch1); // sends potentiometer value byte
  Wire.endTransmission(); // stop transmitting

  pot_val_offset_ch1 = EEPROM.read(1); // retrieve the offset value from
EPROM memory
  Wire.beginTransmission(byte(B1010000)); // start transmission ch1 offset
  Wire.write(byte(B11000000)); // sends instruction byte (write to ram)
  Wire.write(pot_val_offset_ch1); // sends potentiometer value byte
  Wire.endTransmission(); // stop transmitting
}
```

APPENDIX. B EPS Bootstrap Automatic Calibration

APPENDIX. B. 1 Data Acquisition

This function is designed to run on a National Instruments (NI) [135] PXIe1071 computer in the MATLB® [108] numerical computing environment, with a NI PXI-6124 data acquisition (DAQ) card inserted into PXI slot 3 of the PC. The EPS sensing electrode and a stimulus electrode are mounted on opposite sides of a cuboid rock specimen. The output of the restively coupled smart EPS and the stimulus electrode are connected to analogue inputs of the NI DAQ and the stimulus electrode is also connected to an analogue output of the NI DAQ.

The MATLAB® [108] function shown below applies a step voltage signal to the stimulus electrode and records the response of the EPS and rock from the EPS output signal at different values of bootstrap feedback percentage. The EPS control interface must be put into auto bootstrap calibration mode, in order to communicate with the MATLAB® [108] function running on the PC. The IO connections are described in detail in section 4.6 of this thesis.

```
function [ n] = DataAquisitionCalibration(
sample_rate,SaveFileLocation,PulsePeriod,LowPot,HighPot)
% DATA AQUISITION CALIBRATION: - This function sets up two analogue
% inputs (ai0 & ai1) channels and one analogue output (ao0). A restively
% coupled smart EPS is connected to ai0 and stimulus electrode is connected
% to ao0 and ai1. A 5V square wave is fed into the rock sample and its
% response is measured at various bootstrap levels defined by the
% limits LowPot and Highpot.

%   Sample rate: sampling rate of acquisition and output stimulus
%   SaveFileLocation: location of calibration data
%   PulsePeriod: period of stimulus
%   LowPot: lower pot position for bootstrap feedback (min 70%)
%   HighPot: upper pot position for bootstrap feedback (max 110%)

%% convert bootstrap range to pot position
LowPot=(LowPot-70)/(40/256); % low wiper position
HighPot=(HighPot-70)/(40/256); % high wiper position
HighPot = round(HighPot); % round to nearest whole number
LowPot = round(LowPot); % round to nearest whole number

%% fixes NI clock chassis bug in DAQmx
daq.reset
daq.HardwareInfo.getInstance('DisableReferenceClockSynchronization',true);

%% set up the acquisition channels and sample rate
s = daq.createSession('ni'); % start session
addAnalogInputChannel(s,'PXI1Slot3', 'ai0', 'Voltage'); % add Input channel
EPS
addAnalogInputChannel(s,'PXI1Slot3', 'ai1', 'Voltage'); % add Input channel
stimulus
s.Rate = sample_rate % sample rate Hz

%% save data to file listener
fid1 = fopen(SaveFileLocation,'w'); % create binary file log.bin with data
identifier fid1
lg = addlistener(s,'DataAvailable',@(src, event)logData(src, event, fid1));
% save the data to the binary file
```

```
%% real time plot listener
lh = addlistener(s,'DataAvailable', @(src,event) plot(event.TimeStamps,
event.Data)); % plot the graph every time the index exceeds a value
s.NotifyWhenDataAvailableExceeds = sample_rate; % plot graph once per
second

%% start the acquisition
s.IsContinuous = true; % acquire the data until stop command given
s.startBackground(); % the acquisition can run in parallel with other
executions in MATLAB

%% whilst the acquisition is happening send the output signal and COM port
data
% setup the analogue output channels
p = daq.createSession('ni'); % start session
addAnalogOutputChannel(p,'PXI1Slot3', 'ao0', 'Voltage'); % add output
channel
p.Rate = sample_rate; % sample rate Hz

%% set up serial port communication with EPS control interface
q = serial('COM4'); % port in which EPS control interface is connected
set(q,'BaudRate',9600); % serial coms board rate
fopen(q); % open the serial communication
for n = LowPot:HighPot; % execute over the set bootstrap range
        n=n % display current wiper position in command window
        fwrite(q,n,'uint16','sync'); % send pot wiper position via com port
        % output step signal via analogue output to stimulus electrode
        outputSingleScan(p,5); % output 5V
        pause(PulsePeriod/2); % duration 2 seconds
        outputSingleScan(p,0); % Output 0V
        pause(PulsePeriod/5); % duration 5 seconds
end

%% close the serial port communication
 fclose(q)
 delete(q)
 clear q

%% stop acquisition and delete the listeners
s.stop; % stops the data acquisition
delete(lh) % delete the listener so it is not used in the next acquisition
delete(lg) % delete the listener so it is not used in the next acquisition

end % end of the function
```

APPENDIX. B. 2 Optimum bootstrap feedback calculation

The function is designed to run in the MATLAB® [108] numerical computing environment on a standard PC. The function interprets the binary data produced from the automatic bootstrap calibration data acquisition function (Appendix. B. 1) and calculates the optimal EPS bootstrap feedback percentage.

The function plots the step response data so the user can enter the value of bootstrap positive feedback in which the EPS becomes unstable. The function then calculates which step response has the fastest settling time and displays the fastest setting time along with the corresponding value of bootstrap feedback. This value of bootstrap feedback can then be used as a ball park figure for material testing experiments, in order to achieve the lowest frequency pressure stimulated voltage (PSV) response from the particular material being tested. A detailed description of the automatic bootstrap calibration procedure is described in section 4.6.

```
function [ time, EPS, Stimulus, settling_times, shortest_times] =
ReadCalibrationData(FileName,sample_rate,window_size,pulseperiod, LowPot,
HighPot)
% READ CALIBRATION DATA: - This function opens a binary file containing the
% auto bootstrap calibration data, applies signal processing to remove
% unwanted offsets and noise and plots the step response data for the user
% to evaluate when the bootstrap feedback % becomes unstable. The function
% then computes the fastest EPS setting time, plots the fastest step
% response and displays the optimal bootstrap feedback % to the
% command window.

%   FileName: binary file containing the auto bootstrap calibration data
%   sample_rate: sample rate used for data acquisition
%   window_size: data smoothing window size (moving average)
%   pulseperiod: period of stimulus
%   LowPot: lower pot position for bootstrap feedback (min 70%)
%   HighPot: upper pot position for bootstrap feedback (max 110%)

%% convert bootstrap value to pot positions
LowPot=(LowPot-70)/(40/256); % convert bootstrap feedback % to pot wiper
position
HighPot=(HighPot-70)/(40/256); % convert bootstrap feedback % to pot wiper
position
HighPot = round(HighPot); % round to nearest whole number
LowPot = round(LowPot); % round to nearest whole number

%% read the binary file
fid2 = fopen(FileName,'r'); % open the binary data file
[data,count] = fread(fid2,[3,inf],'double'); % read the 3 columns of data
time, EPS output, stimulus
fclose(fid2); % close the binary file

%% split the data into time, EPS and stimulus then plot data
time = data(1,:); % time data
EPS = data(2:2,:); % EPS output data (response)
Stimulus  = data(3:3,:); % stimulus  data (step input)

%% filter the data and remove DC offset
EPS=EPS'; % change to column data
EPS=EPS*-1; % invert because EPS is an inverting amplifier
% notch filter data
```

```
wo = 50/(sample_rate/2);  bw = wo/35; % filter signal with sampling
frequency (fs) at 50hz
[b,a] = iirnotch(wo,bw); % generate notch filter
EPS=filter(b,a,EPS); % filter the EPS data
% moving average filter
EPS = tsmovavg(EPS,'s',window_size,1); % simple moving average
% remove initial offset
 start_val = sum(EPS(window_size:1:window_size+sample_rate))/sample_rate; %
average initial 1 second of data
 if start_val > 0
    EPS = EPS - start_val; % remove initial offset
 elseif start_val < 0
     EPS = EPS + start_val; % remove initial offset
 else
     EPS=EPS; % do nothing if there is no offset
 end

 %% plot the experiment for evaluation
 figure(1);
 % configure the bootstrap vector
 n= sample_rate*pulseperiod; x=(LowPot:1:HighPot)';
 r=repmat(x,1,n)';
 r=r(:)';
 BootstrapVal= (r*(40/256)) +70;
 z = size(EPS,1)-size(BootstrapVal,2); % size difference of EPS signal and
bootstrap vector
 % plot the data
 figure(1); % first figure to be plotted
 plot3(time(z+1:end),EPS(z+1:end),BootstrapVal); % plot time vs. response
voltage vs. bootstrap feedback value
 title('Instability Region Selection Graph') % graph title
 xlabel('Time [S]') % x-axis label
 ylabel('EPS RT0 [V]') % y-axis label
 zlabel('Bootstrap feedback [%]') % z-axis label

%% ask the user what value of bootstrap the EPS become unstable
 prompt = 'Choose a bootstrap value in the instability region, but before
railing occurs? '; % print prompt message to command window
x = input(prompt); % variable in which user enters maximum stable bootstrap
perecentage
HighPot= (x-70)/(40/256); % reconfigure maximum bootstrap percentage base
on users input

%% calculate settling times
% split the stimulus pulse responses into sections. 1 section per bootstrap
adjustment
[peakLoc, peakMag]=peakfinder(diff(EPS), 0.0001,0.02); % find the start of
each rising slope

for i =LowPot-LowPot+1:HighPot-LowPot % execute over the stable bootstrap
range
    EPS_single= EPS(peakLoc(i+1) -
(sample_rate*(pulseperiod/2)*0.05):peakLoc(i+1) +
sample_rate*(pulseperiod/2)*0.95); % response section start 5% before peak
and 10% before next peak
    time_single=time(peakLoc(i+1)-
(sample_rate*(pulseperiod/2)*0.05):peakLoc(i+1) +
sample_rate*(pulseperiod/2)*0.95); % time section start 5% before peak and
10% before next peak
```

```
    time_single=time_single - time_single(1); % reset the start time of
each section to zero (used for plotting)
    time_store{i}=time_single; % store time section data for later
    EPS_single= EPS_single - EPS_single(1);% remove response offset of each
section (used for plotting)
    EPS_store{i}=EPS_single; % store response data section for later

    settling_times{i}=stepinfo(EPS_single,time_single); % work out the step
response settling time of the current section
    bootstrapVal=  repmat(70 + ((i + LowPot)*0.1563),1,size(EPS_single,1));
% reformat the bootstrap feedback percentage vector

    figure(2); % the second figure to be plotted
    plot3(time_single,EPS_single,bootstrapVal)% plot the section response
(individual step response)
    title('Individual rise time plot') % graph title
    xlabel('Time [S]') % x-axis label
    ylabel('EPS RT0 [V]') % y-axis label
    zlabel('Bootstrap feedback [%]') z-axis label

    grid on; % enable plotting grid
    hold all; % plots different colour individual step response each time
end

%% find the shortest settling time
for i = LowPot-LowPot+1:HighPot-LowPot % execute over the stable bootstrap
range
    shortest_times(i)= settling_times{1,i}.SettlingTime; % extract the
settling times from the step response structure
end
[r,c]=find(shortest_times==min(min(shortest_times))); % fastest settling
time location

BootstrapVal = (70+(LowPot*0.1563)) + (c*0.1563); % bootstrap feedback
percentage corresponding fastest settling time value
shortest_time=min(shortest_times); % fastest settling time value

%% plot the optimum bootstrap response
figure(3); % 3rd figure to be plotted
plot(time_store{c},EPS_store{c}); % plot the fastest step response
title('Optimum Bootstrap responce') % graph title
xlabel('Time [S]') % x-axis label
ylabel('EPS RT0 [V]') % y-axis label
zlabel('Bootstrap feedback [%]') % z-axis label

%% display the settling time and bootstrap value
display(['Optium Boostrap Value:', num2str(BootstrapVal)]) % display
bootstrap value corresponding to fastest step response
display(['With settling time:', num2str(shortest_time)])  % display fastest
setting time of step responses
end
```

APPENDIX. C PSV event detection

The PSV event detection function is designed to run the MATLAB® [108] numerical computing environment on a PC. The function operates on the binned PSV data and is used to extract PSV events and outputs the event times, event amplitudes, cumulative number of events and high pass filtered (HPF) PSV data.

The binned PSV data is HPF to extract the high frequency transient PSV signals associated with cracking events. The `peakfinder` function is then used to find the local maxima and minima of the HPF PSV signal. Local maxima and minima that are larger than 2% of the PSV voltage range in magnitude compared to surrounding data are classified as PSV events. Detailed information about PSV and AE event detection is described in section 4.7.1.

```
function [EPcume, Z, PeakMagEP, PeakLocEP] = EP_event_detection(EP)
% EP EVENT DETECTION: - This function high pass filters the binned PSV data
% to extract the high frequency transients associated with cracking.
% It then uses the peak finder function to detect the local maxima and
% minima 2% greater in amplitude than surrounding data. The
% detected peaks are extracted as PSV events and cumulative number of
% events.

    % EPcume: PSV cumulative number of PSV events per bin
    % Z: HPF PSV data
    % PeakMagEP: PSV event amplitude
    % PeakLocEP: PSV event time

x = EP; % binned PSV data copied to variable

%% remove any low frequency components
y = smooth(x); % smooth the data
Z = x-y; % HPF PSV data

%% calculate the cumulative events
[peakLocEP peakMagEP] = peakfinder(Z,((max(Z)-min(Z))/50)); %
peakfinder(data, sel) detect peaks using 2% difference
EP_hits = zeros(length(Z),1); % create empty vector of PSV events
EP_hits(peakLocEP) = peakMagEP; % fill vector with PSV event amplitudes
EPcume =EP_hits./EP_hits; % Covert hit amplitudes to vector of ones
EPcume(isnan(EPcume))=0; % replace isnan with zeros
EPcume = cumsum(EPcume); % calculate the cumulative number of events
end
```